

Ministry of Education and Science of the Russian Federation
Saint Petersburg National Research University of Information
Technologies, Mechanics, and Optics

NANOSYSTEMS:
PHYSICS, CHEMISTRY, MATHEMATICS

2020, volume 11(4)

Наносистемы: физика, химия, математика

2020, том 11, № 4



NANOSYSTEMS:

PHYSICS, CHEMISTRY, MATHEMATICS

ADVISORY BOARD MEMBERS

Chairman: V.N. Vasiliev (*St. Petersburg, Russia*),
V.M. Buznik (*Moscow, Russia*); V.M. Ievlev (*Voronezh, Russia*), P.S. Kop'ev (*St. Petersburg, Russia*), N.F. Morozov (*St. Petersburg, Russia*), V.N. Parmon (*Novosibirsk, Russia*),
A.I. Rusanov (*St. Petersburg, Russia*),

EDITORIAL BOARD

Editor-in-Chief: I.Yu. Popov (*St. Petersburg, Russia*)

Section Co-Editors:

Physics – V.M. Uzdin (*St. Petersburg, Russia*),
Chemistry, material science – V.V. Gusarov (*St. Petersburg, Russia*),
Mathematics – I.Yu. Popov (*St. Petersburg, Russia*).

Editorial Board Members:

V.M. Adamyan (*Odessa, Ukraine*); O.V. Al'myasheva (*St. Petersburg, Russia*);
A.P. Alodjants (*Vladimir, Russia*); S. Bechta (*Stockholm, Sweden*); J. Behrndt (*Graz, Austria*);
M.B. Belonenko (*Volgograd, Russia*); A. Chatterjee (*Hyderabad, India*); S.A. Chivilikhin
(*St. Petersburg, Russia*); A.V. Chizhov (*Dubna, Russia*); A.N. Enyashin (*Ekaterinburg, Russia*),
P.P. Fedorov (*Moscow, Russia*); E.A. Gudilin (*Moscow, Russia*); V.K. Ivanov
(*Moscow, Russia*), H. Jónsson (*Reykjavik, Iceland*); A.A. Kiselev (*Durham, USA*);
Yu.S. Kivshar (*Canberra, Australia*); S.A. Kozlov (*St. Petersburg, Russia*); P.A. Kurasov
(*Stockholm, Sweden*); A.V. Lukashin (*Moscow, Russia*); I.V. Melikhov (*Moscow, Russia*);
G.P. Miroshnichenko (*St. Petersburg, Russia*); I.Ya. Mittova (*Voronezh, Russia*); Nguyen
Anh Tien (*Ho Chi Minh, Vietnam*); V.V. Pankov (*Minsk, Belarus*); K. Pankrashkin (*Orsay, France*);
A.V. Ragulya (*Kiev, Ukraine*); V. Rajendran (*Tamil Nadu, India*); A.A. Rempel
(*Ekaterinburg, Russia*); V.Ya. Rudyak (*Novosibirsk, Russia*); D Shoikhet (*Karmiel, Israel*);
P Stovicek (*Prague, Czech Republic*); V.M. Talanov (*Novocherkassk, Russia*); A.Ya. Vul'
(*St. Petersburg, Russia*); A.V. Yakimansky (*St. Petersburg, Russia*), V.A. Zagrebnev
(*Marseille, France*).

Editors:

I.V. Blinova; A.I. Popov; A.I. Trifanov; E.S. Trifanova (*St. Petersburg, Russia*),
R. Simoneaux (*Philadelphia, Pennsylvania, USA*).

Address: University ITMO, Kronverkskiy pr., 49, St. Petersburg 197101, Russia.

Phone: +7(812)312-61-31, **Journal site:** <http://nanojournal.ifmo.ru/>,

E-mail: popov1955@gmail.com

AIM AND SCOPE

The scope of the journal includes all areas of nano-sciences. Papers devoted to basic problems of physics, chemistry, material science and mathematics inspired by nanosystems investigations are welcomed. Both theoretical and experimental works concerning the properties and behavior of nanosystems, problems of its creation and application, mathematical methods of nanosystem studies are considered.

The journal publishes scientific reviews (up to 30 journal pages), research papers (up to 15 pages) and letters (up to 5 pages). All manuscripts are peer-reviewed. Authors are informed about the referee opinion and the Editorial decision.

CONTENT

MATHEMATICS

- R.N. Ganikhodjaev, R.R. Kucharov, K.A. Aralova
Positive fixed points of Lyapunov operator 373

PHYSICS

- Bhimanand Pandurang Gajbhare, J.S.V.R. Krishna prasad, S.R. Mishra
Peristaltic pumping through non-Darcy porous medium in an electroosmotic flow with entropy analysis 379

- Vipul Shukla, Dr. Amit Patel
Effect of doping concentration on optical and electrical properties of intrinsic n-type ZnO (i-ZnO) and (Cu, Na and K) doped p-type ZnO thin films grown by chemical bath deposition method 391

- M.A. Moskalenko, I.S. Lobanov, V.M. Uzdin
Demagnetizing fields in chiral magnetic structures 401

CHEMISTRY AND MATERIAL SCIENCE

- A.V. Pokropivny, A.N. Enyashin, A.S. Smolyar, V.A. Kuts, V.G. Gurin, S.A. Antipov, P.M. Silenko, Yu.M. Solonin
Supercritical fluid synthesis and possible properties of “cubic graphite” 408

- P.P. Fedorov, M.N. Mayakova, A.A. Alexandrov, V.V. Voronov, D.V. Pominova, E.V. Chernova, V.K. Ivanov
Synthesis of NaYF₄:Yb, Er up-conversion luminophore from nitrate flux 417

- T. Vidya Sagar, T. Subba Rao, N. Raghuram
Temperature dependent structural, morphological, FTIR, optical, magnetic properties of NiMgZn ferrites 434

- A.S. Garde
Large scale synthesis and characterization of cadmium sulfide nanoparticles by simple chemical route 444

- V. Gupta, P.K. Verma, A. Gupta, V. Kant, P. Kumar, M. Sharma
Comparative evaluation for wound healing potentials of bulk and nano forms of zinc oxide ointment 453

G.A. Glushnev, Kanbar Ayat, V.A. Keskinov, N.A. Charykov, K.N. Semenov, Z.K. Shaimardanov, B.K. Shaimardanova, N.A. Kulenova, D.G. Letenko Solubility phase equilibrium in ternary system fulleranol C₆₀(OH)₂₄ and praseodymium salt: PrCl₃-C₆₀(OH)₂₄-H₂O at 25°C	462
A.T. Nguyen, V.Y. Nguyen, I.Ya. Mittova, V.O. Mittova, E.L. Viryutina, C.Ch.T. Hoang, Tr.L.T. Nguyen, X.V. Bui, T.H. Do Synthesis and magnetic properties of PrFeO₃ nanopowders by the co-precipitation method using ethanol	468
M.I. Chebanenko, K.D. Martinson, I.V. Matsukevich, V.I. Popkov The effect of MgO additive on the g-C₃N₄ performance in electrochemical reforming of water-ethanol solution	474
E.S. Ulyanova, D.A. Zamyatin, V.Yu. Kolosov, E.V. Shalaeva Visible light photoluminescence in TiO₂/CdS nanopowders synthesized by sol-gel route: effect of gel aging time	480
Venkatesh Yepuri, R.S. Dubey, Brijesh Kumar Fabrication and characterization of spectrally selective glazing dielectric multilayer structures	488
Information for authors	493

Positive fixed points of Lyapunov operator

R. N. Ganikhodjaev, R. R. Kucharov, K. A. Aralova

National University of Uzbekistan, 100174, Tashkent, Uzbekistan

ramz3364647@yahoo.com

DOI 10.17586/2220-8054-2020-11-4-373-378

In this paper, fixed points of Lyapunov integral equation are found and considered the connections between Gibbs measures for four competing interactions of models with uncountable (i.e. $[0, 1]$) set of spin values on the Cayley tree of order two.

Keywords: Lyapunov integral operator, fixed points, Cayley tree, Gibbs measure.

Received: 13 January 2020

Revised: 9 August 2020

1. Introduction

Spin models on a graph or in continuous spaces form a large class of systems considered in mechanics, biology, nanoscience, etc. Some of them have a real physical meaning, others have been proposed as suitably simplified models of more complicated systems. The geometric structure of the graph or a physical space plays an important role in such investigations. For example, in order to study the phase transition problem on a cubic lattice Z^d or in space one uses, essentially, the Pirogov-Sinai theory; see [1–3]. A general methodology of phase transitions in Z^d or \mathbb{R}^d was developed in [4]; some recent results in this direction have been established in [5,6] (see also the bibliography therein).

During last years, an increasing attention was given to models with a *uncountable* many spin values on a Cayley tree. Until now, one considered nearest-neighbor interactions ($J_3 = J = \alpha = 0$, $J_1 \neq 0$) with the set of spin values $[0, 1]$ (for example, [7–12]).

In [13] it is described that splitting Gibbs measures on Γ_2 by solutions to a nonlinear integral equation for the case $J_3^2 + J_1^2 + J^2 + \alpha^2 \neq 0$ which a generalization of the case $J_3 = J = \alpha = 0$, $J_1 \neq 0$. Also, it is proven that periodic Gibbs measure for Hamiltonian (1) with four competing interactions is either *translation-invariant* or $G_k^{(2)}$ – *periodic*.

In this paper, we consider Lyapunov’s operator with degenerate kernel. In [11], Fixed points of Lyapunov’s operator with special degenerate kernel are studied. The present paper is a continuation of the paper [11], i.e., we give full description of fixed points of Lyapunov’s operator with another special degenerate kernel.

A Cayley tree $\Gamma^k = (V, L)$ of order $k \in \mathbb{N}$ is an infinite homogeneous tree, i.e., a graph without cycles, with exactly $k + 1$ edges incident to each vertex. Here V is the set of vertices and L that of edges (arcs). The distance $d(x, y)$, $x, y \in V$ is the number of edges of the path from x to y . Let $x^0 \in V$ be a fixed and we set

$$W_n = \{x \in V \mid d(x, x^0) = n\}, \quad V_n = \{x \in V \mid d(x, x^0) \leq n\},$$

$$L_n = \{l = \langle x, y \rangle \in L \mid x, y \in V_n\},$$

If the distance from x to y equals one then we say x and y are nearest neighbors and use the notation $l = \langle x, y \rangle$. The set of the direct successors of x is denoted by $S(x)$, i.e.

$$S(x) = \{y \in W_{n+1} \mid d(x, y) = 1\}, \quad x \in W_n.$$

We observe that for any vertex $x \neq x^0$, x has k direct successors and x^0 has $k + 1$. The vertices x and y are called second neighbor which is denoted by $\succ x, y \prec$, if there exist a vertex $z \in V$ such that x, z and y, z are nearest neighbors. We will consider only second neighbors $\succ x, y \prec$, for which there exist n such that $x, y \in W_n$. Three vertices x, y and z are called a triplet of neighbors and they are denoted by $\langle x, y, z \rangle$, if $\langle x, y \rangle$, $\langle y, z \rangle$ are nearest neighbors and $x, z \in W_n$, $y \in W_{n-1}$, for some $n \in \mathbb{N}$.

Now, we consider models with four competing interactions where the spin takes values in the set $[0, 1]$. For some set $A \subset V$ an arbitrary function $\sigma_A : A \rightarrow [0, 1]$ is called a configuration and the set of all configurations on A we denote by $\Omega_A = [0, 1]^A$. Let $\sigma(\cdot)$ belong to $\Omega_V = \Omega$ and $\xi_1 : (t, u, v) \in [0, 1]^3 \rightarrow \xi_1(t, u, v) \in R$, $\xi_i : (u, v) \in [0, 1]^2 \rightarrow \xi_i(u, v) \in R$, $i \in \{2, 3\}$ are given bounded, measurable functions.

We consider models with four competing interactions where the spin takes values in the unit interval $[0, 1]$. Given a set $\Lambda \subset V$ a configuration on Λ is an arbitrary function $\sigma_\Lambda : \Lambda \rightarrow [0, 1]$, with values $\sigma(x)$, $x \in \Lambda$. The set of all

configurations on Λ is denoted by $\Omega_\Lambda = [0, 1]^\Lambda = \Omega$ and denote by \mathcal{B} the sigma-algebra generated by measurable cylinder subsets of Ω .

Fix bounded, measurable functions $\xi_1 : (t, u, v) \in [0, 1]^3 \rightarrow \xi_1(t, u, v) \in R$ and $\xi_i : (u, v) \in [0, 1]^2 \rightarrow \xi_i(u, v) \in R, i = 2, 3$. We consider a model with four competing interactions on the Cayley tree which is defined by a formal Hamiltonian

$$\begin{aligned}
 H(\sigma) = & -J_3 \sum_{\langle x,y,z \rangle} \xi_1(\sigma(x), \sigma(y), \sigma(z)) - J \sum_{\langle x,y \rangle} \xi_2(\sigma(x), \sigma(y)) \\
 & - J_1 \sum_{\langle x,y \rangle} \xi_3(\sigma(x), \sigma(y)) - \alpha \sum_x \sigma(x),
 \end{aligned} \tag{1}$$

where the sum in the first term ranges all triples of neighbors, the second sum ranges all second neighbors, the third sum ranges all nearest neighbors, and $J, J_1, J_3, \alpha \in R \setminus \{0\}$.

Let $h : [0, 1] \times V \setminus \{x^0\} \rightarrow \mathbb{R}$ and $|h(t, x)| = |h_{t,x}| < C$ where x_0 is a root of Cayley tree and C is a constant which does not depend on t . For some $n \in \mathbb{N}, \sigma_n : x \in V_n \mapsto \sigma(x)$ and Z_n is the corresponding partition function we consider the probability distribution $\mu^{(n)}$ on Ω_{V_n} defined by:

$$\mu^{(n)}(\sigma_n) = Z_n^{-1} \exp \left(-\beta H(\sigma_n) + \sum_{x \in W_n} h_{\sigma(x),x} \right), \tag{2}$$

$$Z_n = \int \dots \int_{\Omega_{V_{n-1}}^{(p)}} \exp \left(-\beta H(\tilde{\sigma}_n) + \sum_{x \in W_n} h_{\tilde{\sigma}(x),x} \right) \lambda_{V_{n-1}}^{(p)}(d\tilde{\sigma}_n), \tag{3}$$

where

$$\underbrace{\Omega_{W_n} \times \Omega_{W_n} \times \dots \times \Omega_{W_n}}_{3 \cdot 2^{p-1}} = \Omega_{W_n}^{(p)}, \quad \underbrace{\lambda_{W_n} \times \lambda_{W_n} \times \dots \times \lambda_{W_n}}_{3 \cdot 2^{p-1}} = \lambda_{W_n}^{(p)}, \quad n, p \in \mathbb{N},$$

Let $\sigma_{n-1} \in \Omega_{V_{n-1}}$ and $\sigma_{n-1} \vee \omega_n \in \Omega_{V_n}$ is the concatenation of σ_{n-1} and ω_n . For $n \in \mathbb{N}$ we say that the probability distributions $\mu^{(n)}$ are compatible if $\mu^{(n)}$ satisfies the following condition:

$$\int \int_{\Omega_{W_n} \times \Omega_{W_n}} \mu^{(n)}(\sigma_{n-1} \vee \omega_n) (\lambda_{W_n} \times \lambda_{W_n})(d\omega_n) = \mu^{(n-1)}(\sigma_{n-1}). \tag{4}$$

By Kolmogorov’s extension theorem, there exists a unique measure μ on Ω_V such that, for any n and $\sigma_n \in \Omega_{V_n}, \mu(\{\sigma|_{V_n} = \sigma_n\}) = \mu^{(n)}(\sigma_n)$. The measure μ is called *splitting Gibbs measure* corresponding to Hamiltonian (1) and function $x \mapsto h_x, x \neq x^0$ (see [7, 8, 14, 15]).

We denote:

$$K(u, t, v) = \exp \{ J_3 \beta \xi_1(t, u, v) + J \beta \xi_2(u, v) + J_1 \beta (\xi_3(t, u) + \xi_3(t, v)) + \alpha \beta (u + v) \}, \tag{5}$$

and

$$f(t, x) = \exp(h_{t,x} - h_{0,x}), \quad (t, u, v) \in [0, 1]^3, \quad x \in V \setminus \{x^0\}.$$

The following statement describes conditions on h_x guaranteeing the compatibility of the corresponding distributions $\mu^{(n)}(\sigma_n)$.

Proposition 1 [16] The measure $\mu^{(n)}(\sigma_n), n = 1, 2, \dots$ satisfies the consistency condition (4) iff for any $x \in V \setminus \{x^0\}$ the following equation holds:

$$f(t, x) = \prod_{\langle y,z \rangle \in S(x)} \frac{\int_0^1 \int_0^1 K(t, u, v) f(u, y) f(v, z) dudv}{\int_0^1 \int_0^1 K(0, u, v) f(u, y) f(v, z) dudv}, \tag{6}$$

where $S(x) = \{y, z\}, \langle y, x, z \rangle$ is a ternary neighbor.

2. Lyapunov operator with degenerate kernel

Let $\varphi_1(t)$, $\varphi_2(s)$ and $\varphi_3(u)$ are positive functions from $C_0^+[0, 1]$. We consider Lyapunov’s operator A (see [9,17]):

$$(Af)(t) = \int_0^1 \int_0^1 (\varphi_1(t) + \varphi_2(s) + \varphi_3(u)) f(s)f(u)dsdu.$$

and quadratic operator P on \mathbb{R}^3 by the rule

$$P(x, y, z) = (\alpha_{11}x^2 + xy + xz, \alpha_{21}x^2 + \alpha_{22}xy + \alpha_{22}xz, \alpha_{31}x^2 + \alpha_{33}xy + \alpha_{33}xz).$$

Here,

$$\begin{aligned} \alpha_{11} &= \int_0^1 \varphi_1(s)ds > 0; \\ \alpha_{22} &= \int_0^1 \varphi_2(s)ds > 0, \quad \alpha_{21} = \int_0^1 \varphi_1(s)\varphi_2(s)ds > 0; \\ \alpha_{33} &= \int_0^1 \varphi_3(s)ds > 0, \quad \alpha_{31} = \int_0^1 \varphi_1(s)\varphi_3(s)ds > 0. \end{aligned}$$

The existence of fixed points of Lyapunov’s operator A is proved in [16]. A sufficient condition of uniqueness of fixed points of Lyapunov operator A is given (see [8]).

Lemma 2.1 *Lyapunov’s operator A has a nontrivial positive fixed point iff the quadratic operator P has a nontrivial positive fixed point, moreover, $N_{fix}^+(A) = N_{fix}^+(P)$.*

Proof (a) Put

$$\begin{aligned} \mathbb{R}_3^+ &= \{(x, y, z) \in \mathbb{R}^3 : x \geq 0, y \geq 0, z \geq 0\}, \\ \mathbb{R}_3^> &= \{(x, y, z) \in \mathbb{R}^3 : x > 0, y > 0, z > 0\}. \end{aligned}$$

Let Lyapunov’s operator A has a nontrivial positive fixed point $f(t) \in C_0^+[0, 1]$. Let

$$x_1 = \int_0^1 f(u)du, \tag{7}$$

$$x_2 = \int_0^1 \varphi_2(u)f(u)du, \tag{8}$$

and

$$x_3 = \int_0^1 \varphi_3(u)f(u)du, \tag{9}$$

Clearly, $x_1 > 0, x_2 > 0, x_3 > 0$, i.e. $(x_1, x_2, x_3) \in \mathbb{R}_3^>$. Then, for the function $f(t)$, the equality

$$f(t) = \varphi_1(t)x_1^2 + x_1x_2 + x_1x_3 \tag{10}$$

holds.

Consequently, for parametrs c_1, c_2, c_3 from the equality (7), (8) and (9), we have the three identities:

$$\begin{aligned} x_1 &= x_1(\alpha_{11}x_1 + x_2 + x_3), \\ x_2 &= x_1(\alpha_{21}x_1 + \alpha_{22}x_2 + \alpha_{22}x_3), \\ x_3 &= x_1(\alpha_{31}x_1 + \alpha_{33}x_2 + \alpha_{33}x_3). \end{aligned}$$

Therefore, the point (c_1, c_2) is fixed point of the quadratic operator P .

(b) Assume, that the fixed point x_0, y_0, z_0 is a nontrivial positive fixed point of the quadratic operator P , i.e. $(x_0, y_0, z_0) \in \mathbb{R}_3^>$ and number x_0, y_0, z_0 satisfies the following equalities

$$\begin{aligned} x_0(\alpha_{11}x_0 + y_0 + z_0) &= x_0, \\ x_0(\alpha_{21}x_0 + \alpha_{22}y_0 + \alpha_{22}z_0) &= y_0, \\ x_0(\alpha_{31}x_0 + \alpha_{33}y_0 + \alpha_{33}z_0) &= z_0. \end{aligned}$$

Similarly, we can prove that the function $f_0(t) = \varphi_1(t)x_0^2 + x_0y_0 + x_0z_0$ is fixed point of Lyapunov’s operator A and $f_0(t) \in C_0^+[0, 1]$. This completes the proof.

3. Positive fixed points of the quadratic operators in cone \mathbb{R}_3^+

We define quadratic operator (QO) \mathcal{Q} in cone \mathbb{R}_3 by the rule

$$\mathcal{Q}(x, y, z) = (a_{11}x^2 + xy + xz, a_{21}x^2 + a_{22}xy + a_{22}xz, a_{31}x^2 + a_{33}xy + a_{33}xz).$$

3.1-lemma *If the point $\omega = (x_0, y_0, z_0) \in \mathbb{R}_2^+$ is fixed point of QO \mathcal{Q} , then x_0 is a root of the quadratic algebraic equation*

$$(a_{21} + a_{31} - a_{11}a_{22} - a_{11}a_{33})x^2 + (a_{11} + a_{22} + a_{33})x - 1 = 0 \tag{11}$$

Proof Let the point $\omega = (x_0, y_0, z_0) \in \mathbb{R}_3^+$ be a fixed point of QO \mathcal{Q} . Then

$$\begin{aligned} a_{11}x_0^2 + x_0y_0 + x_0z_0, & \quad a_{21}x_0^2 + a_{22}x_0y_0 + a_{22}x_0z_0, \\ a_{31}x_0^2 + a_{33}x_0y_0 + a_{33}x_0z_0. & \end{aligned}$$

Using the bellowing equalities, we obtain:

$$\begin{aligned} y_0 + z_0 &= 1 - a_{11}x_0 \\ y_0 &= x_0(a_{21}x_0 + a_{22}(1 - a_{11}x_0)) \\ z_0 &= x_0(a_{31}x_0 + a_{33}(1 - a_{11}x_0)) \\ y_0 + z_0 &= x_0(a_{21}x_0 + a_{22}(1 - a_{11}x_0)) + x_0(a_{31}x_0 + a_{33}(1 - a_{11}x_0)) = \\ &= (a_{21} + a_{31} - a_{11}a_{22} - a_{11}a_{33})x_0^2 + (a_{22} + a_{33})x_0 = a_{11}x_0 \end{aligned}$$

By the last equality, we get:

$$(a_{21} + a_{31} - a_{11}a_{22} - a_{11}a_{33})x_0^2 + (a_{11} + a_{22} + a_{33})x_0 - 1 = 0.$$

This completes the proof.

3.2-lemma *If the positive number x_0 is root of the quadratic algebraic Eq.(11), then the point $\omega_0 = (x_0, x_0(a_{21}x_0 + a_{22}(1 - a_{11}x_0)), x_0(a_{31}x_0 + a_{33}(1 - a_{11}x_0)))$ is fixed point of QO \mathcal{Q} .*

Proof Let x_0 be a root of the quadratic Eq.(11), i.e.,

$$\begin{aligned} &(a_{21} + a_{31} - a_{11}a_{22} - a_{11}a_{33})x_0^2 + (a_{11} + a_{22} + a_{33})x_0 - 1 = 0. \\ &x_0(a_{11}x_0 + y_0 + z_0) = \\ &= x_0(a_{11}x_0 + x_0(a_{21}x_0 + a_{22}(1 - a_{11}x_0)) + x_0(a_{31}x_0 + a_{33}(1 - a_{11}x_0))) = \\ &= x_0(a_{11}x_0 + (a_{21} + a_{31} - a_{11}a_{22} - a_{11}a_{33})x_0^2 + (a_{22} + a_{33})x_0) = \\ &= x_0((a_{21} + a_{31} - a_{11}a_{22} - a_{11}a_{33})x_0^2 + (a_{11} + a_{22} + a_{33})x_0 - 1 + 1) = x_0(0 + 1) = x_0 \end{aligned}$$

Then

$$y_0 + z_0 = 1 - a_{11}x_0.$$

From the last equality, we get:

$$\begin{aligned} &a_{21}x_0^2 + a_{22}x_0y_0 + a_{22}x_0z_0 = \\ &= x_0(a_{21}x_0 + a_{22}(y_0 + z_0)) = x_0(a_{21}x_0 + a_{22}(1 - a_{11}x_0)), \\ &a_{31}x_0^2 + a_{33}x_0y_0 + a_{33}x_0z_0 = \\ &= x_0(a_{31}x_0 + a_{33}(y_0 + z_0)) = x_0(a_{31}x_0 + a_{33}(1 - a_{11}x_0)). \end{aligned}$$

This completes the proof.

We put

$$\mu_0 = a_{21} + a_{31} - a_{11}a_{22} - a_{11}a_{33}, \quad \mu_1 = a_{11} + a_{22} + a_{33}$$

and define polynomial $P_2(x)$:

$$P_2(x) = \mu_0x^2 + \mu_1x - 1. \tag{12}$$

Theorem 3.3 *QO \mathcal{Q} has a unique nontrivial positive fixed point.*

Proof To prove the Theorem, we use properties of the polynomial $P_2(x)$. It is known that there are two roots of the polynomial. They are:

$$\begin{aligned} x_1 &= \frac{-\mu_1 + \sqrt{\mu_1^2 + 4\mu_0}}{2\mu_0} \\ x_2 &= \frac{-\mu_1 - \sqrt{\mu_1^2 + 4\mu_0}}{2\mu_0} \end{aligned}$$

I Let $\mu_0 > 0$. In this case, $x_1 > 0$ and $x_2 < 0$.

$$\begin{aligned}
 1 - a_{11}x_1 &= 1 - \frac{-\mu_1 + \sqrt{\mu_1^2 + 4\mu_0}}{2\mu_0} a_{11} = \\
 &= \frac{2\mu_0 + a_{11}\mu_1 - \sqrt{(\mu_1^2 + 4\mu_0)a_{11}^2}}{2\mu_0} > \\
 &> \frac{2\mu_0 + a_{11}\mu_1 - \sqrt{\mu_1^2 a_{11}^2 + 4\mu_0\mu_1 a_{11}}}{2\mu_0} > \\
 &> \frac{2\mu_0 + a_{11}\mu_1 - \sqrt{\mu_1^2 a_{11}^2 + a_{11}\mu_0\mu_1 + 4\mu_0\mu_1 a_{11}}}{2\mu_0} = 0
 \end{aligned}$$

i.e., $1 - a_{11}x_1 > 0$. It means:

$$\begin{aligned}
 y_1 &= x_1(a_{21}x_1 + a_{22}(1 - a_{11}x_1)) > 0, \\
 z_1 &= x_1(a_{31}x_1 + a_{33}(1 - a_{11}x_1)) > 0.
 \end{aligned}$$

II Let $\mu_0 < 0$. In this case, $x_1 > 0$ and $x_2 > 0$.

Clearly,

$$(P_2(x))' = 2\mu_0 x + \mu_1 \tag{13}$$

and $P_2' \left(\frac{-\mu_1}{2\mu_0} \right) = 0$. Moreover, the function $P_2(x)$ is an increasing function on $\left(-\infty, \frac{-\mu_1}{2\mu_0} \right)$ and it is a decreasing function on $\left(\frac{-\mu_1}{2\mu_0}, \infty \right)$.

If we put $x' = \frac{-\mu_1}{2\mu_0}$, then

$$x_1 < x' < x_2.$$

II.I Let $x' = \frac{-\mu_1}{2\mu_0} < \frac{1}{a_{11}}$.

$$a_{11}\mu_1 < -2\mu_0 \tag{14}$$

Then $x_1 < \frac{1}{a_{11}}$ and from $1 - a_{11}x_1 > 0$. Moreover,

$$(x_1, y_1, z_1) \in \mathbb{R}_3^+$$

By other hand, we have the following identity:

$$1 - a_{11}x_2 = \frac{2\mu_0 + a_{11}\mu_1 + a_{11}\sqrt{\mu_1^2 + 4\mu_0}}{2\mu_0}$$

By (14):

$$\begin{aligned}
 &2\mu_0 + a_{11}\mu_1 + a_{11}\sqrt{\mu_1^2 + 4\mu_0} > \\
 &> 2\mu_0 + (-2\mu_0) + a_{11}\sqrt{\mu_1^2 + 4\mu_0} = a_{11}\sqrt{\mu_1^2 + 4\mu_0} > 0.
 \end{aligned}$$

From the last inequality,

$$1 - a_{11}x_2 < 0$$

and

$$(x_2, y_2, z_2) \notin \mathbb{R}_3^+.$$

II.II Let $x' = \frac{-\mu_1}{2\mu_0} > \frac{1}{a_{11}}$. We have:

$$1 - a_{11}x_1 = \frac{2\mu_0 + a_{11}\mu_1 - a_{11}\sqrt{\mu_1^2 + 4\mu_0}}{2\mu_0}$$

Consequently,

$$\begin{aligned}
 a_{21} + a_{31} &> 0, \\
 a_{21} + a_{31} - a_{11}a_{22} - a_{11}a_{33} + a_{11}^2 + a_{11}a_{22} + a_{11}a_{33} &> a_{11}, \\
 \mu_0 + a_{11}\mu_1 &> a_{11}^2, \\
 4\mu_0(\mu_0 + a_{11}\mu_1) &< 4\mu_0(a_{11}^2), \\
 a\mu_0^2 + 4a_{11}\mu_0\mu_1 + a_{11}^2\mu_1^2 &< a_{11}^2\mu_1^2 + 4\mu_0a_{11}^2, \\
 (2\mu_0 + a_{11}\mu_1)^2 &< (a_{11}\sqrt{\mu_1^2 + 4\mu_0})^2,
 \end{aligned}$$

$$2\mu_0 + a_{11}\mu_1 < a_{11}\sqrt{\mu_1^2 + 4\mu_0},$$

$$2\mu_0 + a_{11}\mu_1 - a_{11}\sqrt{\mu_1^2 + 4\mu_0} < 0.$$

From the last identity:

$$1 - a_{11}x_1 > 0,$$

and

$$(x_1, y_1, z_1) \in \mathbb{R}_3^+.$$

By the other hand, $x_2 > x' > \frac{1}{a_{11}}$. So, $1 - a_{11}x_2 < 0$ and $(x_2, y_2, z_2) \notin \mathbb{R}_3^+$.

References

- [1] Pigorov S.A., Sinai Ya.G. Phase diagrams of classical lattice systems (Russian). *Theor. and Math. Phys.*, 1975, **25**, P. 358–369.
- [2] Pigorov S.A., Sinai Ya.G. Phase diagrams of classical lattice systems. Continuation (Russian). *Theor. and Math. Phys.*, 1976, **26**, P. 61–76.
- [3] Sinai Ya.G. *Theory of phase transitions: Rigorous Results*, Pergamon, Oxford, 1982.
- [4] Kotecky R., Shlosman S.B. First-order phase transition in large entropy lattice models. *Commun. Math. Phys.*, 1982, **83**, P. 493–515.
- [5] Mazel A., Suhov Y., Stuhl I. A classical WR model with q particle types. *J.Stat.Phys.*, 2015, **159**, P. 1040–1086.
- [6] Mazel A., Suhov Y., Stuhl I., Zohren S. Dominance of most tolerant species in multi-type lattice Widom-Rowlinson models. *Journ. Stat. Mech.*, 2014, P. 08010.
- [7] Eshkabilov Yu.Kh., Haydarov F.H. On positive solutions of the homogeneous Hammerstein integral equation. *Nanosystems: Physics, Chemistry, Mathematics*, 2015, **6**(5), P. 618–627.
- [8] Eshkabilov Yu.Kh., Rozikov U.A., Haydarov F.H. Non-uniqueness of Gibbs measure for models with uncountable set of spin values on a Cayley Tree. *Journal Statistical Physics*, 2012, **147**, P. 779–794.
- [9] Eshkabilov Yu.Kh., Rozikov U.A., Haydarov F.H. Uniqueness of Gibbs measure for models with uncountable set of spin values on a Cayley tree. *Math.Phys.Anal.Geom.*, 2013, **16**, P. 1–17.
- [10] Eshkabilov Yu.K., Haydarov F.H., Nodirov Sh.D. Positive fixed points of quadratic operators and Gibbs measures. *Positivity*, 2016, **20**(4), P. 929–943.
- [11] Eshkabilov Yu.Kh., Haydarov F.H. Lyapunov operator L with degenerate kernel and Gibbs measures. *Nanosystems: Physics, Chemistry, Mathematics*, 2017, **8**(5), P. 553–558.
- [12] Rozikov U.A. *Gibbs measures on a Cayley trees*, World Sci. Pub, Singapore, 2013.
- [13] Rozikov U.A., Haydarov F.H. Four competing interactions for models with an uncountable set of spin values on a Cayley tree. *Theor. Math. Phys.*, 2017, **191**(2), P. 748–761.
- [14] Krasnosel'ski M.A. *Positive Solutions of Operator Equations*. Gos. Izd. Moscow, 1969, Russian.
- [15] Nirenberg L. *Topics in nonlinear functional analysis*. AMS, Courant Lec. Notes in Math, 6, N.Y., 2001.
- [16] Haydarov F.H. Fixed points of Lyapunov integral operators and Gibbs measures. *Positivity*, 2018, **22**(4), P. 1165–1172.
- [17] Georgii H.O. *Gibbs Measures and Phase Transitions*, 2nd edn. de Gruyter Studies in Mathematics, vol. 9. Walter de Gruyter, Berlin, 2011.

Peristaltic pumping through non-Darcy porous medium in an electroosmotic flow with entropy analysis

Bhimanand Pandurang Gajbhare^{1,2}, J. S. V. R. Krishna prasad³, S. R. Mishra⁴

¹Research Scholar, Kavayitri Bahinabai Chaudhari North Maharashtra University, Jalgaon, India

²Department of Mathematics, Vaidyanath College Parli-Vaijanath, Beed-431515, Maharashtra, India

³Department of Mathematics, Moolji Jaitha College, Jalgaon-425001, Maharashtra, India

⁴Department of Mathematics, Siksha O Anusandhan Deemed to be University, Khandagiri square, Bhubaneswar-751030, Odisha, India

bpgajbhare@gmail.com, krishnaprasadsivr@yahoo.com, satyaranjan_mshr@yahoo.co.in

DOI 10.17586/2220-8054-2020-11-4-379-390

Pumping of peristaltic fluid is a vehicle via liquid that is accomplished due to a dynamic rush through a distensible cylinder containing liquids which extends along its length. Peristaltic pumping occurs in a lower pressure region to a higher pressure region. As a principle of peristaltic pumping, various applications are used for the blood pumping in different parts of the human body, pharmacological drug delivery systems and in industries, sanitary fluid transport, etc. Therefore, peristaltic pumping via a non-Darcy porous medium in an electroosmotic flow has been discussed in the current investigation. To exhibit the existence of a porous medium, Darcy Forchheimer model is deployed. The electro-magnetohydrodynamic flow of fluid passing a symmetric channel and the novelty of the study are due to the entropy analysis. Analytical approach such as perturbation technique is employed to reduce the higher order coupled transformed equation into its lower order decoupled form and then numerical treatment is made to obtain the approximate solutions. The characteristics of the contributing parameters are presented via graphs and the numerical computations are exhibited through tabular form. Present outcome warrants a good correlation with earlier result in particular case. However, the main findings are elaborated in the results and discussion section.

Keywords: electroosmotic flow, peristaltic pumping, Darcy–Forchheimer model; approximate analytical method, perturbation technique.

Received: 30 March 2020

Revised: 26 June 2020

Final revision: 15 July 2020

1. Introduction

The development of entropy is a phenomenon of material that is related to the degree of randomness in the system. Moreover, from the second law of thermodynamics, entropy of the system increases due to the irreversible process related to in real time. When entropy output takes place, then energy norm/status decreases. Therefore, it is of vital importance to record the distribution of entropy production in the fluid to maintain the energy norm/status during fluid flow or to minimize entropy production. Proficient energy consumption during the construction of thermal devices is the primary objective. This goal may be achieved by reducing the generation of entropy in thermodynamic processes. Entropy processing is viewed as a suitable solution with the growth of industry and improved engineering capabilities to achieve more efficiency in industrial processes. The lost resources cannot be recovered but steps for the irreversibility can be taken. The pioneering work of Bejan [1] is for implementing this concept through the minimization of entropy output. Afterwards, Sciacovelliet al. [2] introduced the study of entropy output as a design method. Zhao and Liu [3] revealed the production of entropy in open-and close-ended microconduct for the electro-kinetically flowing stream. Rashidi et al. [4] enlightened the development of entropy in a rotating disc for a steady flow with porous material. Afridi et al. [5] studied the analysis of entropy in a MHD stagnation point flow (boundary layer) for the behavior of Joule and friction heating. Gull et al. [6] carried out the amount of production of entropy of MDJN (molybdenum disulfide Jeffrey nanofluid) mixed convection Poiseuille flow, and recorded that the effects of pressure gradient and buoyancy in the mixed convection. Saqib et al. [7] examined the same amount of entropy in an electrically conducting nanofluid of different forms traveling on an infinite length vertical plate embodying with porous medium. Due to its immense applications in electronics cooling systems, nuclear reactors, and heat exchangers, the natural convection cycle inside the channel walls is a key attraction to the researchers in the last few decades. The efficient use of energy and the best possible use of resources prompted inquiries to improve the efficiency of industrial procedures. Several recent studies are reported [8–14] which explore the results of entropy analysis. Because of the vast applications in several industries, micro-fluids have gained considerable attention over the last few decades. The young academicians have used electrokinetic-based micro-fluids as it is very a powerful mechanism for manipulating and regulating the fluid flow in micro-devices. Microfluidics is also important in biofluids like concentration of DNA,

isolation of species, and fluid amalgamation. This can be used to analyze various biological properties. Coulomb force induces the electroosmotic flow through the micro-channel, driven by the electric potential. Electroosmosis is the counter-ions movement in the diffused portion of the double-layer current. This process of electroosmotic fluid flowing by peristaltic pumping in a non-Darcy porous medium, as it can be used in hemodialysis, is a very physiological significant test. Cameselle and Reddy [15] focused on advancing and developing the electroosmotic flow to remove pollution from soil. Zhou et al. [16] have been researching how electroosmotic processes are influenced by electrode material. With the impact of magnetic field, Tripathi et al. [17] studied the peristaltic motion of electrically driven fluids.

Aforesaid literature review suggests a way to study on the entropy analysis of the electro-magnetohydrodynamics flow and electroosmotic flow in a symmetric channel via non-Darcy porous medium. Darcy–Forchheimer model is considered for the present investigation. Approximate analytical technique, such as perturbation technique along with numerical technique is employed to handle the transformed non-dimensional coupled form of equations. Further, the flow phenomena along with the analysis of entropy generation are obtained by discussing the characterizing parameters via graphs and tables.

2. Mathematical model

The problem considered in the present investigation is based on the Darcy Forchheimer model for the flow characteristics of peristaltic pumping accompanied by electroosmosis via a non-Darcy porous matrix. A flow of viscous two-dimensional fluid passes in a micro channel wall with temperature T_w , where the bulk fluid temperature is denoted as T . The wave propagation occurs along \bar{x} direction and the normal direction to the flow is along \bar{y} . It is noteworthy that, about the middle area of the conduit the flow is symmetric, i.e., $\bar{y} = 0$, which is equidistant from the upper, as well as, from the lower boundaries of the conduit $\bar{y} = \bar{h}(\bar{x}, \bar{t})$ and $\bar{y} = -\bar{h}(\bar{x}, \bar{t})$ respectively (Fig. 1). Moreover, due to symmetric flow, it is sufficient to discuss the flow phenomena within the domain $0 \leq \bar{y} \leq h$. An electric field of strength E_0 is exerted along the parallel direction of the micro-channel and magnetic field of strength B_0 , which is applied in the transverse direction of the flow.

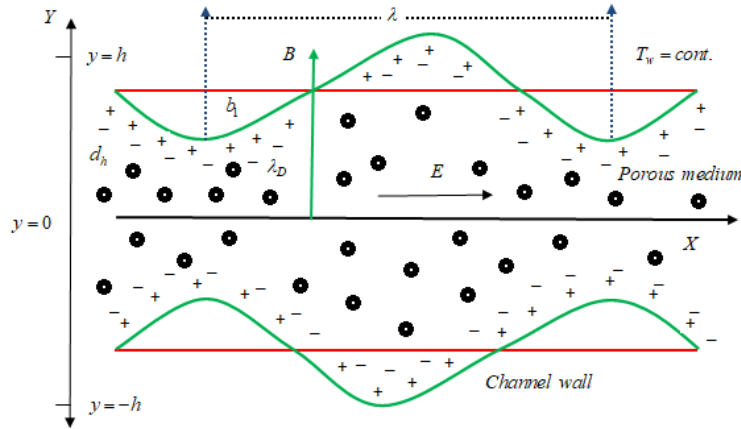


FIG. 1. Flow configuration of peristaltic pumping

Here,

$$\bar{h}(\bar{x}, \bar{t}) = d_h - \bar{b}_1 \cos^2 \frac{\pi}{\lambda} (\bar{x} - c_1 \bar{t}), \tag{1}$$

where d_h , the half-width of the channel, λ , the wavelength, b_1 , the amplitude, and c_1 , velocity of the wave.

2.1. Electrical potential distribution

The electric potential in the symmetric channel is imposed following, the Poisson–Boltzmann equation and described as:

$$\nabla^2 \bar{\phi} = -\frac{\rho_e}{\varepsilon \varepsilon_0}, \tag{2}$$

and the ion within the double layer is also proportional to Boltzmann factor $e^{-z_e \bar{\phi} / K_B T_{av}}$. Where $\bar{\phi}$, the potential of electroosmotic flow, ρ_e , density of ionic charge, ε , constant (dielectric), and ε_0 permeability. The value of ε_0 is $8.854 \times 10^{-12} Fm^{-1}$.

From the Boltzmann equation, both the positive and negative ions number densities are:

$$n^\pm = n_0 e^{(\mp z e \bar{\phi} / K_B T_{av})}, \tag{3}$$

Where n_0 , the average of both then negative and positive ions obtained from buffer solution, z , the ionic valence, e , the charge of electron, T_{av} , the average temperature, and K_B , the Boltzmann constant. Following [19], the total charge is considered as:

$$\rho_e = ez(n^+ - n^-) = -2n_0 ez \sinh\left(\frac{ez\bar{\phi}}{K_B T_{av}}\right). \tag{4}$$

Therefore, from Eqs. (3) and (4) the Poisson–Boltzmann Eq. (2) is approximated as:

$$\frac{d^2\bar{\phi}}{d\bar{y}^2} = \frac{-2n_0 ez}{\epsilon\epsilon_0} \sinh\left(\frac{ez\bar{\phi}}{K_B T_{av}}\right). \tag{5}$$

In general, introduced the following dimensionless variables for the governing equations are

$$\begin{cases} \delta = \frac{d_h}{\lambda}, & Re = \frac{\rho c_1 d_h}{\mu}, & \beta = \frac{U_{HS}}{c_1}, & U_{HS} = \frac{E_0 \epsilon \epsilon_0 \zeta}{\mu}, & \nu = \frac{\mu}{\rho}, & H_m = B_0 d_h \sqrt{\frac{\sigma}{\mu}}, & \Omega^2 = \frac{d_h^2}{k^*}, \\ \varphi = \frac{\bar{\phi}}{\zeta}, & y = \frac{\bar{y}}{d_h}, & x = \frac{\bar{x}}{\lambda}, & t = \frac{c_1 \bar{t}}{\lambda}, & h = \frac{\bar{h}}{d_h}, & b_1 = \frac{\bar{b}_1}{d_h}, & \theta = \frac{T - T_w}{\frac{q d_h}{k}} p = \frac{\bar{p} d_h^2}{c_1 \lambda \mu}, & u = \frac{\bar{u}}{c_1}, \\ v = \frac{\bar{v}}{c_1 \delta}, & C_F = c_{k^*} \frac{c_1 d_h^2}{\nu k^*}, & Pr = \frac{\mu C_p}{K}, & Br = \frac{\mu c_1^2}{q d_h}, & \gamma = \frac{\sigma d_h E_0^2}{q}. \end{cases} \tag{6}$$

With the help of non-dimensional quantities as well as variables from equation (6), equation (5) becomes:

$$\frac{d^2\varphi}{dy^2} = \frac{d_h^2}{\lambda_D^2 \alpha} \sinh(\alpha\varphi), \tag{7}$$

where α is the ionic energy parameter, λ_D is the Debye length.

Across the middle of the channel, the potential function is symmetric therefore, the boundary conditions are:

$$\begin{cases} \frac{d\varphi}{dy} = 0, & \text{at } y = 0; \\ \varphi = 1, & \text{at } y = h. \end{cases} \tag{8}$$

The solution of equation (7), with their corresponding boundary conditions (8) can be stated as:

$$\phi = \frac{\cosh(my)}{\cosh(mh)}. \tag{9}$$

Here, m is the electroosmotic parameter where $m = d_h/\lambda_D$.

3. Flow analysis

Flow of electroosmotic fluid by the peristaltic pumping in a non-Darcy porous medium can be modeled as:

$$\frac{\partial \bar{u}}{\partial \bar{x}} + \frac{\partial \bar{v}}{\partial \bar{y}} = 0, \tag{10}$$

$$\rho \left(\frac{\partial \bar{u}}{\partial \bar{t}} + \bar{u} \frac{\partial \bar{u}}{\partial \bar{x}} + \bar{v} \frac{\partial \bar{u}}{\partial \bar{y}} \right) = -\frac{\partial \bar{p}}{\partial \bar{x}} + \mu \left(\frac{\partial^2 \bar{u}}{\partial \bar{x}^2} + \frac{\partial^2 \bar{u}}{\partial \bar{y}^2} \right) - \sigma \bar{B}_0^2 \bar{u} + \rho E_0 - \frac{\mu}{k^*} \bar{u} - \frac{\rho c_{k^*}}{\sqrt{k^*}} \bar{u} \sqrt{\bar{u}^2 + \bar{v}^2}, \tag{11}$$

$$\rho \left(\frac{\partial \bar{v}}{\partial \bar{t}} + \bar{u} \frac{\partial \bar{v}}{\partial \bar{x}} + \bar{v} \frac{\partial \bar{v}}{\partial \bar{y}} \right) = -\frac{\partial \bar{p}}{\partial \bar{y}} + \mu \left(\frac{\partial^2 \bar{v}}{\partial \bar{x}^2} + \frac{\partial^2 \bar{v}}{\partial \bar{y}^2} \right) - \frac{\mu}{k^*} \bar{v} - \frac{\rho c_{k^*}}{\sqrt{k^*}} \bar{v} \sqrt{\bar{u}^2 + \bar{v}^2}, \tag{12}$$

$$\begin{aligned} \rho c_p \left(\frac{\partial \bar{T}}{\partial \bar{t}} + \bar{u} \frac{\partial \bar{T}}{\partial \bar{x}} + \bar{v} \frac{\partial \bar{T}}{\partial \bar{y}} \right) = \\ K \left(\frac{\partial^2 \bar{T}}{\partial \bar{x}^2} + \frac{\partial^2 \bar{T}}{\partial \bar{y}^2} \right) + \phi + \sigma \bar{B}_0^2 \bar{u}^2 + \sigma E_0^2 + \frac{\mu}{k^*} (\bar{u}^2 + \bar{v}^2) - \frac{\rho c_{k^*}}{\sqrt{k^*}} [(\bar{u}^2 + \bar{v}^2) \sqrt{\bar{u}^2 + \bar{v}^2}], \end{aligned} \tag{13}$$

$$\phi = \mu \left[2 \left(\frac{\partial \bar{u}}{\partial \bar{x}} \right)^2 + 2 \left(\frac{\partial \bar{v}}{\partial \bar{y}} \right)^2 + \left(\frac{\partial^2 \bar{v}}{\partial \bar{x}^2} + \frac{\partial^2 \bar{v}}{\partial \bar{y}^2} \right) \right]. \tag{14}$$

In equation (11) the first term is pressure gradient, second term is inertia force, third and fourth terms are the magnetic and electric fields respectively, fifth term is the porosity and the sixth term is the use of drag force. For equation (13), the first term of the right hand side is the pressure gradient, second term is inertia force, third term is

porosity, and fifth term is drag force. Similarly, forequation (14), first term of right hand side is thermal diffusion, second term is viscous dissipation, third and fourth terms are the Joule dissipations due to magnetic and electric field, fifth term is Darcy dissipation due to the inclusion of porosity and the last term is drag force.

Where φ represents the inclusion of viscous dissipation in the pumping process.

Implementing (6) on the governing equations (11)–(13) using equation (14) the transformed equations are expressed as:

$$Re\delta \left(\frac{\partial}{\partial t} + u \frac{\partial}{\partial x} + v \frac{\partial}{\partial y} \right) u = -\frac{\partial p}{\partial x} + \left(\delta^2 \frac{\partial^2 u}{\partial x^2} + \frac{\partial^2 u}{\partial y^2} \right) - (H_m^2 + \Omega^2) u + \beta m^2 \phi - c_F u \sqrt{u^2 + \delta^2 v^2}, \quad (15)$$

$$Re\delta^3 \left(\frac{\partial}{\partial t} + u \frac{\partial}{\partial x} + v \frac{\partial}{\partial y} \right) v = -\frac{\partial p}{\partial x} + \delta^2 \left(\delta^2 \frac{\partial^2 v}{\partial x^2} + \frac{\partial^2 v}{\partial y^2} \right) - \delta^2 (\Omega^2) v + \beta m^2 \phi - \delta^3 c_F u v \sqrt{u^2 + \delta^2 v^2}, \quad (16)$$

$$Re Pr \delta \left(\frac{\partial}{\partial t} + u \frac{\partial}{\partial x} + v \frac{\partial}{\partial y} \right) \theta = \left(\delta^2 \frac{\partial^2 \theta}{\partial x^2} + \frac{\partial^2 \theta}{\partial y^2} \right) + \gamma + Br \left[2\delta^2 \left(\frac{\partial u}{\partial x} \right)^2 + 2\delta^2 \left(\frac{\partial v}{\partial x} \right)^2 \right] - \delta^2 (\Omega^2) v + \beta m^2 \varphi - \delta^3 c_F u v \sqrt{u^2 + \delta^2 v^2}. \quad (17)$$

In the case of long wave length and low Reynolds number i.e. neglecting the term containing δ , the above expression can be represented as:

$$\frac{\partial p}{\partial x} = \frac{\partial^2 u}{\partial y^2} - (H^2 + \Omega^2)u + \beta m^2 \varphi - C_F u^2, \quad (18)$$

$$\frac{\partial p}{\partial y} = 0, \quad (19)$$

$$\frac{\partial^2 \theta}{\partial y^2} + \gamma + Br \left(\frac{\partial u}{\partial y} \right)^2 + (H^2 + \Omega^2)Br u^2 - C_F Br u^3 = 0. \quad (20)$$

Eliminating pressure gradient from the dimensionless equations (18) and (19), the equation for flow of electroosmotic fluid can be written as:

$$\frac{\partial^3 u}{\partial y^3} - (H^2 + \Omega^2) \frac{\partial u}{\partial y} + \beta m^2 \frac{\partial \varphi}{\partial y} - C_F \frac{\partial u^2}{\partial y} = 0. \quad (21)$$

Now, we define the stream function ψ , such as $u = \frac{\partial \psi}{\partial y}$, $v = -\frac{\partial \psi}{\partial x}$ satisfying the continuity equation (10). Equations (18), (20) and (21) can be written as:

$$\frac{\partial p}{\partial x} = \frac{\partial^3 \psi}{\partial y^3} - (H^2 + \Omega^2) \frac{\partial \psi}{\partial y} + \beta m^2 \varphi - C_F \left(\frac{\partial \psi}{\partial y} \right)^2, \quad (22)$$

$$\frac{\partial^2 \theta}{\partial y^2} + \gamma + Br \left(\frac{\partial^2 \psi}{\partial y^2} \right)^2 + (H^2 + \Omega^2) Br \left(\frac{\partial u}{\partial y} \right)^2 - C_F \frac{\partial}{\partial y} \left(\frac{\partial \psi}{\partial y} \right)^2 = 0, \quad (23)$$

$$\frac{\partial^4 \psi}{\partial y^4} - (H^2 + \Omega^2) \frac{\partial^2 \psi}{\partial y^2} + \beta m^2 \frac{\partial \varphi}{\partial y} - C_F \frac{\partial}{\partial y} \left(\frac{\partial \psi}{\partial y} \right)^2 = 0, \quad (24)$$

where the boundary conditions in terms of ψ , the stream function are:

$$\begin{cases} \frac{\partial^2 \psi}{\partial y^2} = 0, & \psi = 0, & \frac{\partial \theta}{\partial y} = 0 & \text{at } y = 0; \\ \frac{\partial \psi}{\partial y} = 0, & \psi = F, & \theta = 0 & \text{at } y = h. \end{cases} \quad (25)$$

Where the wave travelling along the conduit with a height h . Here, additional stream function and boundary conditions are introduced in order to solve the differential equation of order four. The non-dimensional form of the flow rate is defined as $F = Q_0 e^{-At}$, while A and Q_0 are constants. The sign depends upon the constant Q_0 . If $Q_0 < 0$, then $F < 0$; similarly $F > 0$ if $Q_0 > 0$. If the flow rate is positive, then it represents the flow in the direction of peristaltic pumping, however, the direction is opposite, if the flow rate is negative i.e., also known as reverse pumping. It is one of the experimental investigations of Kikuchi [18], that the blood flow rate decreases exponentially with the time rate. Further, it is suggested that the changes in the flow rate are independent of structural details of micro-channel.

4. Solution methodology

In order to get the solution of the higher-order differential equations (22)–(24) first of all these equations are perturbed by using perturbation parameter C_F as it is very small and expressed as:

$$\begin{cases} \psi = \psi_0 + C_F\psi_1 + O(C_F)^2, \\ p = p_0 + C_Fp_1 + O(C_F)^2, \\ \theta = \theta_0 + C_F\theta_1 + O(C_F)^2. \end{cases} \tag{26}$$

4.1. Zeroth order equations

$$\frac{\partial^4\psi_0}{\partial y^4} - (H^2 + \Omega^2)\frac{\partial^2\psi_0}{\partial y^2} + \beta m^2\frac{\partial\varphi}{\partial y} = 0, \tag{27}$$

$$\frac{\partial p_0}{\partial x} = \frac{\partial^3\psi_0}{\partial y^3} - (H^2 + \Omega^2)\frac{\partial\psi_0}{\partial y} + \beta m^2\varphi = 0, \tag{28}$$

$$\frac{\partial p_0}{\partial y} = 0, \tag{29}$$

$$\frac{\partial^2\theta_0}{\partial y^2} + \gamma + Br\left(\frac{\partial^2\psi_0}{\partial y^2}\right)^2 + (H^2 + \Omega^2)Br\left(\frac{\partial\psi_0}{\partial y}\right)^2 = 0, \tag{30}$$

$$\begin{cases} \frac{\partial^2\psi_0}{\partial y^2} = 0, & \psi_0 = 0, & \frac{\partial\theta_0}{\partial y} = 0 & \text{at } y = 0; \\ \frac{\partial\psi_0}{\partial y} = 0, & \psi_0 = F, & \theta_0 = 0 & \text{at } y = h. \end{cases} \tag{31}$$

4.2. First order equations

$$\frac{\partial^4\psi_1}{\partial y^4} - (H^2 + \Omega^2)\frac{\partial^2\psi_1}{\partial y^2} - \frac{\partial}{\partial y}\left(\frac{\partial\psi_0}{\partial y}\right)^2 = 0, \tag{32}$$

$$\frac{\partial p_1}{\partial x} = \frac{\partial^3\psi_1}{\partial y^3} - (H^2 + \Omega^2)\frac{\partial\psi_1}{\partial y} - \left(\frac{\partial\psi_0}{\partial y}\right)^2 = 0, \tag{33}$$

$$\frac{\partial p_1}{\partial y} = 0, \tag{34}$$

$$\frac{\partial^2\theta_1}{\partial y^2} + 2Br\left(\frac{\partial^2\psi_0}{\partial y^2}\right)^2\left(\frac{\partial^2\psi_1}{\partial y^2}\right)^2 + 2(H^2 + \Omega^2)Br\left(\frac{\partial\psi_1}{\partial y}\right)\left(\frac{\partial\psi_0}{\partial y}\right) + Br\left(\frac{\partial\psi_0}{\partial y}\right)^3 = 0, \tag{35}$$

$$\begin{cases} \frac{\partial^2\psi_1}{\partial y^2} = 0, & \psi_1 = 0, & \frac{\partial\theta_1}{\partial y} = 0 & \text{at } y = 0; \\ \frac{\partial\psi_1}{\partial y} = 0, & \psi_1 = 0, & \theta_1 = 0 & \text{at } y = h. \end{cases} \tag{36}$$

Further, the set of differential equations are solved numerically employing Runge–Kutta fourth order method and the iterative procedure of the method is expressed as follows.

Here, Eqs. (27), (30), (32) and (35) behave in the sense of ordinary differential equation with given boundary conditions and the transformation into the set of first order differential equations with initial conditions are as follows.

Let,

$$\psi_0 = y_1, \quad \psi'_0 = y_2, \quad \psi''_0 = y_3, \quad \psi'''_0 = y_4, \quad \theta_0 = y_5, \quad \theta'_0 = y_6.$$

Hence,

$$\begin{aligned} \psi_0^{iv} &= (H^2 + \Omega^2)y_3 - \beta m^2\varphi', \\ \theta_0'' &= -\gamma - Br(y_3)^2 - (H^2 + \Omega^2)Br(y_2)^2. \end{aligned}$$

Also,

$$\psi_1 = y_7, \quad \psi'_1 = y_8, \quad \psi''_1 = y_9, \quad \psi'''_1 = y_{10}, \quad \theta_1 = y_{11}, \quad \theta'_1 = y_{12}.$$

Therefore,

$$\begin{aligned} \psi_1^{iv} &= (H^2 + \Omega^2)y_9 + 2y_2y_3, \\ \theta_1'' &= -2Br(y_3)^2(y_9)^2 - 2(H^2 + \Omega^2)Br(y_8)(y_2) - Br(y_2)^3. \end{aligned}$$

And the initial conditions are:

$$\begin{cases} y_3(0) = 0, & y_1(0) = 0, & y_6(0) = 0, & y_9(0) = 0, & y_7(0) = 0, & y_{12}(0) = 0, \\ y_2(0) = s_1, & y_4(0) = s_2, & y_5(0) = s_3, & y_8(0) = s_4, & y_7(0) = s_5, & y_{11}(0) = s_6. \end{cases}$$

However, the assumed initial conditions are obtained using shooting technique and the results are verified till we get a desired accuracy of 10^{-6} .

4.3. Analysis of entropy generation

The intensity of irreversibility that takes place in any thermal procedure is observed by Entropy production. The mathematical expression for the rate of local entropy production is:

$$S_G = \frac{k}{T_w^2} \left[\left(\frac{\partial T}{\partial x} \right)^2 + \left(\frac{\partial T}{\partial y} \right)^2 \right] + \frac{1}{T_w} \varphi + \frac{\sigma E_0^2}{T_w} + \frac{\sigma B_0^2}{T_w} [u^2 + v^2] + \frac{\mu}{k^* T_w} [u^2 + v^2] + \frac{\rho C_{k^*}}{\sqrt{k^* T_w}} [(u^2 + v^2) \sqrt{u^2 + v^2}]. \quad (37)$$

The above expression exhibits the dimensional form of entropy production due to thermal irreversibility, irreversibility due to various factors like friction, joule dissipation and porous matrix. The characteristic entropy production is defined as:

$$S_{CG} = \frac{k \left(\frac{qd_h}{k} \right)^2}{T_w^2 d_h^2}. \quad (38)$$

The non-dimensional form of entropy production can be obtained by utilizing Eqs. (37) and (38), and can be stated as:

$$Ns = \frac{S_G}{S_{CG}} = \frac{T_w^2 d_h^2}{k \left(\frac{qd_h}{k} \right)^2} S_G, \quad (39)$$

$$Ns = \left(\frac{\partial \theta}{\partial y} \right)^2 + \frac{1}{\eta} \left[Br \left(\frac{\partial u}{\partial y} \right)^2 + \gamma + (H_m^2 + \Omega^2) Bru^2 + c_F Bru^3 \right]. \quad (40)$$

Total entropy generation in terms of stream function is expressed as:

$$Ns = \left(\frac{\partial \theta}{\partial y} \right)^2 + \frac{1}{\eta} \left[Br \left(\frac{\partial^2 \psi}{\partial y^2} \right)^2 + \gamma + (H_m^2 + \Omega^2) Br \left(\frac{\partial \psi}{\partial y} \right)^2 + c_F Br \left(\frac{\partial \psi}{\partial y} \right)^3 \right], \quad (41)$$

where variable η is described as $\eta = [qd_h/kT_w]$. The first term in Eq. (41) denoted as: $N_{tt} = (\partial\theta/\partial y)^2$.

The above expression depicts the production of entropy due to the heat transfer within the conduit. The irreversibility system is dominant over the entropy production number. Bejan number (is defined as the ratio of N_{tt} (thermal irreversibility) to the Ns (total entropy generation)) is used to comprehend the entropy production mechanisms. The Bejan number Be is of the form:

$$Be = \frac{N_{tt}}{Ns} = \left[\frac{\left(\frac{\partial \theta}{\partial y} \right)^2}{\left(\frac{\partial \theta}{\partial y} \right)^2 + \frac{1}{\eta} \left[Br \left(\frac{\partial u}{\partial y} \right)^2 + \gamma + (H_m^2 + \Omega^2) Bru^2 + c_F Bru^3 \right]} \right].$$

The range of the Bejan number is 0 to 1. It is clear that, $Be = 0$ corresponds to the entropy production due to the impacts of several parameters those characterize the entropy. $Be = 0.5$ represents the thermal irreversibility and the irreversibility due to fluid friction, electric field, magnetic field and porous matrix are similar. Thermal irreversibility is dominant when $Be = 1$.

In the present investigation, all these equations are modeled with the consideration of dissipative heat energy. However, in the absence of viscous dissipation, study regarding the contribution of viscous irreversibility in the entropy generation is not considered. Secondly, for $Br = 0$, Bejan number is identically one.

5. Results and discussion

Darcy Forchheimer model for the flow characteristics of peristaltic pumping within a conduit, a channel conveying the biofluid flow, induced by electroosmosis through a non-Darcy porous medium has been considered. In addition to that, magnetic fields, as well as, electric field are applied along the normal and channel direction of the fluid flow, respectively. The required force for electro kinetic flow is produced due to the electric field exerted along the direction of the conduit. The novelty of the present analysis is due to the solution of highly nonlinear coupled transformed governing equations. First, a perturbation technique is used since the equation (24) is of fourth order and due to unavailability of sufficient initial conditions along with equation (23). As a criterion, C_F is introduced as perturbation parameter where $C_F \ll 1$. Henceforth, these equations are reduced to its lower order and still it is a hard task to solve these set of equations analytically, therefore, numerical techniques such as the fourth order Runge–Kutta method in association with shooting technique is employed. Moreover, in the case of peristaltic pumping, the intensity of the irreversibility that takes place in the thermal procedure, the study of entropy generation is also vital. The behavior of the characterizing physical parameter for the pumping with constant pressure gradient on the flow phenomena along with temperature profiles, pressure gradient, entropy and the Bejan number is presented via graphs. In several cases the flow pattern is compared with established results.

5.1. Velocity profiles

The comparison as well as the behavior of several parameters such as Hartmann number, Darcy number and the Forchheimer number is displayed in Fig. 2. Withdrawing the appearance of magnetic field i.e. the absence of Hartmann number, and the Darcy number from the equation (24), the present result validates with the work of Kikuchi [18]. Moreover, the variations of these parameters on the profiles are exhibited. It is a clear indication that, due to the resistance of magnetic field and porosity, the axial velocity decreases in the central region. The fact is, the interaction of the magnetic field in the transverse direction of the axial velocity produces Lorentz force that resists the fluid motion. Further, it is seen that, near the walls of the conduit the effect is reversed. An interesting point to note that the profiles behave with opposite characters from the point of inflection. The behavior of Forchheimer number on the axial velocity is also presented in Fig. 2. However, insignificant enhancement is marked with the increasing Forchheimer number on the velocity profiles. The more hindrance to the flow is marked due to the both Darcy and Forchheimer number. Since, permeability of the porous medium is inversely proportional to both the Darcy and Forchheimer number, higher of these values produces lesser permeability.

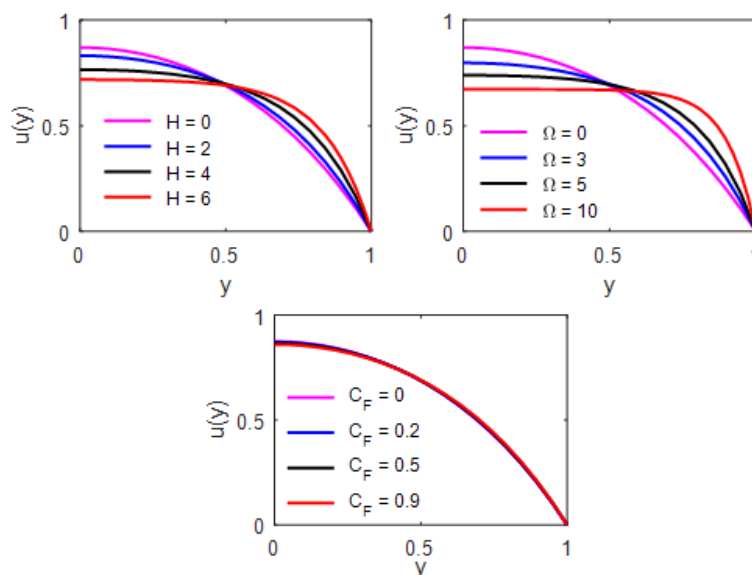


FIG. 2. Velocity profiles for various parameters

5.2. Pumping characteristics

Figure 3 illustrates the characteristic of various physical parameters, such as, Hartmann number, Darcy number, electroosmotic parameter and the Forchheimer number on the peristaltic pumping in the form of pressure gradient. The perception of mechanical pumping is characterized by the peristaltic transport phenomena. From the interaction

of Hartmann numbers it is noteworthy that the magnitude of the pressure gradient increases with increase in Hartmann number. As the conduit is wider than the amount of hike in pressure gradient is less. Therefore, maximum pressure is required for the flow of similar volume of fluid through the channel. Higher Hartmann number produces a stronger Lorentz force and for which more pressure is required to resist the applied force. Moreover, the similar profile is observed due to the enhancement in the values of Darcy number. As similar to the Magnetic field, porosity also a resistive force which enhances the magnitude of pressure gradient. In particular absence of Darcy number, the profile coincides with the earlier established results of Kikuchi [18]. The influence of electroosmosis parameters on the pressure gradient is displayed in Fig. 3. It is defined as the ratio of channel width with the Debye length. However, for lower Debye length values, the pressure gradient with the thickness of the channel decreases. Again the Forchheimer number also affects the pumping characteristics as well which is exhibited in Fig. 3. Both the Darcy and Forchheimer numbers are inversely proportional to each other, described earlier; the symmetrical behavior of the pressure gradient is marked about the middle layer of the channel. Retardation in the profiles is marked throughout the entire domain of the conduit.

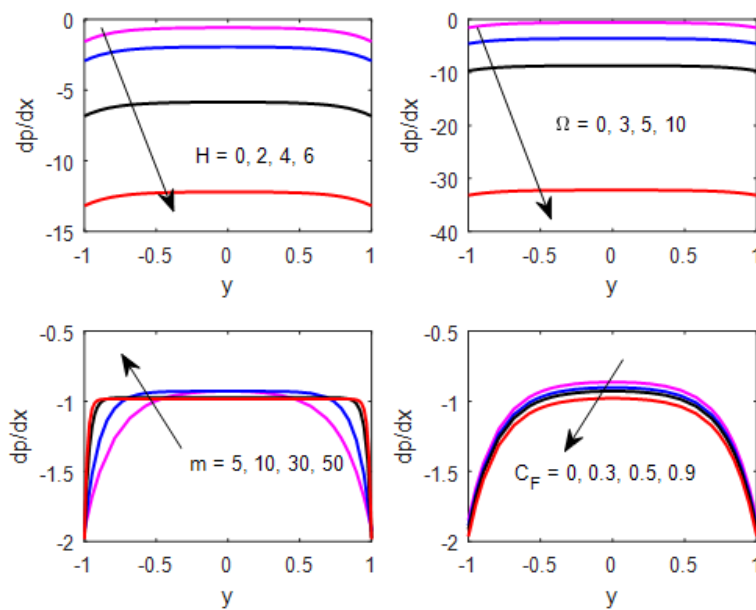


FIG. 3. Peristaltic pumping pressure gradient profile for several parameters

5.3. Temperature profile

In the case of electroosmotic flow, the generation of Joule effect is a built-in characteristic. This is because of the electrolyte. Fig. 4 presents the behavior of the Hartmann number, Joule parameter, Darcy number and the electroosmotic parameter for the fixed values of the other characterizing parameters. It is clear to see that, in the central region of the channel, the temperature of the peristaltic fluid increases due to an increase in Hartmann number. The reason is that, the effect of Lorentz force is stronger in the central region and further the falls in the profile is marked towards the channel walls. This fall in the kinetic energy is accompanied by the enhancement in the thermal energy. Because of brevity, the behavior of the profile is not discussed for entire the region since these are symmetric in nature. Joule heating effect is observed due to the interference of the electric field. It is proportional to the square of the electric field. Therefore, growth in the fluid temperature occurred due to the increase in electric field and is reflected in the central area of the temperature profiles. Moreover, the behavior is insignificant near the walls of the conduit. The impact of the Darcy number is obtained and presented in Fig. 4. It is noteworthy that the profile increases with a higher Darcy number. The boost in the profile is because of the higher Darcy number and the permeability decreases. The behavior of the temperature profile is insignificant for the variation of electroosmotic parameters. Fig. 5 portrays the influence of Brinkmann number and the Forchheimer number on the temperature profiles for the fixed values of other characterizing parameters. Near the center of the conduit, the fluid temperature enhances due to the increase in Brinkmann number. From the definition of Brinkmann number, it is seen that, Boost in the dissipative energy offers higher Brinkmann number and at the same time the molecular conductivity decreases. Because of the same reason, the temperature profile is enhanced. Therefore, it is concluded that, higher Brinkmann number is favorable for enhanced

heat transfer rates. The behavior of Forchheimer parameter on the temperature profile is exhibited in Fig. 5. In the absence of a porous medium, minimum temperature is exhibited within the channel, whereas, higher Forchheimer number is responsible for the lesser permeability of the medium for which the thermal transport enhances.

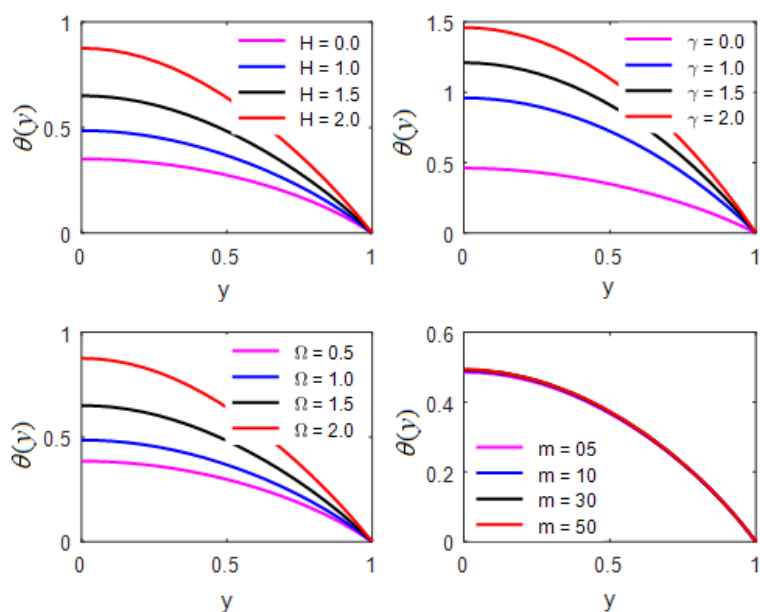


FIG. 4. Fluid temperature for contributing parameters

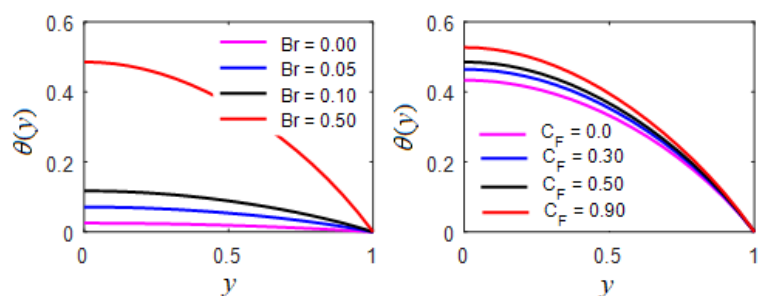


FIG. 5. Fluid temperature for contributing parameters

5.4. Entropy analysis

The thermal energy per unit time is measured by the entropy that is unavailable for doing some useful work due to ordered molecular motion. Its amount also measures the molecular randomness of the system. Fig. 6 elaborates the effects of Joule heating parameter, Hartmann number, Brinkmann number and the Darcy number on the analysis of entropy profiles. It is noted that an increasing Joule heating parameter enhances the value of the entropy near the conduit wall, whereas, at the central region, it becomes linear. Electric field strength helps to enhance the total entropy production. The effect of Hartmann number on the entropy profiles is exhibited in Fig. 6. It is noteworthy that entropy accelerates within the conduit with increasing Hartmann number. In the central area of the channel, due to lesser viscosity the impact is not strong to develop the flow. In the absence of Brinkmann number, i.e., in the case of low viscosity, the amount of entropy is low; as a result, the profile is linear. However, higher Brinkmann numbers produce maximum entropy near the channel wall and in the middle layer it becomes linear. The impact of Darcy number is also similar to that of the behavior of the Hartmann number, as described earlier.

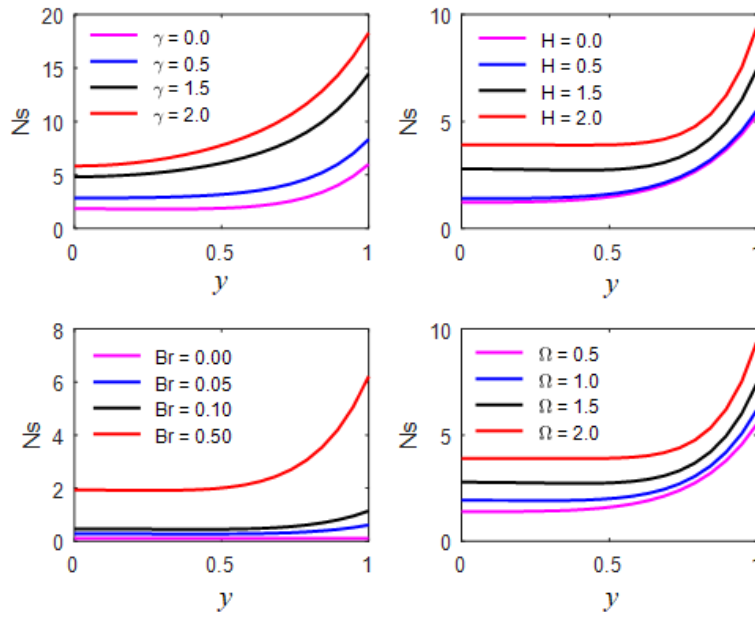


FIG. 6. Entropy production amount for contributing parameters

5.5. Bejan number

Figure 7 portrays the influences of Joule heating parameter, Hartmann number, Brinkmann number and the Darcy number on the Bejan number. It is seen that, for higher values of all these parameters, the growth of the profile is rapid towards the wall of the conduit as the channel width increases. It is obtained by the ratio of heat transfer irreversibility to the total irreversibility due to heat transfer and fluid friction. From the computation, it is clear that the irreversibility of the heat transfer dominates over the total irreversibility for which Bejan number increases. More suitably, Hartmann number and Darcy number favors to enhance the irreversibility processes of the heat transfer.

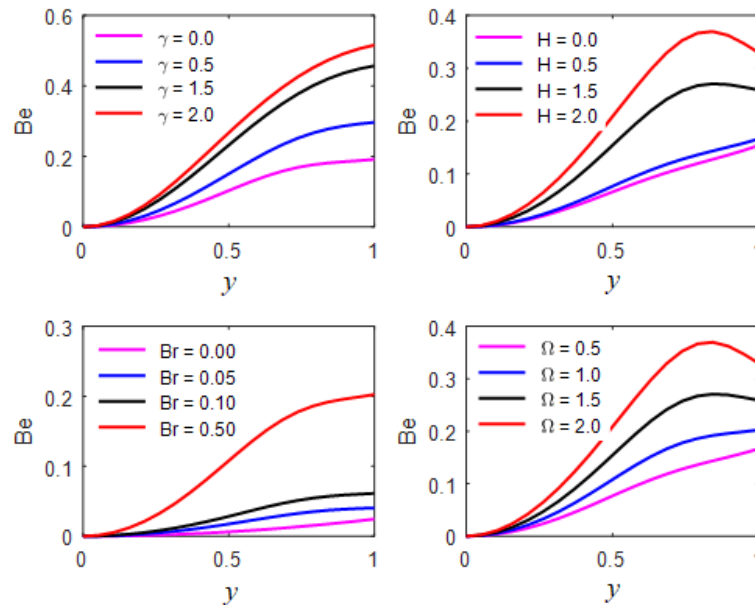


FIG. 7. Bejan number computation for several parameters

6. Conclusion

The current investigation renders in the direction of the electroosmotic flow due to the peristaltic pumping through a non-Darcy conduit in the presence of magnetic field, electric field, Joule heating. The analysis of entropy is also carried out because of the interference of Joule heating. The crux of the present investigation is the solution of a complex partial differential equation in composition with pressure gradient is obtained by both analytically and numerically. A perturbation technique is employed to reduce the PDEs to ODEs and then Runge–Kutta fourth order technique is used to solve the set of transformed ODEs. However, the computation for several contributing parameters are presented via graphs and discussed. The followings are the few concluding remarks from the aforesaid discussions.

- The non-Darcy porous medium and the Hartmann number reduce the axial velocity in the central region of the conduit.
- Electroosmotic parameter boosts the pressure gradient near the channel walls, whereas, in the middle layer, it seems to be steady.
- Interference of Hartmann and Darcy number enhance the fluid temperature.
- Huge amount of Entropy is produced due to the increase of Darcy number and Forchheimer parameter.

7. Nomenclature

ρ_e	density of ionic charge
e	charge of electron
T_{av}	average temperature
δ	wave number
q	heat flux
K_B	Boltzmann constant
Ω^2	Darcy number
H_m	Hartmann number
B_e	Bejan number
Pr	Prandtl number
Br	Brinkman number
C_F	Forchheimer number
γ	joule heating parameter
ν	kinematic viscosity
δ	wave number
Re	Reynolds number
B	mobility of medium
U_{HS}	Helmholtz –Smoluchowski velocity

8. ORCID

Bhimanand Gajbhare <https://orcid.org/0000-0002-1911-8602>.

References

- [1] Bejan A. *Entropy generation minimization*. 2nd ed. Boca Raton: CRC, 1996.
- [2] Sciacovelli A., Verda V., Sciubba E. Entropy generation analysis as a design tool review. *Renew Sustain Energy Rev.*, 2015, **43**, P. 1167–1181.
- [3] Zhao L., Liu L.H. Entropy generation analysis of electro-osmotic flow in open-end and closed-end micro-channels. *Ain Shams Eng J.*, 2017, **8**, P. 623–632.
- [4] Rashidi M.M., Abelman S., Mehr N.F. Entropy generation in steady MHD flow due to a rotating porous disk in a nanofluid. *Int. J. Heat Mass Transf.*, 2013, **62**, P. 515–625.
- [5] Afridi M.I., Qasim M., Khan I., Tlili I. Entropy generation in MHD mixed convection stagnation-point flow in the presence of joule and frictional heating. *Case Stud Therm. Eng.*, 2018, **12**, P. 292–300.

- [6] Gul A., Khan I., Makhanov S.S. Entropy generation in a mixed convection Poiseuille flow of molybdenum disulphide Jeffrey nanofluid. *Results Phys.*, 2018, **9**, P. 947–954.
- [7] Saqib M., Ali F., et al. Entropy generation in different types of fractionalized nanofluids. *Arab. J. Sci. Eng.*, 2018, **44** (1), P. 1–10.
- [8] Adesanya S.O., Falade J.A. Thermodynamics analysis of hydromagnetic third grade fluid flow through a channel filled with porous medium. *Alex Eng. J.*, 2015, **54** (3), P. 615–622.
- [9] Afridi M.I., Qasim M., Shafie S., Makinde O.D. Entropy generation analysis of spherical and non-spherical ag-water nanofluids in a porous medium with magnetic and porous dissipation. *J. Nanofluids.*, 2018, **7** (5), P. 951–960.
- [10] Abbas M.A., Bai Y., Rashidi M.M., Bhatti M.M. Analysis of entropy generation in the flow of peristaltic nanofluids in channels with compliant walls. *Entropy*, 2016, **18** (3), P. 90.
- [11] Rashidi M.M., Bhatti M.M., Abbas M.A., Ali M.E. Entropy generation on MHD blood flow of nanofluid due to peristaltic waves. *Entropy*, 2016, **18** (4), P. 117.
- [12] Qasim M., Hayat Khan Z., Khan I., Al-Mdallal Q.M. Analysis of entropy generation in flow of methanol-based nanofluid in a sinusoidal wavy channel. *Entropy*, 2017, **19** (10), P. 490.
- [13] Alizadeh R., Karimi N., et al. Mixed convection and thermodynamic irreversibilities in MHD nanofluid stagnation- point flows over a cylinder embedded in porous media. *J. Therm. Anal. Calorim.*, 2018, **135**, P. 489–506.
- [14] Shamsabadi H., Rashidi S., Esfahani J.A. Entropy generation analysis for nanofluid flow inside a duct equipped with porous baffles. *J. Therm. Anal. Calorim.*, 2018, **135**, P. 1009–1019.
- [15] Cameselle C., Reddy K.R. Development and enhancement of electro-osmotic flow for the removal of contaminants from soils. *Electrochim. Acta*, 2012, **86**, P. 10–22.
- [16] Zhou J., Tao Y.L., et al. Electro-osmotic strengthening of silts based on selected electrode materials. *Soils Found.*, 2015, **55** (5), P. 1171–1180.
- [17] Tripathi D., Bhushan S., Be'g O.A. Transverse magnetic field driven modification in unsteady peristaltic transport with electrical double layer effects. *Colloids Surf. A*, 2016, **506**, P. 32–39.
- [18] Kikuchi Y. Effect of Leukocytes and platelets on blood ow through a parallel array of microchannels: micro-and Macroow relation and rheological measures of leukocytes and platelate acivities. *Microvasc. Res.*, 1995, **50**, P. 288–300.
- [19] Tripathi D., Bhushan S., Beg O.A. Transverse magnetic field driven modification in unsteady peristaltic transport with electrical double layer effects. *Colloids Surf. A. Physicochem. Eng. Asp.*, 2016, **506**, P. 32–39.

Effect of doping concentration on optical and electrical properties of intrinsic n-type ZnO (i-ZnO) and (Cu, Na and K) doped p-type ZnO thin films grown by chemical bath deposition method

Vipul Shukla¹, Dr. Amit Patel²

¹Gujarat Technological University, Ahmedabad – 382424 Gujarat, India

²Government Engineering College, Godhra – 389001 Gujarat, India

vipuljshukla317@gmail.com

DOI 10.17586/2220-8054-2020-11-4-391-400

Pure ZnO and copper (IB group), sodium (IA group) and potassium (IA group) and doped ZnO thin films on glass substrate by chemical bath deposition method have been studied for Hall effect measurements, resistivity, Raman and photoluminescence (PL). The influence of dopant content on carrier concentration, electrical resistivity, and Hall mobility of the thin films are analyzed. Electrical conductivity measurements of ZnO are carried out by two probe method and activation energy for the electrical conductivity of pure and doped ZnO is found out. The Raman scattering of the pure ZnO and doped ZnO shows the first and second orders of polar and non-polar modes. Raman spectra confirms the hexagonal wurtzite structure of pure and doped ZnO with E_2 (high) mode at 439 cm^{-1} and presence of other possible defects. Photoluminescence (PL) at room temperature results indicate the emission occurs at close band lines and the outcomes are identified with a few inherent imperfections in the doped ZnO thin films. The PL results demonstrate the upgraded optoelectronic properties, specifically, the carriers for long life span is executed by the oxygen opportunities. Raman spectroscopy and photoluminescence confirm existence of zinc interstitials (Zni) as well as oxygen vacancies (Vo). Resistivity as low as $15\ \Omega\text{-cm}$, Hall mobility as high as $6.2\text{ cm}^2/\text{Vs}$ and effective carrier concentration as high as $1.70 \times 10^{17}\text{ e}^-/\text{cm}^3$ have been obtained.

Keywords: Raman spectroscopy, photoluminescence spectroscopy, electrical properties, pure and doped ZnO, thin films.

Received: 14 April 2020

Revised: 11 July 2020

1. Introduction

Zinc oxide (ZnO) with its one of a kind physical and synthetic properties e.g. high chemical stability and high electrochemical coupling coefficient, wide scope of radiation absorption and high photostability, is a multifunctional material [1,2]. ZnO is an n-type semiconductor, its electrical conductivity is mainly due to excess zinc at interstitial positions. ZnO works as a potential applicant for the optoelectronics, photonics, piezoelectric and solar cell applications because of its specific band gap (3.37 eV) and expansive exciton binding energy (60 meV) at room temperature [3,4]. ZnO exhibits greatest variety of nanostructures. ZnO is the key material for various potential applications such as photodetectors, laser diode, sensors, flexible and polymer based solar cells and an electrode in dye sensitized solar cells. Many research groups are working for the development of ZnO nanostructures based white light emitting diode (LED) as an alternative source to enable bright and energy saving light sources [5–7]. Electrical properties of ZnO thin films doped with materials like Cu are very useful for optoelectronic applications [8] however efficiency of such films found limited due to formation of donor compensating point defects [9]. Coulomb interactions between dopant and acceptor-like defects, such as oxygen interstitial lead to bound complexes [10,11]. The combination of p-type and n-type material reduces the recombination rate of photo generated electrons and holes [12].

We performed methodical Raman spectroscopy studies to examine the vibrational symmetry qualities of the pure doped ZnO films. Progress in metal doped ZnO works are effectively encouraging possibility for spintronics and photonics applications because of their one of a kind properties [13,14]. Raman spectra indicated a successful incorporation of K ions into the ZnO lattice [15]. Moreover, the Raman spectroscopy is a versatile technique to study the doping agent incorporation and impurity induced modes of ZnO nanoparticles doped with metals [16]. By introducing various ions in the crystal lattice of ZnO, its optical properties can be modified [17].

PL emission spectroscopy is a traditional technique to determine optical properties and internal defects of metal doped ZnO nanostructures [18]. ZnO is an n-type semiconductor. ZnO is expected to be p-doped by elements of IA group (such Li, Na, and K), IB group (such as Cu, Ag, Au), or V–A group (such as N, P, As, Sb) [19]. Electrical properties of ZnO vary significantly due to carrier concentration, mobility and resistivity. The Hall effect is the most extensively used method to measure the electrical properties. Resistivity and Hall Measurements were made by the van der Pauw method [20,21] to study the conductivity phenomena across square-shaped samples. Doping of various impurity elements in ZnO shows different functions and improved properties of semiconductor compounds

such as electrical, optical and mechanical, which facilitate the development of many electronic and optoelectronic devices [22–24].

Many investigations are carried out to improve the characteristics of ZnO thin films by doping in it with various materials. However, investigations of Cu, Na and K doped ZnO thin films are very scarce, also, to the best of our knowledge, there is no study which compares the effects of these dopants on electrical and optical properties of ZnO. Moreover, most studies are concentrated around the ZnO thin films developed by physical routes and little research has been done on the same developed by chemical route. Thus, it is of interest to us to investigate the influence of the Cu, Na and K dopant elements on the properties of ZnO thin films deposited by chemical routes. Therefore, we set out an easy, well-grounded and low-cost method for growing and doping ZnO with Cu, K and Na dopant using Chemical Bath Deposition, in aqueous solution. Influence of doping on electrical and optical parameters like resistivity, conductivity, mobility, carrier concentration, band gap values and ionization energies of impurity levels were investigated.

2. Experimental details

Pure ZnO thin films were synthesized by chemical bath deposition method following the same procedure as reported earlier [25]. Aqueous solutions of 0.1 M 20 ml copper chloride, 0.1 M 20 ml sodium chloride and 0.1 M 20 ml potassium chloride were added to 0.1 M 60 ml zinc chloride solution for the growth of copper doped ZnO (Cu:ZnO), sodium doped ZnO (Na:ZnO) and potassium doped ZnO (K:ZnO) respectively. After that it was mixed with aqueous ammonia solution.

3. Measuring instruments

Reni shaw in Via Raman Microscope with a laser excitation source ($\lambda = 514$ nm) was used to record Raman scattering spectra at room temperature. PL (photoluminescence) spectrum of all the samples were recorded at room temperature using a Shimadzu RF-5301 PC spectro-fluoro- photometer under an excitation wavelength of $\lambda = 325$ nm and the emission spectra was recorded at the wavelength range of 350 – 550 nm. Ozone free Xenon-quartz lamp of 150 W was used for excitation. Hall-effect measurements were carried out in the van der Pauw configuration (DNE 21A) at room temperature for the determination of type of conduction mechanism, Hall mobility and carrier concentration. Electrical conductivity and activation energy were determined by the two probe resistivity measurement performed on all the samples from room temperature to 200 °C.

4. Result and discussion

4.1. Raman spectroscopy

In order to determine the presence of dopant-resulted defects and deficiency in lattice of source crystal, especially with regards to material separate on or second level states in material, Raman spectroscopy is used as an adaptable technique. The vibrational properties of all the four films are investigated by Raman spectra. ZnO thin films with hexagonal wurtzite structure fit into the P63mc position group. The first-class Raman scattering involves only the optical phonons at Γ point of the Brillouin zone for the ideal ZnO crystal lattice. As per the group theory, wurtzite ZnO should be with optical modes and they can be formulated by the following equation:

$$\Gamma_{\text{opt}} = 1A_1 + 2B_1 + 1E_1 + 2E_2,$$

where, two polar branches A_1 and E_1 modes split into longitudinal optical (LO) and transversal optical (TO) segments having difference in their frequencies, as macroscopic electric fields are related with the LO type phonons. As a First order Raman-active modes, the A_1 , E_1 and E_2 modes are considered. In order to investigate the effect of doping of Cu, Na and K on host ZnO vibrational properties are investigated for pure as well as doped thin films. Raman spectra for pure ZnO, Cu: ZnO, Na: ZnO and K: ZnO are shown in Fig. 1 and results are summarized. At 138, 338, 439 and 605 cm^{-1} , peaks representing E_{2L} , $2E_{MO}$, E_{2H} and A_{1LO} respectively, the fundamental modes of hexagonal ZnO are observed. Polar mode A_1 (LO) at around 605 cm^{-1} is also found present in all doped samples. This peak is shifted to lower energy. All the shifting and broadening of phonon modes represent the scattering contributions outside the Brillouin zone center. A_1 (LO) mode of phonon is usually referred to the complexes having zinc interstitial defect and vacancy created by oxygen in ZnO lattice. The defect complexes of zinc interstitial and oxygen vacancy in ZnO lattice can represent using a A_1 (LO) type mode of phonon [26]. These interstitial incorporation of Cu, Na and K might have caused significant structural disorder in ZnO, producing the observed changes in the line width and position of the Raman peaks.

Raman spectra presented in Fig. 1 show several peaks at 138, 338, 439, 605 and 1123 cm^{-1} correspond to E_2 (low), E_2 (high) – E_2 (low), E_2 (high), A_1 (LO) and $2(\text{LO})$ vibration modes respectively. The peak at 338 cm^{-1} was attributed to second order phonon method because of multiple phonon processes [27]. E_2 (high) mode of pure

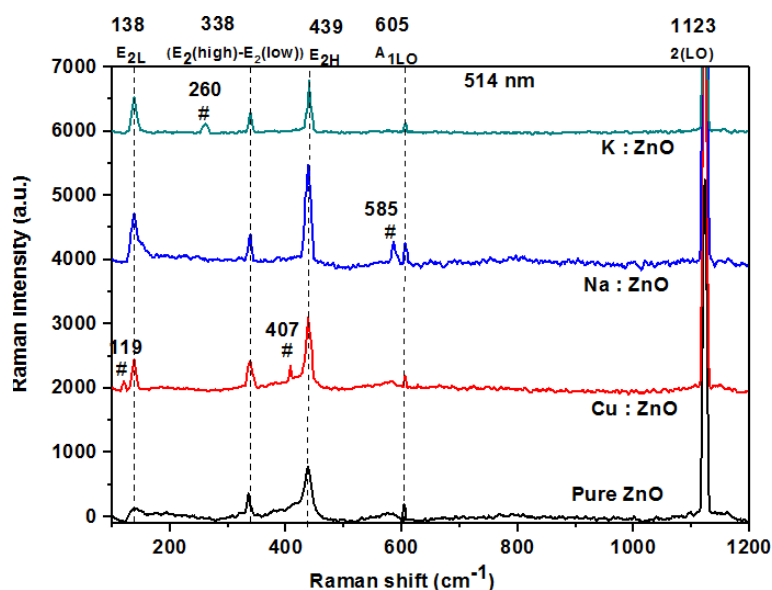


FIG. 1. Raman spectra of undoped and doped ZnO films grown on glass. The background has been removed, and the spectra have been vertically offset for clarity

and doped ZnO can be attributed to the good crystallinity of the films and this mode indicates the band characteristic of wurtzite-structured ZnO [28]. The A_1 (LO) (605 cm^{-1}) and 2LO (1123 cm^{-1} , which is normally inactive in the infrared) are respectively the first and second order of the LO phonons at the Γ center of the Brillouin zone. These vibrations were shown to present a resonant profile and are attributed to localized excitations that are strongly coupled to the lattice through the Fröhlich interactions [29].

Finally, we point out that some of the additional peaks appear in the spectra of ZnO thin films with certain dopant species, indicating host lattice defects in the ZnO structure only, which is shown with “#” such as the peak at 119 and 407 cm^{-1} for the Cu doped, at 585 cm^{-1} for the Na doped, and at 260 cm^{-1} for K doped thin films. These modes seem to be related to the individual dopants, and may be used as indication for their incorporation.

4.2. Photoluminescence studies

Effect of doping on the optical properties was also investigated by photoluminescence (PL) spectra of all the four thin films at room temperature. Emission PL spectra with excitation wavelength of 325 nm has been recorded.

There are two parts in the emission spectrum of ZnO thin film: Excitonic near band edge (NBE) emission in the UV region, with energy approximately the band gap of ZnO and the deep level emission (DLE) in the visible region arising from intrinsic defects as well as extrinsic impurities. The DLE shows numerous peaks subjected to the nature of intrinsic defects, their complexes and extrinsic impurities. The concentration of these defects and impurities transform the pattern and status of peaks in terms of position.

TABLE 1. PL peak position of pure and doped samples

Thin Film	Peak position at wavelength $\lambda_{ex} = 325 \text{ nm}$		
	NBE (Near band edge emission) Violet emission	DLE (Deep level emission) Blue emission	DLE (Deep level emission) Green emission
Pure ZnO	380 nm (3.27 eV)	484 nm (2.56 eV)	534 nm (2.32 eV)
Cu:ZnO	386 nm (3.21 eV)	—	520 nm (2.38eV)
Na:ZnO	397 nm (3.12 eV)	—	—
K:ZnO	392 nm (3.16 eV)	486 nm (2.55 eV)	—

In the present study the PL peak at 380, 386, 397 and 392 nm correspond to photon energy 3.27, 3.21, 3.12 and 3.16 eV for pure ZnO, Cu:ZnO, Na:ZnO and K:ZnO respectively are smaller than band gap of the ZnO at room

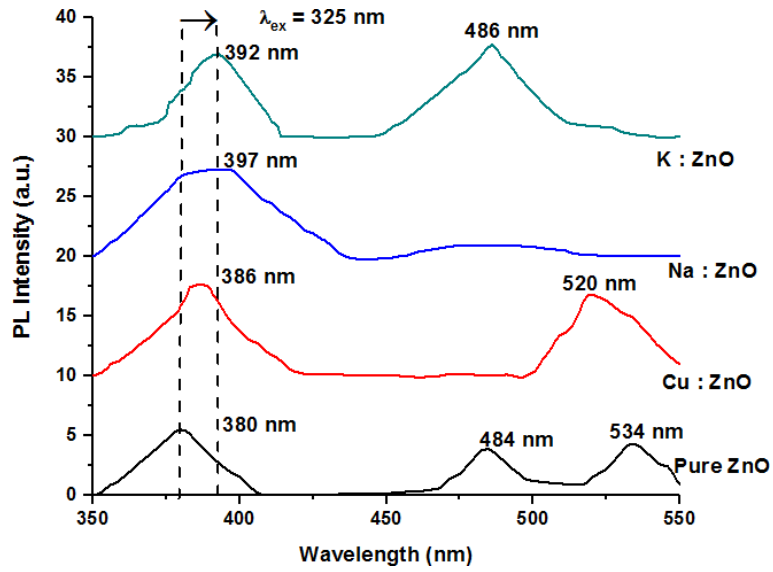


FIG. 2. Red-shift of the UV peaks in PL spectra for the Cu-, Na- and K- doped ZnO compared to the undoped ZnO thin films

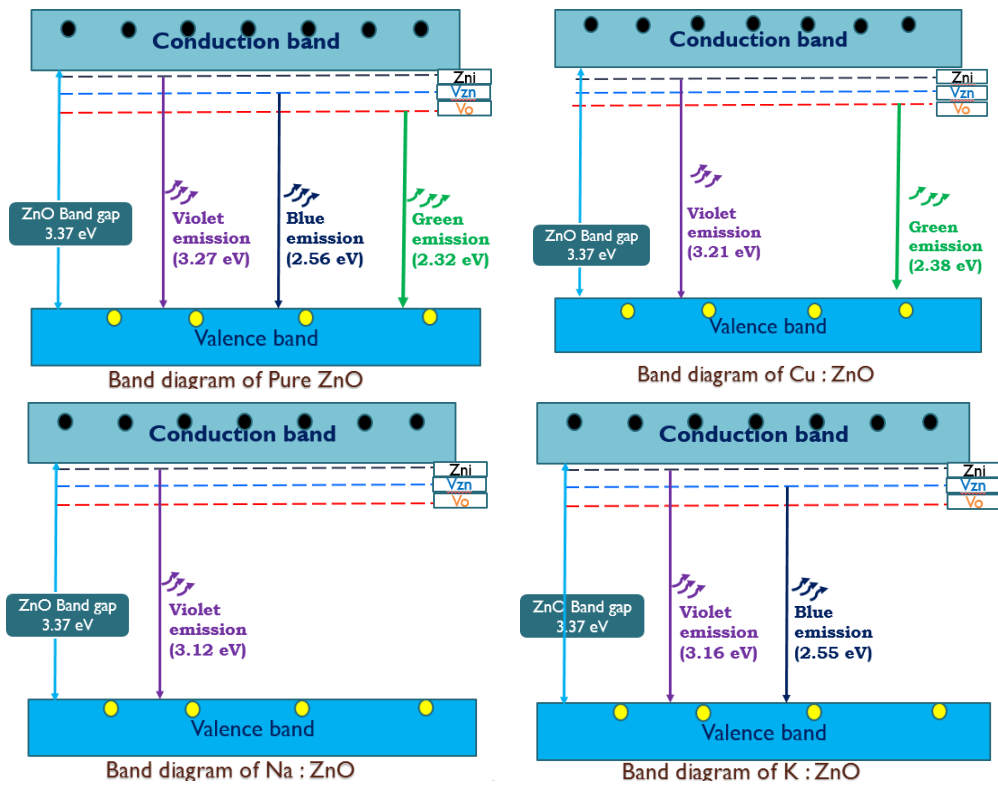


FIG. 3. Band diagram of Pure ZnO and Cu, Na and K doped ZnO thin films

temperature (3.37 eV), which is not due to the band-band transition between valence band and conduction band but it's a near band emission (NBE), which are due to the recombination of free excitons. The deep level emission (DLE) peaks recorded at 484 – 486 nm are mainly due to oxygen vacancies (Vo) in the compounds and zinc interstitials [30]. The green band at 534 and 520 nm for pure ZnO and Cu doped ZnO thin films are mainly due to the oxygen related effects like zinc interstitials (Zni), oxygen vacancies (Vo) and antisite oxygen (Ozn). The violet emission presumably resulted from a close relation with defects such as interstitial Zn atoms (Zni) and ions in the ZnO lattice.

In the case of pure ZnO, oxygen vacancies play an important role in the origin of green peak at ~534 nm. However, the precise mechanism of green emission in ZnO is not yet assured and energy levels of various defects stated in literature differ greatly. Moreover, several reports hint that the green emission in ZnO is a result of oxygen vacancies and Cu impurities. Dingle pointed that the charge transfer from impurity states (Cu^{2+}) to concerned valence band is positively factor of green luminescence in Cu-ZnO [31]. In addition to this model as suggested by Garces et al. [32], Cu may be either in Cu^+ or Cu^{2+} state. It is referred that monovalent state (Cu^+) will contribute structure with less emission as a result of donor-acceptor pair recombination in which shift from the copper acceptor to superficial donor impurity happens. In the present research, green luminescence in undoped ZnO, may be caused by the presence of constitutional defects in ZnO. Moreover, there is slight possibility of oxygen vacancy, which is also an explanation of green emission in pure ZnO. However, a fair intensification in green emission in Cu: ZnO samples points out the contribution of Cu in green emission. It also recommends that the improved green emission is predominantly owing to copper-impurities. Thus, enhancement in n-type conductivity (Table 2) and appearance of green emission after copper doping in ZnO supports that the Cu is doped in ZnO lattice that is the cause of green emission. CuO film is an effective absorbing layer in the field of solar energy [33].

TABLE 2. Optical and electrical data of Pure ZnO and Cu, Na and K doped ZnO thin films deposited on glass substrate with various doping concentrations

Sample	Resistivity ρ (Ω cm)	Conductivity σ (S/cm)	Mobility μ (cm^2/Vs)	Hall coefficient R_H (cm^3/C)	Carrier concentration n (e^-/cm^3)	Activation Energy E_a (eV)
Pure ZnO	72.14	0.0139	0.525	37.84	1.651×10^{17}	0.038
0.1M Cu:ZnO	78.57	0.0127	0.603	47.40	1.318×10^{17}	0.034
0.2M Cu:ZnO	59.29	0.0169	0.744	44.10	1.418×10^{17}	0.033
0.3M Cu:ZnO	45.00	0.0222	0.876	39.40	1.585×10^{17}	0.029
0.4M Cu:ZnO	35.71	0.0280	1.064	38.00	1.644×10^{17}	0.027
0.5M Cu:ZnO	15.00	0.0667	2.447	36.70	1.703×10^{17}	0.027
0.1M Na:ZnO	72.14	0.0139	5.877	424.00	1.473×10^{16}	0.057
0.2M Na:ZnO	67.86	0.0147	4.509	306.00	2.043×10^{16}	0.057
0.3M Na:ZnO	60.71	0.0165	3.047	185.00	3.375×10^{16}	0.047
0.4M Na:ZnO	43.57	0.0230	1.985	86.50	7.227×10^{16}	0.035
0.5M Na:ZnO	22.86	0.0438	3.588	82.00	7.620×10^{16}	0.033
0.1M K:ZnO	78.57	0.0127	2.456	193.00	3.236×10^{16}	0.048
0.2M K:ZnO	70.00	0.0143	2.557	179.00	3.498×10^{16}	0.045
0.3M K:ZnO	56.43	0.0177	2.446	138.00	4.531×10^{16}	0.017
0.4M K:ZnO	35.00	0.0286	3.714	130.00	4.792×10^{16}	0.023
0.5M K:ZnO	20.00	0.0500	6.200	124.00	5.033×10^{16}	0.020

The red-shift in UV emission is observed in PL spectra of doped ZnO. This red-shift in the UV emission could be an outcome to get p-type ZnO. A widening of the band-gap indicated ZnO doping with donors; while p-type ZnO has indicated reduced band-gap whenever doped with acceptors.

4.3. Electrical measurements

4.3.1. *Resistivity measurements.* Temperature dependence of electrical resistivity of pure and doped ZnO thin films with different dopant concentrations was measured by two probe resistivity measurement method from room temperature to 200 °C. The resistivity (ρ) of the samples was calculated by using the formula:

$$\rho = \frac{RA}{l},$$

where R is the resistance, A is the cross sectional area and l is the length of a thin film.

Resistivity of a 0.1 M Pure ZnO is 72.14 $\Omega\cdot\text{cm}$ but by increasing the precursor concentration from 0.1 to 0.5 M of Cu, Na and K doped ZnO, the resistivity value decreases as shown in Table 2. The decrease in resistivity of Cu, Na and K doped ZnO thin films with concentration might be due to the capture of free electrons in ZnO lattice by the empty lower energy 3d Cu states.

The electrical conductivity of the Cu:ZnO, Na:ZnO and K:ZnO films depended on the oxygen vacancies and the contribution from the Zn–Cu, Zn–Na and Zn–K interstitial atoms. The resistivity of the Cu:ZnO, Na:ZnO and K:ZnO films decreased from 78.57 to 15 Ωcm , 72.14 to 22.86 Ωcm and 78.57 to 20 Ωcm as the doping concentration increased from 0.1 M to 0.5 M respectively. The conductivity was increased because of the reduction in the grain-boundary scattering. The carrier concentration of pure ZnO is $1.651 \times 10^{17} \text{e}^-/\text{cm}^3$ and for Cu: ZnO, Na: ZnO and K:ZnO films is increased from 1.318×10^{17} to $1.703 \times 10^{17} \text{e}^-/\text{cm}^3$, 1.473×10^{16} to $7.620 \times 10^{16} \text{e}^-/\text{cm}^3$ and 3.236×10^{16} to $5.033 \times 10^{16} \text{e}^-/\text{cm}^3$ as the doping concentration increased from 0.1 M to 0.5 M respectively. Mobility of the pure ZnO film was found to be 0.525 cm^2/Vs , by adding impurity like Cu and K mobility is increased from 0.60 to 2.45 cm^2/Vs and 2.46 to 6.2 cm^2/Vs but for Na doped it decreases from 5.88 to 3.59 cm^2/Vs as the doping concentration increased from 0.1 M to 0.5 M respectively which showed improvements in the properties of the doped thin films (Table-2).

4.3.2. *Activation energy.* The energy required to shift charge from one primarily neutral species to another is called as activation energy and written by E_a . This is identical to the electrostatic binding energy of the charge to the species. When these charge carriers are being excited to at least activation energy from the Fermi-level, there will be channeling from one species to another. These species or small particles are called crystals. The activation energy is associated with film conductivity [31] and correlated by this formula:

$$\sigma = \sigma_0 e^{-[E_a/2k_B T]},$$

where, σ_0 is the conductivity at 0 °C and k_B is the Boltzmann constant and T is the absolute temperature. The equation can be written as:

$$\ln \sigma = \frac{-E_a}{2k_B T} + \ln \sigma_0.$$

This equation is equivalent to a straight line equation, $y = mx + c$. So that can be determined from the slope of the straight line. From the graph of $\ln \sigma$ Vs $1/T$, can be calculated by using the relation:

$$E_a = \left(\frac{-\ln \sigma}{1/T} \right) \times 2k_B \text{ (eV)}.$$

The activation energy represents the location of trap levels below the conduction band. In the present study activation energies of the undoped and Cu, Na and K doped ZnO films were studied and recorded in Table 2. The activation energy can be extracted from the slopes of the fitting lines. Fig. 4 shows the variation of $\log \rho$ with reciprocal of temperature for the Cu, Na and K doped ZnO thin film. It is observed that resistance increases with increasing temperature indicating semiconducting nature of the films. From the slopes of $\log \rho$ Vs $1000/T$ plots the values of activation energies (Table 2) were calculated using the formula:

$$\text{Activation energy } E_a = 2.303 \times k_B \times 10^3 \times \left(\frac{-E_a}{R} \right) \text{ (eV)},$$

where $k_B = 8.602 \times 10^{-5} \text{ eV/K}$.

4.3.3. *Measurements of Hall parameters.* Hall measurements have been carried out at room temperature. In order to obtain p-type of ZnO it is necessary provide the compensation of native donor defects such as oxygen vacancies and interstitial zinc atoms by doping. The defects in hydrogen interstitial and oxygen vacancy and the addition of the Cu, Na and K dopant produced carriers in the films. Usually the concentration of these defects in ZnO is very large. Thus, that demands very high concentration of acceptors. P-type ZnO is difficult to obtain due to their low solubility in ZnO, wide band gap and low valence band energy. The self-compensation from donors and high ionization energy of acceptors are the two main problems hindering the enhancement of free hole concentration. Current limitations to p-doping limit electronic and optoelectronic applications of ZnO, which usually require junctions of n-type and

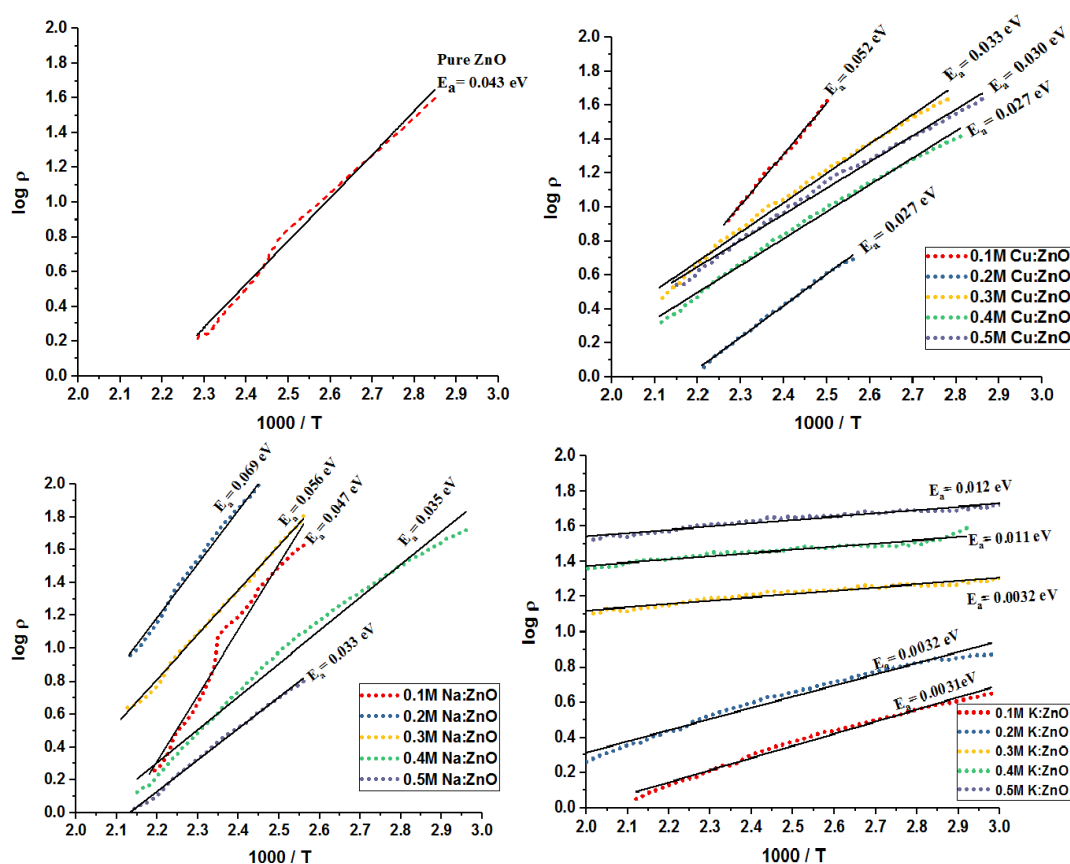


FIG. 4. Curve between $\log \rho$ and $1000/T$ of pure and doped ZnO thin films

p-type material. Known p-type dopants include group-I elements Li, Na, K; group-V elements N, P and As; as well as copper and silver. However, many of these form deep acceptors and p-type conduction is not significant at room temperature [1].

The Hall effect study is to compute the type of carriers. The activation energy relies on the donor carrier concentration and energy levels of the impurity. An increment in donor carrier concentration brings the Fermi level up in the energy gap and results in the reduction of activation energy [34].

Hall effect measurements had conducted on a sample grown on glass substrate as the magnetic field diverse from 0.1 to 1.5T. Hall effect measurement is conducted for the sixteen thin films, one film of 0.1 M pure ZnO and five films of Cu, K and Na doped ZnO each, for the variation of doping concentration from 0.1 to 0.5 M. The Hall coefficient is defined as:

$$R_H = \frac{V_H \times t}{I \times B},$$

where R_H is Hall coefficient, V_H is Hall voltage, t is the thickness of the film, I is the current passing through the conductor and B is the magnetic field. The Hall coefficient reveals the nature of the charge carriers, their concentration in the conductor, and their charge. The formula of carrier concentration (n) and mobility (μ) are:

$$R_H = \frac{-1}{n \times q},$$

$$\mu = \frac{R_H}{\rho},$$

where n is the concentration of the carriers, q is the charge of a single carrier.

Figure 5 shows the variation in the different electrical transport parameters such as the resistivity (ρ), the Hall coefficient (R_H), the carrier (electron-hole) concentration (n) and the mobility (μ) for the variation in doping concentration of the doped thin films. It is concluded that in all samples, resistivity and ionization energy decreases with increasing doping concentration. Also carrier concentration increases with doping concentration. The graph of mobility Vs doping concentration, mobility seems to be increasing with doping concentration in all samples for Cu and

K doping but for Na doping mobility decreases for 0.3 M concentration then it is increases as precursor concentration increases. Also the rate of the increment is very low in copper-doped ZnO thin films. The negative value of the Hall coefficient (R_H) for the pure ZnO film indicates its n-type conducting nature whereas; the positive values of R_H for all of the doped ZnO films signify their p-type conductivity. The carrier (electron) concentration for the undoped ZnO is found to be $1.651 \times 10^{17} \text{ cm}^{-3}$. On the other hand, both the carrier (hole) concentration and the carrier mobility in all doped ZnO films are found to increase gradually as we change the doping concentration from 0.1 to 0.5 M. The p-type conductivity mainly arises due to the doping of the alkali metals in ZnO. The doped films do not contain a significant amount of Vo which acts as a donor within the ZnO films. The substitution of monovalent alkali ions (Na^+ and K^+) at the Zn^{2+} ion sites can introduce holes into the system [35, 36].

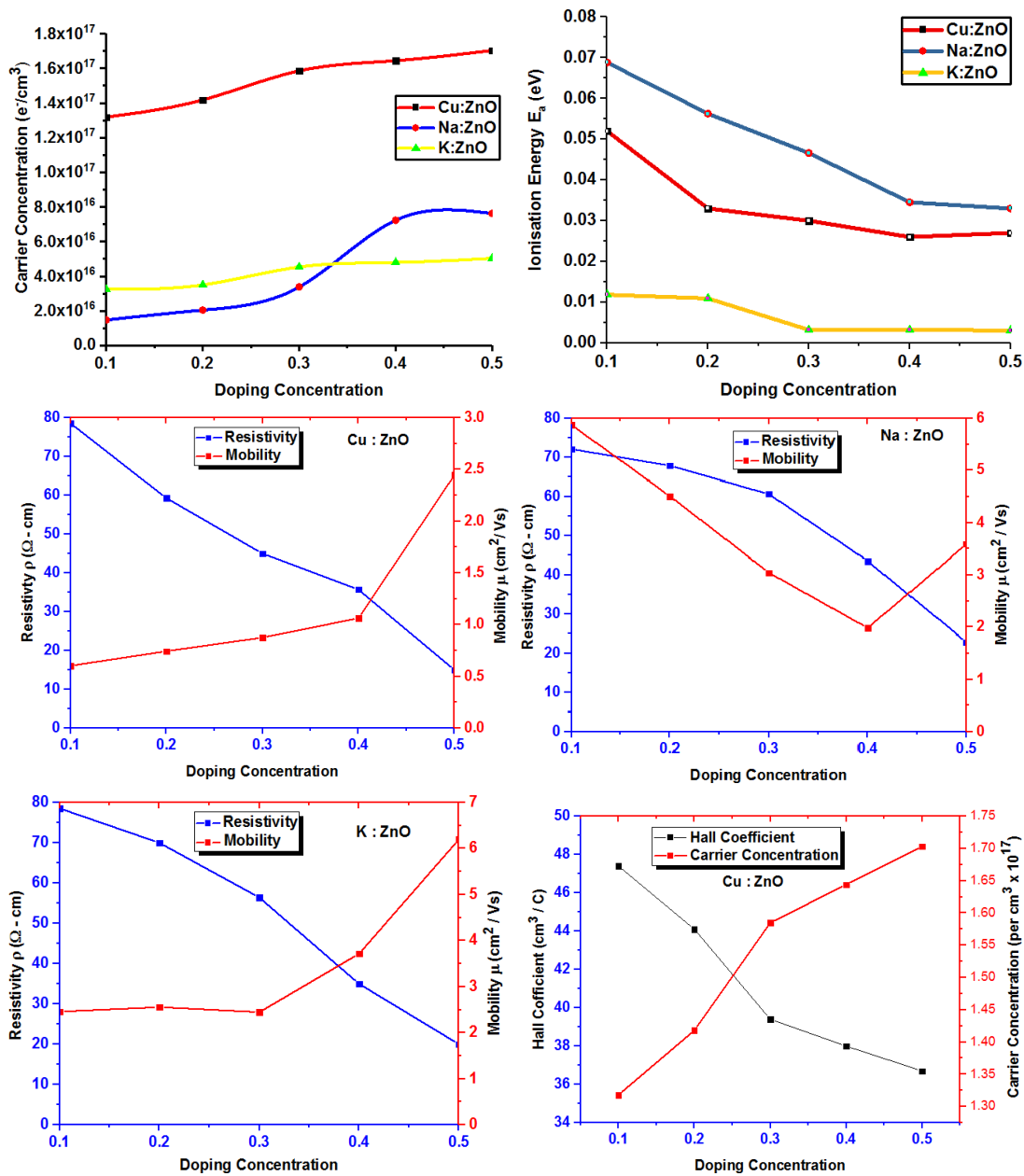


FIG. 5. Shows variation in resistivity (ρ), carrier concentration (n), mobility (μ) and ionization energy (E_a) of a Cu, Na and K doped ZnO thin films with variation in doping concentration from 0.1 to 0.5 M

5. Conclusion

In summary, complete and careful comparison of pure ZnO and copper (Cu), potassium (K) and sodium (Na) doped ZnO thin films has been carried out. All three dopants improve film optical and electrical properties compared to undoped ZnO. The Raman spectra show that the intensity of the dominant peak changes with different dopant; compared to the ZnO thin film, the shifting of peaks is due to lattice defects and lattice disorder. Decrease in band gap supports optical properties of crystalline structures. Green deep-level emission obtained in PL is potentially important for solar cell devices. The synchronous Raman and photoluminescence examinations have the preferred standpoint to correspond with the changes observed in the optical property of the semiconducting materials. Hall effect results show that a growth condition is suitable for p-type doped ZnO thin films with high carrier concentration. Also, chemical bath deposition method to grow doped ZnO increases stability of p-type ZnO. The positive value of Hall voltage of all doped thin films measured using Van der Pauw method with four point electrode fixture is in agreement with the red shift in PL spectra of p-type doping. The decrease in resistivity of all three doped thin films compared with ZnO films is attributed to the replacement of Zn^{2+} by Cu^{2+} , Na^+ and K^+ ions respectively. The resistivity of all doped thin films decrease with increase in doping concentration. As the concentration of impurity increases, both the conductivity and mobility of thin films increase. Activation energy has been observed to decrease with an increase in dopant concentration as well as change in dopant. ZnO thin films doped with Cu, Na and K has the capability to increase its conductivity without adversely modifying other properties. The deposited films find suitable for photocells and solar cell gadgets.

References

- [1] Segets D., Gradl J., et al. Analysis of optical absorbance spectra for the determination of ZnO nanoparticle size distribution, solubility, and surface energy. *ACS Nano*, 2009, **3**, P. 1703–1710.
- [2] Lou X. Development of ZnO series ceramic semiconductor gas sensors. *J. Sens. Trans. Technol.*, 1991, **3**, P. 1–5.
- [3] Wang J.X., et al. Free-standing ZnO–CuO composite nanowire array films and their gas sensing properties. *Nanotechnology*, 2011, **22** (32), P. 1–7.
- [4] Janotti A., Van De Walle C.G. Fundamentals of zinc oxide as a semiconductor. *Reports Prog. Phys.*, 2009, **72** (126501), P. 14–29.
- [5] Wang Z.L. Zinc oxide nanostructures: growth, properties and applications. *J. Phys. Condens. Matter*, 2004, **16**, P. R829–R858.
- [6] Gomez J.L., Tigli O. Zinc oxide nanostructures: From growth to application. *Journal of Materials Science*, 2013, **48** (2), P. 612–624.
- [7] Schmidt-Mende L., Macmanus-Driscoll J.L. ZnO: nanostructures, defects, and devices. *Materials Today*, 2007, **10** (5), P. 40–48.
- [8] Rana V.S., Rajput J.K., Pathak T.K., Purohit L.P. Cu sputtered Cu/ZnO Schottky diodes on fluorine doped tin oxide substrate for optoelectronic applications. *Thin Solid Films*, 2019, **679**, P. 79–85.
- [9] Hamza Taha M.K., et al. Control of the compensating defects in Al-doped and Ga-doped ZnO nanocrystals for MIR plasmonics. *RSC Adv.*, 2017, **7** (46), P. 28677–28683.
- [10] Sett D., Basak D. Toward understanding the role of VZn defect on the photoconductivity of surface-passivated ZnO NRs. *J. Phys. Chem. C*, 2017, **121** (44), P. 24495–24504.
- [11] Ghosh S., Mallick A., et al. A novel blanket annealing process to achieve highly transparent and conducting Al doped ZnO thin films: Its mechanism and application in perovskite solar cells. *Sol. Energy*, 2018, **174**, P. 815–825.
- [12] Varghese J., Vinodkumar R. Effect of CuO on the photoluminescence quenching and photocatalytic activity of ZnO multilayered thin films prepared by sol-gel spin coating technique. *Mater. Res. Express*, 2019, **6** (10), P. 1–27.
- [13] Pearton S.J., et al. Transition Metal Doped ZnO for Spintronics. *MRS Proceedings*, 2007, **999**, 0999-K03-04.
- [14] Silambarasan M., Saravanan S., Soga T. Mn-doped ZnO nanoparticles prepared by solution combustion method. *E-Journal of Surface Science and Nanotechnology*, 2014, **12**, P. 283–288.
- [15] Sajjad M., Ullah I., et al. Structural and optical properties of pure and copper doped zinc oxide nanoparticles. *Results Phys.*, 2018, **9**, P. 1301–1309.
- [16] Sato-Berrú R.Y., Vázquez-Olmos A., Fernández-Osorio A.L., Sotres-Martnez S. Micro-Raman investigation of transition-metal-doped ZnO nanoparticles. *J. Raman Spectrosc.*, 2007, **38**, P. 1073–1076.
- [17] Bhattacharyya P., Basu P.K., et al. Noble metal catalytic contacts to solgel nanocrystalline zinc oxide thin films for sensing methane. *Sensors Actuators B*, 2008, **129** (2), P. 551–557.
- [18] Wu L., Wu Y., Lü W. Preparation of ZnO Nanorods and optical characterizations. *Phys. E Low-Dimensional Syst. Nanostructures*, 2005, **28** (1) P. 76–82.
- [19] Habeebullah A., Alabi A.B., et al. Synthesis and Characterization of a dual-doped Zinc Oxide [(Na,N):ZnO] Nanoparticles by Wet Chemical Method. *African Review of Physics*, 2018, **13** (5), P. 29–38.
- [20] Petersen D.H., Hansen O., Lin R., Nielsen P.F. Micro-four-point probe Hall effect measurement method. *J. Appl. Phys.*, 2008, **104** (1), 0137110.
- [21] Moulzolf S.C., Frankel D.J., Lad R.J. In situ four-point conductivity and Hall effect apparatus for vacuum and controlled atmosphere measurements of thin film materials. *Rev. Sci. Instrum.*, 2002, **73** (6), P. 2325–2330.
- [22] Bhosle V., Tiwari A., Narayan J. Electrical properties of transparent and conducting Ga doped ZnO. *J. Appl. Phys.*, 2006, **100** (3), 033713.
- [23] Postica V., et al. Multifunctional Materials: A Case Study of the Effects of Metal Doping on ZnO Tetrapods with Bismuth and Tin Oxides. *Adv. Funct. Mater.*, 2017, **27**, P. 1–15.
- [24] Tiginyanu I., et al. Strong light scattering and broadband (UV to IR) photoabsorption in stretchable 3D hybrid architectures based on Aero-graphite decorated by ZnO nanocrystallites. *Sci. Rep.*, 2016, **6** (1), P. 1–11.

- [25] Shukla V.J., Patel A.J. Influence of Multiple Layers on Chemical Bath Deposited ZnO Thin Films. *Int. J. Res. Appl. Sci. Eng. Technol.*, 2018, **6** (3), P. 268–274.
- [26] Gayen R.N., Sarkar K., et al. ZnO films prepared by modified sol-gel technique. *Indian Journal of Pure & Applied Physics*, 2011, **49**, P. 470–477.
- [27] Zhou H., et al. Raman studies of ZnO: Co thin films. *Physica Status Solidi (A) Applications and Materials Science*, 2007, **204** (1), P. 112–117.
- [28] Liu X., Afzaal M., et al. Conducting ZnO thin films with an unusual morphology: Large flat microcrystals with (0 0 0 1) facets perpendicular to the plane by chemical bath deposition. *Materials Chemistry and Physics*, 2011, **127**, P. 174–178.
- [29] Livneh T., Sterer E. Effect of Pressure on the Resonant Multiphonon Raman Scattering in UO₂. *Phys. Rev. B: Condens. Matter Mater. Phys.*, 2006, **73**, 085118.
- [30] Singh A.K., Viswanath V., Janu V.C. Synthesis, effect of capping agents, structural, optical and photoluminescence properties of ZnO nanoparticles. *Journal of Luminescence*, 2009, **129** (8), P. 874–878.
- [31] Dingle R. Luminescent Transitions Associated With Divalent Copper Impurities and the Green Emission from Semiconducting Zinc Oxide. *Phys. Rev. Lett.*, 1969, **23** (11), P. 579–581.
- [32] Garces N.Y., et al. Role of copper in the green luminescence from ZnO crystals. *Appl. Phys. Lett.*, 2002, **81** (4), P. 622–624.
- [33] Peryakov D.S., Rembeza S.I., Menshikova T.G., Palkovnikov V.E. Influence of Annealing on the Electrophysical Properties of Copper Oxide (II) Thin Film, Prepared by Sol-Gel Method. *Nano Hybrids and Composites*, 2020, **28**, P. 48–52.
- [34] Kumar R., Khare N. Temperature dependence of conduction mechanism of ZnO and Co-doped ZnO thin films. *Thin Solid Films*, 2008, **516** (6), P. 1302–1307.
- [35] Park C.H., Zhang S.B., Wei S.H. Origin of p-type doping difficulty in ZnO: The impurity perspective. *Phys. Rev. B: Condens. Matter Mater. Phys.*, 2002, **66**, 073202.
- [36] Rauch C., Gehlhoff W., et al. Lithium related deep and shallow acceptors in Li-doped ZnO nanocrystals. *J. Appl. Phys.*, 2010, **107**, 024311.

Demagnetizing fields in chiral magnetic structures

M. A. Moskalenko^{1,2}, I. S. Lobanov^{1,3}, V. M. Uzdin^{1,3}

¹ITMO University, 197101 St. Petersburg, Russia

²Science Institute, University of Iceland, 107 Reykjavk, Iceland

³Department of Physics, St. Petersburg State University, St. Petersburg 198504, Russia

moskalenko.mary@gmail.com, lobanov.igor@gmail.com, v.uzdin@mail.ru

PACS 75.10.Hk, 75.40.Mg, 75.78.Cd

DOI 10.17586/2220-8054-2020-11-4-401-407

A method for calculating the magnetic dipole-dipole interaction in topological magnetic systems has been developed. It can be used to calculate stable states and minimum energy paths that determine the magnetic transition in chiral magnetic structures. Instead of directly summing the dipole interactions between magnetic moments/magnetic elements, we solve a local equation for demagnetizing fields. The states corresponding to the local energy minimum can be found using the Lagrange method for the conditional extrema. The efficiency of the algorithm has been demonstrated by calculating the dependence of the size and shape of magnetic skyrmions and anti-skyrmions on the magnitude of magnetization.

Keywords: topological magnetic structures, skyrmions, demagnetizing fields.

Received: 1 August 2020

Revised: 18 August 2020

1. Introduction

Chiral magnetic structures have attracted much attention in recent years due to the discovery in these systems of localized non-collinear states that can move very rapidly under the action of a spin-polarized electric current [1, 2]. In micromagnetic models, these states cannot be destroyed by continuous transformation of magnetization, and it is believed that they are topologically protected from thermal fluctuations [3,4]. In real systems magnetic moments localized on the site of discrete lattice and it is possible to say only about topological stabilization. In lattice model stability of such system can be estimated on the basis of transition state theory (TST) for magnetic degrees of freedom [5, 6].

Usually, the properties of skyrmions (Sk), as well as other topological structures, are studied within the framework of the Heisenberg-type Hamiltonian, which includes exchange, anisotropy, external magnetic field, and the Dzyaloshinskii-Moriya interaction (DMI) [5]. All these interactions decay rapidly with distance. This model correctly describes, for example, small Sk in thin PdFe films on the Ir (111) surface, observed experimentally [7]. However, such Sk are stable only at very low temperatures of the order of 10 K. Sk stable at room temperature in ferromagnetic (FM) materials are larger in size, and to describe their behavior it is necessary to take into account the magnetic dipole-dipole interaction which is responsible for the creation of demagnetizing fields. In the first approximation, this interaction can be introduced into the theory by renormalizing the anisotropy parameters [8]. However, more accurate calculations of the energy associated with demagnetizing fields are needed to describe the topological structures of micron sizes [9] and especially three-dimensional magnetic systems [10, 11]. Moreover, the stability of Sk with a size of 100 nm and more, according to [12], is always determined by the dipole-dipole interaction. So, if we want to have small stable Sk as future bits of computer memory, we must accurately evaluate the contribution of the demagnetizing fields. The development of methods for manipulating the dipole interaction in magnetic micro- and nanostructures and theoretically estimating its contribution to energy is very important for practical applications, since it allows one to control the size and stability of topological systems. Suppression of the dipole interaction in antiferromagnetic (AF) and ferrimagnetic chiral structures, for example, made it possible to create Sk of about 10 nm in size that are stable at room temperature [13]. Small room temperature Sk in artificial antiferromagnets, also use the reduction of stray fields in multilayer systems with AF interlayer coupling [14].

The lifetime of the topological states of systems without strong dipole interaction at an arbitrary temperature can be evaluated using standard TST approach. It was done for Sk in AF [15] and for small-size Sk in ferromagnetic (FM) materials [6]. Such calculations for FM micromagnetic structures are a challenging problem due to the number of degrees of freedom and need to correctly take into account the dipole-dipole interaction. There are effective methods for calculating the saddle points on the energy surface and the activation energy of Sk annihilation for systems containing millions of magnetic moments [16]. But even the calculating the energy surface for systems with a significant contribution from the dipole-dipole interaction and demagnetizing fields is still a very difficult task.

Below, we present an efficient algorithm for calculating the demagnetizing field and show its efficiency by the example of calculating Sk and antisymions (ASk) in a FM system with different saturation magnetization.

2. Micromagnetic and discrete models

The magnetic texture in the micromagnetic approach will be described by the vector field $\mathbf{m}(\mathbf{r})$, where \mathbf{r} is the coordinate of a point in the magnetic sample, and \mathbf{m} is the unit vector in the direction of the local magnetization at this point. The local magnetization value is a fast variable and is assumed to be equal to the fixed saturation magnetization M_s . Below we consider a thin film modeled by the part of the x-y plane $\Omega = [0, d]^2$ with periodic boundary conditions. The energy E of the magnetic state is expressed in terms of the energy density w as follows:

$$E = \int_{\Omega} w(\mathbf{r}) d\mathbf{r}, \quad w = w_{ex} + w_{DMI} + w_K + w_{demag},$$

where we take into account contribution of exchange w_{ex} , DMI w_{DMI} , anisotropy w_K and demagnetizing field w_{demag} . Assuming that the exchange is isotropic:

$$w_{ex} = t\mathcal{A}(\nabla\mathbf{m})^2, \quad (\nabla\mathbf{m})^2 = \left(\frac{\partial\mathbf{m}}{\partial x}\right)^2 + \left(\frac{\partial\mathbf{m}}{\partial y}\right)^2,$$

here \mathcal{A} is the exchange stiffness and t is the film thickness. For simplicity, consider uniaxial anisotropy with an easy axis perpendicular to the film (parallel to the $\hat{\mathbf{z}}$ axis):

$$w_K = -t\mathcal{K}(\mathbf{m} \cdot \hat{\mathbf{z}})^2,$$

where parameter of anisotropy $\mathcal{K} > 0$. The DMI energy is expressed in terms of Lifshitz invariant

$$L_{jk}^{(i)} = m_j \frac{\partial m_k}{\partial j} - m_k \frac{\partial m_j}{\partial i}, \quad w_{DMI} = t(\mathcal{D}_x L_{xz}^{(x)} + \mathcal{D}_y L_{yz}^{(y)}).$$

If $\mathcal{D}_x = \mathcal{D}_y = \mathcal{D}$, meta(stable) states of SkS can exist in the system, if $\mathcal{D}_x = -\mathcal{D}_y = \mathcal{D}$, then ASkS can be formed. The exchange stiffness and the anisotropy constant are independent of the magnetic texture and are the same for both Sk and ASk structures. Micromagnetic parameters are selected according to [17] to be

$$t = 0.6 \text{ (nm)}, \quad \mathcal{A} = 16 \text{ (pJ/m)}, \quad \mathcal{K} = 200 \text{ (kJ/m}^3\text{)}, \quad \mathcal{D} = 2 \text{ (mJ/m}^3\text{)}. \quad (1)$$

Saturation magnetization M_s varies from 10^3 to $4 \cdot 10^4$ (A/m).

The energy of the demagnetizing field is determined by its density:

$$w_{demag} = -\frac{\mu_0}{2} M_s \mathbf{m} \cdot \mathbf{H}_{demag},$$

where \mathbf{H}_{demag} is the demagnetizing field, which can be found from the Maxwell equations:

$$\nabla \cdot \mathbf{B} = 0,$$

$$\nabla \times \mathbf{H}_{demag} = 0,$$

where $\mathbf{B} = \mu_0(\mathbf{H}_{demag} + M_s \mathbf{m})$ is the induction of the demagnetizing field. The second condition can be satisfied introducing the potential Φ of the field: $\mathbf{H}_{demag} = -\nabla\Phi$. From the first condition we have:

$$\nabla \cdot \mathbf{H}_{demag} = -M_s \nabla \cdot \mathbf{m}.$$

Therefore the potential Φ can be found from the Poisson equation:

$$\nabla^2 \Phi = M_s \nabla \cdot \mathbf{m}. \quad (2)$$

It is worth noting that in three dimensions the equation can be solved in terms of the Green's function:

$$\Phi(\mathbf{r}) = -M_s \int \frac{\nabla_{\mathbf{r}'} \cdot \mathbf{m}(\mathbf{r}')}{4\pi|\mathbf{r} - \mathbf{r}'|} d\mathbf{r}' = M_s \int \mathbf{m}(\mathbf{r}') \cdot \frac{\mathbf{r} - \mathbf{r}'}{4\pi|\mathbf{r} - \mathbf{r}'|^3} d\mathbf{r}'.$$

Restoring the demagnetizing field from the potential and substituting the result into the energy density, we obtain the standard expression for the energy of the dipole-dipole interaction:

$$w_{demag}(\mathbf{r}) = -\mu_0 M_s^2 \int \frac{3(\mathbf{m}(\mathbf{r}') \cdot \Delta)(\mathbf{m}(\mathbf{r}) \cdot \Delta) - \mathbf{m}(\mathbf{r}') \cdot \mathbf{m}(\mathbf{r})}{4\pi|\mathbf{r} - \mathbf{r}'|^3} d\mathbf{r}', \quad \Delta = \frac{\mathbf{r} - \mathbf{r}'}{|\mathbf{r} - \mathbf{r}'|}. \quad (3)$$

To compute the dipole-dipole energy, it is necessary to sum over all pairs of magnetic moments in the system, which is computationally expensive. To overcome this difficulty, the Fourier transform is often used, which converts the convolution in the expression for energy to multiplication with a function; however, the approach is applicable only to simple domain such as a square or a cube. Another method for calculating the demagnetizing energy is to obtain

the demagnetizing field numerically, which in many cases is faster than using the Green's function. This approach has been previously used with finite element discretization. Below we develop a finite-difference discretization method that leads to a lattice-type model of the magnetic system.

The state is specified by the directions of the magnetic moment \mathbf{S}_n , determined at the sites of the square lattice n . Let's denote by \mathbf{r}_n the site position n . The energy in the lattice representation contains the same contributions as above:

$$E = E_{ex} + E_{DMI} + E_K + E_{demag}.$$

Each energy contribution is an approximation of the integral in the micromagnetic model above, rewritten in terms of the values of the magnetic moments $\mathbf{m} \approx \mathbf{S}_n$ localized near points $\mathbf{r} \approx \mathbf{r}_n$. For example energy of anisotropy becomes:

$$E_K = -K \sum_n (\mathbf{S}_n \cdot \hat{\mathbf{z}})^2.$$

Anisotropy constant in lattice model K is proportional to \mathcal{K} , but it also depends on the size of integration cell. If \mathbf{n} are points of a square lattice with lattice constant a , then $K = \mathcal{K}a^2t$.

Derivatives in expressions for w_{ex} and w_{DMI} can be estimated by finite differences:

$$\nabla \mathbf{m}(\mathbf{r}_n) = \left(\frac{\mathbf{S}_{n1} - \mathbf{S}_n}{a}, \frac{\mathbf{S}_{n2} - \mathbf{S}_n}{a}, 0 \right),$$

where \mathbf{S}_{n1} and \mathbf{S}_{n2} are nearest neighbors magnetic moment to \mathbf{S}_n along x-axis and y-axis, respectively. Eliminating constant addenda in exchange energy contributions, we get:

$$\left(\frac{\partial \mathbf{m}(\mathbf{r}_n)}{\partial x} \right)^2 \approx \frac{2}{a^2} (1 - \mathbf{S}_{n1} \cdot \mathbf{S}_n), \dots$$

the Heisenberg exchange energy is obtained in the following form:

$$E_{ex} = -J \sum_{\langle n,k \rangle} \mathbf{S}_n \cdot \mathbf{S}_k,$$

where the Heisenberg exchange constant $J = 2At$, and the sum is taken over all pairs $\langle n, k \rangle$ of magnetic moments (each pair is taken only once). Similarly, the DMI energy can be expressed as follows:

$$E_{DMI} = - \sum_{\langle n,k \rangle} \mathbf{D}_{n,k} \cdot (\mathbf{S}_n \times \mathbf{S}_k),$$

where all DM vectors $\mathbf{D}_{n,k}$ have the same length $D > 0$ and are directed along $\hat{\mathbf{y}}$, if k is on the right to n , and along $-\hat{\mathbf{x}}$, if k is above n ; here $\hat{\mathbf{x}}, \hat{\mathbf{y}}$ are basis vectors of x and y axes. The DM vectors are connected to the micromagnetic model by the identity $|D| = \mathcal{D}a$. In simulation we used 100×100 square lattice with the following parameters:

$$a = 4 \text{ (nm)}, J = 1.92 \cdot 10^{-20} \text{ (J/bond)}, D = 4.8 \cdot 10^{-21} \text{ (J/bond)}, K = 1.92 \cdot 10^{-21} \text{ (J/spin)}. \quad (4)$$

The demagnetizing energy is discretized accordingly to:

$$E_{demag} = -\frac{\mu_0 \mu}{2} \sum_n \mathbf{H}_n \cdot \mathbf{S}_n,$$

where $\mu = M_s a^2 t$ is value of magnetic moment, and $\mathbf{H}_n \approx \mathbf{H}_{demag}(\mathbf{r}_n)$ is the demagnetizing field at the point \mathbf{r}_n . The demagnetizing field is found from a discretization of Poisson equation (2). We use a five-point stencil for the second derivatives with respect to x and y , which gives us a Laplacian of the form $\Delta^2 \Phi \approx a^{-2} L \Phi$, where

$$L \Phi_{x,y} = \frac{-\Phi_{x-2,y} + 16\Phi_{x-1,y} - 30\Phi_{x,y} + 16\Phi_{x+1,y} - \Phi_{x+2,y}}{12} + \frac{-\Phi_{x,y-2} + 16\Phi_{x,y-1} - 30\Phi_{x,y} + 16\Phi_{x,y+1} - \Phi_{x,y+2}}{12},$$

here (x, y) are coordinates of the moment n on the square lattice. Approximating divergence $\nabla \cdot \mathbf{m}(\mathbf{r}_n) \approx a^{-1} G \mathbf{S}_n$ in r.h.s of (2) with central finite differences:

$$G \mathbf{S}_{x,y} = \frac{\mathbf{S}_{x+1,y} - \mathbf{S}_{x-1,y}}{2} + \frac{\mathbf{S}_{x,y+1} - \mathbf{S}_{x,y-1}}{2},$$

we obtain the Poisson equation in the discrete form:

$$L \Phi = a M_s G \mathbf{S}.$$

The last equation is a system of linear algebraic equations, which gives solution upto additive constant. It is convenient to impose additional restriction on value of Φ at arbitrary point, e.g. $\Phi_{0,0} = 0$. Then, formally, the potential can be

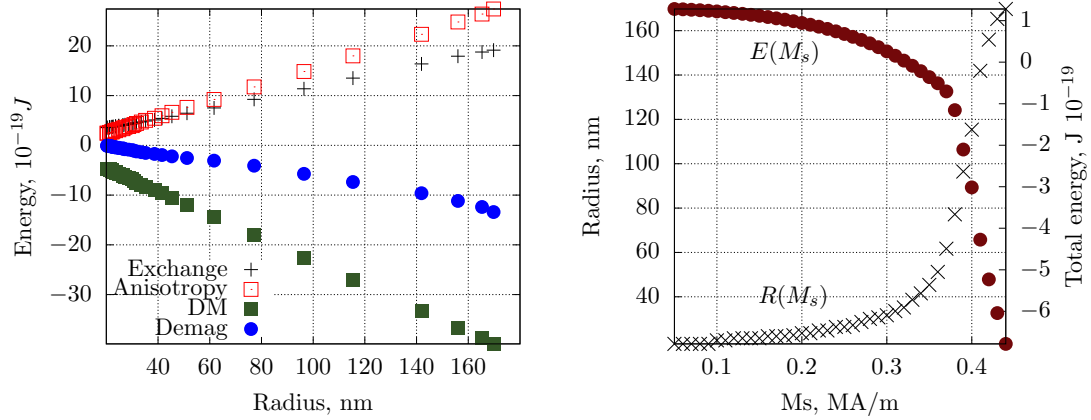


FIG. 1. Contributions of different interactions in the total energy (left) and dependencies of the total energy (solid circles) and radius (crosses) (right) for Sk in the Sk lattice on the saturation magnetization M_s . Metastable states are computed in 100×100 lattice with periodic boundary conditions and lattice constant 4 nm. Film thickness t is set to 0.6 nm, and $J = 1.92 \cdot 10^{-20}$ J/bond, $D = 0.25J$, $K = 0.1J$.

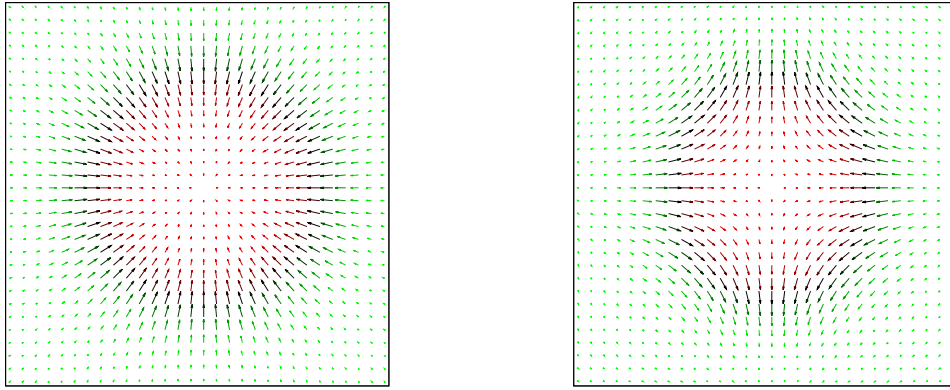


FIG. 2. Single Sk (left) and ASk (right) from the magnetic texture of a square lattice with a distance between Sk (ASk) equal to 400 nm. Simulation is carried out for a 100×100 square lattice with a lattice constant $a = 4$ (nm) for the parameters $J = 1.92 \cdot 10^{-20}$ J/bond, $D = 0.25J$, $K = 0.1J$, $M_s = 0.4MA/m$. Only part of moments is shown to make the figure readable. The colors encode the direction of the magnetic moments: green - up, red - down.

found as $\Phi = aM_s L^{-1}GS$, and the demagnetizing field is given by $\mathbf{H} = -M_s QL^{-1}GS$, where Q is gradient expressed in terms of central finite differences:

$$QU_{x,y} = \left(\frac{U_{x+1,y} - U_{x-1,y}}{2}, \frac{U_{x,y+1} - U_{x,y-1}}{2}, 0 \right).$$

It is worth noting, that the demagnetizing field obtained as a solution of the discretized Poisson equation does not coincide with the common expression for dipole-dipole interaction in lattice model, obtained as discretization of (3):

$$-\frac{\mu}{4\pi} \sum_{n,k} \frac{3(\mathbf{S}_n \cdot \Delta)(\mathbf{S}_k \cdot \Delta) - \mathbf{S}_n \cdot \mathbf{S}_k}{|\mathbf{r}_n - \mathbf{r}_k|^3}, \text{ where } \Delta = \frac{\mathbf{r}_n - \mathbf{r}_k}{|\mathbf{r}_n - \mathbf{r}_k|},$$

though the energies coincide in the continuous limit. Numeric solution to the discrete version of the Poisson equation can however be found much faster, than direct summation in dipolar interaction or as inversion of matrix L .

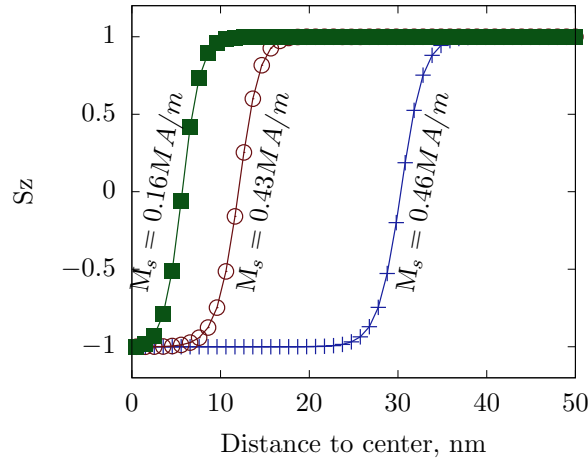


FIG. 3. ASk crosssection along lattice generator for various values of saturation magnetization M_s . ASk radius grows as M_s increases. The increase is due to a shift of the domain wall on the boundary of ASk rather than scaling of the particle shape without dipole interaction. The core part of the ASk is formed of spins perfectly aligned opposite to FM phase orientation. The domain wall width is also increases for larger magnetization, but slower than radius.

3. Chiral states in demagnetizing field

In addition to the well-studied Sk magnetic structures, in recent years, ASk have attracted attention [9, 17]. There are many similarities between these textures, which makes it easy to predict the properties of ASks based on the well-known properties of Sk. The texture of magnetization for Sk and ASk can be matched to each other using the transformation:

$$m_x \leftrightarrow m_x, \quad m_y \leftrightarrow -m_y, \quad m_z \leftrightarrow m_z.$$

Without demagnetizing fields the mapping preserves energy, if DM constants are transformed in the same way as the magnetization. Consequently, a small Sk and an ASk have the same energy surfaces and stability against thermal fluctuations. However, for a large size chiral states, the dipole-dipole interaction plays an important role. The demagnetizing fields for Sk and ASk are significantly different, have different symmetries, leading to distinct shapes of the magnetic structures for a large dipole-dipole interaction.

In this section, we compute (meta)stable Sk and ASk states in the presence of demagnetizing field using the lattice model developed in the previous section. The micromagnetic parameters given by (1) are chosen according to [17]. Numerical analysis was carried out for a square lattice of 100×100 cells with a lattice constant of 4 (nm). Periodic boundary conditions were applied for both axes, which led to a significant contribution to the energy of dipole-dipole interaction between images of a particle lying on opposite sides of the boundary. Our model is close to modeling the Sk (ASk) lattice with a distance between individual Sk (ASk) 400 (nm), in contrast to the model in [17], where isolated objects were considered. The size of a Sk without dipole interaction is much smaller than the size of a domain, therefore, its energy, radius and shape are practically not affected by an increase in the simulated volume. For a sufficiently large value of M_s , which determines the strength of the dipole interaction, the size of Sk becomes larger, and the contribution of the long-range dipole interaction increases. Therefore, Sk cannot be considered isolated.

Metastable Sk and ASk states were computed using custom optimizer based L-FBGS method. Iterations of L-FBGS method were applied only to magnetic moment directions \mathbf{S}_n , while demagnetization field potential Φ was computed on each iteration by another solver. In [18] it was shown that L-FBGS method significantly increase convergence speed even for minimum energy path computation. The potential Φ was obtained for given moments \mathbf{S}_n as solution do discrete Poisson equation by conjugate gradient method, using the potential from previous iteration as an initial approximation. The method demonstrated reasonable convergence rate, providing solution with l^∞ norm of gradient less than $10^{-5} J$ in 1000 iterations for most considered states. Operations on magnetic moments \mathbf{S}_n were performed in Cartesian coordinates as stated in the previous section, that differs from commonly used representation of spins in spherical coordinates, stereographic projections [10] or using rotation matrices [19]. Computations in Cartesian coordinates are simple and often faster than usage of other coordinates, see [20]. To take into account constrains on value of magnetic moments, gradients of energy over \mathbf{S}_n should be projected to the tangent space of the constrains manifold. Equivalently Lagrange function can be introduced for energy and on Lagrange multiplier for each constrain

$S_n^2 = 1$, then numerical optimization can be applied to the Lagrange function. To ensure that constraints are satisfied, after each iteration of L-BFGS every direction S_n should be divided by its length.

We computed (meta)stable Sk state for saturation magnetization in range $M_s = 0.05 - 0.45$ (MA/m). Increasing the magnetization, preserving other exchanges constant, increases the role of demagnetizing field in stabilization of the solitonic state. Increase of M_s decrease total energy of the Sk lattice in non-linear manner, leading to rapid drop in energy about $M_s = 0.4$ (MA/m) making Sk lattice ground state for larger M_s , as shown in Fig. 1. The radius of Sk grows moderately for M_s below 0.3 (MA/m), after the threshold Sk size grows rapidly being restricted by repulsion between Sk in Sk lattice. Energy (as well as separate contributions) demonstrates perfect linear dependence on the Sk radius for considered values of M_s , see Fig. 1. In contrast to [17] DMI interaction contribute more in absolute value than demagnetizing field, due to partial cancellation of dipole-dipole interaction with other Sk in the Sk lattice.

Sk preserves its circular shape even for large M_s . In contrast ASk changes its shape to a square one for large M_s , see e.g. shape of ASk and Sk in the corresponding lattice for $M_s = 0.3$ (MA/m) in Fig. 2. The same behaviour was observed in [17]. Shape dependence on saturation magnetization is show in Fig. 3. It can be seen that central part of the ASk is almost precisely in ferromagnetic state, with spins however directed opposite to ferromagnetic phase outside of the Sk. The central “core” part of ASk expands as M_s grows, but domain-wall part of the ASk increases its width moderately. The behaviour is similar to change in anisotropy as expected, since effective anisotropy is commonly used to describe part of the effect of the demagnetizing fields.

4. Conclusion

We have described an approach to computation the demagnetization fields in the framework of the widely used discrete-lattice magnet model. This approach can provide a faster alternative to dipole-dipole interaction computation used e.g. in MuMAX [21] and in OOMMF [18, 22]. The approach has been applied to study square lattices ASk and Sk, and the results are in qualitative agreement with the analysis of isolated ASk (Sk) in [17].

Acknowledgements

This work was funded by Russian Science Foundation (Grant 19-42-06302).

References

- [1] Fert A., Reyren N., Cros V. Magnetic skyrmions: advances in physics and potential applications. *Nature Reviews Materials*, 2017, **2**, P. 17031.
- [2] Finocchio G., Büttner F., Tomasello R., Carpentieri M., Kläui, M. Magnetic skyrmions: from fundamental to applications. *Journal of Physics D: Applied Physics*, 2016, **49**(42), P. 423001.
- [3] Nagaosa N., Tokura Y. Topological properties and dynamics of magnetic skyrmions. *Nature nanotechnology*, 2013, **8**(12), P. 899–911.
- [4] Bogdanov A. N. and Yablonskii D. A., Thermodynamically stable vortices in magnetically ordered crystals. The mixed state of magnets. *Zh. Eksp. Teor. Fiz.*, 1989, **95**(1), P. 178–182.
- [5] Bessarab P.F., Uzdin V.M., Jónsson H. Harmonic transition-state theory of thermal spin transitions. *Physical Review B*, 2012, **85**(18), P. 184409.
- [6] Uzdin V.M., Potkina M.N., Lobanov I.S., Bessarab P.F., Jónsson H. Energy surface and lifetime of magnetic skyrmions. *Journal of Magnetism and Magnetic Materials*, 2018, **459**, P. 236–240.
- [7] Wiesendanger R. Nanoscale magnetic skyrmions in metallic films and multilayers: a new twist for spintronics. *Nature Reviews Materials*, 2016, **1**(7), P. 1–11.
- [8] Lobanov I.S., Jónsson H., Uzdin V.M. Mechanism and activation energy of magnetic skyrmion annihilation obtained from minimum energy path calculations. *Physical Review B*, 2016, **94**(17), P. 174418.
- [9] Nayak A. K., Kumar V., Ma T., Werner P., Pippel E., Sahoo R., Damay F., Rössler U. K., Felser C., Parkin S. S. P. Magnetic antiskyrmions above room temperature in tetragonal Heusler materials. *Nature*, 2017, **548**(7669), P. 561–566.
- [10] Rybakov F.N., Borisov A.B., Blügel S., Kiselev N.S. New type of stable particlelike states in chiral magnets. *Physical review letters*, 2015, **115**(11), P. 117201.
- [11] Vlasov S.M., Uzdin V.M., Leonov A. O. Skyrmion flop transition and congregation of mutually orthogonal skyrmions in cubic helimagnets. *Journal of Physics: Condensed Matter*, 2020, **32**(18), P. 185801.
- [12] Büttner F., Lemesh I., Beach G. S. Theory of isolated magnetic skyrmions: From fundamentals to room temperature applications. *Scientific reports*, 2020, **8**(1), P. 1–12.
- [13] Caretta L., Mann M., Büttner F., Ueda K., Pfau B., Günther C. M., Hensing P., Churikova A., Klose C., Schneider M., Engel D. Fast current-driven domain walls and small skyrmions in a compensated ferrimagnet. *Nature nanotechnology*, 2018, **13**(12), P. 1154–1160.
- [14] Legrand W., Maccariello D., Ajejas F., Collin S., Vecchiola A., Bouzehouane K., Reyren N., Cros V., Fert A. Room-temperature stabilization of antiferromagnetic skyrmions in synthetic antiferromagnets. *Nature materials*, 2020, **19**(1), P. 34–42.
- [15] Potkina M.N., Lobanov I.S., Jónsson H., Uzdin V.M. Skyrmions in antiferromagnets: Thermal stability and the effect of external field and impurities. *Journal of Applied Physics*, 2020, **127**(21), P. 213906.
- [16] Lobanov I.S., Potkina M.N., Jónsson H., Uzdin V.M. Truncated minimum energy path method for finding first order saddle points. *Nanosystems: physics, chemistry, mathematics*, 2017, **8**(5), P. 586–595.
- [17] Camosi L., Rougemaille N., Fruchart O., Vogel J., Rohart S. Micromagnetics of antiskyrmions in ultrathin films. *Physical Review B*, 2018, **97**(13), P. 134404.

- [18] Donahue M. J., Porter D. G. OOMMF User's Guide, Version 1.0. Interagency Report NISTIR 6376, National Institute of Standards and Technology, Gaithersburg, MD. 1999.
- [19] Ivanov A.V., Dagbartsson D., Tranchida J., Uzdin V. M., Jonsson H. Efficient optimization method for finding minimum energy paths of magnetic transitions *Journal of Physics: Condensed Matter*, 2020, **32**(34), P. 345901.
- [20] Lobanov I. S., Uzdin V. M. The lifetime of big size topological chiral magnetic states. Estimation of the pre-exponential factor in the Arrhenius law, 2020. arXiv preprint, arXiv:2008.06754.
- [21] Vansteenkiste A., Leliaert J., Dvornik M., Helsen M., Garcia-Sanchez F., and Van Waeyenberge B. The design and verification of MuMax3. *AIP Advances*, 2014, **97**, P. 107133.
- [22] Sachdev S. Handbook of magnetism and advanced magnetic materials, 2006.

Supercritical fluid synthesis and possible properties of “cubic graphite”A. V. Pokropivny^{1,2}, A. N. Enyashin³, A. S. Smolyar^{1,4}, V. A. Kuts⁵, V. G. Gurin⁵,
S. A. Antipov⁵, P. M. Silenko¹, Yu. M. Solonin¹¹Frantsevich Institute for Problems of Materials Science NASU, Kyiv, Ukraine²G. V. Kurdyumov Institute for Metal Physics, NASU, Kyiv, Ukraine³Institute of Solid State Chemistry UB RAS, Ekaterinburg, Russia⁴M.P. Semenenko Institute of Geochemistry, Mineralogy and Ore Formation NASU, Kyiv, Ukraine⁵Institute of Magnetism NASU, Kyiv, Ukraine

apokr@ukr.net, enyashin@ihim.uran.ru

PACS 81.10.Dn, 61.66.Bi, 61.48.+c, 61.50.Ah**DOI 10.17586/2220-8054-2020-11-4-408-416**

We report on supercritical fluid synthesis of an intermediate carbon phase – austite – at a pressure of 180 MPa and temperatures 500–700°C from soot as a precursor and supercritical carbon dioxide as a solvent. According to the results of electron and X-ray diffractions, spectral measurements and density-functional theory calculations, the observed carbon phase is proved to be cubic with a lattice parameter value of 8.96 ± 0.05 Å and a possible structural type as for KFI zeolite.

Keywords: crystal growth, carbon allotropes, electron microscopy, X-ray diffraction, DFT calculations.

Received: 15 June 2020

Revised: 10 July 2020

1. Introduction

Supercritical fluid synthesis is a common method for the high-pressure high-temperature synthesis of different oxides, sulfides, nitrides, carbon phases as well as self-assembling of nanomaterials [1, 2]. Different gases can be employed for creating pressure during supercritical fluid synthesis as an inert medium (He, Ar) or a solvent and a chemical reagent (H₂, N₂, H₂O, CO₂ etc.). The dissolving capacity of fluids is rapidly increased with increasing of the pressure, which is also important for supercritical fluid extraction. On the other hand, the velocity of crystallization in supercritical medium is increased up to 0.1–0.3 mm/h, which is at least five times greater than for hydrothermal methods. Moreover, crystals formed from the gas phases may have a high degree of perfection, in comparison with other methods.

In 1963 Aust and Drickamer claimed on synthesis of a new cubic carbon phase (henceforth, austite) by transformation from single crystal of graphite at 15 GPa and 180 K [3]. There was a sharp rise of resistance with pressure at this point, accompanied by drifting upward with time – a behavior typical of a sluggish first-order phase transition. The mixture of new phase with graphite was found to have the density of 2.35–2.4 g/cm³ with the float-sink tests. X-ray diffraction analysis of the partially transformed mixture showed that this phase could be cubic with the lattice parameter of 5.545 Å, having 24 atoms per unit cell and a crystal density of ~ 2.8 g/cm³ [3].

In 1967 Bandy reported, that Drickamer rejected on the facts of the synthesis of austite in a private communication [4]. Therefore, the discovery of a new phase in carbon phase diagram was not accepted by the scientific community. It should be noted that authors [3] had not published official refutation of their work. Presumably the indisputable authority of Bandy misled other scientists, who could confirm or refute completely their extraordinary results. As a result, in 1974 the pattern of this phase (No 18-311) was deleted from the database. Nevertheless, at the moment several forms of diamond, nanotubes, fullerenes, a large number of carbon fullerites, and other allotropic modifications have been discovered on carbon phase diagram, hence, an observation of new carbon phase is not a surprise since the last half of twentieth century [5].

However, the austite-like phases have been repeatedly observed after Aust and Drickamer. Namely, Fedoseev et. al. reproduced an austite-like phase during the growth of diamond from the gas phase [6], by Smolyar et. al. with a supercritical fluid treatment of graphite [7], and, possibly, by Shterenberg et. al. from channel black with a heat treatment at 1250°C in the presence of Ni at 3.7 MPa [8]. The hardness of austite was found to be intermediate, namely 1–5 GPa [7]. Shumilova et. al. discovered austite-like phase in the nature among the products of graphite mineralization [9]. The mineral lignite from Dakota Star Mines [10], the existence of which was questionable, could also be hypothesized as this phase. The structure was interpreted for the first time as a cubic lattice of C₂₄ fullerenes arranged as zeolite-like LTA lattice [11, 12].

In the last two decades, other new phases of carbon and boron nitride attract outstanding interest of the same or even higher level, as fullerenes and nanotubes do. All of these new materials can be used in the architectures of future devices or, alternatively, as advanced materials with prominent absorption properties or superhardness. Among these new phases as the C_8 phase [13], E-phase of boron nitride [14, 15] and fulborene $B_{12}N_{12}$ [16] are remarkable. Crystal structures of these phases were proposed quite recently, although they were synthesized in the last half of the twentieth century. The problem of structure determination and attribution of new forms of carbon and BN is ordinary due to their small mass yields after synthesis, unlike that, for example, nanotubes and fullerenes, and due to low atom weight of constituent elements. Theoretically, several hypothetical zeolite-like carbon structures (ATO, KAN, ATN, AFI etc.) are proposed for future identifications [17–26].

The goal of this work is to obtain a sample of austite phase (“cubic graphite”) using the supercritical fluid synthesis from soot and to revise the structural data on the received samples. The density-functional theory methods are employed to supply the results of experiments.

2. Experimental part

2.1. Synthesis and characterization

Equipment for supercritical fluid synthesis represents the reactor with an inner holder for the samples, aggregates for compressions and cleaning of gas, heating system, and automatic control system. The equipment allows one to create the gas pressures up to 1 GPa for a short time period (0.5–1 h) and to maintain the pressure during the long time period (hours, days) [1–7].

The soot was used as a precursor and supercritical carbon dioxide as a solvent. It was saturated in the reactor at pressure 95 MPa for 25 hours at ambient temperature. After that, the temperature was cyclically increased and reduced in the intervals of 500–700°C during 4 hours at pressure 180 MPa. The reaction product was observed as polycrystalline plates and as separate crystals in the soot.

Transformed soot powders were studied using different physical methods. X-ray powder diffraction (XRPD) patterns were received on DRON-2 diffractometer in the range of $2\theta = 5^\circ\text{--}90^\circ$ at $Cu_{K\alpha}$ radiation. Electron diffraction (ED) patterns were obtained at room temperature with a Philips EM-400T transmission electron microscope, operating at acceleration voltage of 100 kV. The samples were prepared by crushing in a mortar and dispersal of the synthesized crystallites in ethanol, and subsequent deposition on a grid containing holes. The elemental composition of the plates of new phase was studied with the JEOL spectrometer.

2.2. Computational details

The calculations were performed within the framework of the density-functional theory (DFT) using the SIESTA 4.0 implementation [27, 28]. The exchange–correlation potential within the Generalized Gradient Approximation (GGA) with the Perdew–Burke–Ernzerhof parametrization was used. The core electrons were treated within the frozen core approximation, applying norm-conserving Troullier–Martins pseudopotentials. The valence electrons for C were taken as $2s^22p^2$. The pseudopotential core radii were chosen, as suggested by Martins, and equal to 1.3 a_B for s - and p -states of C. In all calculations double- ζ basis set was used. The k-point mesh was generated by the method of Monkhorst and Pack with a cutoff 10 Å for the k-point sampling. The real-space grid used for the numeric integrations was set to correspond to the energy cutoff of 200 Ry. All calculations were performed using variable-cell and atomic position relaxations, with convergence criteria corresponding to the maximum residual stress of 0.1 GPa for each component of the stress tensor, and the maximum residual force component of 0.01 eV/Å.

Apart from the geometry optimization using DFT method, the stability, mechanical and thermal properties were tested using geometry optimization and molecular-dynamics (MD) simulations within the framework of the density-functional tight-binding method (DFTB) [29] in Γ -point approximation as implemented in the deMon software [30]. The structures were MD annealed during 20 ps with the time step of 1.0 fs as canonical (NVT) ensembles at temperatures $T = 300$ and 600 K using global Berendsen thermostat with the time constant 100 fs.

The optimized geometry of all carbon allotropes was used to simulate theoretical XRD spectra for wavelength $\lambda = 1.5406$ Å ($Cu_{K\alpha}$ radiation). All structures were considered as periodic 3D crystals. The smearing of reflection profiles was approximated with correction for the isotropic atomic temperature factor [31].

3. Results and Discussion

3.1. Electron diffraction analysis

ED patterns from both untransformed soot and synthesized crystal are collected in Fig. 1. It should be noted that synthesized particles were found to be hard, in comparison with starting material, in good agreement with previous research of this phase [7]. The test samples consisted of crystalline microparticles of 10 to 100 μm in size. The

observed crystals were solid, unlike carbon black, but crumble well in an agate mortar. Therefore, their hardness may be estimated as the one not exceeding 6.5–7.0 units on the Mohs scale. Microparticles of untransformed soot were amorphous or badly-crystalline with the characteristic parameter of 3.6 Å, hence, larger than that for graphite. The patterns of the synthesized sample can be attributed without any restriction to a cubic phase with the characteristic lattice parameter 8.96 ± 0.05 Å.

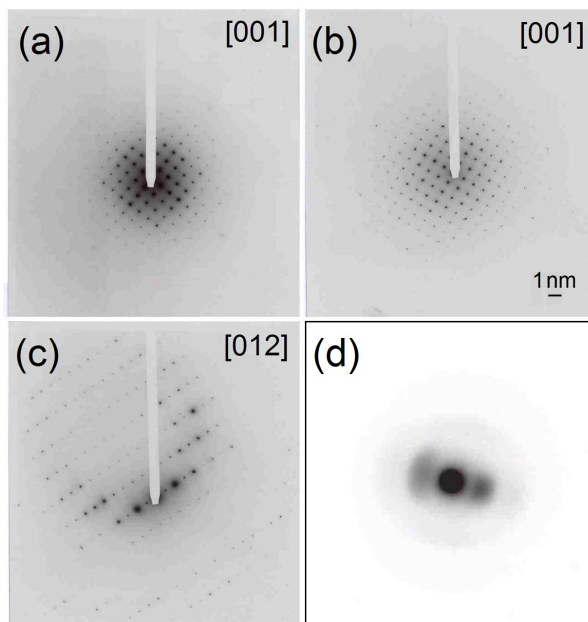


FIG. 1. Electron diffractograms in different projections (a-c) for the carbon samples prepared using supercritical fluid synthesis and in comparison to the diffractogram for the carbon precursor (d). Common scale bar is given in (b)

Qualitative analysis of the elemental composition using TEM spectrometer reveals only carbon, and, possibly, light elements in the samples under investigations. Using spectral quantitative analysis at the surface of the polycrystal plates, the composition was found to be 98–99 at% of carbon, with the 0.5–1 at% of oxygen and much less than 1 % of other elements. Thus, the phase is really a pure carbon, while oxygen is likely adsorbed on the surface, and the rest elements are impurities arising from the reactor and from the sample preparation for the spectrometer.

3.2. X-ray diffraction analysis

Results of XRPD analysis of the sample of powders are listed in column 1 of Table 1. For comparison, the theoretical XRD reflections of austite have been calculated with the JSV computer code for the structure proposed as carbon KFI zeolite [32] with the space group $Im-3m$ (column 2 of Table 1). The hkl indices, d_{hkl} -spacings (prior to brackets), relative intensities (in brackets) and recalculated lattice parameters (after brackets) are tabulated. Interpretation of reciprocal spaces clearly indicates the presence of a single cubic phase of 8.95 ± 0.15 Å, in excellent agreement with the results of electron diffraction. Simultaneously, the lattice parameter of the austite sample from [3] (column 3 of Table 1) can be found slightly greater, which may be related to the difference in sample preparation. Rietveld refinements are not possible because the powders of new phase are pyrogenetically bound to graphite or some other form of carbon. This is not the only problem associated with carbon or boron nitride phases.

Column 2 of Table 1 shows the results of model powder diffraction for zeolite-like KFI carbon with the lattice constant $a = 8.95$ Å. The calculated diffraction patterns from the proposed KFI structure correlate well with those from our sample and from report of Aust et al. [3]. There are (200), (222) and (330) main calculated reflexes for the proposed structure. Experimentally, two of them are presented for our sample in good agreement with the calculations. Though, main experimental reflexes (110), (200), (220), (332) have only weak analogs of theoretical reflexes as calculated for zeolite-like KFI carbon. The synthesized phase should have a texture along (220) and (110) planes, since their two reflexes rank first in intensity. The (222) strong reflex is not observed by Aust et al. [3], but it is observed from our samples. And vice versa (422) reflex is observed by Aust et al. [3], but it is not observed from our sample.

TABLE 1. Theoretically derived as for carbon KFI zeolite (column 2), and experimental XRPD patterns (column 3 and 4) with corresponding lattice parameters (in Å after brackets). Subscripts in column 1 denote the formerly ascribed indices for this phase [3]. X-ray diffraction pattern of the experimental samples contains additionally several peaks of different intensities, which correspond to other phases

<i>hkl</i>	Theoretical KFI structure for $a = 8.95 \text{ \AA}$	Experimental in our work	Experimental [3]
100		9.10 (5), $a = 9.10$	
110	6.329 (6)	6.27 (30), $a = 8.87$	
111		5.30 (5), $a = 9.17$	
200	4.475 (100)	4.42 (15), $a = 8.84$	
210 ₍₁₁₀₎		3.95 (10), $a = 8.83$	
211	3.654 (< 1)	3.61 (10), $a = 8.84$	
220 ₍₁₁₁₎	3.164 (3)	3.17 (100), $a = 8.96$	3.208 (10), $a = 9.07$
310 ₍₂₀₀₎	2.830 (10)	2.80 (10), $a = 8.85$	2.770 (50), $a = 8.76$
222	2.584 (41)	2.55 (10), $a = 8.83$	2.467 (50), $a = 8.90$
321	2.392 (< 1)	2.365 (10), $a = 8.85$	
400 ₍₂₁₁₎	2.238 (3)	2.214 (10), $a = 8.86$	
330, 411	2.110 (25)		
420	2.001 (5)	2.00 (20), $a = 8.94$	
332	1.908 (5)	1.932 (30), $a = 9.06$	1.961 (10), $a = 8.99$
421 ₍₂₂₀₎		1.932 (30), $a = 8.85$	
422 ₍₂₂₁₎	1.827 (4)		1.844 (10), $a = 9.03$
510, 431	1.755 (< 1)		
521	1.634 (1)		
440 ₍₂₂₂₎	1.582 (1)	1.589 (5), $a = 8.99$	1.600 (10), $a = 9.05$
433, 530	1.535 (3)		
442, 600 ₍₃₂₁₎	1.492 (< 1)		1.485 (10), $a = 8.91$
532	1.452 (6)		

It should be noted here that a set of structural transformations influence on the powder diffraction patterns. The essential differences in peaks distribution exist not only for different method of genesis, but also from probe to probe of the same method. In particular, sample of [3] is more textured with a poor set of diffraction lines in comparison with our sample. Nevertheless, first three XRD peaks can be fairly attributed to the peaks of our sample.

3.3. DFT computational data

The preliminary experimental results for observed cubic carbon phase with the lattice parameter $\sim 8.95 \text{ \AA}$ suggest the model corresponding to zeolite-like KFI lattice, which impose the unit cell consisting of 96 C atoms – C_{96} (*vide infra*). Here, we employ several DFT approaches to infix the possible crystal structure of synthesized carbon phase as austite, confirming its dynamical and mechanical stabilities. Apart from the zeolite-like KFI C_{96} , the diamond with face-centered cubic lattice was chosen as a reference system to study structural, electronic and elastic properties. In addition, similar calculations were also performed for other porous carbon – C_{24} fullerite with simple cubic lattice (or LTA carbon zeolite), where C_{24} fullerenes are connected by square-like edges [11,12]. While the properties of diamond are profoundly established from both experimental and theoretical views, the C_{24} fullerite was selected due to its structural relativity to C_{96} (Fig. 2). The convenient KFI structure of C_{96} can be represented as a primitive body-centered cubic lattice of C_{48} building blocks. The latter have the shape of truncated cuboctahedra and are assembled by means of hexagonal edges creating a characteristic motif of hexagonal prisms. Yet, simple cubic lattice of C_{24} fullerite may be also represented as composed of the same C_{48} building blocks linked via square-like edges, which form a primitive face-centered cubic lattice.

The calculated structural, electronic and mechanical properties of diamond have validated the calculational approaches used in this work and demonstrated their fair adequacy for the reproduction of basic properties of carbon

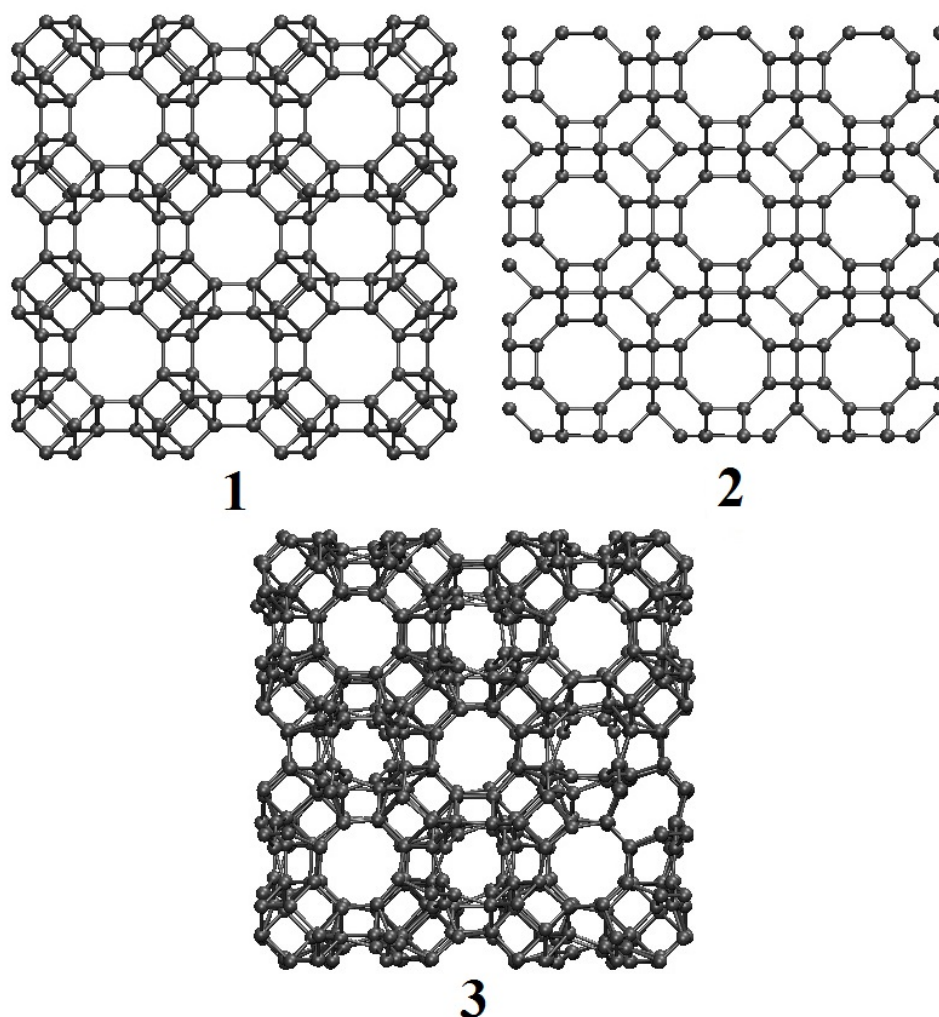


FIG. 2. Structures of subtle carbon allotropes studied in this work: the fragments of austite C_{96} with zeolite-like KFI lattice ($bcc-C_{48}$) (1) and C_{24} with zeolite-like LTA lattice ($fcc-C_{48}$) (2) after GGA-DFT geometry optimization; the fragments of austite C_{96} after DFTB molecular-dynamics simulations at 600 K (3)

allotropes (Table 2). The error in the estimation of lattice parameter does not exceed 0.3 %. In agreement with the experimental data, the cubic diamond is characterized as a wide band gap semiconductor with non-direct type of transition from Γ -point to $(2/3)\Gamma$ -X point (Fig. 3). As in many DFT approaches, the value of the band gap obtained after DFT-GGA calculations is underestimated by ~ 1 eV. In turn, DFTB approach typically overestimates the band gap, while the features of the band structure are as well fairly reproduced. The values of the bulk modulus estimated either from total energy curve or calculated from independent elastic constants may be found in the fair agreement with the experimental value (Tables 2 and 3). In general, apart of the band gap estimations, both employed calculational methods yield equivalent results.

The calculations of C_{96} allotrope were performed using primitive body-centered cubic unit cell, which contains 48 atoms. The lattice of subtle C_{96} allotrope preserves bcc-structure after the geometry optimization (Fig. 2). Contrary to the diamond, the band structure calculation at DFT-GGA level reveals that C_{96} is a semiconductor with the smaller and direct band gap of about 2.6 eV (Table 2). However, the partial densities of states at the valence band of both carbon allotropes have dominant $2pC$ character.

A highly strained coordination of sp^3 -hybridized carbon atoms in C_{96} cannot be energy gainful and the total energy calculations evidence the lower stability of C_{96} carbon comparing to the diamond almost on ~ 1 eV per C-atom. The first hint at the dynamical stability of this lattice was given using molecular dynamics simulations of the supercell consisting of 16 C_{48} building blocks. A reasonably high stability of C_{96} allotrope can be revealed in the absence of external pressure and at temperature of 300 K, when no change in the structure can be obtained and the

TABLE 2. Main characteristics of C_{96} carbon allotrope (KFI-like lattice), C_{24} fullerite (LTA-like lattice) and diamond in conventional cubic lattice representation: number of atoms in the unit cell Z , relative formation energy (ΔE , in eV/atom), lattice parameter (a , in Å), mass density (ρ , in g/cm³), bulk modulus (B , GPa) and band gap (E_g , in eV), as calculated at different DFT levels

System	Method	Z	ΔE	a	ρ	B	E_g
fcc-diamond	DFT GGA	8	0.0000	3.58	3.47	493	4.20
	DFTB		0.0000	3.58	3.47	487	7.73
	exp. [25]			3.57	3.52	442	5.46-5.6
sc- C_{96} or bcc- C_{48}	DFT GGA	96	0.8382	9.29	2.39	285	2.61
	DFTB		1.0659	9.35	2.34	276	7.15
sc- C_{24} or fcc- C_{48}	DFT GGA	24	0.7501	5.93	2.30	290	2.42
	DFTB		0.8892	5.95	2.27	280	7.15

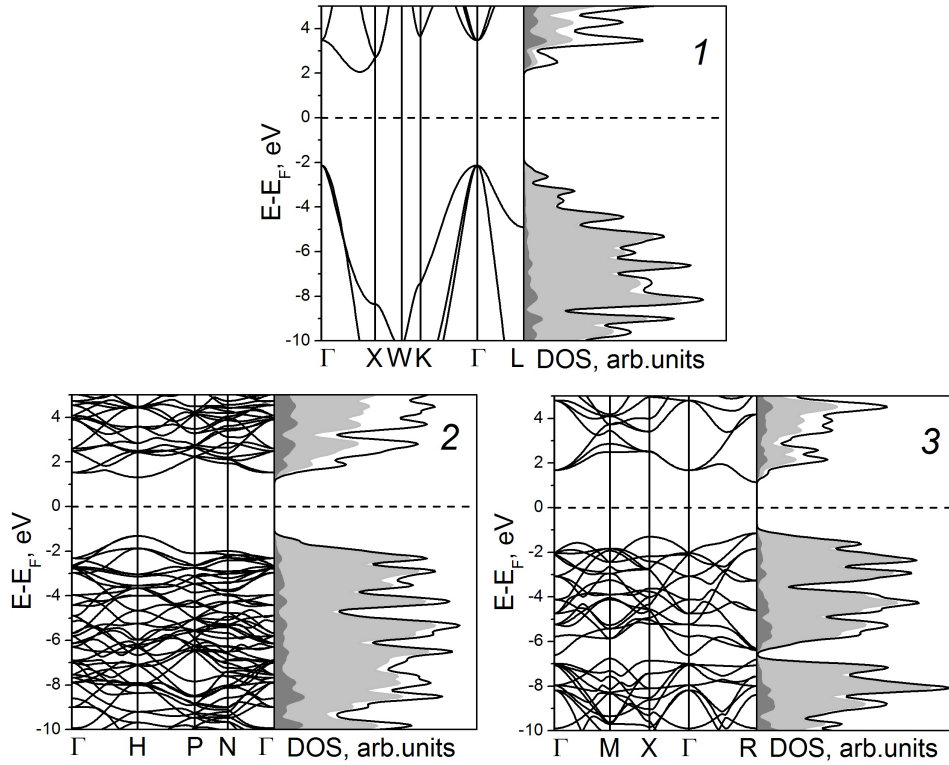


FIG. 3. Band structure and densities of states (DOS) for cubic diamond (1), for austite C_{96} with zeolite-like KFI lattice (or bcc- C_{48}) (2) and for C_{24} fullerite with zeolite-like LTA lattice (or fcc- C_{48}) (3) calculated within DFT-GGA approach. 2pC and 2sC partial densities of states are painted in light gray and gray, respectively

atom motions are not accompanied with the break of chemical bonds. However, the structure of C_{96} undergoes a considerable destruction with the partial destruction of hexagonal prisms and occurrence of double C=C bonds at $T = 600$ K (Fig. 2).

Thereafter, the stability of the lattice was estimated in more details by means of the widely used condition of intrinsic stability, i.e. when the Gibbs free energy of the crystal is in a local minimum with respect to small structural deformations. In terms of elastic constants (C_{ij}), this stability criterion (so-called mechanical stability) for cubic crystals requires that $(C_{11} - C_{12}) > 0$, $(C_{11} + 2C_{12}) > 0$, and $C_{44} > 0$. In the framework of less sophisticated DFTB method the values of three independent elastic constants (C_{11} , C_{12} and C_{44}) were evaluated and compared with those of diamond (Table 3). These constants satisfy the aforementioned conditions. Thus, we may assert that the proposed C_{96} allotrope should be intrinsically stable.

Calculated elastic constants allow to estimate several other important mechanical properties, which are listed along with available experimental values in Table 3: bulk modulus $B = (C_{11} + 2C_{12})/3$, compressibility $\beta = 1/B$, shear modulus $G = (3C_{44} + C_{11} - C_{12})/5$, Pugh's indicator $k = G/B$, tetragonal shear moduli $G' = 1/2(C_{11} - C_{12})$, Young's modulus $Y = 9BG/(3B + G)$, Cauchy pressure $CP = C_{12} - C_{44}$, Poisson's ratio $\nu = 1/2(1 - Y/3B)$, Zener anisotropy index, $A_Z = 2C_{44}/(C_{11} - C_{12})$.

The Young's modulus Y of a material is defined as a ratio of linear stress to linear strain, which determines its stiffness. In our study, the Young's modulus of C_{96} lattice is found to be $Y = 475$ GPa, thus, the material will show a rather high stiffness.

Brittle/ductile behavior is one of many important mechanical characteristics of a material, which is closely related to its reversible compressive deformation and fracture ability. Often, the ductile/brittle nature of a material is related to its Cauchy pressure CP : if CP is negative, the material is expected to be brittle. Another most widely used materials' malleability measure is the Pugh's index k [34]. Namely, at $k < 0.57$, a material behaves in a ductile manner, and vice versa, at $k > 0.57$, it demonstrates brittleness. According to both indicators (Table 3), C_{96} carbon allotrope should behave as a brittle material.

Elastic anisotropy of crystals reflects a different bonding character in different directions and has an important implication since it correlates with the possibility to induce microcracks in materials. The elastic anisotropy can be estimated using the Zener's anisotropy index A_Z [35]. For isotropic crystals, $A_Z = 1$, and the deviations of A_Z from unity define the extent of elastic anisotropy. From this point of view, C_{96} allotrope with $A_Z = 0.65$ should be elastically quite isotropic.

The calculated elastic parameters allow estimate Vickers hardness of the material (H_V) in a few simplified ways. Generally, the hardness of a material is characterized experimentally by indentation and depends strongly on plastic (irreversible) deformation. However, a set of empirical relationships between Vickers hardness and elastic properties was proposed. Herein, the following semi-empirical correlations between Vickers hardness and shear, Young's modulus, and Pugh's index were applied [36, 37]: $H_V(1) = 0.1769G - 2.899$; $H_V(2) = 0.0608Y$; $H_V(3) = 2(k^2G)^{0.585} - 3$. Present numerical estimations of H_V (Table 3) demonstrate that all three correlations give comparable values and suggest that the C_{96} allotrope should be a hard material.

As was previously mentioned, C_{96} or bcc- C_{48} lattice is related to the lattice of C_{24} fullerite or fcc- C_{48} . Thus, the simultaneous fabrication of both these carbon allotropes might be expected. In addition, the stability, electronic and mechanical properties were estimated also for C_{24} fullerite at the same levels of theory (Tables 2 and 3, Fig. 3). Noteworthy, the latter phase characterized earlier by Pokropivny et al [11, 12] is slightly more stable, than C_{96} , and posses very similar trends in the mechanical stability of lattice and in the electronic properties. Obviously, the co-production or the production of individual C_{24} fullerite under the same experimental conditions of supercritical fluid synthesis cannot be fully excluded.

TABLE 3. Mechanical properties of sp^3 carbon allotropes as obtained after DFTB calculations: independent elastic constants (C_{ij} , in GPa), bulk modulus (B , in GPa), compressibility (β , in GPa^{-1}), shear modulus (G , in GPa), Pugh's indicator (k), tetragonal shear moduli (G' , in GPa), Young's modulus (Y , in GPa), Cauchy's pressure (CP , in GPa), Poisson's ratio (ν), Zener's anisotropy index (A_Z), and Vickers hardness (H_V , in GPa)

System	C_{11}	C_{12}	C_{44}	B	β
fcc-diamond	1103.5 (1079*)	178.8 (124*)	602.2 (578*)	487 (442*)	0.0021
sc- C_{96} (bcc- C_{48})	607.0	109.7	161.7	275	0.0036
sc- C_{24} (fcc- C_{48})	550.7	145.4	259.7	281	0.0036
System	G	k	G'	Y	CP
fcc-diamond	546	1.12	462 (478*)	1192 (1050*)	-423.4
sc- C_{96} (bcc- C_{48})	196	0.71	249	475	-52.0
sc- C_{24} (fcc- C_{48})	237	0.84	203	555	-114.3
System	ν	A_Z	$H_V(1)$	$H_V(2)$	$H_V(3)$
fcc-diamond	0.09 (0.1*)	1.30	93.7	72.5	88.2
sc- C_{96} (bcc- C_{48})	0.21	0.65	31.8	28.9	30.8
sc- C_{24} (fcc- C_{48})	0.17	1.28	39.0	33.7	37.0

* experimental values from Ref. [33]

4. Summary

In 1963 Aust and Drickamer [3] found a new phase during transformation of graphite at high pressures. In 2004 a few members of our group offered the structure of this phase on the basis of available data. At that time, the phase was indexed in the cubic system with a period of ~ 5.55 Å with the structure of LTA zeolite [11, 12]. With the support from electron diffraction technique the lattice parameter has been refined and its revised value is found to be approximately ~ 9 Å instead of ~ 5.55 Å, according to previous experimental data [3] and theoretical [11, 12] reports. The synthesized austite is suggested as carbon phase C_{96} with zeolite-like KFI lattice (space group $Im - 3m$) in accordance with analysis of electron and X-ray diffraction patterns. As independent method, DFT calculations confirm the mass density, dynamical and mechanical stability of the proposed structure.

In the present experimental work the high level of nucleation of new crystalline carbon phase from disordered material is for the first time observed without additional catalysts, with only supercritical carbon dioxide as a solvent. The presence of graphite and, possibly, chaoite and C_8 sodalite phases [13] as concomitant products of synthesis indirectly confirms an assumption that new carbon phases are relatively stable and not rare. Indeed, more than 15 allotropes of carbon have been discovered in nature [38]. Apart from the C_{96} carbon allotrope with KFI-like structure a wealth of other carbon allotropes might be potentially fabricated under extreme conditions of fluid synthesis. Being fabricated under the conditions far from equilibrium, not all these phases can be hosted at the classical phase diagram of carbon, what can entangle their confident identification and characterization.

While the basic structural, electronic and mechanical properties have been established theoretically, the experimental characterization of newly fabricated carbon C_{96} phase still remains in its infancy. A set of new synthesis experiments, in particular, under different pressure-temperature and kinetic parameters are planned to increase the yield of cubic carbon and to reveal in details the formation mechanism. The latter would facilitate the understanding of phase transformations between numerous known and hypothetical carbon allotropes from experimental point-of-view, and further stimulate the search of new applications of these phases, e.g., in electronics.

Acknowledgments

We acknowledge M. Czank and W. Depmeier for their assistance with Electron diffraction method according to DFG visiting grant. A.E. acknowledges a support from ISSC UB RAS (theme AAAAA19-119031890025-9). Visualizations of atomic structures and MD trajectories were performed using VMD software (www.ks.uiuc.edu/Research/vmd/) [39].

References

- [1] Holmes J.D., Lyons D.M., Ziegler K.J. Supercritical fluid synthesis of metal and semiconductor nanomaterials. *Chemistry Eur. J.*, 2003, **23**, P. 2144–2150.
- [2] Smolyar A.S., Barcholenko V.A., Kuts V.A., Gurin V.G., Archipov A.P., Maloshtan S.A., Razvadovsky N.A., Svyato V.P., Klimovich A.P. UA patent No 98084606. Bulletin No 6, 2002.
- [3] Aust R.B., Drickamer H.C. Carbon: a new crystalline phase. *Science*, 1963, **140**, P. 817; Deleted pattern No 18-311.
- [4] Bandy F.P., Kasper J.S. Hexagonal diamond – a new form of carbon. *J. Chem. Phys.*, 1967, **46**, P. 3437–3446.
- [5] Pokropivny V.V., Ivanovsky A.L. New nanoforms of carbon and boron nitride. *Russ. Chem. Rev.*, 2008, **77**, P. 837–874.
- [6] Fedoseev D.V., Deryagin B.V., Varnin V.P., Vnukov S.P., Teremetskaya I.G., Polyanskaya N.D. Polymorphism in carbon-boron nitride systems. *Dokl. Akad. Nauk SSSR*, 1976, **228**, P. 371–374.
- [7] Smolyar A.S., Sozin Yu.I., Barholenko V.A., Maloshtan S.N., Kuts V.A., Gurin V.G., Arhipov A.P., Gerasimov A.Yu., Razvadovskii N.A., Titenko A.N. Fluid synthesis of carbon phases. *J. Superhard Mater.*, 2002, **2**, P. 79.
- [8] Shterenberg I., Bogdanova S. Influence of nickel on graphitization of carbon materials at high-pressures and temperatures. *Inorg. Mater.*, 1979, **15**, P. 632–636.
- [9] Shumilova T.G., Kablis G.N., Pushkarev E.V. Typomorphic features of graphite mineralization of probable alternative high-pressure sources of diamond: cubic graphite. *Dokl. Earth Sciences*, 2002, **387**, P. 958–961.
- [10] Wild R., Schellenbaum R. X-ray diffraction studies of mineral matter in North Dakota Lignite. *Proc. North Dakota Acad. Sci.*, 1951, **5**, P. 40–42.
- [11] Pokropivny V.V., Pokropivny A.V. Structure of “cubic graphite”: simple cubic fullerite C_{24} . *Phys. Solid State*, 2004, **46**, P. 392–394.
- [12] Pokropivny A.V. X-ray diffraction analysis of austite (cubic graphite), a novel carbon $[C_{24}]$ -LTA zeolite. *Physics Low-Dim. Struct.*, 2006, **2**, P. 64–68.
- [13] Pokropivny A.V., Volz S. C_8 phase: supercubane, tetrahedral, BC-8 or carbon sodalite? *Phys. Status Sol. B*, 2012, **249**, P. 1704–1708.
- [14] Pokropivny A.V. Structure of the boron nitride E-phase: diamond lattice of $B_{12}N_{12}$ fullerenes. *Diam. Relat. Mat.*, 2006, **15**, P. 1492–1495.
- [15] Pokropivny A.V., Volz S. Hybrid porous nanotube crystal networks for nanostructured device applications. *J. Mater. Sci.*, 2013, **48**, P. 2953–2960.
- [16] Pokropivny V.V., Smolyar A.S., Pokropivny A.V. Fluid synthesis and structure of a new boron nitride polymorph-hyperdiamond fulborenite $B_{12}N_{12}$ (E phase). *Phys. Solid State*, 2007, **49**, P. 591–598.
- [17] Baburin I.A., Proserpio D.M., Saleev V.A., Shipilova A.V. From zeolite nets to sp^3 carbon allotropes: a topology-based multiscale theoretical study. *Phys. Chem. Chem. Phys.*, 2015, **17**, P. 1332–1338.

- [18] Hu M., Zhao Z., Tian F., Oganov A.R., Wang Q., Xiong M., Fan C., Wen B., He J., Yu D., Wang H.-T., Xu B., Tian Y. Compressed carbon nanotubes: a family of new multifunctional carbon allotropes. *Sci. Rep.*, 2013, **3**, 1331.
- [19] Belenkov E.A., Brzhezinskaya M.M., Greshnyakov V.A. Novel carbon diamond-like phases LA5, LA7 and LA8. *Diam. Relat. Mat.*, 2014, **50**, P. 9–14.
- [20] Belenkov E.A., Greshnyakov V.A. Diamond-like phases formed from fullerene-like clusters. *Phys. Solid State*, 2015, **57**, P. 2331–2341.
- [21] Belenkov E.A., Brzhezinskaya M.M., Greshnyakov V.A. Crystalline structure and properties of diamond-like materials. *Nanosystems: Physics Chemistry Mathematics*, 2017, **8**, P. 127–136.
- [22] Belenkov E.A., Greshnyakov V.A. Modeling of phase transitions of graphites to diamond-like phases. *Phys. Solid State*, 2018, **60**, P. 1294–1302.
- [23] Greshnyakov V.A., Belenkov E.A. Structures of diamond-like phases. *J. Exp. Theor. Physics*, 2011, **113**, P. 86–95.
- [24] Kvashnina Y.A., Kvashnin D.G., Kvashin A.G., Sorokin P.B. New allotropic forms of carbon based on D-60 and D-20 fullerenes with specific mechanical characteristics. *JETP Lett.*, 2017, **105**, P. 419–425.
- [25] Kvashnina Y.A., Kvashnin A.G., Popov M.Y., Kulnitskiy A.A., Perezhogin I.A., Tyukalova E.V., Chernozatonskii L.A., Sorokin P.B., Blank V.D. Toward ultra-incompressible carbon materials: computational simulation and experimental observation. *J. Phys. Chem. Letters*, 2015, **6**, P. 2147–2152.
- [26] Kvashnina Y.A., Kvashnin A.G., Sorokin P.B. Investigation of new superhard carbon allotropes with promising electronic properties. *J. Appl. Phys.*, 2013, **114**, P. 183708.
- [27] Ordejon P., Artacho E., Soler J.M., Self-consistent order-N density-functional calculations for very large systems. *Phys. Rev. B*, 1996, **53**, P. R10441.
- [28] Soler J.M., Artacho E., Gale J.D., Garcia A., Junquera J., Ordejon P., Sanchez-Portal D. The SIESTA method for ab initio order-N materials simulation. *J. Phys. Condens. Matter*, 2002, **14**, P. 2745–2780.
- [29] Porezag D., Frauenheim T., Köhler T., Seifert G., Kaschner R., Construction of tight-binding-like potentials on the basis of density-functional theory: application to carbon. *Phys. Rev. B*, 1995, **51**, P. 12947.
- [30] Köster A.M., Flores R., Geudtner G., Goursot A., Heine T., Patchkovskii S., Reveles J.U., Vela A., Salahub D., *deMon*, Version 1.2; NRC: Ottawa, 2004.
- [31] Caglioti G., Paoletti A., Ricci F.P. Choice of collimators for a crystal spectrometer for neutron diffraction. *Nucl. Instr. Meth.*, 1958, **3**, P. 223–228.
- [32] Baerlocher Ch., McCusker L.B., Olson D.H. Atlas of zeolite framework types. Elsevier, Amsterdam, 2007, 404 p.
- [33] <http://www.ioffe.ru/SVA/NSM/Semicond/Diamond/>
- [34] Pugh S.F. Relations between the elastic moduli and plastic properties of polycrystalline pure metals. *Phil. Mag.*, 1954, **45**, P. 822–843.
- [35] Zener C.M., Siegel S. Elasticity and anelasticity of metals. *J. Phys. Chem.*, 1949, **53**, P. 1468.
- [36] Teter D.M. Computational alchemy: the search for new superhard materials. *MRS Bull.*, 1998, **23**, P. 22–27.
- [37] Chen X.Q., Niu H., Li D., Li Y. Modeling hardness of polycrystalline materials and bulk metallic glasses. *Intermetallics*, 2011, **19**, P. 1275–1281.
- [38] Shumilova T.G. Mineralogy of natural carbon (in Russian). Ural Branch of Russian Academy of sciences, Ekaterinburg, 2003, 316 p.
- [39] Humphrey W., Dalke A., Schulten K., VMD: visual molecular dynamics. *J. Mol. Graphics*, 1996, **14**, P. 33–38.

Synthesis of NaYF₄:Yb, Er up-conversion luminophore from nitrate flux

P. P. Fedorov^{1*}, M. N. Mayakova¹, A. A. Alexandrov¹, V. V. Voronov¹,
D. V. Pominova¹, E. V. Chernova¹, V. K. Ivanov²

¹Prokhorov General Physics Institute of the Russian Academy of Sciences, 119991, Moscow, Russia

²Kurnakov Institute of General and Inorganic Chemistry of the Russian Academy of Sciences,
119991, Moscow, Russia

*ppfedorov@yandex.ru

PACS 81.07.Bc, 76.30.Kg

DOI 10.17586/2220-8054-2020-11-4-417-423

The behavior of nanoparticle ensembles was studied using of NaRF₄ hexagonal phases. The evolution of particles in the process of rapid and productive synthesis from flux as a result of a chemical reaction was investigated. A low-temperature synthesis process in the medium of sodium nitrate was used. Synthesis of the samples of up-conversion phosphor NaY_{0.78}Yb_{0.2}Er_{0.02}F₄ was performed from rare-earth nitrates at 350 – 430 °C for 15 – 500 min. NaF was used as the fluorinating agent. Powder X-ray phase analysis and scanning electron microscopy revealed a rapid transformation of the cubic alpha modification into a hexagonal phase, followed by the transformation of nanoparticles into hexagonal prisms of micron sizes. The up-conversion luminescence energy yield increased as the reaction time increased.

Keywords: sodium yttrium fluoride, fluorite crystal structure, gagarinite crystal structure, flux, sodium nitrate.

Received: 15 April 2020

Revised: 30 April 2020

1. Introduction

The hexagonal phases formed in NaF–RF₃ (R – rare earth elements, REE) systems are effective matrices for anti-Stokes luminescence. They are phases of variable composition of the general formula Na_{3x}R_{2–x}F₆, and their composition is close to the ratio 50:50, according to which they are usually attributed the formula β-NaRF₄. These phases are low-temperature ones, as compare with cubic fluorite-type α-NaRF₄ phases. β-NaRF₄ phases, when co-doped with Yb–Er, Yb–Tm, or Yb–Ho ions, are well known as effective up-conversion phosphors that convert IR radiation to the visible spectral range [1, 2]. The number of publications devoted to these materials is huge, see for example [3–13]. The main areas of their potential application are biomedical applications and lighting sources [11–13]. The NaY_{0.78}Yb_{0.2}Er_{0.02}F₄ is the optimized composition. Functional characteristics of these materials depend strongly on the granulometry of the resulting nano- and micro-powders, and the mechanisms of phase formation, growth and agglomeration of particles are of crucial importance.

β-NaRF₄ powders can be prepared by a broad variety of methods [11, 13–16]. Until now, several techniques have been employed for the synthesis of hexagonal NaRF₄’ phases, both individual and co-doped ones, including solid-state synthesis [14, 15, 17], co-precipitation from water [18–22] and organic solvents [23], hydrothermal [12, 24, 25], solvothermal [26–30], mechanochemical [31], ionic liquid-assisted [32, 33] and molten salt/flux methods [18, 33–43], etc.

Among the various methods of synthesis, much attention is drawn to the first melt-solution method proposed by Batsanova [18, 38, 44], which consists in the reaction of REE nitrates with sodium fluoride, which acts as a fluorinating agent. As a flux, low-melting sodium nitrate is used. The method is characterized by simple hardware design, high performance, environmental friendliness and low cost. We have shown [45] that in this way it is easy to obtain powders of equilibrium hexagonal phases formed in systems of sodium fluoride with REE fluorides RF₃ (R = Pr–Lu, Y).

The purpose of this work is to use this synthesis technique to prepare an up-conversion phosphor NaYF₄:Yb,Er and test its effectiveness.

2. Experimental details

2.1. Sample preparation

The samples were synthesized by spontaneous crystallization from a solution in a melt. The synthesis was based on the following equation:



The starting chemicals were sodium fluoride (NaF, Lanhit®), purity mark “P.A.”), yttrium nitrate hexahydrate ($Y(NO_3)_3 \cdot 6H_2O$, Lanhit®, purity 99.99 %), ytterbium nitrate hexahydrate ($Yb(NO_3)_3 \cdot 6H_2O$, Lanhit®, purity 99.99 %), erbium nitrate pentahydrate ($Er(NO_3)_3 \cdot 5H_2O$, Lanhit®purity 99.99 %) and sodium nitrate ($NaNO_3$, Chimmed Group, purity mark “CP”) as a solvent. The raw materials were carefully mixed, transferred to a porcelain-glazed crucible, and placed in a furnace for synthesis. The ratio of components was: a seven-fold excess of the fluorinating agent from the stoichiometric composition (eq. 1), the mass fraction of the solvent ($NaNO_3$) was 35 %. The temperature range was from 320 to 350 °C (see Table 1). The heating speed was 10 °C/min for all samples. The sample holding time at the maximum temperature (τ , min) was from 15 to 500 minutes. The resulting residue was extracted from the crucible and washed several times with doubly distilled water.

TABLE 1. Synthesis conditions and hexagonal unit cell parameters of $NaY_{0.78}Yb_{0.2}Er_{0.02}F_{4.0}$ powders

No.	T , °C	τ , min	Unit cell parameters, Å	
			a	c
1	320	15	5.975(1)	3.5111(7)
2	330	30	5.9757(4)	3.5137(3)
3	340	45	5.9726(2)	3.5165(2)
4	350	60	5.9713(2)	3.5154(1)
5	350	180	5.9705(2)	3.5181(1)
6	350	500	5.9731(1)	3.5167(2)

2.2. Sample characterization

X-ray diffraction analysis (XRD) was performed on a Bruker D8 Advance diffractometer with Cu ($K\alpha$) radiation. The obtained data were processed by the TOPAS software package. When calculating the lattice parameters, the space group P63/m was set.

The Carl Zeiss NVision 40 electron microscope (Zeiss, Germany) was used for scanning electron microscopy (SEM) and energy dispersive X-ray spectroscopy (EDX) in high vacuum mode, at an accelerating voltage of 20 kV. Images were generated using a backscattered electron detector (BSE) and a secondary electron detector (SE).

The spectroscopic analysis included registering the spectra of up-conversion luminescence and diffusely scattered laser radiation within the range of 300 – 1000 nm, and calculating the energy yield of up-conversion luminescence. Luminescence studies were performed using a laser-induced luminescent spectroscopy unit that includes a fiber-optic spectroanalyzer LESA-01-BIOSPEC [46]. The values of the energy yield of up-conversion luminescence in the visible range of the spectrum were measured using a setup in which the test sample was placed in a modified integrating sphere produced by Avantes. Excitation of up-conversion luminescence was performed by a laser with a wavelength of 974 nm (“Biospek”, Moscow, Russia) and a power of 1 W. Spectral data were analyzed using the UnoMomento spectrum processing program, taking into account the hardware function of the spectrometer and the integrating sphere.

3. Results and discussion

The results of XRD analysis are presented in Fig. 1. For a short synthesis time, a mixture of cubic and hexagonal phases is obtained. A half-hour exposure of the reaction mixture in the melt leads to the formation of a pure hexagonal phase. Further increase in the heat treatment duration does not lead to a change in the phase composition of the samples. The values of lattice parameters of hexagonal phase are presented in Table 1.

Electron microscopy data are shown on Figs. 2 and 3. The initially formed ensemble of nanoparticles (Fig. 2(a,b)) generates the formation of elongated particles of micron sizes. The grain size distribution of the samples is not uniform. Elongated particles have an approximately hexagonal faceting corresponding to their crystallographic symmetry. Trigonal prisms are distinguishable. However, microcrystals that are approximately characterized by these simple habit forms have a huge number of rough defects and are splices of smaller crystals. These results are similar to what we previously observed in the synthesis of $NaRF_4$ phases [45].

EDX data show that the actual composition of synthesized samples corresponds to the nominal one. Admixtures of other elements were not recorded.

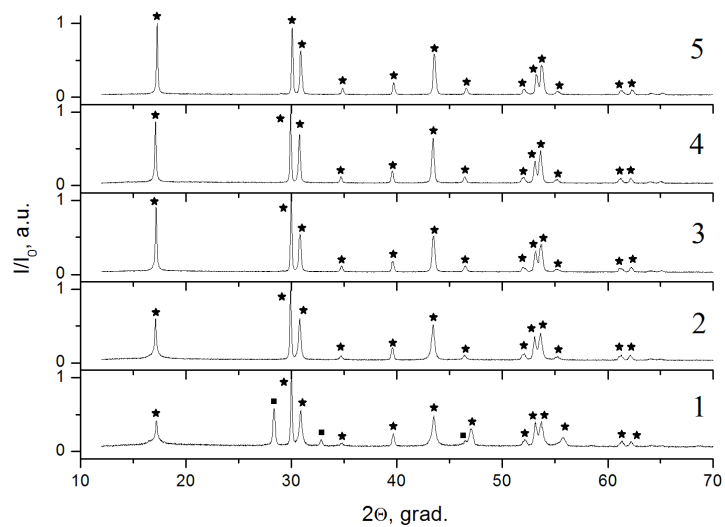


FIG. 1. X-ray powder diffraction patterns of the samples. Stars denote the peaks of the hexagonal NaRF_4 phase, and squares denote the cubic one. Sample numbers are the same as in the Table 1

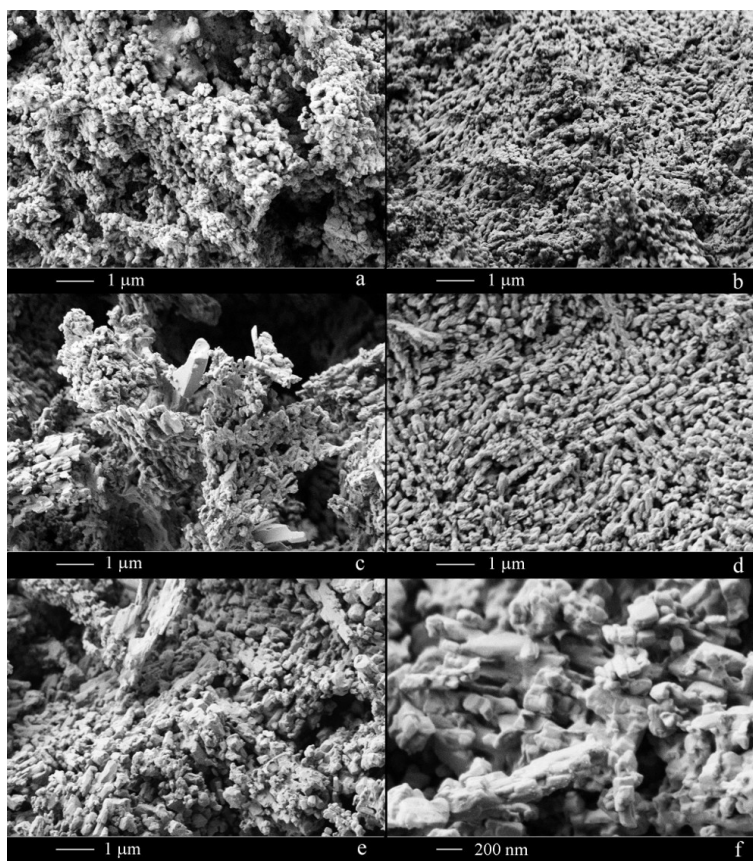


FIG. 2. SEM images of samples 1–3. (a) and (b) – the sample 1; (c) and (d) – the sample 2; (e) and (f) – the sample 3

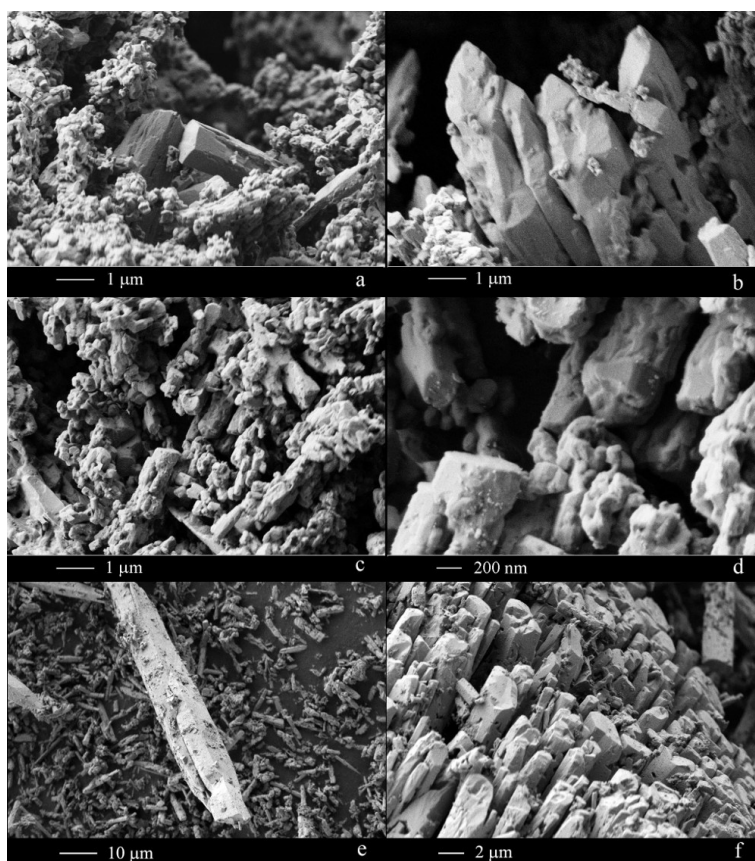


FIG. 3. SEM images of samples 4–6. (a) and (b) – the sample 4; (c) and (d) – the sample 5; (e) and (f) – the sample 6

It should be noted that the cubic α -phase is a high-temperature phase in NaF-RF_3 systems, and it is non-equilibrium one under our synthesis conditions. Cubic-hexagonal transitions ($\alpha \rightarrow \beta$ transitions) in NaRF_4 phases have been reported in the numerous publications describing NaRF_4 phase syntheses by a variety of techniques [4–11]. Temperature increase and/or extension of the synthesis duration promote the aforementioned $\alpha \rightarrow \beta$ phase transition. This transformation, which is also observed in our experiment when the thermal treatment time is increased to 30 min (see Fig. 1), is an actual realization of the Ostwald's step rule [47, 48].

Bard et al. [12] attempted to interpret this transformation as a manifestation of non-classical crystal growth by the oriented attachment of nanoparticles. This assumption should be considered untenable [49]. In view of the different structures of α and β polymorphs, one should realize that beta-phase cannot be built from the pieces of the alpha-phase. A change in the coordination number (CN) of the rare earth ions (CN 8 for cubic α phase and CN 9 for hexagonal β phase) unequivocally requires complete recrystallization of the formed cubic nanoparticles.

On the other hand, the enlargement of beta phase particles during thermal annealing fits well into the scheme of non-classical crystal growth by agglomeration of particles [50, 51]. The poor faceting of the formed crystallites is a confirmation of this [52].

The results of the luminescent studies are presented on the Fig. 4 and in the Table 2.

The luminescence spectra of the samples are typical for this luminophore and show green (510 – 575 nm) and red (625 – 670 nm) bands, corresponding to the radiative transitions of the erbium ions: ${}^2\text{H}_{11/2}, {}^4\text{S}_{3/2} \rightarrow {}^4\text{I}_{15/2}$ and ${}^4\text{F}_{9/2} \rightarrow {}^4\text{I}_{15/2}$, respectively.

Changes in the synthesis duration had a tangible effect on luminescence efficiency of the samples. As the exposure time increased, the energy yield of up-conversion luminescence increased monotonously. At the same time, the ratio of red and green luminescence bands changed slightly.

The results shown in the Table 2 allow the following conclusions. The difference in the values of energy yield may be accounted for by the larger size of the particles (resulting from the longer synthesis), which leads to an increase in the surface area-to-volume ratio. Similar phenomena (surface quenching effect) have been observed for upconversion $\text{NaGdF}_4:\text{Yb,Tm}$ nanoparticles [53] and for the intrinsic exciton luminescence in MF_2 nanocrystals also [54, 55].

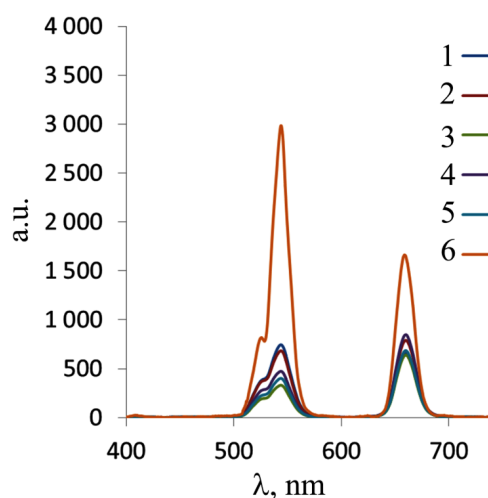


FIG. 4. Luminescence spectra of samples 1–6. The wavelength of the pumping laser is 974 nm

TABLE 2. Estimated external energy yield (EQ) of up-conversion luminescence of Er³⁺ ions of NaY_{0.78}Yb_{0.20}Er_{0.02}F_{4.0} powder samples measured in integrating sphere, %

No.	EQ, %	EQ ₁ %, red band	EQ ₂ %, green band	EQ ₁ /EQ ₂
1	0.73	0.0033	0.0040	0.80
2	0.85	0.0044	0.0041	1.06
3	0.50	0.0032	0.0019	1.70
4	0.68	0.0041	0.0027	1.54
5	0.57	0.0034	0.0023	1.50
6	2.25	1.08	1.17	0.92

4. Conclusion

Our studies have shown the possibility of synthesizing an effective up-conversion phosphor NaYF₄:Yb, Er by a chemical reaction in a sodium nitrate flux. The target hexagonal phase is formed from the primary non-equilibrium cubic nanophase in accordance with the Ostwald's step rule. The resulting particles quickly grow in size with the formation of micron-sized particles that have a rough hexagonal habit with strong symmetry violations and multiple defects. The implementation of a non-classical mechanism of crystal growth by directed agglomeration of particles is assumed. An increase in the particle size results in an increase in the efficiency of up-conversion luminescence.

Acknowledgements

The work was preformed under the RFBR grant 18-29-12050mk. The authors are grateful to Dr. A. E. Baranchikov for his assistance in conducting research and to Dr. S. V. Kuznetsov for helpful discussions. All experiments were performed on the equipment kindly provided by the Centre for Collective Use of Prokhorov General Physics Institute of the Russian Academy of Sciences and the Centre for Collective Use of Kurnakov Institute of General and Inorganic Chemistry of the Russian Academy of Sciences.

References

- [1] Ovsyankin V.V., Feofilov P.P. On the mechanism of combination of electron excitations in activated crystals. *JETP Lett.*, 1966, **3**, P. 322–323.
- [2] Auzel F.E. Compteur quantique par transfert d'énergie entre deux ions de terres rares dans un tungstate mixte et dans un verre. *C. R. Acad. Sci. B*, 1966, **262**, P. 1016–1019.
- [3] Krämer K., et al. Hexagonal Sodium Yttrium Fluoride Based Green and Blue Emitting Upconversion Phosphors. *Chemistry of Materials*, 2004, **16**, P. 1244–1251.
- [4] Mai H.-X., et al. Size- and Phase-Controlled Synthesis of Monodisperse NaYF₄:Yb,Er Nanocrystals from a Unique Delayed Nucleation Pathway Monitored with Upconversion Spectroscopy. *The Journal of Physical Chemistry C*, 2007, **111**, P. 13730–13739.
- [5] Li C., et al. Two-Dimensional -NaLuF₄ Hexagonal Microplates. *Crystal Growth & Design*, 2008, **8**, P. 923–928.
- [6] Zhang F., et al. Shape, Size, and Phase-Controlled Rare-Earth Fluoride Nanocrystals with Optical Up-conversion Properties. *Chemistry European Journal*, 2009, **15**, P. 11010–11019.
- [7] Yang L.V., et al. White emission by Frequency Up-Conversion in Yb³⁺-Ho³⁺-Tm³⁺ Triply Doped Hexagonal NaYF₄ Nanorods. *The Journal of Physical Chemistry C*, 2009, **113**, P. 18995–18999.
- [8] Zhang F., et al. Photoluminescence Modification in Upconversion Rare-Earth fluoride Nanocrystal Array Conducted Photonic Crystals. *Journal of Materials Chemistry*, 2010, **20**, P. 3895–3900.
- [9] Liu Q., et al. Sub-10nm Hexagonal Lanthanide-Doped NaLuF₄ Upconversion Nanocrystals for Sensitive Bioimaging in Vivo. *Journal American Chemical Society*, 2011, **133**, P. 17122–17125.
- [10] Nordmann J., et al. Synthesis of β-Phase NaYF₄:Yb,Er Upconversion Nanocrystals and Nanorods by Hot-Injection of Small Particles of the α-Phase. *Zeitschrift für Physikalische Chemie*, 2015, **229**, P. 247–262.
- [11] Naccache R., Yu Q., Capobianco A. The Fluoride Host: Nucleation, Growth, and Upconversion of Lanthanide-Doped Nanoparticles. *Advanced Optical Materials*, 2015, **3**, P. 482–509.
- [12] Bard A.B., et al. Mechanistic Understanding of Non-Classical Crystal Growth in Hydrothermally Synthesized Sodium Yttrium Fluoride Nanowires. *Chemistry of Materials*, 2020, **32** (7), P. 2753–2763.
- [13] Fedorov P.P., Luginina A.A., Kuznetsov S.V., Osiko V.V. Nanofluorides. *Journal of Fluorine Chemistry*, 2011, **132** (12), P. 1012–1039.
- [14] *Gmelin Handbuch der anorganischen Chemie. Syst. Nummer 39: Seltenerdelemente. Teil C3: Sc, Y, La und Lanthanide. Fluoride, Oxifluoride und zugehörige Alkalidoppelverbindungen.* Berlin, Springer Vlg., 1976.
- [15] Sobolev B.P. *The Rare Earth Trifluorides. Part 1. The High Temperature Chemistry of the Rare Earth Trifluorides.* Institut d'Estudis Catalans, Barcelona, Spain, 2000.
- [16] Fedorov P.P., Luginina A.A., Popov, A.I. Transparent oxyfluoride glass ceramics. *J. Fluor. Chem.*, 2015, **172**, P. 22–50.
- [17] Fedorov P.P. Systems of Alkali and Rare-Earth Metal Fluorides. *Russian Journal of Inorganic Chemistry*, 1999, **44**, P. 1703–1727.
- [18] Batsanova L.R. Rare-earth fluorides. *Russ. Chem. Rev.*, 1971, **40** (6), P. 465–484.
- [19] Fedorov P.P., Kuznetsov S.V., et al. Coprecipitation from aqueous solutions to prepare binary fluorides. *Russ. J. Inorg. Chem.*, 2011, **56**, P. 1525–1531.
- [20] Fedorov P.P., et al. Soft Chemical Synthesis of NaYF₄ Nanopowders. *Russian Journal Inorganic Chemistry*, 2008, **53**, P. 1681–1685.
- [21] Yi G.S., Lu H.C., et al. Synthesis, Characterization, and Biological Application of Size-Controlled Nanocrystalline NaYF₄:Yb, Er Infrared-to-Visible Up-Conversion Phosphors. *Nano Lett.*, 2004, **4**, P. 2191–2196.
- [22] Cao C., Zhang X., et al. Ultraviolet and blue up-conversion fluorescence of NaY_{0.793x}Tm_{0.007}Yb_{0.2}Gd_xF₄ phosphors. *J. Alloys Compd.*, 2010, **505** (1), P. 6–10.
- [23] Wang F., Deng R., Liu X. Preparation of core-shell NaGdF₄ nanoparticles doped with luminescent lanthanide ions to be used as upconversion-based probes. *Nature Protocol*, 2014, **9**, P. 1634–1644.
- [24] Sobolev B.P., Mineev D.A., Pashutin V.P. Low-temperature hexagonal polymorph NaYF₄ with gagarinite-type structure. *Dokl. AN SSSR*, 1963, **150**, P. 791–794 (in Russian).
- [25] Liang L.F., Wu H., et al. Enhanced blue and green upconversion in hydrothermally synthesized hexagonal NaY_{1-x}Yb_xF₄:Ln³⁺ (Ln³⁺ = Er³⁺ or Tm³⁺). *J. Alloys Compd.*, 2004, **368**, P. 94–100.
- [26] Wang Q., Tan M.C., et al. A Solvothermal Route to Size- and Phase-Controlled Highly Luminescent NaYF₄:Yb, Er Up-Conversion Nanocrystals. *J. Nanosci. Nanotechnol.*, 2010, **10** (3), P. 1685–1692.
- [27] Liu J.-N., Bu W., et al. Simultaneous nuclear imaging and intranuclear drug delivery by nuclear-targeted multifunctional upconversion nanoprobe. *Biomaterials*, 2012, **33** (29), P. 7282–7290.
- [28] Chen F., Bu W., et al. Gd³⁺ Ion Doped Upconversion Nanoprobes: Relaxivity Mechanism Probing and Sensitivity Optimization. *Adv. Funct. Mater.*, 2013, **23** (3), P. 298–307.
- [29] Guo J., Ma F., et al. Solvothermal synthesis and upconversion spectroscopy of monophase hexagonal NaYF₄:Yb³⁺/Er³⁺ nanosized crystallines. *J. Alloys Compd.*, 2012, **523**, P. 161–166.
- [30] Yu S., Wang Z., Gao R., Meng L. Microwave-assisted synthesis of water-disperse and biocompatible NaGdF₄:Yb, Ln@NaGdF₄ nanocrystals for UCL/CT/MR multimodal imaging. *J. Fluorine Chem.*, 2017, **200**, P. 77–83.
- [31] Lu J., Zhang Q., Saito F. Mechanochemical synthesis of Nano-sized complex fluorides from pair of different constituent fluoride compounds. *Chem. Letters*, 2002, **31** (12), P. 1176–1177.
- [32] Bartůněk V., Pinc J., et al. Tunable rapid microwave synthesis of up-converting hexagonal NaY_xGd_yYb_zEr_(1-x-y-z)F₄ nanocrystals in large quantity. *J. Fluor. Chem.*, 2015, **178**, P. 56–60.
- [33] Fedorov P.P., Alexandrov A.A. Synthesis of Inorganic Fluorides from Molten Salt Fluxes and Ionic Liquid Mediums. *J. Fluorine Chem.*, 2019, **227**, 109374.
- [34] Suzuki S., Teshima K., et al. Low-Temperature Flux Growth and Upconversion Fluorescence of the Idiomorphic Hexagonal-System NaYF₄ and NaYF₄:Ln (Ln = Yb, Er, Tm) Crystals. *Cryst. Growth Des.*, 2011, **11** (11), P. 4825–4830.
- [35] Suzuki S., Teshima K., et al. Novel fabrication of NIR-vis upconversion NaYF₄:Ln (Ln = Yb, Er, Tm) crystal layers by a flux coating method. *J. Mater. Chem.*, 2011, **21**, P. 13847–13852.
- [36] Ding M., Chen D., et al. Molten salt synthesis of β-NaYF₄:Yb³⁺, Ln³⁺, (Ln = Er, Tm, and Ho) micro/nanocrystals with controllable morphology and multicolor upconversion luminescence. *Sci Adv. Mater.*, 2017, **9**, P. 688–695.

- [37] Zhang X., Yang P., et al. Facile and mass production synthesis of β -NaYF₄:Yb³⁺,Er³⁺/Tm³⁺ 1D microstructures with multicolor up-conversion luminescence. *Chem. Commun.*, 2011, **47** (44), P. 12143–12145.
- [38] Batsanova L.R., Kupriyanova A.K., Doroshenko V.I. Study of the interaction of the rare-earth nitrates with sodium fluorides in molten NaNO₃. *Inorg. Mater.*, 1971, **7**, P. 1876–1877 (In Russian).
- [39] Suzuki S., Teshima K., et al. Novel fabrication of NIR-vis upconversion NaYF₄:Ln (Ln = Yb, Er, Tm) crystal layers by a flux coating method. *J. Mater. Chem.*, 2011, **21**, P. 13847–13852.
- [40] Suzuki S., Teshima K., et al. Low-temperature flux growth and upconversion fluorescence of the idiomorphic hexagonal-system NaYF₄ and NaYF₄:Ln (Ln = Yb, Er, Tm) crystal. *Cryst. Growth. Des.*, 2011, **11**, P. 4825–4830.
- [41] Zhang X., Yang P., et al. Facile and mass production synthesis of β -NaYF₄:Yb³⁺, Er³⁺/ Tm³⁺ 1D microstructures with multicolor up-conversion luminescence. *Chem. Commun.*, 2011, **47**, P. 12143–12145.
- [42] Ding M., Lu C., et al. Facile synthesis of β -NaYF₄:Ln³⁺ (Ln = Eu, Tb, Yb/Er, Yb/Tm) microcrystals with down- and up-conversion luminescence. *J. Mater. Sci.*, 2013, **48**, P. 4989–4998.
- [43] Huang X.Y., Hu G.H., et al. Molten-salt synthesis and upconversion of hexagonal NaYF₄:Er³⁺:Yb³⁺ micro-/nano-crystals. *J. Alloys Compd.*, 2014, **616**, P. 652–661.
- [44] Fedorov P.P., et al. The melt of sodium nitrate as a new medium for synthesis of fluorides. *Inorganics*, 2018, **6**, P. 38–55.
- [45] Fedorov P.P., et al. Preparation of “NaRF₄” phases from the sodium nitrate melt. *J. Fluorine Chem.*, 2019, **218**, P. 69–75.
- [46] Ryabova A. V., et al. Spectroscopic research of upconversion nanomaterials based on complex oxide compounds doped with rare-earth ion pairs: Benefit for cancer diagnostics by upconversion fluorescence and radio sensitive methods. *Photon Lasers Med.*, 2013, **2**, P. 117–128.
- [47] Ostwald W. Studien über die Bildung und Umwandlung fester Körper. *Zeitschrift für Physikalische Chemie*, 1897, **22**, P. 289–330.
- [48] Threlfall T. Structural and thermodynamics explanation of Ostwalds rule. *Organic Process Research and Development*. 2003, **7**, P. 1017–1027.
- [49] Fedorov P.P. Comment on the paper A.B. Bard, X. Zue, G. Zhu, et al. A Mechanistic Understanding of Non-Classical Crystal Growth in Hydrothermally Synthesized Sodium Yttrium Fluoride Nanowires. *Chem. Mat.*, 2020, accepted for publication.
- [50] Ivanov V.K., Fedorov P.P., Baranchikov A.Y., Osiko V.V. Oriented Aggregation of Particles: 100 Years of Investigations of Non-Classical Crystal Growth. *Russian Chemical Review*, 2014, **83**, P. 1204–1222.
- [51] De Yoreo J.J., et al. Crystallization by particle attachment in synthetic, biogenic, and geologic environments. *Science*, 2015, **349** (6247), aaa6760.
- [52] Fedorov P.P., Osiko V.V. Relationship between the Faceting of Crystals and Their Formation Mechanism. *Doklady Physics*, 2019, **64** (9), P. 353–355.
- [53] Wang F., Wang J., Liu X. Direct evidence of a surface quenching effect on size-dependent luminescence of upconversion nanoparticles. *Angew. Chem. Int. Ed.*, 2010, **49**, P. 7456–7460.
- [54] Demkiv T., et al. Intrinsic luminescence of SrF₂ nanoparticles. *Journal of Luminescence*, 2017, **190**, P. 10–15.
- [55] Vistovskyy V.V., et al. The luminescence of BaF₂ nanoparticles upon high-energy excitation. *Journal of Applied Physics*, 2014, **116**, 054308.

Temperature dependent structural, morphological, FTIR, optical, magnetic properties of NiMgZn ferrites

T. Vidya Sagar*, T. Subba Rao, N. Raghuram

Dept. of Physics, Sri Krishnadevaraya University, Anantapuramu-515003, A.P, India

tvidyasagar83@gmail.com

DOI 10.17586/2220-8054-2020-11-4-434-443

NiMgZn ferrites with chemical composition $\text{Ni}_{0.2}\text{Mg}_{0.3}\text{Zn}_{0.5}\text{Fe}_2\text{O}_4$ nanomaterials were synthesized using the sol-gel technique. The various properties of the samples prepared at three different calcination temperatures (T) of 400, 450 and 500 °C/5 hr were studied. The X-ray diffraction study confirmed the single-phase cubic spinel structure (JCPDS 08-0234) for 400 & 500 °C calcined samples and with Fe_2O_3 as an impurity phase for 450 °C calcined sample with lattice parameter values 8.296 to 8.376 Å. The surface morphology and EDX spectra observed with field emission scanning electron microscope (FESEM) images confirmed the nano-sized irregular shaped grain development at low calcination temperatures. The force constants are determined using FTIR spectroscopy confirmed the M–O bonds present in ferrites. Optical band gap properties studied and found that NiMgZn ferrites have band gaps in semiconducting region from 1.68 to 1.75 eV. The susceptibility-temperature (χ - T) dependence is studied using a Bartington MS2B Dual Frequency instrument in heating and cooling modes and magnetic transition temperature (T_c) were determined. The highest magnetic susceptibility of 1293 is observed for 500 °C calcined material. By using VSM, the M–H loop, magnetic properties are studied, which showed that this material is ferrimagnetic. Also, the magnetic moments and saturation magnetizations (M_s) are calculated. The maximum saturation magnetization 97.20 emu/g is observed for 400 °C calcined sample.

Keywords: ferrites, sol-gel, X-ray diffraction, magnetic properties.

Received: 28 March 2020

Revised: 30 April 2020

Final revision: 13 May 2020

1. Introduction

Spinel ferrites having a variety of applications in the fields of data storage, transformer cores, anti-bacterial activities, soft magnetic applications, biomedical, sensors, high frequency components, LTCC devices, super capacitors, microwave absorption, photo catalytic activity and drug delivery etc. [1–4].

The properties of spinel ferrites ($\text{A}^{+2}\text{Fe}_2^{+3}\text{O}_4$ A: Cations such as Ni^{+2} , Co^{+2} , Zn^{+2} , Mn^{+2} , Cr^{+2} , Mg^{+2} , etc.) depend on various parameters, such as synthesis, particle size, morphology and cationic distributions at the tetrahedral and octahedral positions in the unit cell etc. Many studies have been performed by introducing non-magnetic ions such as Mn, Zn, Cu, Sn, Mg, etc. to observe the changes in the magnetic and other properties of spinel ferrites using different synthesis methods. The magnetic parameters vary due to the cationic transition from A, B sites. This can be done by substitution of different Zn^{+2} , Mg^{+2} , Mn^{+2} , Cu^{+2} , etc. At the nanoparticle scale the properties of spinel ferrites are significantly different compared to that of bulk materials because of their size and stoichiometry. Nano-scaled ferrites are used in many applications like sensor applications, bio-medical applications, data storage [5–8]. Also, nano ferrites are used for microwave absorption and EMI shielding properties [9]. The magnetic properties may be enhanced significantly at the nano scale [14].

MN Akhtar prepared NiMgZn ferrites using sol-gel method at 650 °C for 4 hours and showed that they are useful for microwave absorption and High Frequency applications [1].

S. Ramesh et al. prepared NiZnCo and NiZnMn ferrites using sol-gel auto combustion method at 1200 °C have showed that these ferrites can be used in the transformer cores and inductors upto several MHz [5].

Rohit Sharma et al. prepared Ni doped Mg–Zn spinel ferrites using co precipitation method at 900 °C and they can be used in high density information storage, magnetic recording and memory devices [8].

In our present work, we synthesized nano NiMgZn ferrites via sol-gel method, as it has many advantages, such as uniform reaction rates, compositional control, low cost synthesis, etc. The majority of research mentioned above has synthetic temperatures above 500 °C. Hence, we decided to study the properties of NiMgZn ferrites calcined at three temperatures 400, 450 and 500 °C for 5 hr. The synthesized samples were characterized by XRD, FESEM, EDX, FTIR, UV and VSM.

2. Experimental procedure

$\text{Fe}(\text{NO}_3)_3 \cdot 9\text{H}_2\text{O}$, $\text{Ni}(\text{NO}_3)_2 \cdot 6\text{H}_2\text{O}$, $\text{Zn}(\text{NO}_3)_2 \cdot 6\text{H}_2\text{O}$, $\text{Mg}(\text{NO}_3)_3 \cdot 6\text{H}_2\text{O}$, and $\text{C}_6\text{H}_8\text{O}_7$ (citric acid, anhydrous), NH_3 (25 %) solution were used as precursor materials. The stoichiometric weighed amounts of these metal nitrates were completely dissolved in 50 ml of distilled water. This solution was then added to 50 ml of citric acid solution. The molar ratio of these nitrates and citric acid is fixed as 1:1. Then the solution is stirred for 30 minutes to obtain a clear solution using a magnetic stirrer with hot plate. After this ammonia solution was added drop-wise using a burette to achieve a pH value of 7 for the solution with stirring it simultaneously. The solution is continuously stirred with a rotation speed 470 rpm. Condensation reaction occurs between the adjacent metal nitrates and the molecules of citrates, yielding a polymer network in colloidal dimensions known as sol. The stirring is continued for 1 hr. Then, the solution was slowly evaporated by intensive stirring and heating for 6 hr at 80 °C and was kept at that temperature until the solution turned into a gel. The gel was then calcined at 400, 450, 500 °C for 5 hr in a furnace. The resulting powder was finely grounded using an agate mortar. Then this powders was characterized using the X-ray diffractometer (XRD, Bruker, $\text{CuK}\alpha$ $\lambda = 0.15406$ nm), field-emission scanning electron microscope (FE-SEM, Ultra 55, Carl Zeiss), magnetic susceptibility measurement (χ - T curves) with Bartington MS2WFP furnace system (40 – 700 °C), FTIR spectrometer and UV-Visible Spectrometer for structural, morphological, magnetic susceptibility and optical properties.

3. Results and discussion

3.1. X-Ray diffraction studies

The two-theta versus counts plots of NiMgZn ferrites were as shown in Fig. 1 for 400, 450, and 500 °C. These X-ray diffraction peaks (111), (220), (311), (222), (400), (422), (511), (440), (620), (533) revealed the cubic spinel structure (JCPDS 08-0234). The average crystallite size (D) was determined using the Scherrer formula: $0.9\lambda/\beta \cos \theta$, for major peaks and for (311) planes, where λ is the wavelength (0.15406 nm) of $\text{CuK}\alpha$ radiation, β is the full width half maxima (FWHM) and θ is the diffraction angle [13]. The material calcined at 450 °C showed the presence of Fe_2O_3 [3, 14, 15]; this may be due to the incomplete decomposition or non-reacted pre cursors at that temperature as well as lattice distortion. The results of XRD data were displayed in Table 1.

TABLE 1. Structural Parameters of NiMgZn Ferrites calcined at different temperatures

S. No	Calcination Temperature (°C)	a (Å) ± 0.001	V (Å) ³ ± 0.001	Avg D nm ± 1.0	2θ For 311 planes	D nm from 311 plane nm ± 1.0	ρ_x g/cm ³ ± 0.0001	ρ_b g/cm ³ ± 0.001	Porosity $P(\%)$ ± 0.001	Specific Surface Area $S(\text{m}^2/\text{g})$ (6000/ $\rho_b \cdot D_{311}$)
1	400	8.374	587.217	46.7	35.52	38.1	5.1429	4.314	16.117	36.50
2	450	8.296	570.960	15.5	35.88	12.4	5.2893	4.463	15.622	108.50
3	500	8.376	587.638	54	35.52	47	5.1392	4.521	12.029	28.24

It was found that the crystalline size was about 15.5 nm for the 450 °C calcined material; this was attributed due to the high FWHM values observed and other two samples are 46.7 and 54 nm. The 450 °C calcined sample had small average crystalline size and comparable with the crystallite size observed with (311) plane. This may be due to the high micro strain produced either in synthesis processes or calcination temperature. The lattice parameter $a = b = c$ is 8.374, 8.296 and 8.376 Å are calculated from (311) plane using Bragg's equation $a = \frac{\sqrt{11} \cdot 1.5406}{\sin \theta}$ Å show the densification of unit cell at 450 °C which was observed in X-Ray density. The interplanar spacing for d_{311} is 2.769, 2.750 and 2.737 nm respectively, calculated from the formula $d_{311} = \frac{a}{\sqrt{11}}$. The X-Ray density is determined from $\rho_x = \frac{n \cdot MW}{N_a \cdot a^3}$, where MW is the molecular weight of the sample equal to 227.36 g/mole, N_a is the Avogadro's number – 6.023×10^{23} atoms/mole, a is the lattice parameter and $n = 8$, the effective number of atoms for a face-centered cubic structure. The maximum X-Ray density was found to be 5.2893 g/cm³ is for 450 °C calcinated sample. The bulk densities are measured by preparing pellets which is calculated from $\rho_b = \frac{m}{3.14 \cdot r^2 \cdot t}$, where m is the mass,

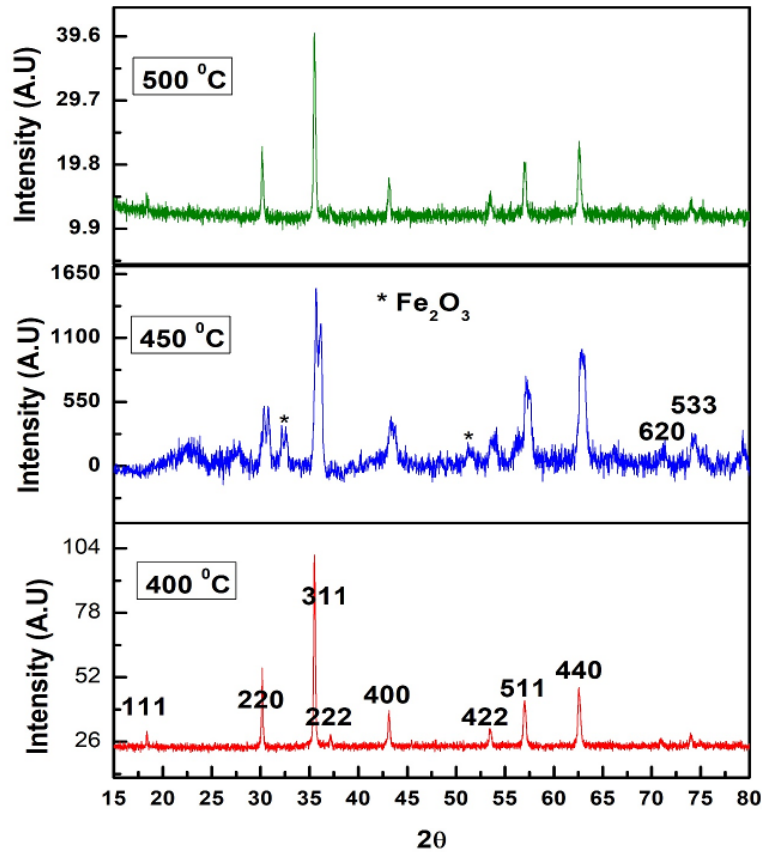


FIG. 1. X-Ray diffraction pattern of NiMgZn Ferrite calcined at 400, 450, 500 °C

r is the radius and t is the thickness of the pellets prepared. The bulk density shows increasing trend for increase in calcination temperature due to expanding of grains over the surface. The porosity (P) can be calculated using the equation $P \% = \left[1 - \frac{\rho_b}{\rho_x} \right] \times 100$ was found to be decreased with increasing calcination temperature, because of improvement in the crystallinity of the samples [12, 13]. The specific surface area is high for 450 °C calcinated sample about 108.50 m²/g. Even though this surface area is high there is no significant influence on the other properties is observed. This may be due to partial ferrite phase formation at 450 °C.

3.2. Surface morphology study

The surface morphology and EDX images of the ferrite samples of the pellets prepared were shown in the Fig. 2(a,b and c) respectively. The morphology observed is similar for three calcination temperatures, whereas the 400 °C calcinated sample showed irregular grains, the 450 °C calcinated sample showed a uniform grain structure. The 500 °C calcinated sample showed densified grains agglomerated at some places. The crystallinity improved well with an increase in temperature. For all samples, the particle size is in the range of nm.

The EDX study is used to perform to know the stoichiometric & elemental details of the composition. The EDX data of the samples prepared is listed in the Table 2. The EDX data provides the elemental composition of Ni, Mg, Zn, Fe and O. All the samples have the nearest stoichiometry to the Ni_{0.2}Mg_{0.3}Zn_{0.5}Fe₂O₄ composition prepared and it is represented in Table 2.

3.3. FTIR spectroscopy

Figure 3 shows the FTIR spectra recorded in the 200 – 1000 cm⁻¹ range for NiMgZn ferrites calcined at different temperatures. The absorption bands and the tetrahedral, octahedra force constants were determined from the formula $K_t = 4\pi^2 c^2 \nu_t \mu_m$ and $K_o = 4\pi^2 c^2 \nu_o \mu_m$, where $c = 2.99 \times 10^{10}$ cm/s and μ_m is the reduced mass of Fe⁺³ and O⁻² equal to 2.60×10^{-23} g [1]. The absorption bands were observed in the 430 to 564 cm⁻¹ range. The observed absorption bands confirmed the formation of spinel ferrites. The force constants determined for three different calcination temperatures were shown in the Table 3. The table shows as the temperature increased, the cations preferentially

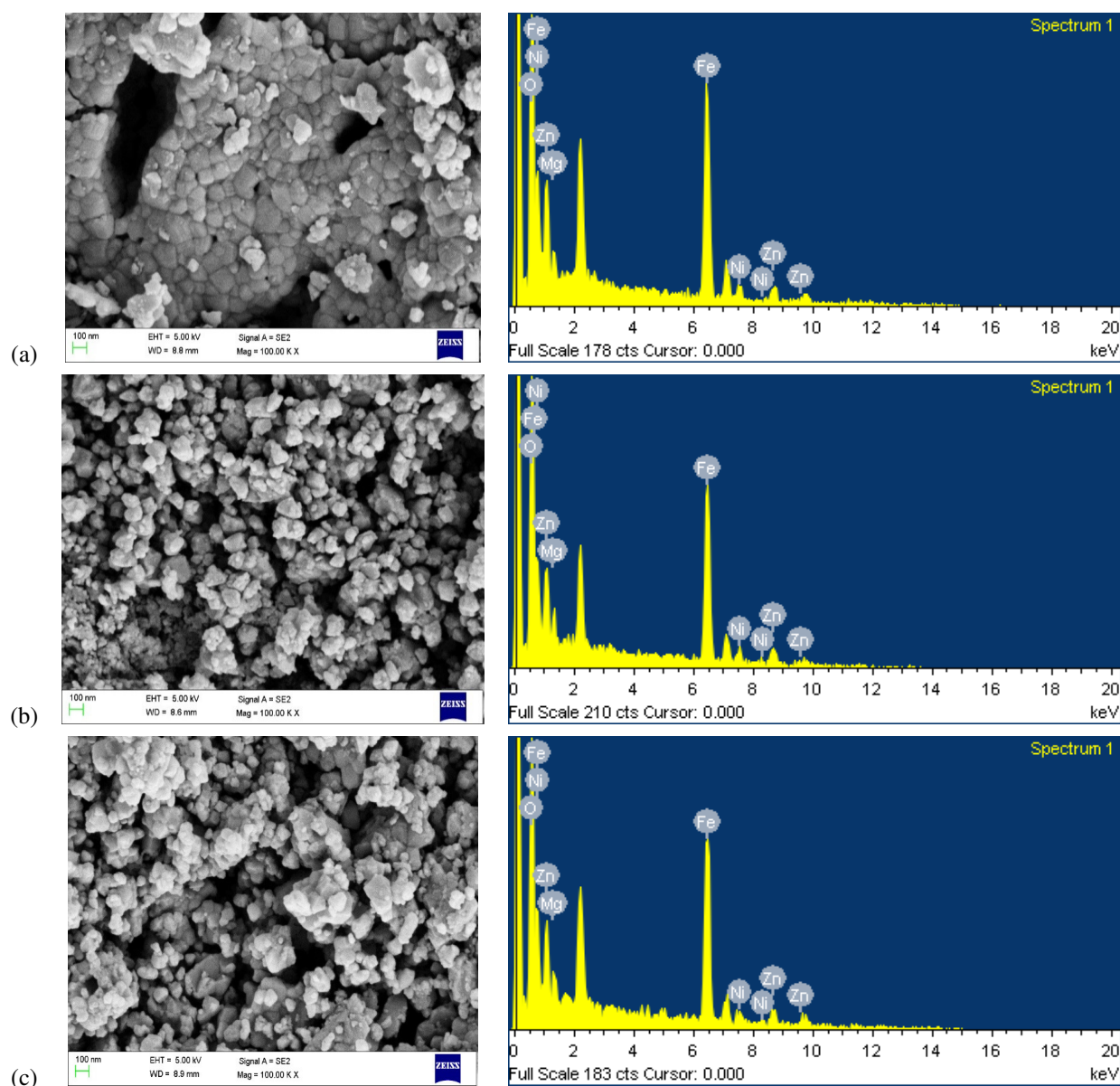


FIG. 2. FESEM Images of NiMgZn Ferrites calcined at 400 (a), 450 (b), 500 (c) °C and EDX Data

TABLE 2. EDS Data of NiMgZn Ferrites

Element and (composition)	400 °C			450 °C			500 °C		
	Weight % 100 %	Atomic %	Calculated composition ± 0.001	Weight % 100 %	Atomic %	Calculated composition ± 0.001	Weight % 100 %	Atomic %	Calculated composition ± 0.001
Ni (0.2)	6.12	3.50	0.256	5.21	3.08	0.237	6.59	3.90	0.299
Mg (0.3)	2.84	3.93	0.287	2.83	4.04	0.310	2.42	3.46	0.265
Zn (0.5)	14.33	7.37	0.539	15.29	8.11	0.623	13.21	7.02	0.538
Fe (2)	50.66	30.48	2.228	52.65	32.70	2.51	53.76	33.45	2.564
O (4)	26.05	54.71	4	24.02	52.07	4	24.02	52.17	4

occupied the octahedral sites, hence increase in the force constants at octahedra sites was observed. Some other absorption bands are due to O–H, C–H and COO groups which are not shown in the figure. The Debye temperature is used to study the vibrations of lattice. The Debye temperatures were calculated from $\theta_D = \frac{hc\nu_{\text{average}}}{k_B}$ [3, 16] and depicted in Table 3. The Debye temperatures were found increase with an increase in the calcination temperature. This is attributed due to the increase in the wave number related to Me–O at tetragonal site. The increasing trend of Debye temperatures indicates the reduction of the lattice vibrations due to an increase in the calcination temperature linked with improved crystallinity.

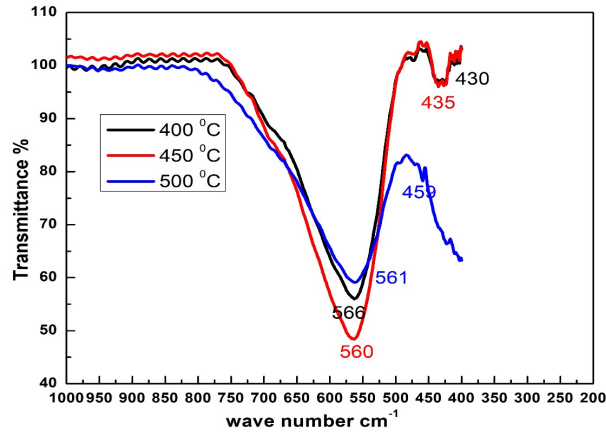


FIG. 3. FTIR spectra of NiMgZn ferrite indicating prominent M–O bonds

TABLE 3. The force constants obtained from FTIR spectroscopy & optical band gap from UV-Visible spectroscopy at tetrahedral and octahedral sites for NiMgZn ferrites

S. No	Calcination Temperature °C	ν_t cm ⁻¹	ν_o cm ⁻¹	$K_t \times 10^5$ Dyne/cm	$K_o \times 10^5$ Dyne/cm	Debye Temperatures θ_D (K)	E_g (eV)
1	400	564	430	2.918	1.695	713.195	1.68
2	450	566	435	2.937	1.735	718.217	1.73
3	500	560	461	2.877	1.948	732.567	1.75

3.4. UV-Visible spectroscopy

UV-Visible spectroscopy was used to determine the optical band gaps of the materials. The diffuse reflectance spectra (DRS) were recorded using UV-Visible spectrophotometer in the 240 – 2600 nm range for the NiMgZn ferrites. The Kubelka–Munk function (function of reflectance) was calculated using the relation $F(R) = (1 - R)^2/2R$, where R can reflect the reflectance. It is a well-known fact that the $F(R)$ is directly proportional to the absorption coefficient (α). Hence, in place of α , the numerical value of $F(R)$ would be considered. By using the equation $(\alpha hv)^n = K(hv - E_g)$, where hv indicated the photon's energy, n reflected exponent and the rest of the symbols have their general meaning. Herein, n can provide the information related to the kind of transition between valency (V_B) and conduction bands (C_B). That is, for direct transition of charges between V_B and C_B , n value is equal to 2 while for indirect transition n is to be 0.5. As we are considered only direct transition of charges from the two bands so that $n = 2$ was taken for determining the E_g values [17]. The plot of $(\alpha hv)^2$ Vs hv graphs of NiMgZn ferrites calcined at three calcination temperatures (T) values shown in Fig. 4(a,b,c). After plotting the graphs, the linear portion of each plot was extrapolated towards the direction of x -axis. The photon energy position intersected portion of the plot was the optical band gap of the sample E_g . From the last column of Table 3, it was observed that the E_g values of all compositions were increased with an increase in the calcination temperature. The NiMgZn ferrites compositions calcined at 400 – 500 °C showed the increasing trend of E_g value from 1.68 to 1.75 eV. This kind of behavior can be commonly explained by the localized and delocalized electrons. The localized electrons increased with the increasing calcination temperature, such that the band gap increased and it indicated a structure with fewer oxygen defects.

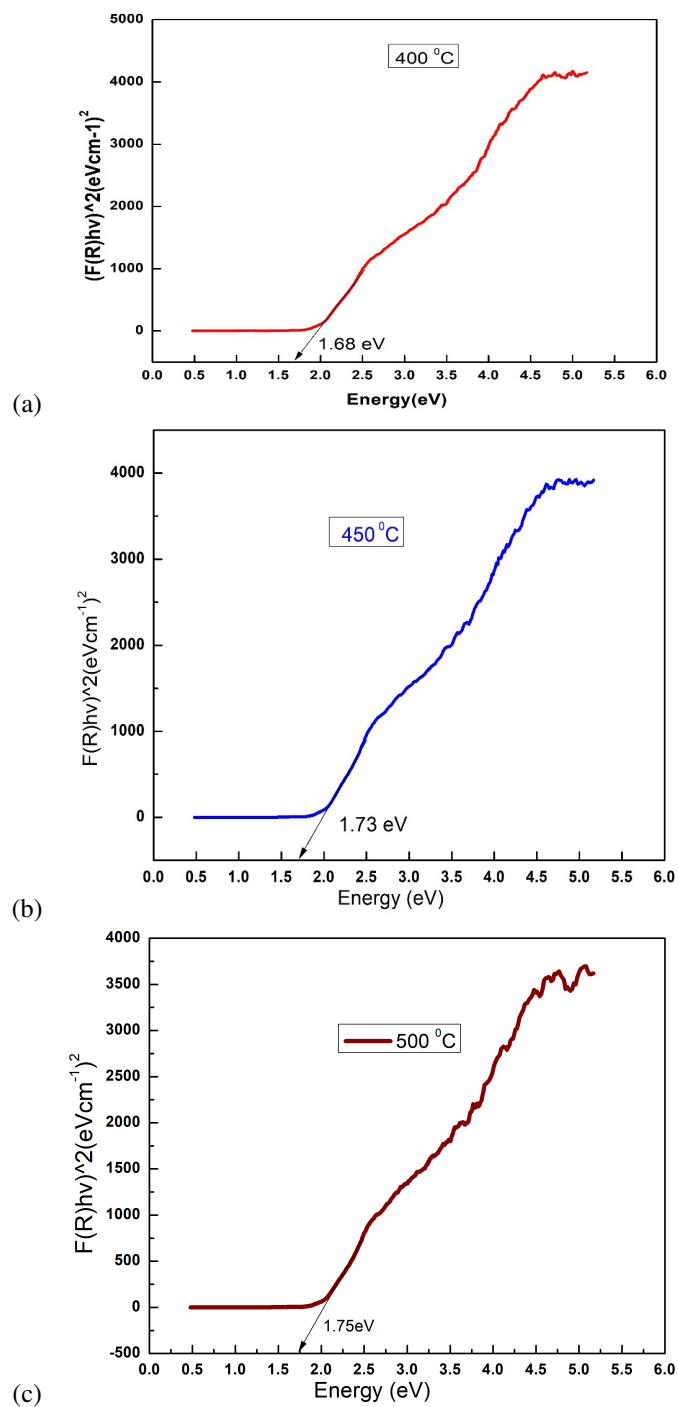


FIG. 4. Optical Band gap of Nano NiMgZn ferrites calcined at 400 (a), 450 (b) and 500 (c) °C

3.5. Susceptibility of NiMgZn ferrites

The susceptibilities were recorded in heating mode and cooling mode using a Bartington MS2B Dual Frequency instrument from 40 – 700 °C in order to study the magnetic temperature and shown in Fig. 5. With this, we can estimate the ferrimagnetic to paramagnetic behavior of the samples. Both the heating and cooling mode curves showed the same trend. The samples calcined at 400 and 500 °C are exhibiting perfect ferromagnetic to paramagnetic behavior, while the sample calcined at 450 °C showed deviation from ferromagnetic behavior; this may due to the significant formation of Fe_2O_3 at that temperature, which was observed in XRD. Since the magnetic susceptibility depends on the type of dopant and microstructure, the deviation of nature is due to the formation of Fe_2O_3 [3, 15, 18]. The susceptibility recorded at 40 °C for all samples increased with calcination temperature. The magnetic transition temperature (T_c) increased from 438 to 446 °C and then decreased to 418 °C.

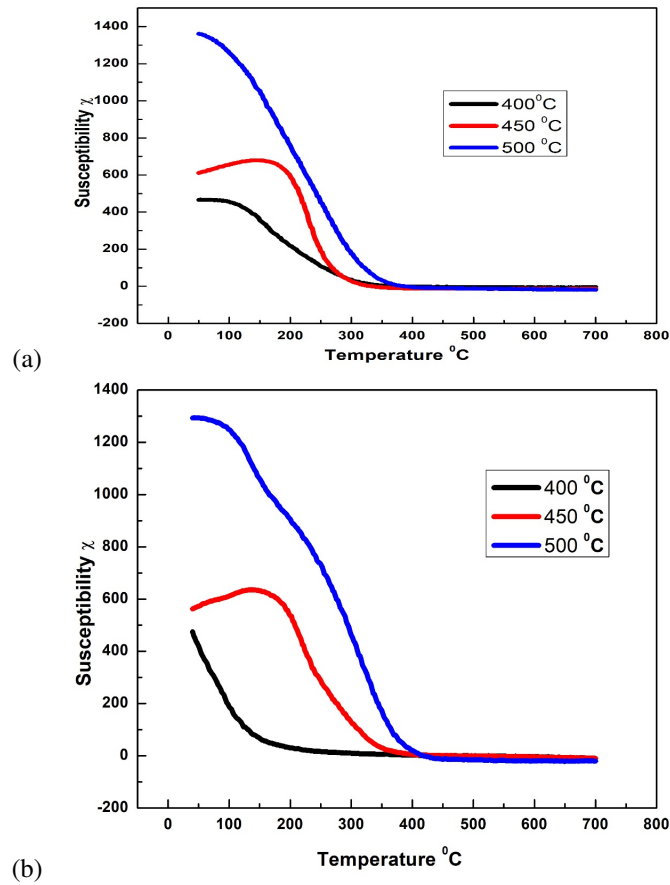


FIG. 5. Susceptibility and temperature graph in cooling (a) and heating (b) mode

3.6. M–H loop analysis

Figure 6 represents the room temperature hysteresis behavior of the NiMgZn ferrites calcined at different temperatures over the field range from –15 to +15 k Oe at room temperature. The various magnetic parameters, such as remanent magnetization (M_r), saturation magnetization (M_s), M_r/M_s , Magnetic moment (n_B) in Bohr magnetons (μ_B), Coercive field (H_c), Anisotropy constant (K_{ac}) are shown in the Table 4. The remanent magnetization decreased with calcination temperature; also, the saturation magnetization decreased from 97.20 to 90.20 emu/g. The coercivity decreased with an increase in the calcination temperature. This can be attributed to a decrease in the ferrimagnetic nature. The decreased coercivity of the samples can be explained on the basis of magnetic crystalline-anisotropy, which depends on various parameters such as cationic distribution, specific surface area, grain size, density, synthesis method, etc [8]. Magnetic moments also decrease from 3.95 to 3.67. This can be explained as follows. As the temperature increases the concentration of Fe ions on B site will be decreased so that, the magnetic moment at B site will be decreased and magnetic moment at A site be increases due to increase in the concentration of Fe ions at A site as a result the net magnetic moment will be decreased according to Neel’s model [20, 22]. However, with the

formation of iron oxide for the 450 °C calcined sample, more Fe⁺³ ions occupy the A sites. By comparing the samples calcined at 400 and 500 °C, we can conclude that as the calcination temperature increased Fe ions will occupied more A sites compared to B sites, and hence, the magnetic moment decreased. The squareness values all are less than 0.5 indicates the contribution of uniaxial anisotropy of the synthesized nano ferrites. Due to small values of coercivity and remanence magnetization, this material can be used in high frequency electronic instruments. Also, the increase in the calcination temperature reduced the canting effect of Zn in the ferrites [14, 21].

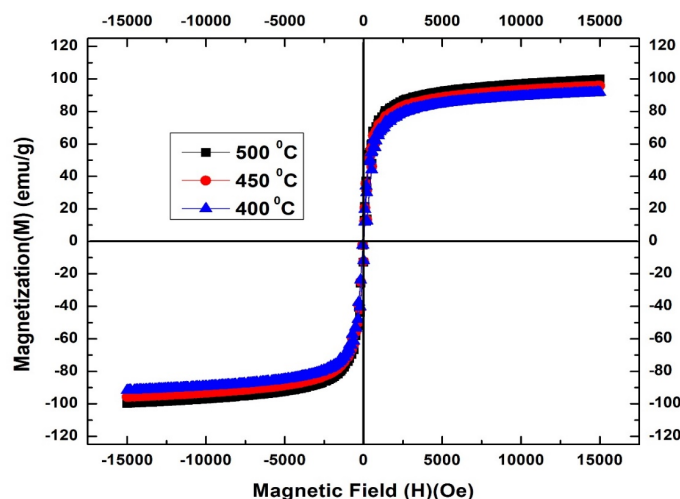


FIG. 6. M–H curves of NiMgZn ferrites

TABLE 4. The magnetic parameters of the nano NiMgZn ferrites

S. No	Calcination Temperature °C	M_r (emu/g)	M_s (emu/g)	M_r/M_s	n_B (emu/g) = $\frac{MW \cdot M_s}{5585}$	H_c (Oe)	Anisotropy constant (erg/cc) $K_{ac} = \frac{H_c M_s}{0.96}$	T_m (°C) heating mode	χ at 40 °C
1	400	13.80	97.20	0.1419	3.95	48.36	4896.45	438	453
2	450	12.62	95.76	0.1318	3.89	47.25	4713.19	446	663
3	500	5.01	90.20	0.0555	3.67	42.65	4007.32	418	1293

A comparative study of present work with the related compositions is represented in Table 5.

4. Conclusions

NiMgZn ferrites were synthesized by the sol-gel method. This ferrites had a spinel cubic structure with lattice parameter ranges from 8.296 to 8.376 Å and crystalline size about 15.47 to 54.02 nm. The presence of iron oxide major phase is observed for the sample calcinated at 450 °C. The FESEM-EDX images confirms the uniform grains and desired elements present in all samples prepared. The FTIR spectrum shows the prominent absorption bands in the 430 – 564 cm⁻¹ range, confirming the spinel ferrites were formed. The optical band gaps are found to be 1.68 to 1.7 eV, showing the semiconducting nature of the ferrites. The susceptibility and temperature study confirm the ferromagnetic nature decreased as the temperature increased. The ferromagnetic susceptibilities at 40 °C varied from 453 to 1293. The saturation magnetization and coercivity decreased with increase of calcination temperatures as a greater number of Fe⁺³ ions occupy the tetrahedral sites. The samples prepared at 400 and 450 °C are ferrimagnetic in nature, whereas the sample prepared at 500 °C displays a soft magnetic nature. These ferrite materials have potential applications in photocatalytic activity, drug delivery and other ferrimagnetic applications.

TABLE 5. Comparative data of NiMgZn ferrites prepared by various researchers

S. No	a (Å)	D (nm)	M_s (emu/g)	H_c (Oe)	μ_B	S (m ² /g)	$K_t \times 10^5$ (dyne/cm ²)	$K_0 \times 10^5$ (dyne/cm ²)	Band gap (eV)	Work and method
1	8.345-8.364	13.0-18.4	14.59-58.45	18.56-131.25	1.74-6.94		2.8788-3.1094	2.0278-2.3877		M.N. Akhtar et al. Ni _{0.5} Mg _x Zn _{0.5-x} Fe ₂ O ₄ (sol-gel) [1]
2	8.363-8.386	19.00-28.863								D.H. Bodade et al. Mg _{0.7-x} Ni _x Zn _{0.3} Fe ₂ O ₄ (sol-gel auto combustion method) [2]
3	8.349-8.388	40.06-42.89	24.7-57.6	64.6-107.0		27.03-31.17	2.141-2.279	1.275-1.323	-	P. Tiwari et al. Mg _{0.7-x} Ni _{0.3} Zn _x Fe ₂ O ₄ (Solution combustion method) [3]
4	8.3846-8.4116	43.58-59.40	25.30-57.84	18.69-125.58	0.99-2.26				4.50-5.60	R. Sharma Mg _{0.5} Zn _{0.5-x} Ni _x Fe ₂ O ₄ (Co precipitation) [8]
5	8.368-8.404	36-59	30.4-43.1	11.9-65.8	1.17-1.82					Gabal et al. Ni _{0.8-x} Zn _{0.2} Mg _x Fe ₂ O ₄ (sol-gel) [19]
6	8.345-8.4052	12.9-23.9	29-106	72.45-122.34						A. Ghosh et al. Mg _{0.7-x} Ni _{0.3} Zn _x Fe ₂ O ₄ (sol-gel auto combustion method) [23]
7	8.296-8.376	15.5-54.0	90.20-97.20	42.65-48.36	3.67-3.95	28.18-108.50	2.773-2.937	1.695-1.948	1.68-1.79	Present study

Acknowledgements

The author is thankful to Prof. T. Subbarao for his encouragement. The author is also thankful to Micro and Nano Characterization Facility, IISc, Bangalore for providing various characterization facilities under external user.

Data availability statement

Data will be made immediately available based on the request.

Declaration of competing interest

The authors declare that we have no conflicts of interest.

References

- [1] Majid Niaz Akhtar, A. Rahman, A.B. Sulong, Muhammad Azhar Khan. Structural, Spectral, Dielectric and Magnetic Properties of Ni_{0.5}Mg_xZn_{0.5-x}Fe₂O₄ Nanosized ferrites for Microwave absorption and High Frequency Applications. *Ceramics International*, 2017, **43** (5), P. 4357–4365.
- [2] Bobade D.H., Rathod S.M., Mane M.L. Sol-gel auto-combustion synthesis, structural and enhanced magnetic properties of Ni²⁺ substituted nanocrystalline Mg–Zn spinel ferrite. *Physica B*, 2012, **407**, P. 3700–3704.
- [3] Tiwari P., Verma R., et al. Effect of Zn addition on structural, magnetic properties and anti-structural modelling of magnesium-nickel nano ferrite. *Material Chemistry and Physics*, 2019, **229**, P. 78–86.
- [4] Asther Hossain A.K.M., Biswas T.S., et al. Investigation of structural and magnetic properties of polycrystalline Ni_{0.50}Zn_{0.50-x}Mg_xFe₂O₄ spinel ferrites. *Material Chemistry and Physics*, 2010, **120**, P. 461–467.
- [5] Ramesh S., Dhana Lakshmi B., et al. Effect of Mn/Co substitutions on the resistivity and dielectric properties of nickel-zinc ferrites. *Ceramics International*, 2016, **42** (8), P. 9591–9598.
- [6] Zeng Aixiang, Yuan Jun. Study of Sol-Gel Auto-combustion Method Prepared Ni_{0.6-x}Zn_{0.4}Mg_xFe₂O₄. *Advanced Materials Research*, 2012, **463–464**, P. 1052–1056.
- [7] Tatarchuk T., Bououdina M., Judith Vijaya J., John Kennedy L. Spinel Ferrite Nanoparticles: Synthesis, Crystal Structure, Properties, and Perspective Applications. In: Fesenko O., Yatsenko L. (eds) *Nanophysics, Nanomaterials, Interface Studies, and Applications. NANO 2016. Springer Proceedings in Physics*, 2017 **195** P. 305–325.

- [8] Rohit Sharma, Prashant Thakur, Pankaj Sharma, Vineet Sharma. Ferrimagnetic Ni²⁺ doped Mg–Zn spinel ferrite nanoparticles for high density information Storage. *Journal of Alloys and Compounds*, 2017, **704**, P. 7–17.
- [9] Chandrababu Naidu Kadiyala, Madhuri Wuppulluri. Microwave Processed Bulk and Nano NiMg Ferrites: A Comparative Study on X-band Electromagnetic Interference Shielding Properties. *Materials Chemistry and Physics*, 2017, **187**, P. 164–176.
- [10] Xia A., Liu S., et al. Hydrothermal Mg_{1-x}Zn_xFe₂O₄ spinel ferrites: Phase formation and mechanism of saturation magnetization. *Materials Letters*, 2013, **105**, P. 199–201.
- [11] Sasaki T., et al. Continuous synthesis of fine MgFe₂O₄ nanoparticles by supercritical hydrothermal reaction. *Journal of Supercritical Fluids*, 2010, **53**, P. 92–94.
- [12] Xiqian Zhao, Aimin Sun, et al. Effects of Mg Substitution on the Structural and Magnetic Properties of Ni_{0.2}Mg_xCo_{0.8-x}Fe₂O₄ Nanoparticle Ferrites. *Journal of Superconductivity and Novel Magnetism*, 2019, **32**, P. 2589–2598.
- [13] Cullity B.D. *Elements of X-Ray diffraction*. Second ed. Addison-Wesley, Reading MA, 1978.
- [14] Rajinder Kumar, Hitanshu Kumar, Manoj Kumar, Ragini Raj Singh. Enhanced Saturation Magnetization in Cobalt Doped Ni–Zn Ferrite Nanoparticles. *Journal of Superconductivity and Novel Magnetism*, 2015, **28**, P. 3557–3564.
- [15] Satalkar M., Kane S.N., et al. Synthesis and soft magnetic properties of Zn_{0.8-x}Ni_xMg_{0.1}Cu_{0.1}Fe₂O₄ (x = 0.0–0.8) ferrites prepared by sol-gel auto-combustion method. *Journal of Alloys and Compounds*, 2014, **615**, P. S313–S316.
- [16] Tatarchuk T.R., Paliychuk N.D., et al. Effect of cobalt substitution on structural, elastic, magnetic and optical properties of zinc ferrite nanoparticles. *Journal of Alloys and Compounds*, 2018, **731**, P. 1256–1266.
- [17] Chandra Babu Naidu K., Madhuri W. Determination of activation energies from complex impedance parameters of microwave sintered NiMgZn ferrites. *Mechanics, Materials Science and Engineering*, 2017, **9**.
- [18] Muddassar Naeem, Nazar Abbas Shah, Iftikhar Hussain Gul, Asghari Maqsood. Structural, electrical and magnetic characterization of Ni–Mg Spinel ferrites. *Journal of Alloys and Compounds*, 2009, **487**, P. 739–743.
- [19] Gabal M.A., Bayoumy W.A. Effect of composition on structural and magnetic properties nanocrystalline Ni_{0.8-x}Zn_{0.2}Mg_xFe₂O₄ ferrite. *Polyhedron*, 2010, **29**, P. 2569–2573.
- [20] Yoon Mi Kwon, Min-Young Lee, et al. Structural and Magnetic Properties of Ni_{0.6}Zn_{0.4}Fe₂O₄ Ferrite Prepared by Solid State Reaction and Sol-gel. *Journal of Magnetism*, 2014, **19** (1) P. 64–67.
- [21] Jadhav, Swati, et al. Effect of Cr ions on physical properties of Cu–Zn ferrite nano-particles. *International Journal of Basic and Applied Research*, 2011, **1**, P. 50–53.
- [22] Cullity B.D., Graham C.D. *Introduction to magnetic materials*, Wiley, IEEE Press, 2008.
- [23] Ghosh A., Satalkar M., et al. Soft Magnetic Properties of Mg_{0.7-x}Ni_{0.3}Zn_xFe₂O₄ ferrites synthesized by sol-gel auto combustion technique without post-preparation thermal treatment. *International Journal of Modern Physics: Conference Series*, 2013, **22**, P. 28–34.

Large scale synthesis and characterization of cadmium sulfide nanoparticles by simple chemical route

A. S. Garde

Department of Physics, SPH Arts, Science and Commerce College Nampur Dist. Nasik 423 204,
Savitribai Phule University Pune, Maharashtra, India

arungarde@yahoo.co.in

DOI 10.17586/2220-8054-2020-11-4-444-452

Large scale cadmium sulfide nanoparticles were synthesized by simple chemical route. The microstructure of cadmium sulfide nanoparticles was characterized by X-ray diffraction pattern (XRD) FESEM, FTIR and UV-visible spectroscopy. The XRD results showed that there was a transformation from cubic to hexagonal crystalline phase. The W–H plots show the size and nature of the strain incorporated in peak broadening of X-ray diffraction peaks. Some of the observed peak broadening can be attributed to crystallite size and microstrain effects, dislocation density, hkl-dependent peak broadening and peak shifts are clearly associated with stacking faults. The refractive index of the CdS nanoparticles was estimated to 2.22. The optical band gap of the synthesized CdS nanoparticles was calculated by Tauc relation and found to be 3.45 eV. The dependence of the blue shift and optical band gap on the quantum size effect was confirmed by UV-Visible spectroscopy. FTIR study confirmed that the –C–O and –OH groups of thio glycerol can readily bind with CdS nanoparticles.

Keywords: CdCl₂, material behavior-XRD, microstructure, FESEM, UV-visible spectroscopy, FT-IR.

Received: 31 March 2020

Revised: 13 May 2020

1. Introduction

Nanotechnology is the most promising technology that can be applied in almost all spheres of life, ranging from pharmaceuticals, defense, electronics, transportation, heat transfer, as well as sports and aesthetics. Cadmium sulfide is one of the most studied materials, with a band gap of 2.43 eV and also these are ideal quantum confined semiconductors due to its optical and electronic properties [1]. For fabrication of p-n junction solar cells, CdS (n-type material) along with p-type materials like copper indium gallium diselenide (CIGS), copper zinc tin sulfide (CZTS), gallium arsenide (GaAs), indium phosphide (InP), cadmium telluride (CdTe) etc. have been used [2, 3]. Due to wide band gaps, CdS is used as window material carriers, which improve solar cell efficiency [4]. Also, it is primarily used in solar cell and a variety of electronic devices. The photoconductive and electroluminescent properties of cadmium sulfide have been applied in manufacturing a variety of consumer goods. CdS is an attractive visible-light photocatalyst because of its desired band gap, oxidation and reduction potential. CdS may also act as important sensitizers, which can sensitize the wide band gap semiconductor and this improves the photocatalytic activity and stability of the photocatalyst [5]. II–VI semiconductor nanoparticles are currently of great interest for their practical applications, such as zero dimensional quantum confined materials in light emitting diodes [6], photo detectors [7], FET [8], photoluminescence [9], infrared photo detector [10], and environmental and biological sensors [11]. There are many ways to prepare semiconductor nanoparticles, including some physical methods, such as low pressure, gas evaporation method, chemical methods such as settling, hydrolysis, hydrothermal, sol-gel, electric spark, sluggish precipitation [12]. Cadmium sulfide nanoparticles is an extremely insoluble and stable, so sulfide producing microorganisms can be used at contamination site to detoxify the heavy metals [13]. Apart from chemical synthesis, another well-known route for CdS nanoparticle synthesis is the biosynthesis of CdS nanoparticles, which can be carried out by using microorganisms, fungi and plants. In that synthesis, the microbes involved should isolate the Cd⁺² ions from their metal solution and accumulate them in a reduced state by different enzymes and metabolites secreted by their activity [13]. Various morphologies of CdS nanocrystals have been previously reported, such as flakes [14], spheres [15], dendrites [16] nanowires nanorods [17] and other structures were dominant.

The aim of present work is to prepare large scale cadmium sulfide nanoparticles using a simple chemical route and to investigate their microstructure and optical properties.

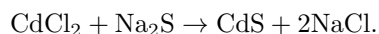
2. Experimental

2.1. Chemicals used

Cadmium (II) Chloride (CdCl_2 AR 99 % Pure), Sodium sulfide flakes Na_2S (99 % pure) from Vishal and 1-Thioglycerol ($\text{HSCH}_2\text{CH}_2\text{OH}$) from Loba Chem. of analytical grade, were purchased and used without further chemical treatment and purification. Na_2S and $\text{HSCH}_2\text{CH}_2\text{OH}$ were used as reducing agent. De-ionized water was prepared in our laboratory and it was used as solvent throughout the preparation.

2.2. Synthesis of cadmium sulfide nanoparticles

A 25 ml of 1 molar Cadmium (II) Chloride (CdCl_2 , AR 99 % pure) solutions was prepared by dissolving in de-ionized water. Solutions of 2.0 M Na_2S were prepared in 50 ml de-ionized water. A 25 ml of CdCl_2 solution were heated continuously at 90°C temperature under vigorous stirring on magnetic stirrer with heater (electrical/mechanic). 2.0 molar concentration of sodium sulfide (Na_2S) solution was added drop wise to formation of stoichiometry solution. Then, 1-thioglycerol was added to the reaction medium. Thioglycerol ($\text{HSCH}_2\text{CH}_2\text{OH}$) was used as a capping agent, leading to the formation of colloidally-stable CdS nanoparticles with controlled aspect ratios. Capping agent is widely used for preparation of nanoparticles because the hydroxyl group confers solubility in water and lowers the volatility. The heating and mixing continued till the color changed to gradually turned from light to dark yellow. The yellow product was collected by centrifugation at 5000 rpm for 20 minutes and washed three times with ethanol and double distilled water. Dark yellow color indicated the formation of fine nanoscale cadmium sulfide particles from thioglycerol-assisted reduction [18]. The obtained product was dried under IR lamp for few hours and sintered at 200°C in air for 1 hour. Various optimization studies were performed to investigate the size and shapes of CdS nanoparticles. The whole process was completed within 5 – 6 hours. Molar concentration ratio of solution was increased then large scale of nanoparticles was obtained. The chemical reaction is as follows:



2.3. Material characterization

The cadmium sulfide nanoparticles were characterized by X-ray diffraction technique [Bruker D-8 model, DMAX-2500, $\text{CuK}\alpha$ ($\lambda = 1.542 \text{ \AA}$) radiation] for structural analysis and determination of grain size for Bragg's angle (2θ) from 20 to 80 degree. The crystallites size was determined by using Debye Scherrer formula [19]:

$$D = \frac{0.9\lambda}{\beta \cos \theta}. \quad (1)$$

The dislocation density (δ) was calculated from equation:

$$\delta = \frac{n}{D^2}, \quad (2)$$

where n is a factor and D is the crystallite size [20].

RMS microstrain (ϵ) was determined using a Williamson and Hall plot. The slope of the plot of $\frac{\beta \cos \theta}{\lambda}$ versus $\frac{2 \sin \theta}{\lambda}$ gives the value of the RMS microstrain. The stacking fault probability was calculated from the peak shift using the following equation:

$$\therefore \alpha = \frac{2\pi^2 \Delta(2\theta)}{45\sqrt{3} \tan \theta(hkl)}. \quad (3)$$

The calculated values of lattice parameters for cubic crystal structure were estimated by using Nelson–Riley plots [20]:

$$\therefore f(\theta) = \frac{1}{2} \left[\left(\frac{\cos^2 \theta}{\sin \theta} \right) + \left(\frac{\cos^2 \theta}{\theta} \right) \right]. \quad (4)$$

The UV-visible optical absorption spectra were measured in the 200 – 400 nm range. A record spectrophotometer (JASCO UV-VIS-NIR Model No.V-670) was used for these optical measurements. The infrared spectrum was measured at room temperature in the wave number range 400 – 4000 cm^{-1} by a Fourier Transform infrared spectrophotometer (FT/IR-6100 Shimadzu). For that analysis, the samples were pulverized into fine powder and then mixed with KBr powder in a weight ratio of (1:100).

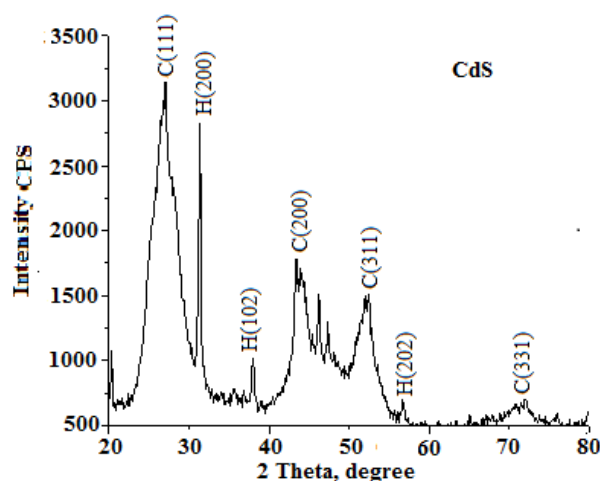


FIG. 1. XRD pattern of CdS nanoparticles sintered at 200 °C

3. Results and discussion

3.1. X-Ray diffraction (XRD)

Figure 1 shows an XRD pattern of CdS nanoparticles sintered at 200 °C plotted in the range 20 – 80 °.

In this pattern, the significantly broader hump and less intense peaks in the XRD pattern that were observed are indicative of the small size for the CdS nanoparticles and they are in agreement with small FWHM peaks. This also confirms the stoichiometric nature of nanoparticles. The line broadening of the peak was used to calculate the average crystallite size of the CdS nanoparticles using the Scherrer formula [19]. The XRD pattern shows number of peaks of CdS nanoparticles phases, indicating a face centered cubic structure for the cadmium sulfide [JCPDS Card No. 89-0440]. It contains a minor wurtzite hexagonal phase of CdS [JCPDS Card No. 80-006]. CdS phase was most often appear in synthesized colloidal CdS particles, but the macro scale phase of CdS is normally with the hexagonal structure [21]. I have been obtained cubic phase as well as minor hexagonal phase in the present preparation of CdS nanoparticles. The observed peaks show the presence of cadmium sulfide phases which match well with reported JCPDS data confirming pure CdS phase structure. The XRD pattern of the CdS nanoparticles exhibits prominent, broad peaks at 2θ values of 26.81, 31.32, 37.94, 43.96, 51.28, 58.89 and 71.22 which could be indexed to scattering from (1 1 1), (2 0 0), (1 0 2), (2 2 0), (3 1 1), (2 0 2), and (3 3 1) planes respectively of cubic and wurtzite hexagonal structure of CdS [22]. The higher peak intensities of the XRD pattern are due to the better crystallinity and larger grain size and can be attributed to particle agglomeration. It has been observed that (111) reflections are of maximum intensity, which indicates that CdS nanoparticles have a preferred orientation in the (111) plane. One shoulder sharp intense peak at 2θ value of 31.32 was identified scattering from (200) plane (JCPDS-010705-0581). The measured peaks are in good agreement with other studies.

It is evident from the following (Table 1) that the data obtained are well matched with the standard values of CdS crystal [23].

3.1.1. Nelson–Riley plots. The spacing between diffracting planes (d) of synthesized CdS nanoparticles was calculated from the Bragg equation

$$n\lambda = 2d \sin \theta.$$

Lattice parameter of the cubic ($a = b = c$) and hexagonal ($a = b \neq c$) crystal is calculated using the formula,

$$\frac{1}{d^2} = \frac{h^2}{a^2} + \frac{k^2}{a^2} + \frac{l^2}{a^2} \quad \text{and} \quad \frac{1}{d^2} = \frac{h^2}{a^2} + \frac{k^2}{a^2} + \frac{l^2}{c^2},$$

where, d is the atomic lattice spacing, h , k and l are miller indices; a is the lattice parameter of the crystal. Crystal lattice parameter and cell volume of cubic and hexagonal structure of CdS was observed from XRD pattern. It was found to be 5.8168 & 5.1506 Å and 196.81 and 108.89 Å³ respectively. The calculated values of the lattice parameters for cubic crystal structure were estimated by using Nelson–Riley plots [24].

Figure 2 shows the Nelson–Riley curve was plotted of error function by the extrapolation $f(\theta)$ against lattice parameter (a) for cubic and hexagonal (c) crystal were obtained. By using eq. (4), the extrapolation $f(\theta)$ was calculated. The corrected values of lattice parameter were estimated for cubic (a) and hexagonal (c) crystal is 5.760 and 5.198 Å.

TABLE 1. Observed and calculated diffraction angles, d-spacing, crystallite size with (hkl) planes cadmium sulfide nanoparticles

Observed diffracting angle (2θ) degrees	Calculated diffracting angle (2θ) degrees	Observed d-Spacing in Å	Calculated d-Spacing in Å	hkl (Planes)	Crystallite size in nm	Lattice parameter of the crystal (a)
26.81	28.22	3.3214	3.3257	C(111)	38.55	5.7603
31.32	32.51	2.8644	2.8562	H(200)	43.92	5.4817
37.94	36.62	2.3660	2.3718	H(102)	50.95	3.9655
43.96	44.22	2.0598	2.0595	C(220)	51.63	5.8251
51.28	52.10	1.7336	1.7817	C(311)	46.60	5.9092
58.89	58.27	1.5499	1.5684	H(202)	48.56	4.7722
71.22	72.71	1.3187	1.3244	C(331)	41.33	5.7729

The lattice parameters corresponding to each peak reflections were plotted against a Nelson–Riley function and the precise lattice parameter were taken from the intercept out of linear fit. The Nelson–Riley curve showed a high quality of crystallization of CdS nanoparticles. They are in good agreement with the results of JCPDS data.

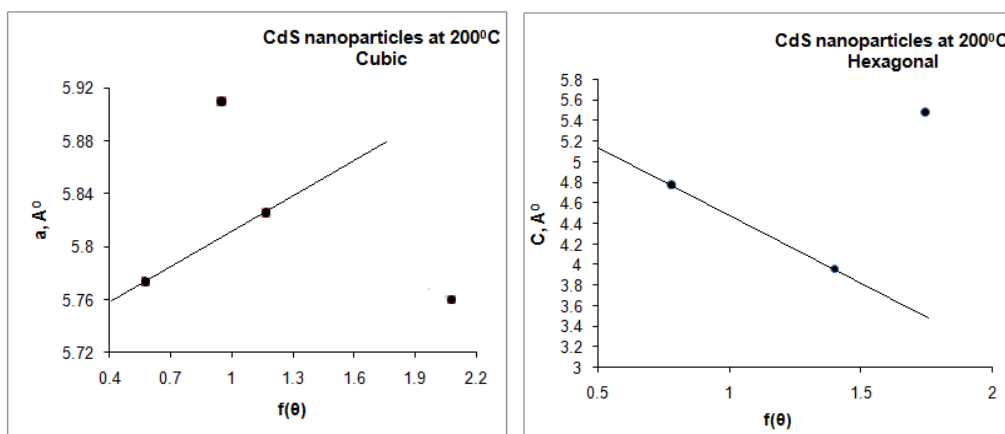


FIG. 2. Nelson–Riley plot for lattice parameters for CdS nanoparticles synthesized by simple chemical route

When the temperature is increased, crystallinity tends to increase with decrease in lattice constant ($a = 6.29, 5.88, 5.87$ and 5.85 Å) and increase in the particle size [25]. Particle growth usually occurs via the mechanism of Ostwald ripening. Larger particles grow on account of dissolution of smaller ones. As a result, the particle size increases continuously during the growth as temperature increases [26].

3.1.2. Dislocation density. The dislocation density is the length of dislocation lines per unit volume of the crystal this means crystallographic defect with in a structure of crystal which contains an abrupt change in the arrangement of atoms. In the literature, dislocation strongly influences many of the properties of materials, such as slip, surfaces, interfaces, irradiation, pining, climb etc.

The X-ray diffraction pattern of CdS analysis has been used to determine the dislocation density. Accordingly, it was observed that the crystallite size of the CdS nanoparticles is inversely proportional to dislocation density. The dislocation density was calculated using Williamson and Smallman's equation (2). The dislocation density for the synthesized CdS nanoparticles was estimated to be $0.4989 \times 10^{15} \text{ m}^{-2}$. Fig. 3 shows variation of crystallite size with dislocation density of the CdS nanoparticles sintered at 200°C .

3.1.3. RMS Microstrain (ϵ). X-ray diffraction line broadening profile is mainly caused by non-ideal optics of the instrument and microstructure imperfections in the crystals. The micro structural line broadening can be subdivided

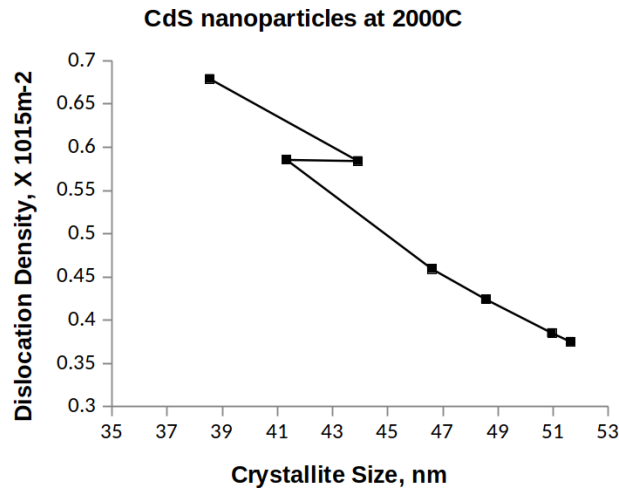


FIG. 3. Variation of dislocation density against crystallite size of CdS nanoparticles

into size broadening and strain broadening [27]. Fig. 4(a) shows the plot of $\beta \cos \theta$ against $2 \sin \theta$ with different deformations at ambient air. The points in the W–H are scattered, which is attributed to line broadening is termed anisotropic. $\beta \cos \theta$ is not a monotonic function of $2 \sin \theta$. The RMS microstrain introduced in the sample is possibly due to stacking fault within the crystallites. Since the preparation of nanoparticles is carried out at 90 °C aerobically, some stress is expected to be introduced, which can result in stacking fault. The microstrain from the Williamson and Hall regression is satisfied because the plots have completely seen distributed in the whole of the graphic. The precise RMS microstrain was taken from the intercept out of linear fit. The value of RMS microstrain is on the lower side compared to that reported 0.4944 by chemical precipitation technique. It was possibly due to large value of average crystallite size (~50 nm) of the powder samples [28].

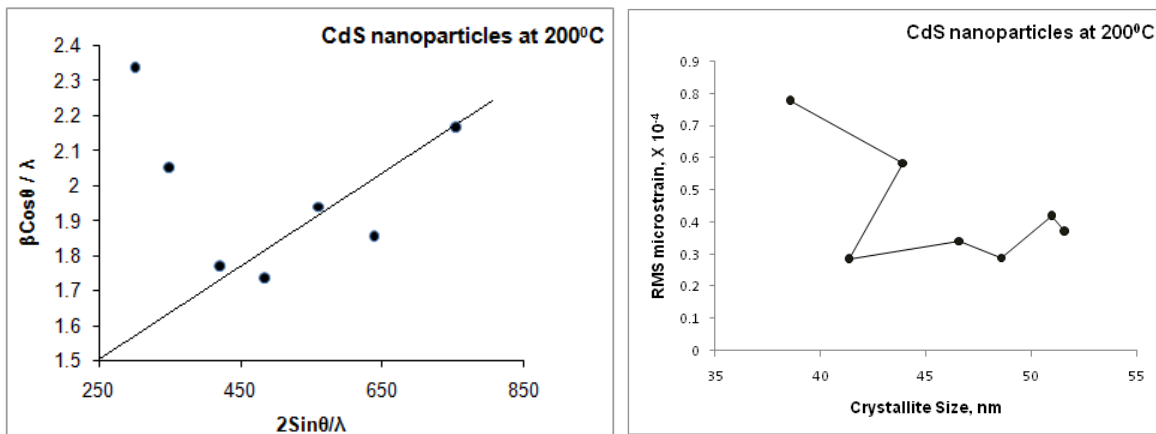


FIG. 4. $\beta \cos \theta$ against $2 \sin \theta$ of CdS nanoparticles (Williamson–Hall plots) (a) and microstrain against crystallite size of CdS nanoparticles (b)

The Williamson–Hall method is one of the simplest methods which clearly differentiates between size-induced and strain-induced peak broadening by considering the peak width as a function of $2\theta(hkl)$. These estimated values of microstrain indicate a decreasing trend with increases crystallite size with diffraction angle in X-ray diffraction line broadening profile [29] as shown in Fig. 4(b). The calculation of RMS micro strain was done by Williamson–Hall method.

Microstructure parameters of CdS nanoparticles powder sample as shown in Table 2.

3.1.4. Stacking Fault Probability (α). A stacking fault is a planar imperfection that arises from the stacking of one atomic plane out of sequence with another while the lattice on either side of the fault is perfect. The defect is associated with shifting of the planes two theta values of X-ray diffraction profile. It arises when one atomic plane sets out of series than others to start piling up; on the other hand lattice remains surpassing. Due to stacking fault only the

TABLE 2. Microstructure parameters of cadmium sulfide nanoparticles powder sample

Observed diffraction angle (2θ) degrees	Calculated diffraction angle (2θ) degrees	hkl (Planes)	Crystallite size, nm (D)	Dislocation density, m^2 (δ) $\times 10^{15}$	Stacking fault probability α	RMS micro strain (e) $\times 10^{-4}$
26.81	28.22	C(111)	38.55	0.67901	0.47640	0.77644
31.32	32.51	H(200)	43.92	0.58413	0.34231	0.58530
37.94	36.62	H(102)	50.95	0.38522	0.30966	0.41894
43.96	44.22	C(220)	51.63	0.37514	0.05194	0.36940
51.28	52.10	C(311)	46.60	0.45931	0.13777	0.34185
58.89	58.27	H(202)	48.56	0.42407	0.08855	0.29066
71.22	72.71	C(331)	41.33	0.58542	0.16774	0.28448

position of peak shows variation from JCPDS for its corresponding sample [30]. The stacking fault probability was calculated using eq. (3). Some of the observed peak broadening can be attributed to fine crystallite size and micro strain effects, anomalous plane (hkl) dependent peak broadening and peak shifts are clearly associated with stacking faults. Whenever the observed value of stacking fault is higher in a particular material then the exact cross slip dislocation can be found. The presence of stacking faults gives rise to a shift in the peak positions of different reflections with respect to ideal positions of a fault free sintered sample [31, 32]. The optimized synthesized conditions preferred plane orientation of CdS nanoparticles with larger crystallite size, lower RMS strain, dislocation density and stacking fault probability are obtained. Fig. 5 represent variation of RMS strain, dislocation density, stacking fault probability with diffraction angle of CdS nanoparticles sample at 200 °C.

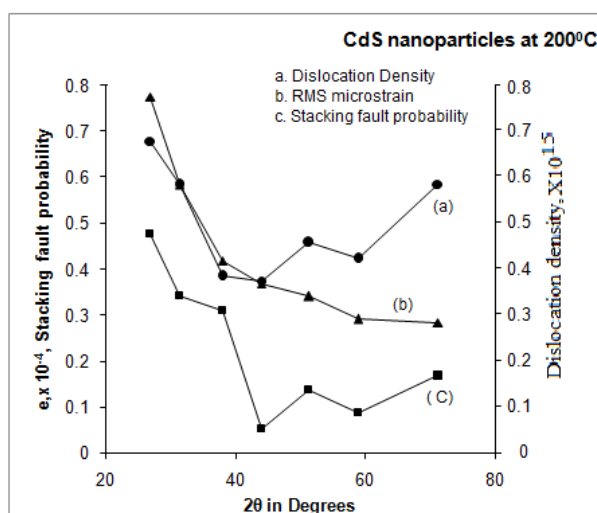


FIG. 5. Variation of RMS strain, dislocation density, stacking fault probability with diffraction angle (2θ) of CdS nanoparticles at 200 °C

Figure 6 shows the FESEM image of CdS nanoparticles sintered at 200 °C. The FESEM micrograph clearly illustrates the formation of sub-micrometer crystallites distributed over the surface. Agglomeration of large crystallites also seems to be present in overall regions on the surface of the sample. The average particle size evaluated from FESEM micrograph was found to 74.07 nm.

3.2. UV-visible spectrophotometer analysis

The UV-visible optical absorption spectra were recorded at room temperature from a double beam spectrophotometer in the range 200 – 800 nm. A record spectrophotometer (JASCO UV-VIS-NIR Model No.V-670) was used for these optical measurements of cadmium sulfide nanoparticles. Fig. 7 shows absorption in the near UV region

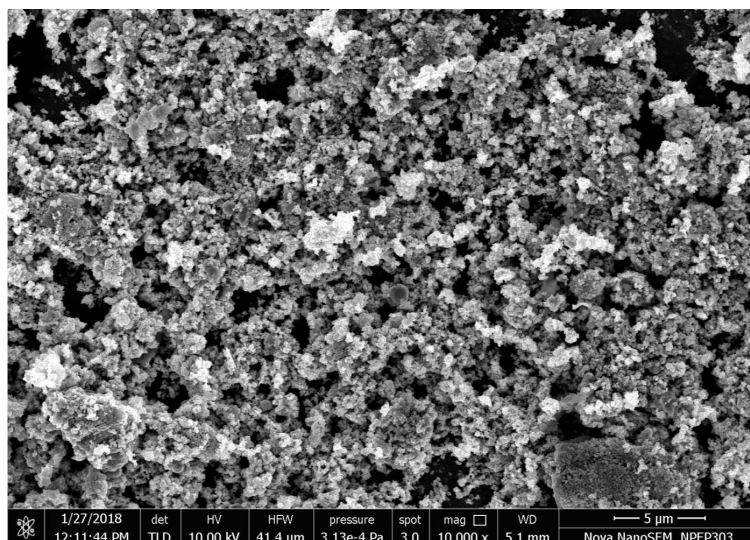


FIG. 6. FESEM image of CdS nanoparticles sintered at 200 °C

arises from electronic transitions associated with in the powder sample. As synthesized CdS nanoparticles sintered at 200 °C, it exhibits a strong absorption band at wavelength near 225 nm with the absorption edge at about 359 nm.

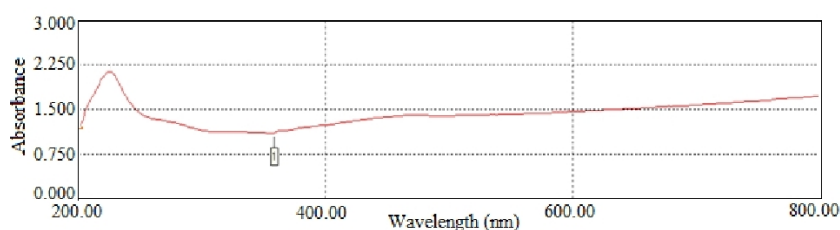


FIG. 7. Optical absorption spectra of CdS nanoparticles sintered at 200 °C

The UV-absorption ability of cadmium sulfide is related with band gap energy. The optical band gap energy was calculated from the dependence of the absorption coefficient on the photon energy using the Tauc relation $(\alpha h\nu) = A(h\nu - E_g)^n$, where A is Tauc's constant, which is a characteristic parameter independent the photon energy, E_g is the band gap of the material. The exponent n depends on the type of transition, for that, it takes values for Direct ($n = 1/2$), indirect ($n = 2$), direct forbidden transition ($n = 3/2$) and forbidden indirect transition ($n = 3$). As a semiconductor, cadmium sulfide has direct allowed transitions, accordingly $n = 1/2$ is chosen [33]. The band gap energy followed direct transition of CdS nanoparticles sintered at 200 °C was found to be 3.45 eV and it was compared with the bulk cadmium sulfide $E_g = 2.42$ eV. It indicates the absorption position depends on the morphologies and crystallite size of CdS. Also, the crystallite size is directly related to the absorption wavelength, As a result, the band gap of the CdS nanoparticles increases, causing a blue-shift in the UV-vis absorption spectra. The band gap energy of CdS nanoparticles has been reported with $E_g = 3.46$ eV [34].

The refractive index of the cadmium sulfide powder sample was calculated using the Herve-Vandamme formula:

$$n = \left[1 + \left(\frac{P}{E_g + Q} \right)^2 \right]^{1/2},$$

where $P = 13 \cdot 6$ eV and $Q = 3 \cdot 4$ eV is standard constant values. The refractive index gives information about vacancies present in the CdS nanoparticles and defines the measurement of density that is, a decrease in the refractive index means a decrease in the material density in the CdS sample. The refractive index of the CdS nanoparticles was found to be 2.22.

3.3. FT-IR spectrophotometer analysis

The infrared spectrum of synthesized cadmium sulfide nanoparticles as in the range of wave number 400 – 4000 cm^{-1} , which identifies the functional groups and chemical bond in the synthesized compound. The infrared

spectra of cadmium sulfide nanoparticles are represented in Fig. 8. The large broad band at 3504 cm^{-1} is ascribed to the O–H stretching of the adsorbed moisture on the cadmium sulfide surface [35]. The bands appearing at 2970 and 2160 cm^{-1} correspond to C–H stretching and bending vibrations. The absorption is sharp and strong peak around 1620 cm^{-1} is assigned to the symmetric bending vibration of the water molecules [36].

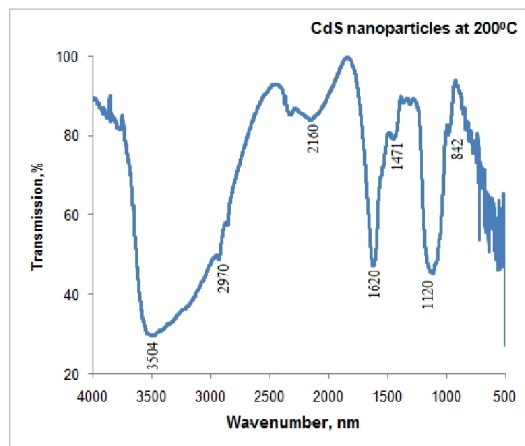


FIG. 8. FTIR of CdS nanoparticles sintered at $200\text{ }^{\circ}\text{C}$

The band at 1471 cm^{-1} is assigned to H–O–H characteristics. The Peak at 1125 cm^{-1} assigned to C–O stretching vibration. This band arises from C–O linkage stretching and C–O–H bending vibrations [37]. The bands located at around 750 cm^{-1} have been attributed to the CO_2 asymmetric stretching vibration. The strong absorption band located at $670 - 470\text{ cm}^{-1}$ was assigned to the Cd–S stretching vibration mode, which confirms the formation of cadmium sulfide [38]. These observations convincingly support template role in thioglycerol in the control of the size of CdS particles. The IR study confirms that the –C–O and –OH groups of thioglycerol can readily bind with CdS nanoparticles [39].

4. Conclusion

Large scale CdS nanoparticles were synthesized by a low cost simple chemical route. The XRD results showed that there was a transformation from a cubic to a hexagonal crystalline phase. The observed d-spacing values were found to be in good agreement with the JCPDS data for cubic and hexagonal cadmium sulfide. This clearly indicated that the prepared material is CdS with cubic and hexagonal structure. The W–H plots showed the size and nature of the strain incorporated in peak broadening of X ray diffraction peaks. The optimized synthetic conditions to CdS nanoparticles with larger crystallite size, lower RMS strain, dislocation density and stacking fault probability were obtained. The refractive index of the CdS nanoparticles was estimated to 2.22. The band gap energy followed direct transition of CdS nanoparticles sintered at $200\text{ }^{\circ}\text{C}$ was found to be 3.45 eV. FTIR study confirms that the –C–O and –OH groups of thioglycerol can readily bind with CdS nanoparticles. The quality and particle size obtained in our CdS nanoparticles suggest that they are suitable for various applications, such as the detection and treatment of cancer and other diseases and for air and water purification.

Acknowledgements

The author thanks the management authorities of M. G. Vidyamandir's Panchavati Nasik for providing all the required Laboratory and infrastructural facilities for doing this work.

References

- [1] Cao Y., Pengfei H., Dianzeng J. Phase and shapecontrolled hydrothermal synthesis of CdS nanoparticles and oriented attachment growth of its hierarchical architectures. *Applied Surface Science*, 2013, **265**, P. 771–777.
- [2] Kumar V., Suryakarthick R., et al. Effect of precursor concentration on the properties and tuning of conductivity between p-type and n-type of $\text{Cu}_{1-x}\text{Cd}_x\text{S}_2$ thin films deposited by single step solution process as a novel material for photovoltaic application. *RSC Advances*, 2015, **5**, P. 23015–23021.
- [3] Aruna Devi R., Latha Z., et al. Synthesis and Characterization of Cadmium Sulfide Nanoparticles by Chemical Precipitation Method. *Journal of Nanoscience and Nanotechnology*, 2015, **15**, P. 8434–8439.
- [4] Singh V., Sharma P., Chauhan P. Synthesis of CdS Nanoparticles with Enhanced Optical Properties. *Materials Characterization*, 2011, **62**, P. 43–52.

- [5] Liu Q., Qi Y., Zheng Y., Song X. Synthesis and enhanced photo catalytic activity of g-C₃N₄ hybridized CdS nanoparticles. *Bulletin of Materials Science*, 2017, **40**, P. 1329–1333.
- [6] Shrivastav D., Hrivastaval Malik M. Enhancing efficiency of organic light emitting diodes through doping of cadmium sulphide nanocrystals and Application. *International Journal of Nanotechnology and Application*, 2014, **4** (4), P. 1–6.
- [7] Nassr I., Najm K., et al. Highly selective CdS: Ag heterojunction for photodetector applications. *AIP Conference Proceedings*, 2019, **2123**, 020031.
- [8] Hetsch F., Zhao N., Kershaw S., Rogach A. Quantum dot field effect transistors. *Material today*, 2013, **16** (9), P. 312–325.
- [9] Lee H., Issam A., et al. Synthesis and Characterizations of Bare CdS Nanocrystals Using Chemical Precipitation Method for Photoluminescence Application. *Journal of Nanomaterials*, 2009, 914501.
- [10] Mahsa A., Naader A. Highly photosensitive near infrared photodetector based on polypyrrole nanoparticle incorporated with CdS quantum dots. *Materials Science in Semiconductor Processing*, 2020, **111** (1), 104964.
- [11] Wilson D., Shepherd L. Chemical and biological sensors for environmental monitoring. *IEEE International Symposium on Circuits and Systems*, Seattle, WA, 2008, P. 1990–1993.
- [12] Liu Z., Wang R., Khan F. Jiang F. Synthesis and characterization of TiO₂ nanoparticles. *Asian Journal of Chemistry*, 2014, **26** (3), P. 655–659.
- [13] Kowshik M., Deshmukh N., et al. Microbial Synthesis of Semiconductor CdS Nanoparticles, Their Characterization, and Their Use in the Fabrication of an Ideal Diode. *Biotechnology and Bioengineering*, 2002, **78** (5), P. 583–588.
- [14] Kadam A., Dhabbe R., Kokate M., Garadkar K. Room temperature synthesis of CdS nanoflakes for photocatalytic properties. *Journal of Materials Science Materials in Electronics*, 2014, **25** (4), P. 1887–1892.
- [15] Gaur R., Jeevanandam P. Effect of anions on the morphology of CdS nanoparticles prepared via thermal decomposition of different cadmium thiourea complexes in a solvent and in the solid state. *New Journal of Chemistry*, 2015, **39** (12), P. 9442–9453.
- [16] Gu Li. Fabrication of 2D and 3D dendritic nano architectures of CdS. *Transactions of Nonferrous Metals Society of China*, 2008, **18** (4), P. 904–907.
- [17] Fernando V., José L., Fierro G., Yerga R. From Nanorods to Nanowires of CdS Synthesized by a Solvothermal Method: Influence of the Morphology on the Photoactivity for Hydrogen Evolution from Water. *Molecules*, 2016, **21** (4), P. 401.
- [18] Devi R., Latha M., et al. Synthesis and Characterization of Cadmium Sulfide Nanoparticles by Chemical Precipitation Method. *Journal of Nanoscience and Nanotechnology*, 2015, **15**, P. 8434–8439.
- [19] Cullity B. *Elements of X-ray diffraction*. Addison-Wesley Publishing Co., 1956.
- [20] Kumar B., Hymavathia B., Subba Rao T. Investigations on physical properties of nanostructured ZnTe thin films prepared by DC reactive magnetron sputtering. *Chalcogen. Lett.*, 2014, **11** (10), P. 509–517.
- [21] Yang J., Zeng J., et al. Formation Process of CdS Nanorods via Solvothermal Route. *Chem. Mater.*, 2000, **12** (11), P. 3259–3263.
- [22] Bially E., Seoudi R., et al. Preparation, Characterization and Physical Properties of CdS nanoparticles with Different Sizes. *Journal of Applied Sciences Research*, 2012, **8** (2), P. 676–685.
- [23] Sama S., Rayarb S., Selvarajanc P. Effect of annealing and dopants on the physical properties of CdS nanoparticles. *Journal of Chemical and Pharmaceutical Research*, 2015, **7** (3), P. 957–963.
- [24] Veerabhadrayya M., Kumari R. Structural Study of Tin Oxide Nanopowders Prepared by Jaggery Mediated Gel Combustion Method. *textit-International Journal of Advanced Scientific Research and Management*, 2019, **4** (7), P. 53–57.
- [25] Kumar S., Chawla A., Kumar N., Chandra R. High temperature powder diffraction study of (Zn, Cd)S and Zn_xCd_{1-x}S nanopowders. *RSC Adv.*, 2011, **1**, P. 1078–1082.
- [26] Aruna Devi R., Latha Z., et al. Synthesis and Characterization of Cadmium Sulfide Nanoparticles by Chemical Precipitation Method. *Journal of Nanoscience and Nanotechnology*, 2015, **15**, P. 8434–8439.
- [27] Garde A., Borse R. Effect of firing temperature on the composition and micro structural parameters of screen printed SnO₂ Thick film resistors. *Sensors and Transducers Journal*, 2010, **113** (2), P. 95–106.
- [28] Singh V., Chauhan P. Structural and optical characterization of CdS nanoparticles prepared by chemical precipitation method. *Journal of Physics and Chemistry of Solids*, 2009, **70**, P. 1074–1079.
- [29] Patra S., Mitra P., Kumar S., Pradhan. Preparation of nano dimensional CdS by chemical dipping technique and their characterization. *Materials Research*, 2011, **14** (1), P. 17–20.
- [30] Warren B. X-Ray Measurement of Stacking Fault Widths in fcc Metals. *Journal of Applied Physics*, 1961, **32**, P. 2428.
- [31] Frank W., Francis G., Biancaneillo S. Stacking faults and crystallite size in mechanically alloyed Cu–Co. *Nano structured materials*, 1995, **6** (1–4), P. 429–432.
- [32] Thanikaikarasan S., Mahalingam T., Raja M., Kim T. Characterization of electroplated Fe Se thin films. *J. Mater. Sci.: Mater. Electron*, 2009, **20**, P. 727–734.
- [33] Kamble M., Rondiya S., et al. Optical, structural and morphological study of CdS nanoparticles: role of sulfur source. *Nanomaterials and Energy*, 2020, **9** (1), P. 72–81.
- [34] Lavand A.B., Malghe Y.S. Visible light photocatalytic degradation of 4-chlorophenol using C/ZnO/CdS Nanocomposites. *Journal of Saudi Chemical Society*, 2015, **19** (5), P. 471–578.
- [35] Verma A., Chandra P., Srivastava A., Shukla R. Optoelectronic studies of commercially and lab prepared cadmium sulfide chalcogenide. *Research & Reviews. Journal of Material Sciences*, 2017, **5** (2), P. 28–34.
- [36] Rao G., Babu B., Stella R. Synthesis and characterization of VO₂⁺ doped ZnO–CdS composite nanopowder. *Journal of Molecular Structure*, 2015, **1081**, P. 254–259.
- [37] Seoudi R., Allehyani S., et al. Preparation, Characterization and Size Control of Chemically Synthesized CdS Nanoparticles Capped with Poly (ethylene glycol). *Journal of Electronic Materials*, 2015, **44**, P. 3367–3374.
- [38] Terrazas E.C., Ambrosio R., González M. A simple method for the synthesis of CdS nanoparticles using a novel surfactant. *Chalcogenide Letters*, 2015, **12** (4), P. 147–153.
- [39] Devamani R., Alagar M. Synthesis and characteristics of copper (II) Phosphate nanoparticles. *Elixir Nanotechnology*, 2013, **61**, P. 16917–16921.

Comparative evaluation for wound healing potentials of bulk and nano forms of zinc oxide ointment

V. Gupta^{1*}, P. K. Verma², A. Gupta³, V. Kant⁴, P. Kumar⁵, M. Sharma¹

¹Department of Chemistry, University of Jammu, India

²Division of Pharmacology & Toxicology, SKUAST-Jammu, J&K, India

³Department of Physics, University of Jammu, J&K, India

⁴Division of Pharmacology & Toxicology, IVRI, Bareilly, UP, India;

Presently: Department of Vety Pharmacology & Toxicology, LUVAS, Hisar, India

⁵Department of Pathology, IVRI, Bareilly, UP, India

*vijaytalgupta@gmail.com

DOI 10.17586/2220-8054-2020-11-4-453-461

Development of nanotechnology has led to massive breakthroughs in the area of wound healing. Recently, metal oxide nanoparticles have shown a broad range of applications in biomedical fields. The lack of potent healing agents for complicated wounds and healing potentials of zinc oxide (ZnO) motivated us to evaluate the wound healing potentials of nano ZnO in comparison to its bulk form in rats. In the present study, single open excision wounds ($2 \times 2 \text{ cm}^2$) were created on the backs of fifteen rats and divided into Group I, II and III. On the wounds of group I, II and III, topical application of ointment base, bulk ZnO (20 %) and ZnO nanoparticles (2 %) was done for 14 days, respectively. Significantly smaller wound area and increased percent wound contraction was evident in the ZnO nanoparticles-treated group. Histopathological analysis revealed that the ZnO nanoparticle-treated wounds possessed reduced numbers of fibroblasts and blood vessels. However, collagen fibers in ZnO treated group were compactly arranged in thick bundles with a well-organized manner and orientation. The newly formed epithelial layer was also covering more area of healing tissue in the ZnO nanoparticle-treated group. The ZnO nanoparticle-treated group also revealed the higher overall wound maturity score, as compared to other groups. In view of this, it might be concluded that topical application of ZnO nanoparticles (2 %) caused faster wound healing and the healing was better than bulk ZnO treatment, even at ten-fold lower concentration.

Keywords: Zinc oxide, nanoparticles, wound healing, collagen, epithelial layer, rats.

Received: 19 April 2020

Revised: 1 May 2020

1. Introduction

During the last few years, nanotechnology has become an emergent interdisciplinary field of research by combining the material science, bio-nanoscience, and technology. It has been considered as the technological innovation of the 21st century. Nanotechnology involves the design, characterization, synthesis and application of different materials, structures, devices and systems by controlling their shape as well as size at the nanometer scale. Research and development in this field at various levels are increasing rapidly. Engineered nanoparticles are key constituents of the nanotechnology industry and number of consumer products containing nanoparticles is rapidly increasing. Nanoparticles have greater potential to cross biological barriers to reach pulmonary connective tissues, lymphatics, blood circulation and critical organs in comparison with micron-sized particles [1–3]. Their smaller size and large surface area also enhance their ability to enter into cells and become more biologically active [4–6]. Nanotechnology has shown tremendous broad application in many fields, including medicine. This technology has become the forefront of research and possesses tremendous potential to revolutionize the medical sector.

Currently, impaired wound healing in humans and animals has become a big challenge in medical and veterinary fields. Although wound healing is a natural phenomenon, the conversion of an acute wound to a chronic wound can occur due to the persistence of chronic conditions (diabetes mellitus, venous stasis ulcers, skin ulcers etc.) resulting in difficulties for wound management. The prevalence of patients with chronic wounds has increased sharply in recent years. The probabilities of occurring of cutaneous wounds are more, as skin is vulnerable to a variety of external factors and resulting in different types of skin damage. The available traditional therapies generally involve high cost and long-lasting treatments with an ulcer relapse rate of above 70 % [7]. Significant efforts have been made towards wound care management in recent years for framing the new therapeutic approaches and technologies, however, satisfactory results have still not been achieved. The innovative and impressive development of nanotechnology has led to massive growth in the direction of nano-drug delivery systems for wound healing and skin regeneration. Additionally, nanoparticles of metals and their oxides have emerged in recent years with a broad range of applications in biomedical field

including antibacterial, anticancer drug/gene delivery, cell imaging, biosensing, transdermal antibiotic patches, cosmetics etc. [8]. It has been observed that nanoparticle of metals and their oxides can exhibit unique functions, which are not observed in bulk phases. In recent years, some studies have revealed the wound healing of many compounds, including metals and their oxides. Application of silver nanoparticles to wounds showed that healing times were less when compared to another standard drug (Povidone-iodine) [9]. Copper nanoparticles have shown acceleration of wound healing via promotion of skin cell migration, proliferation, and neovascularization [19]. Copper nanoparticle-embedded hydrogels have also displayed promising potential for skin tissue regeneration [11]. Thrombin-conjugated iron oxide nanoparticles have caused the enhancement of incisional wound healing [12]. Recently, curcumin nanoformulation enhanced wound repair by inhibiting the inflammatory response, stimulating angiogenesis, inducing fibroblast proliferation as well as enhancing reepithelization and collagen synthesis [13].

Zinc (Zn) is one of the most abundant metallic elements in the body after iron. Zinc regulates DNA synthesis, normal growth, brain development, behavioral responses, reproduction, membrane stability, bone formation, wound healing etc. [14]. Zinc oxide (ZnO) is widely used in several products such as paints, coatings and cosmetic products [15, 16]. ZnO has been declared as "Generally Recognized as Safe" (GRAS) by the US Food and Drug Administration (21, CFR 182, 8991). In zinc-deficient rats, reduced granulation tissue deposition, decreased tensile strengths and delayed wound closure rates have been observed [17, 18]. Zinc has shown to accelerate the wound healing process when applied on open wounds [19]. Additionally, zinc administered topically appears to be beneficial for healing than given orally [20]. Recently, nano ZnO has also been widely researched as potent compound for biological applications due to its excellent antimicrobial, anti-inflammatory and angiogenic properties [21]. ZnO nanoparticles are also considered comparatively inexpensive and somewhat less toxic than other metal oxide nanoparticles. To the best of our knowledge, comparative wound healing studies of bulk and nano ZnO are very limited to claim the better potential of nanoformulation of ZnO. In view of this, the present study was planned to evaluate the wound healing potential of ZnO nanoparticles in comparison to its bulk form.

2. Materials and method

2.1. Chemicals used

All the chemicals used in this study were of analytical grade and used as received without further purification. Zinc acetate and sodium hydroxide were used for the preparation of ZnO nanoparticles, and were purchased from Sigma Aldrich, USA. The ZnO extrapure (99.5 %; Catalogue number: 67062) of analytical grade was purchased from Sisco Research Laboratories (SRL), New Delhi, India. Other chemicals like formaldehyde, acetone, acetic acid, ethanol, white petroleum jelly, xylene etc were also purchased from SRL. Hematoxylin stain, Eosin stain, Biebrich scarlet stain, phosphomolybdic acid, aniline blue etc. were purchased from Himedia, Mumbai, India.

2.2. Synthesis and characterization of ZnO nanoparticles

Zinc acetate [$\text{Zn}(\text{CH}_3\text{COO})_2 \cdot 2\text{H}_2\text{O}$] and sodium hydroxide were the precursors used in the synthesis of ZnO nanoparticles. The ZnO nanoparticles were prepared as per the method described by Rezende et al. [22]. Briefly, an aqueous solution of zinc acetate (0.5 M) was kept on magnetic stirrer at 80 °C for one hour for complete dissolution. Thereafter, aqueous solution of NaOH (2.5 M) was added under high speed and constant stirring. The addition was dropwise (slowly for 45 min) and touching the walls of the vessel till the pH reaches to 12. The reaction was kept for 2 hrs after complete addition of sodium hydroxide. After the completion of reaction, the solution was maintained overnight and the supernatant solution was separated carefully on next day. The remaining solution was centrifuged for 10 min, and the precipitate was removed. Thus, precipitated ZnO nanoparticles were washed three times with triply distilled water and ethanol to remove the byproducts which were bound with the precipitate and then dried in oven at about 60 °C. The white powder obtained is subjected to calcinations at 600 °C for 3 hours. Characterization of synthesized ZnO nanoparticles was carried out by using particle size analyzer (PSA), transmission electron microscopy (TEM) and scanning electron microscopy (SEM). The particle size distribution (PSD) analysis of the synthesized nanoparticles was done by using Malvern Instruments Zetasizer Nano-ZS instrument. The size and morphology of nanoparticles was determined by using Transmission Electron Microscope [Hitachi (H-7500) microscope] operating at 80 kV. The morphology of the particles was observed by a scanning electron microscope (SEM-EDS) using SEM (make JEOL Model JSM-6390LV).

2.3. Preparation of ointments

The ointment base was prepared by mixing the hard paraffin (5 %), soft paraffin (90 %) and lanolin (5 %) by the fusion method. The ointments of bulk ZnO (20 %) and ZnO nanoparticles (2 %) were prepared in this ointment base

by the incorporation method. The prepared ointment base, bulk ZnO ointment and ointment of ZnO nanoparticles were stored at 4 °C till further uses for wound healing studies.

2.4. Cutaneous wound healing study

(a) Wound creation and grouping

Fifteen healthy male Wistar rats (140 – 160 g; 8 – 10 weeks of age) were used in this study. The overnight-fasted rats were anesthetized by intraperitoneal (i.p.) injection of ketamine (50 mg/kg, i.p.) + xylazine (5 mg/kg, i.p.) combination. After achieving the anesthesia, dorsal skin of the rats was shaved and cleaned with 70 % ethanol. After this, a square shaped $2 \times 2 \text{ cm}^2$ ($\approx 400 \text{ mm}^2$) full thickness excision cutaneous wound was created on the back (thoraco-lumber) region. Each operated rat was housed separately in disinfected cages. Surgically wounded rats were equally divided in three groups (five each). *Ad libitum* access to feed and water, 12-hour light-dark cycle and adequate ventilation was provided to rats throughout the entire experiment. The temperature of the experimental room was maintained between 22 – 26 °C during the whole experiment. The details of three groups are given below:

Group I (Control or ointment base-treated): Ointment base was applied topically once daily for 14 days.

Group II (Bulk ZnO-treated): Bulk ZnO (20 %) in ointment base was applied topically once daily for 14 days.

Group III (Nano ZnO-treated): ZnO nanoparticles (2 %) in ointment base was applied topically once daily for 14 days.

The different ointments applied in above mentioned groups were just smeared on the wound area.

(b) Photography of wounds and calculation of wound area as well as percent wound contraction

Photography of each wound was done on days 0, 3, 7 and 14 post-wounding to assess the gross changes in the wounds after different treatments. Each wound margins was traced on a transparent paper with the help of fine tip permanent marker. The area (in mm^2) within the boundaries of each wound tracing was determined planimetrically. The wound area on 0 day of each animal was measured at a predetermined time interval starting at 3 h post-wounding. Thereafter, subsequent measurements of wound areas of all the groups were taken on day 3, 7 and 14 post-wounding. The result of wound measurements was expressed as absolute values and relative values or per cent wound contraction. The absolute values are actual measurements of wounds obtained at each given interval, whereas in relative values the wound contraction is expressed as per cent values of the 0-day measurements and was calculated by Wilson' formula as follows:

$$\% \text{ wound contraction} = \frac{0 \text{ day wound area} - \text{wound area on particular day}}{0 \text{ day wound area}} \times 100.$$

(c) Collection of tissue

Healing tissue of each animal of all the groups was collected under intramuscular general anesthesia (xylazine + ketamine combination). A portion of collected tissue was immediately preserved in 10 % formalin for histopathological studies.

(d) Histopathology

Hematoxylin and Eosin (H&E) staining and scoring:

The collected formalin-fixed tissues were embedded in paraffin wax. Thereafter, approximately 6 μm thick tissue sections were cut. The H & E staining of one set of tissue sections were done for each rat of all groups as per standard method. The stained sections were analyzed and scored under a light microscope at different magnifications. Scoring for the inflammatory cells [23], epithelialization [24] and overall wound maturity [25,26] was done as per the standard methods. Scoring for blood vessel density was done by counting the number of blood vessels in 35 random fields at higher magnification (40 \times). The histopathological properties of different tissue sections and scoring were blindly done.

Masson's trichrome staining for collagen:

The evaluation of collagen synthesis in the healing tissues was determined by using the Masson's trichrome stain. Masson's trichrome staining of each tissue section was done as per standard method. The stained sections were analyzed under a light microscope at different magnifications. In this staining, nuclei stained black; cytoplasm, muscles and erythrocytes as red and collagen stained blue.

2.5. Statistical analysis

Data were analyzed by one and two way analysis of variance (ANOVA) followed by Bonferroni's post-test using the GraphPad Prism v4.03 software program (San Diego, CA, USA). The differences between the different treatment groups were considered statistically significant at $P \leq 0.05$ or lower. All data were expressed as mean \pm standard error of mean (S.E.M.) of five animals.

3. Results and discussion

In our present investigation, the average size of chemically synthesized ZnO nanoparticles observed in Zetasizer was 125.64 nm with a polydispersity index of 0.424. The TEM image of ZnO nanoparticles revealed average size of 70 – 115 nm and spherical shape of particles (Fig. 1a). The SEM analysis of the ZnO nanoparticles further revealed a uniform shape and size for ZnO nanoparticles and aggregations of chemically synthesized nanoparticles (Fig. 1b). It was also evident that nanoparticles were mainly in granules and well crystallized. Therefore, in our present study, the size of the ZnO particles was in the nanometer range. It has been well observed in earlier studies that small size of the nanoparticles allows their internalization into cells, and to interact with biomolecules within or on the cell surface, enabling them potentially to affect cellular responses in a dynamic and selective manner that makes them well suited for biological applications [27]. Additionally, the spherical shape of the nanoparticles is well suited for the efficient topical actions of the nanoparticles.

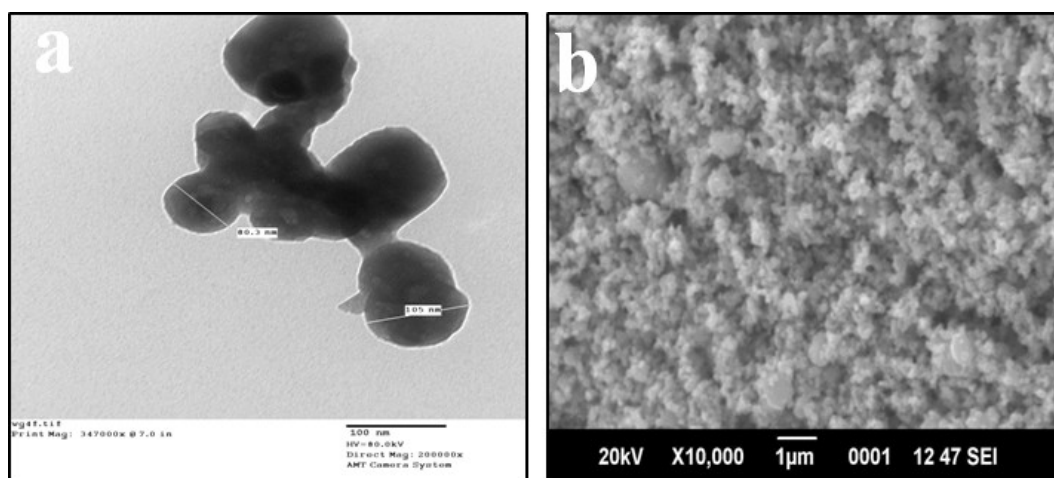


FIG. 1. Representative (a) TEM and (b) SEM image of ZnO nanoparticles

Cutaneous wound healing constitutes an important aspect in rehabilitation medicine. Wound healing has been considered as one of the most vexing problems over the globe. Wounds cause significant morbidity and mortality in humans and animals [28]. Numbers of patients have simple or complicated wounds are increasing day by day. Impairments in the wound healing progress sometimes lead to amputations [29]. Cutaneous wounds cause pain, discomfort, superficial and chronic infection, significant cost associated with the long term treatment. Different treatments available for wound healing are there which include antibiotics, occlusive layers, bandages, poultices and mechanical devices etc. All these treatments become less effective or ineffective for wound healing, when immunity or other body functions of patient are compromised such as diabetes. Thus, there is a current need to develop some compound and formulations to treat such situations and cause faster wound closure. Wound contraction is an important component of wound healing. This involves pulling of surrounding skin circumferentially toward an open wound, which results in wound closure without formation of new tissues [30].

In our present wound healing experiment, all the animals remained healthy during the entire experiment. The feed as well as water intake and physical activity of all tested animals were normal. The topical applications of different formulations did not produce any undesirable effect like itching, hypersensitivity, edema, abscess etc. in any of the animal. The shedding of the scab was earlier in the nano ZnO treated wounds, as compared to other groups. The average time of shedding of scab in nano ZnO treated group was less than seven day, whereas it was around 8 – 10 days in other groups. The scab prevents the contraction of wound. In our present study, applications of ointment having ZnO nanoparticles caused the fast closure of the wounds. Gross photographs of different day's wounds of all the three groups are presented in Fig. 2a. Wound area in all three groups decreased in a time-dependent manner (Fig. 2b). However, percent wound contraction increased in a time-dependent manner in all the three groups. The results of wound area revealed that the wounds treated with ZnO nanoparticles have smaller wound area on respective days, as compared to other groups (Fig. 2a). These findings were further supported by the significantly increased percent wound contraction in ZnO nanoparticles treated group on different days, as compared to control and bulk ZnO treated groups (Fig. 2b). Additionally, bulk ZnO treated group, in comparison to control group, manifested some noticeable decreased wound area and increased percent wound contractions on various days. However, the extent of gross healing effect was more pronounced in the nano ZnO treated group.

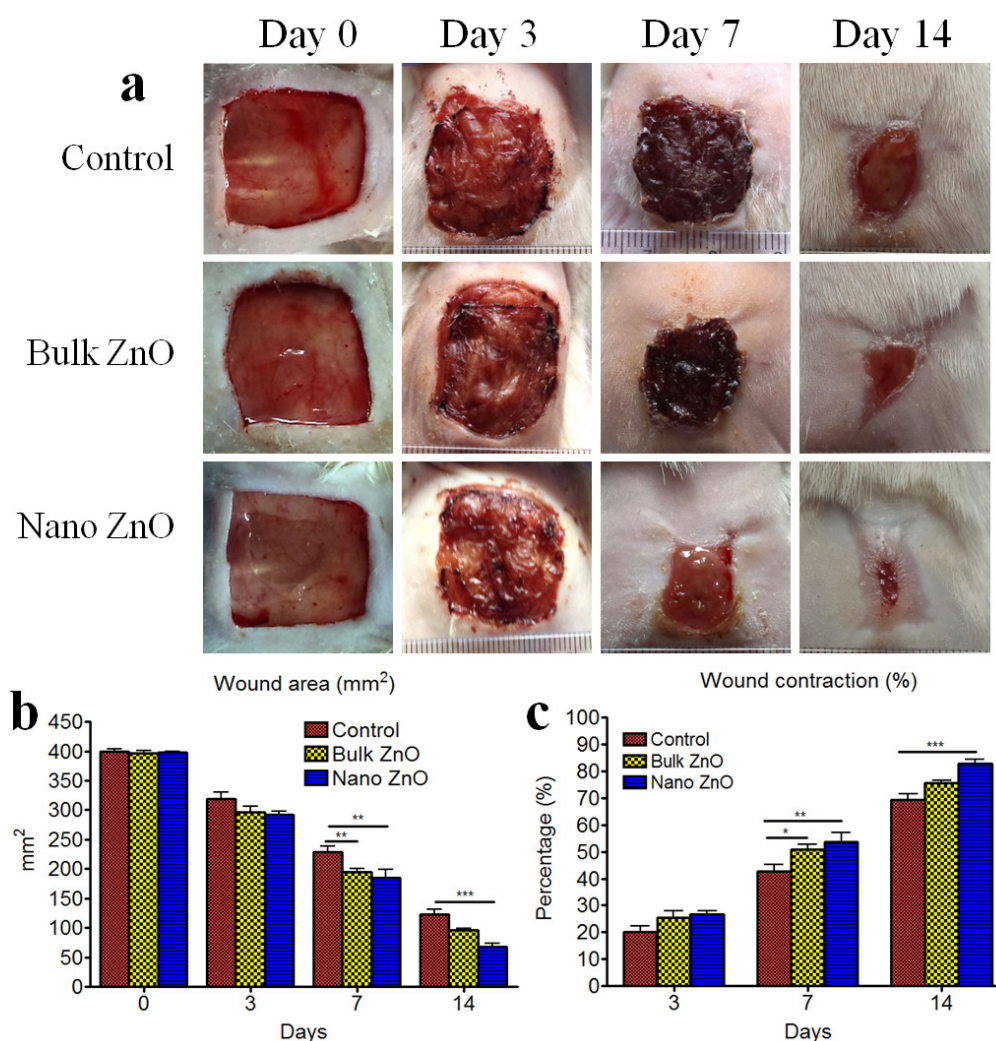


FIG. 2. (a) Gross photographs of wounds of different groups on days 0, 3, 7 and 14 post-wounding; (b & c) Effects of topical application of nano ZnO on (b) wound area and (c) wound contraction in rats. Data are expressed as means \pm SEM. *, ** and *** represent $P < 0.05$, $P < 0.01$ and $P < 0.001$ ($n = 5$)

As, the quality of healed tissue cannot be assessed grossly and sometime tissue showing faster healing on gross observations possesses poor quality and have the chances to get rupture easily. There are various important cells like monocytes, fibroblasts, and epithelial cells etc., which play vital roles for normal wound healing mechanisms. Thus, evaluation of the status of different important cell involved in the healing mechanism help to assess the quality of healing tissue. Therefore, on the last day of experiment, we performed histopathological studies of wound sections for microscopic assessment in order to evaluate the quality of healed tissue in different groups. In histopathological studies, the H&E and Masson's Trichrome staining of the wound sections of different groups was done. The images in Fig. 3a and 3b represent the H&E stained and Masson's Trichrome stained wound sections, respectively of the different groups. The Fig. 3c, 3d, 3e and 3f depict the semi-quantitative score of H&E stained sections for inflammatory cells, blood vessels, epithelialization and wound maturity, respectively. During wound healing, fibroblasts cause production of extracellular matrix (ECM), which is primarily composed of collagen and fibronectin. This ECM provides the suitable scaffold on which granulation tissue formation, keratinocyte migration, and wound contraction occur. Collagen is considered as the major protein of the ECM, which provides wound strength and helps in homeostasis and epithelialization [31]. In present study, the H&E stained sections of all the groups revealed well-formed granulation tissue with variation in proportions of inflammatory cells, fibroblast, blood vessels, collagen formation, extent of epithelialization etc. Several inflammatory cells may stimulate positive feedback mechanism to produce additional cytokines and growth factors at healing site and further play vital role in the proliferative phase of wound repair [32].

However, the inflammatory cells should not persist at wound site for longer durations because secretions of different inflammatory cytokines for longer time may decrease the wound healing. In the present study, mixed types of inflammatory cells were more evident in the control group, as compared to other groups. The inflammatory cells were less prevalent in the ZnO nanoparticle-treated group, which suggested the proper resolution of inflammatory phase in this group. The formation of blood vessels at wound site is necessary for delivery of important components (oxygen and nutrients), and removal of waste metabolites in order to attain proper healing process. Therefore, the healing process of wound gets delayed during impairment of angiogenesis. Angiogenesis starts as early as day 3 after wounding by endothelial migration, proliferation, and tube formation [33]. Thereafter, apoptosis (programmed cell death) of blood vessels starts to occur during the remodeling phase of healing, when there is not a significant requirement for nutrient supply is there, so that proper maturity of healing tissue can take place. In our present study, the numbers of blood vessels were more in control group, as compared to bulk and nano ZnO treated group. The fibroblast dominance was also more evident in the control group as compared to other groups. This revealed that nano ZnO treated wounds have attained better maturity than other treated wounds.

Further, the extracellular matrix provides the tensile strength to the healing wounds and collagen fibers are considered important components of this. The collagen fibers are delicate and loosely arranged during the earlier stages of wound healing. As the wound matures, collagen fibers attain organized pattern and compactness in thicker bundles [34]. In the present investigation, H&E stained and Masson's Trichrome stained wound sections showed that collagen deposition was more in nano ZnO treated group. This group also showed significant organization and compactness of collagen fibers, as compared to control and bulk ZnO treated groups. Thick collagen bundles and wavy pattern of fibers revealed the maturity of collagen fibers in nano ZnO treated group, which was lacking in other groups. Moreover, the quantity and quality of collagen formation was better in the bulk ZnO treated group, as compared to the control group. The formation of an epithelial layer is also vital for wound contraction and proper wound healing. Epithelial layer formation reduces the distance between the wound margins and also protects the wound from outside so that proper healing can take place. Therefore, early formation of epithelial layer is beneficial for the efficient wound healing. In our present study, ZnO nanoparticle-based treatment of wounds resulted in the early regeneration of epithelial layer, which covered the more area of healing tissue. The other treatment groups only showed very partial formation of epithelial layer in few animals. Therefore, the score for epithelialization was more in nano ZnO treated group in our present study. Additionally, the overall wound maturity score was also higher in the ZnO nanoparticles treated group, as compared to control and bulk ZnO treated groups. The H&E stained and Masson's Trichrome stained wound sections of last day of experiment are showing the dominance of fibroblasts, unorganized thin collagen fibers and a greater number of blood vessels in the control group, which revealed that healing process still has not entered in the remodeling phase. However, nano ZnO treated wounds have fewer fibroblast numbers, fewer blood vessels, thick collagen fibers, early formation of epithelial layer etc. All these are the indicators of entry of the healing process in the remodeling phase in nano ZnO treated group. It has been well reported previously that ZnO application on wounds accelerates the healing of acute and chronic wounds and it also possesses antibacterial, antifungal, cytoprotective, and anti-inflammatory properties, which make it a suitable topical wound healing agent [35–37]. Its use for the treatment of various dermatitis, diaper rashes, diaper wipes, blisters, and open skin sores has been also documented [38, 39].

In the last few years, different types of nanoparticles have been synthesized by using several methods; these nanoparticles have shown promising wound healing potentials even in comparison to the standard treatments as well as earlier used their bulk forms. In biomedical fields, the intervention of nanotechnology for any material significantly influences its size, shape, electrical charge, biochemical features such as hydrophobicity, delivery, interaction with biological targets, deeper levels of tissue penetration (either directly through cell membranes or through phagocytosis) and cellular responses (receptor recognition), which can significantly affect the healing processes of any type of wound [40–43]. In a previous study, silver nanoparticles accelerated the wound healing rate by increased wound contraction, increased proliferation and migration of keratinocytes along with a differentiation of fibroblasts into myofibroblasts [44]. Wound healing has been promoted by silica–gold core–shell nanoparticles due to potent anti-inflammatory and antioxidant properties of gold nanoparticles [45]. Moreover, silver nanoparticles application on porcine wounds significantly increased apoptosis of the inflammatory cells present in the dermis, decreased levels of pro-inflammatory cytokines (TNF- α and IL-8) and increased the levels of anti-inflammatory cytokines (IL-4, EGF, KGF, and KGF-2) [46]. Several other nanoparticles of titanium oxide [47], curcumin [48], and copper [49] have also shown significant immunomodulatory effects. The combination preparation having gold nanoparticles, epigallocatechin gallate, and α -lipoic acid significantly accelerated diabetic cutaneous wound healing through angiogenesis regulation and anti-inflammatory effects, and immunoblotting results of this study revealed increased expression of VEGF [50]. Collagen deposition, their structural alignment and tensile strength have been improved by the administration of silver nanoparticles in the healing tissue of cutaneous wounds [51, 52]. These several studies have clearly

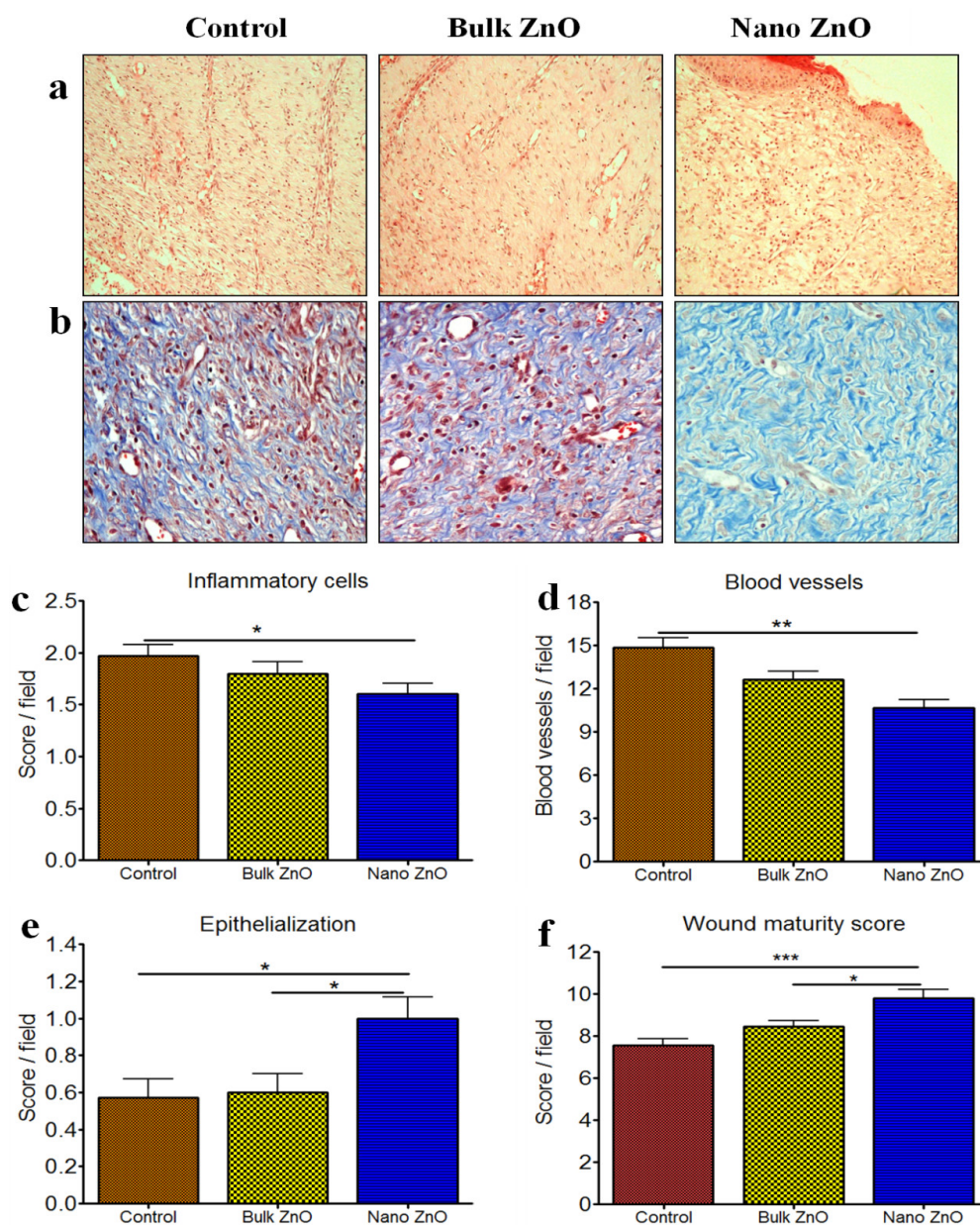


FIG. 3. Representative images of (a) haematoxylin& eosin (H & E) (20 \times) stained and (b) Masson's Trichrome (40 \times) stained wound sections of different treatment groups. Semi-quantitative score of (c) inflammatory cells, (d) blood vessels density, (e) epithelialization and (f) wound maturity in H & E stained cutaneous wound sections of different treatment groups. Data are expressed as mean \pm SEM. * and *** represent $P < 0.05$ and $P < 0.001$

explained that the mechanism of healing is very complex and there is involvement of several cytokine, growth factors, enzymes, cells etc., which markedly influence the outcome of healing process. Moreover, there is not a single pathway by which different metals or metal oxides or other nanoparticles promote the healing mechanisms. The exact mechanism of healing by ZnO is also not known. Apart from diverse pharmacological properties of ZnO, it has been shown to increase the secretion of fibroblast growth factor (FGF), suggesting that zinc in granulating wounds is also possibly capable of up-regulating growth factors [53]. The insulin-like growth factor-I (IGF-I) is vital for homeostasis of epidermis and the zinc-dependent matrix metalloproteinases (MMPs) are required for optimal epithelial migration [54, 55]. Further, ZnO augments the endogenous expression of IGF-I in granulation tissue and can also activate zinc-dependent MMPs to facilitate the migration of keratinocytes [56]. Some researchers have suggested that local applications of ZnO accelerates wound healing by its anti-bacterial, anti-inflammatory, increase reepithelialization and

activation of metalloproteinase enzymes properties [57, 58]. Decreasing the dimension of nanoparticles has a pronounced effect on their physical properties, which significantly differ from those of the bulk material. Therefore, in our present study, the better wound healing potential of nano ZnO in comparison to its bulk form could be due to the novel and distinct physical, chemical, and biological properties and functionality due to their nanoscale size. Thus, in the present study, the increased healing potential of nano form of ZnO in comparison to its bulk form could also be due to the efficient modulation of several cytokines, growth factors, enzymes, cells etc involved in different phases of healing. The potent anti-inflammatory action of nano ZnO may be responsible for faster completion of inflammatory phase and resulting in early entry of wound to proliferative phase. In our present study, nano ZnO (2 %) showed better wound healing potential than bulk ZnO (20 %) even at ten-fold lower concentrations. Thus, nano ZnO, as a promising wound healing agent, can be used for the treatment of different types of wounds. However, some additional studies like healing effect in other species, healing effect in complicated wounds (burn wounds, diabetic wounds etc.), local irritation studies, biocompatibility, toxicity studies, calculation of lethal dose 50 (LD50), stability of nano ZnO formulation, healing effect of lower concentrations of nano ZnO etc. may be required to be conducted before proceeding to clinical studies.

4. Conclusion

On the basis of results obtained for the present study, it might be concluded that topical application of ZnO nanoparticles (2 %) in ointment base caused faster wound healing and the healing was better than bulk ZnO treatment. Thus, nano ZnO might be envisioned as a promising healing agent in future.

References

- [1] Bello D., Martin J., et al. Physicochemical and morphological characterisation of nanoparticles from photocopiers: implications for environmental health. *Nanotoxicology*, 2012, **7** (5), P. 989–1003.
- [2] Demokritou P., Gass S., et al. An in vivo and in vitro toxicological characterisation of realistic nanoscale CeO₂ inhalation exposures. *Nanotoxicology*, 2013, **7** (8), P. 1338–1350.
- [3] Pirela S., Molina R., et al. Effects of copy center particles on the lungs: a toxicological characterization using a Balb/c mouse model. *Inhal. Toxicol.*, 2013, **25** (9), P. 498–508.
- [4] Larsen S.T., Roursgaard M., Jensen K.A., Nielsen G.D. Nano titanium dioxide particles promote allergic sensitization and lung inflammation in mice. *Basic Clin. Pharmacol. Toxicol.*, 2010, **106** (2), P. 114–117.
- [5] Li J.J.E., Muralikrishnan S., et al. Nanoparticle-induced pulmonary toxicity. *Exp. Biol. Med.*, 2010, **235** (9), P. 1025–1033.
- [6] Cohen J., Deloid G., Pyrgiotakis G., Demokritou P. Interactions of engineered nanomaterials in physiological media and implications for in vitro dosimetry. *Nanotoxicology*, 2013, **7** (4), P. 417–431.
- [7] Garcia-Orue I., Gainza G., et al. Nanotechnology approaches for skin wound regeneration using drugdelivery systems. *Nanobiomaterials in Soft Tissue Engineering*, 2016, P. 31–55.
- [8] Mishra P.K., Mishra H., et al. Zinc oxide nanoparticles: a promising nanomaterial for biomedical applications. *Drug Discovery Today*, 2017, **22** (12), P. 1825–1834.
- [9] Akila S., Nanda A. In-Vivo Wound Healing Activity of Silver Nanoparticles: An Investigation. *Int. J. Sci. Res.*, 2014, **3** (7), P. 1208–1212.
- [10] Alizadeh S., Seyedalipour B., et al. Copper nanoparticles promote rapid wound healing in acute full thickness defect via acceleration of skin cell migration, proliferation, and neovascularization. *Biochem. Biophys. Res. Commun.*, 2019, **517** (4), P. 684–690.
- [11] Tao B., Lin C., et al. Copper-nanoparticle-embedded hydrogel for killing bacteria and promoting wound healing with photothermal therapy. *J. Mater. Chem. B*, 2019, **7** (15), P. 2534–2548.
- [12] Ziv-Polat O., Topaz M., Brosh T., Margel S. Enhancement of incisional wound healing by thrombin conjugated iron oxide nanoparticles. *Biomaterials*, 2010, **31** (4), P. 741–747.
- [13] Hamam F., Nasr A. Curcumin-loaded mesoporous silica particles as wound-healing agent: An *in vivo* study. *Saudi J. Med. Med. Sci.*, 2020, **8** (1), P. 17–24.
- [14] Kheradmand F., Mousavi A., Nurmohamadi E. Zinc and molecular mechanisms involved in its homeostasis. *J. Paramed. Faculty*, 2009, **4** (1), P. 34–38.
- [15] Jones N., Ray B., Ranjit K.T., Manna A.C. Antibacterial activity of ZnO nanoparticle suspensions on a broad spectrum of microorganisms. *FEMS Microbiol. Lett.*, 2008, **279**, P. 71–76.
- [16] Wang S.Q., Tooley I.R. Photoprotection in the era of nanotechnology. *Semin. Cutan. Med. Surg.*, 2011, **30**, P. 210–213.
- [17] Prasad A.S., Oberleas D. Thymidine kinase activity and incorporation of thymidine into DNA in zinc-deficient tissue. *J. Lab. Clin. Med.*, 1974, **83**, P. 634–639.
- [18] Sandstead H.H., Lanier V.C., Shepard G.H., Gillespie D.D. Effects of zinc deficiency and zinc supplementation. *Amer. J. Clin. Nutr.*, 1970, **23**, P. 514–519.
- [19] Prasad A.S. Zinc: an overview. *Nutr.*, 1995, **11**, P. 93–99.
- [20] Agren M.S., Chvapil M., Franzén L. Enhancement of re-epithelialization with topical zinc oxide in porcine partialthickness wounds. *J. Surg. Res.*, 1991, **50**, P. 101–105
- [21] Kaushik M., Niranjana R., et al. Investigations on the antimicrobial activity and wound healing potential of ZnO nanoparticles. *Appl. Surf. Sci.*, 2019, **479**, P. 1169–1177.
- [22] Rezende C.P., da Silva J.B., Mohallem N.D.S. Influence of drying on the characteristics of zinc oxide nanoparticles. *Braz. J. Phys.*, 2009, **39**, P. 248–251.

- [23] Hajiaghaalipour F., Kanthimathi M.S., Abdulla M.A., Sanusi J. The effect of *Camellia sinensis* on wound healing potential in an animal model. *Evid. Based Compl. Alt. Med.*, 2013, 386734.
- [24] Abramov Y., Golden B., et al. Histologic characterization of vaginal vs. abdominal surgical wound healing in a rabbit model. *Wound Repair Regen.*, 2007, **15** (1), P. 80–86.
- [25] Greenhalgh D.G., Sprugel K.H., Murray M.J., Ross, R. PDGF and FGF stimulate healing in the genetically diabetic mouse. *Am. J. Pathol.*, 1990, **136**, P. 1235–1246.
- [26] Kant V., Kumar D., et al. Topical application of substance P promotes wound healing in streptozotocin-induced diabetic rats. *Cytokine*, 2015, **73**, P. 144–155.
- [27] Cho K., Wang X., Nie S., Shin D.M. Therapeutic nanoparticles for drug delivery in cancer. *Clin. Cancer Res.*, 2008, **14**, P. 1310–1316.
- [28] Fine N., Mustoe T. Wound Healing. Philadelphia: Lippincott Williams & Wilkins, 2006.
- [29] Wertheimer E. Diabetic skin complications: a need for reorganizing the categories of diabetes-associated complications. *Isr. Med. Assoc. J.*, 2004, **6**, P. 287–289.
- [30] Bae S.H., Bae Y.C., Nam S.B., Choi S.J. A Skin Fixation Method For Decreasing The Influence Of Wound Contraction On Wound Healing In A Rat Model. *Arch. Plast. Surg.*, 2012, **39** (5), P. 457–462.
- [31] Singer A.J., Clark R.A.F. Cutaneous wound healing. *N. Engl. J. Med.*, 1999, **341**, P. 738–746.
- [32] Werner R., Grose S. Regulation of wound healing by growth factors and cytokines. *Physiol. Rev.*, 2003, **83**, P. 835–870.
- [33] Brem H., Folkman J. Angiogenesis and basic fibroblast growth factor during wound healing. In: Friedlander G.E., Lane J.M., (ed.) *Bone Formation and Repair*, Rosemont: American Academy of Orthopedic Surgeons, 1994, P. 213–222.
- [34] Pereira M.C., Pinho C.B., et al. Influence of 670 nm low-level laser therapy on mast cells and vascular response of cutaneous injuries. *J. Photochem. Photobiol. B*, 2010, **98**, P. 188–192.
- [35] Selvam S., Rajiv Gandhi R., et al. Antibacterial effect of novel synthesized sulfated cyclodextrin crosslinked cotton fabric and its improved antibacterial activities with ZnO, TiO₂ and Ag nanoparticles coating. *Int. J. Pharm.*, 2012, **434** (1–2), P. 366–374.
- [36] Subhasree R.S., Selvakumar D., Kumar N.S. Hydrothermal mediated synthesis of ZnO nanorods and their antibacterial properties. *Lett. Appl. NanoBioSci.*, 2012, **1**, P. 2–7.
- [37] Vlad S., Tanase C., et al. Antifungal behaviour of polyurethane membranes with zinc oxide nanoparticles. *Digest J. Nanomater. Biostruct.*, 2012, **7**, P. 51–58.
- [38] Kumar P.T.S., Lakshmanan V.K., et al. Flexible and microporous chitosan hydrogel/nano ZnO composite bandages for wound dressing: in vitro and in vivo evaluation. *ACS Appl. Mater. Interfaces.*, 2012, **4**, P. 2618–2629.
- [39] Shalumon K.T., Anulekha K.H., et al. Sodium alginate/poly vinyl alcohol/nano ZnO composite nanofibers for antibacterial wound dressings. *Int. J. Biol. Macromol.*, 2011, **49**, P. 247–254.
- [40] Hamdan S., Pastar I., et al. Nanotechnology-Driven Therapeutic Interventions in Wound Healing: Potential Uses and Applications. *ACS Cent. Sci.*, 2017, **3**, P. 163–175.
- [41] Lin P.C., Lin S., Wang P.C., Sridhar R. Techniques for physicochemical characterization of nanomaterials. *Biotechnol. Adv.*, 2014, **32**, P. 711–726.
- [42] Ferrari M. Nanogeometry: Beyond drug delivery. *Nat. Nanotechnol.*, 2008, **3**, P. 131–132.
- [43] George S., Lin S., et al. Surface defects on plate-shaped silver nanoparticles contribute to its hazard potential in a fish gill cell line and zebrafish embryos. *ACS Nano*, 2012, **6**, P. 3745–3759.
- [44] Liu X., Lee P.Y., et al. Silver nanoparticles mediate differential responses in keratinocytes and fibroblasts during skin wound healing. *Chem. Med. Chem.*, 2010, **5** (3), P. 468–475.
- [45] Li X., Wang H., et al. Effect of composite SiO₂@AuNPs on wound healing: in vitro and vivo studies. *J. Colloid. Interface Sci.*, 2015, **445**, P. 312–319.
- [46] Nadworny P.L., Landry B.K., et al. Does nanocrystalline silver have a transferable effect? *Wound Repair Regen.*, 2010, **18**, P. 254–265.
- [47] Archana D., Dutta J., Dutta P.K. Evaluation of chitosan nano dressing for wound healing: characterization, in vitro and in vivo studies. *Int. J. Biol. Macromol.*, 2013, **57**, P. 193–203.
- [48] Chereddy K.K., Coco R., et al. Combined effect of PLGA and curcumin on wound healing activity. *J. Control Release*, 2013, **171**, P. 208–215.
- [49] Tiwari M., Narayanan K., et al. Biosynthesis and wound healing activity of copper nanoparticles. *IET Nanobiotechnol.*, 2014, **8**, P. 230–237.
- [50] Chen S.A., Chen H.M., et al. Topical treatment with antioxidants and Au nanoparticles promote healing of diabetic wound through receptor for advanced glycation end-products. *Eur. J. Pharm. Sci.*, 2012, **47**, P. 875–883.
- [51] Guthrie K.M., Agarwal A., et al. Integration of silver nanoparticle-impregnated polyelectrolyte multilayers into murine-splinted cutaneous wound beds. *J. Burn Care Res.*, 2013, **34**, P. 359–367.
- [52] Kwan K.H., Liu X., et al. Modulation of collagen alignment by silver nanoparticles results in better mechanical properties in wound healing. *Nanomed.*, 2011, **7**, P. 497–504.
- [53] Baroni A., Peretto B., et al. Topical amikacin formulation induces fibroblast growth factor and cytokine release from human dermal fibroblasts. *Arch. Dermatol. Res.*, 1999, **291**, P. 296–299.
- [54] Tarnow P., Agren M., Steenfos H., Jansson J.O. Topical zinc oxide treatment increases endogenous gene expression of insulin-like growth factor-I (IGF-1) in granulation tissue from porcine wounds. *Scand. J. Plast. Reconstr. Surg. Hand. Surg.*, 1994, **28**, P. 255–259.
- [55] Agren M.S. Matrix metalloproteinases (MMPs) are required for re-epithelialization of cutaneous wounds. *Arch. Dermatol. Res.*, 1999, **291**, P. 583–590.
- [56] Agren M.S., Steenfos H.H., Tarnow P., Jansson J. Augments endogenous expression of insulin-like growth factor-I (IGF-I) and activates matrix metalloproteinases (MMPs) in wounds. *EWMA J.*, 2001, 138169909.
- [57] Lansdown A.B., Mirastschijski U., et al. Zinc in wound healing: theoretical, experimental, and clinical aspects. *Wound Repair Regen.*, 2007, **15** (1), P. 2–16.
- [58] Iwata M., Takebayashi T., et al. Zinc accumulation and metallothionein gene expression in the proliferating epidermis during wound healing in mouse skin. *Histochem. Cell. Biol.*, 1999, **112** (4), P. 283–290.

Solubility phase equilibrium in ternary system fulleranol $C_{60}(OH)_{24}$ and praseodymium salt: $PrCl_3-C_{60}(OH)_{24}-H_2O$ at $25^\circ C$

G. A. Glushnev¹, Ayat Kanbar¹, V. A. Keskinov¹, N. A. Charykov^{1,2}, K. N. Semenov^{1,4,6},
Z. K. Shaimardanov³, B. K. Shaimardanova³, N. A. Kulenova³, D. G. Letenko⁵

¹St. Petersburg State Technological Institute (Technical University), Moskovsky prospect, 26,
St. Petersburg, 190013, Russia

²St. Petersburg Electrotechnical University “LETI”, ul. Professora Popova 5, 197376 St. Petersburg, Russia

³D. Serikbayev East Kazakhstan state technical university, A. K. Protozanov Street, 69, Ust-Kamenogorsk,
070004, The Republic of Kazakhstan

⁴St. Petersburg State University, 7/9 Universitetskaya emb., St. Petersburg, 199034, Russia

⁵St. Petersburg State University of Architecture and Civil Engineering (SPSUACE), 2nd Krasnoarmeiskaya St. 4,
190005 St. Petersburg, Russia

⁶Pavlov First St. Petersburg State Medical University L'va Tolstogo str. 6–8 St. Petersburg, 197022, Russia
keskinov@mail.ru

PACS 61.48.+c

DOI 10.17586/2220-8054-2020-11-4-462-467

Solubility diagram was investigated by the method of saturation in ampules at $25 \pm 0.02^\circ C$ for 4 hours. The solubility diagram of the $PrCl_3-C_{60}(OH)_{24}-H_2O$ ternary system at $25^\circ C$ occurs as simple eutonics, consisting of two branches, corresponding to the crystallization of crystal-hydrates: $PrCl_3 \cdot 7H_2O$ and $C_{60}(OH)_{24} \cdot 18H_2O$. The diagram contains one non-variant point each – eutonics, which corresponds to saturation with pair of crystal-hydrates simultaneously. The diagram also contains very short branch of $PrCl_3 \cdot 7H_2O$ crystallization, and long branch of $C_{60}(OH)_{24} \cdot 18H_2O$, where the effect of fulleranol salt-out is distinctly observed.

Keywords: fullerene C_{60} , arginine, octo-adduct, lutetium chloride, solubility diagram, ternary system, simple eutonic.

Received: 6 April 2020

Revised: 29 May 2020

1. Introduction

This article continues the cycle of publications, concerning the synthesis, identification and physico-chemical, physical, bio-chemical, biological properties investigation of the amino-acid-light fullerene adducts [1–19]. This article is devoted to the investigation of the solubility diagram for systems containing water soluble fullerene nano-clusters, inorganic salt, including rare earth metals and actinoids, and water, as the solvent [20–24]. In prior research, it was shown, that water soluble fullerene nano-clusters (with amino-acid adducts, poly-hydroxylated forms – fullerenols, complex ethers with carboxylic acids) have a very strong salting-out effect at addition of inorganic salts or their crystal-hydrates, and the salting-out effect is most strongly pronounced for salts of 4-f and 5-f elements, somewhat weaker for the salts of d-elements, and even weaker for the salts of p- and s-elements. So, such 4-f element salts (as $PrCl_3$) may be effectively used for precipitation (by the salting-out effect) of fullerene nano-clusters (as $C_{60}(OH)_{24}$) and it is possible that separation from the matrix solution and purification occurs virtually without losses of nanoclusters. Currently, separation from the matrix solution and purification of fullerene nanoclusters is carried out, as a rule, by multistage (often triple) methanol (or methyl-acetate, or ethanol)-water recrystallization, which leads to the following:

- considerable losses of nanoclusters, because solubility of last ones in methanol with water impurities solutions is more or less considerable;
- nanoclusters for the same reasons contain a significant amount of impurities;
- recrystallization process itself is laborious.

2. Reagents

In the present investigation we used rare earth chloride $PrCl_3$, synthesized from the “chemical pure” oxide Pr_6O_{11} by treatment of “pure for the analysis” HCl with following vacuum drying. Fulleranol $C_{60}-C_{60}(OH)_{24}$ was synthesized by from the bromine derivative $C_{60}Br_{24}$ by the treatment of these product by boiling water-dioxane mixture with the dissolved NaOH. Then sodium fullerenes forms $C_{60}(OH)_{24-\delta}(ONa)_\delta$ were neutralized and washed in the

Soxlet-extractor bymethanol+HCl liquid phase. So, $PrCl_3$ and $C_{60}(OH)_{24}$ with purity ≈ 99.3 and 97.7 mass. %, correspondingly, were synthesized.

3. Experimental method

Solubility diagrams were investigated by the method of saturation in ampules at 25 ± 0.02 °C for 4 hours in the conditions of shaker-thermostate with shaking frequency of ≈ 2 Hz. For the prevention of Pr^{3+} precipitation in the form $Pr(OH)_3$, some drops of HCl was added to the heterogeneous systems, to approximate fixation of pH $\approx 3.0 - 3.5$ a.un.

The concentration of $PrCl_3$ were determined by complexometric titration with trilon-B (disodium salt of ethylenediamine-tetraacetic acid – EDTA), titration conditions were the following: acetic buffer, indicator – 2 – 3 drops of 1-% Xylenol orange solution, color transition from violet to lemon-yellow [25].

Concentration of $C_{60}(OH)_{24}$ was determined with the help of absorption electronic spectroscopy according to optical density at wavelength $\lambda = 330$ nm – D_{330} (Ultraviolet-Visible Electronic Spectro-photometer Shimadzu, wavelength $200 < \lambda < 900$ nm). Typical spectrum for $C_{60}(OH)_{24}$ water solution is represented in Fig. 1(a).

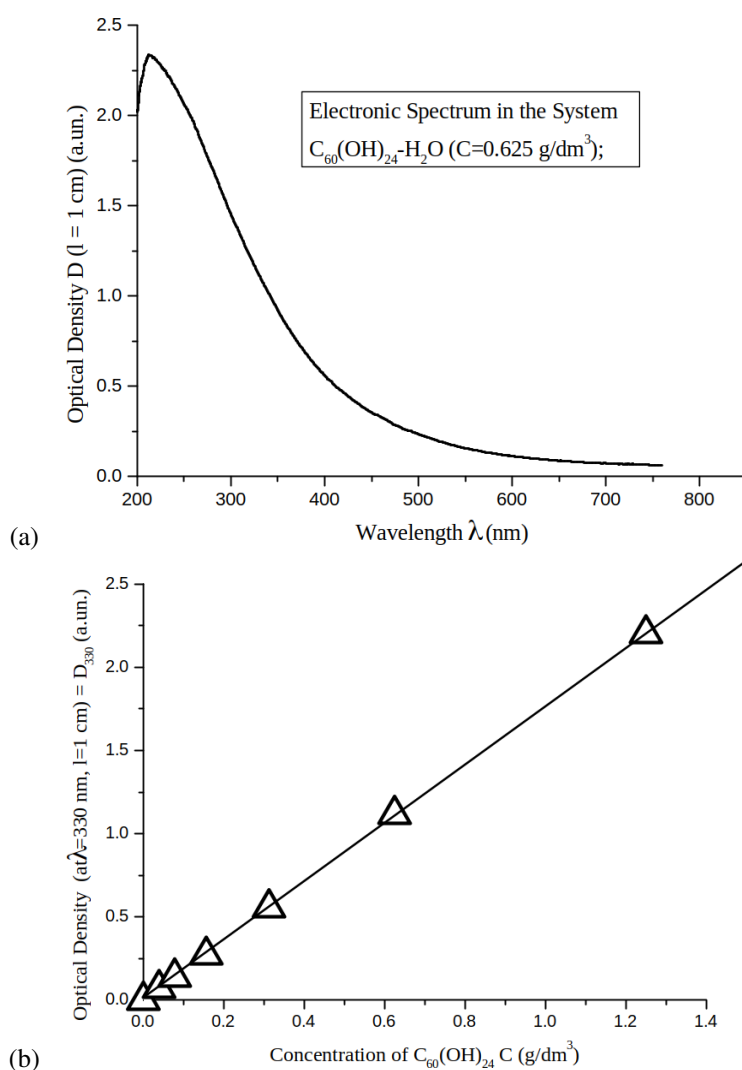


FIG. 1. Electronic spectrum of $C_{60}(OH)_{24}$ water solution (concentration of $C_{60}(OH)_{24}$ $C = 0.625$ g/dm³) (a) and validity of Bouguer-Lambert-Beer Law in $C_{60}(OH)_{24}$ aqueous solutions at wavelength $\lambda = 330$ nm, optical path of $l = 1$ cm (b)

In Fig. 1(b), the validity of Bouguer-Lambert-Beer Law in $C_{60}(OH)_{24}$ water solutions in the nearest UV spectral diapazone is represented. One can see the almost complete linearity of the dependence of optical density at wavelength $\lambda = 330$ nm on the solution concentration. One can see, that, although spectrum has no any expressed absorption

peaks, we can calculate $C_{60}(\text{OH})_{24}$ concentration in g/dm^3 , from optical density at wavelength $\lambda = 330 \text{ nm}$, according to Bouguer–Lambert–Beer law by the formulé:

$$C_{C_{60}(\text{OH})_{24}} (\text{g/dm}^3) = 0.609 \cdot D_{330} \quad (l = 1 \text{ cm}). \quad (1)$$

Density of the solutions were determined with the help of quartz picnometers with operating volume $V \approx 5 \text{ cm}^3$. Errors in the determination of PrCl_3 concentration was $\delta \approx 2.5$ relative %, $C_{60}(\text{OH})_{24}$ $\delta \approx 5$ relative %, density $\delta \approx 0.1$ relative %.

4. Experimental data discussion

Solubility diagram in the ternary system $\text{PrCl}_3\text{--}C_{60}(\text{OH})_{24}\text{--H}_2\text{O}$ at 25°C is represented in the Fig. 2 and Table 1. In Fig. 3, the dependence of the densities of saturated solutions in ternary system $\text{PrCl}_3\text{--}C_{60}(\text{OH})_{24}\text{--H}_2\text{O}$ at 25°C is depicted.

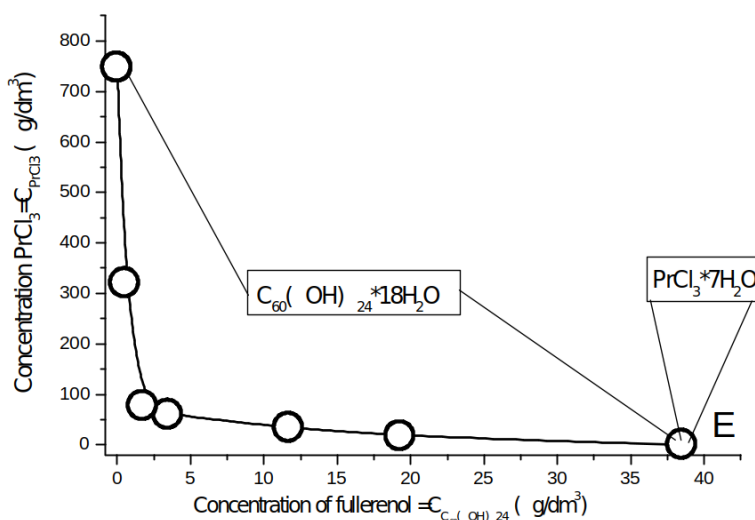


FIG. 2. Solubility in ternary system $\text{PrCl}_3\text{--}C_{60}(\text{OH})_{24}\text{--H}_2\text{O}$ at 25°C

TABLE 1. Solubility in the $\text{PrCl}_3\text{--}C_{60}(\text{OH})_{24}\text{--H}_2\text{O}$ ternary system at 25°C

Num	Density ρ (g/cm^3)	Optical density D (a.u.)	Concentration $C_{60}(\text{OH})_{24}$ (g/dm^3)	Concentration PrCl_3 (g/dm^3)	Solid Phase
1	1.030	68.8	38.5	0.000	$C_{60}(\text{OH})_{24} \cdot 18\text{H}_2\text{O}$
2	1.034	34.5	19.3	17.3	$C_{60}(\text{OH})_{24} \cdot 18\text{H}_2\text{O}$
3	1.041	20.9	11.7	33.9	$C_{60}(\text{OH})_{24} \cdot 18\text{H}_2\text{O}$
4	1.070	6.20	3.47	59.2	$C_{60}(\text{OH})_{24} \cdot 18\text{H}_2\text{O}$
5	1.085	3.13	1.75	77.2	$C_{60}(\text{OH})_{24} \cdot 18\text{H}_2\text{O}$
6	1.329	0.950	0.532	320	$C_{60}(\text{OH})_{24} \cdot 18\text{H}_2\text{O}$
7	1.603	0.025	0.014	747	$C_{60}(\text{OH})_{24} \cdot 18\text{H}_2\text{O} + \text{PrCl}_3 \cdot 7\text{H}_2\text{O}$
8	1.603	—	0.000	747	$\text{PrCl}_3 \cdot 7\text{H}_2\text{O}$

The solubility diagram of in the $\text{PrCl}_3\text{--}C_{60}(\text{OH})_{24}\text{--H}_2\text{O}$ ternary system at 25°C occurs due to simple eutonics [26–28], consisting of two branches, corresponds to crystallization of crystal-hydrates: $\text{PrCl}_3 \cdot 7\text{H}_2\text{O}$ and $C_{60}(\text{OH})_{24} \cdot 18\text{H}_2\text{O}$. Diagrams contains one non-variant point – eutonics, which corresponds to saturation the pair of crystal-hydrates simultaneously. The diagram contains a very short branch for $\text{PrCl}_3 \cdot 7\text{H}_2\text{O}$ and a long branch for $C_{60}(\text{OH})_{24} \cdot 18\text{H}_2\text{O}$ crystallization, where the effect of fulleranol salt-out is observed distinctly.

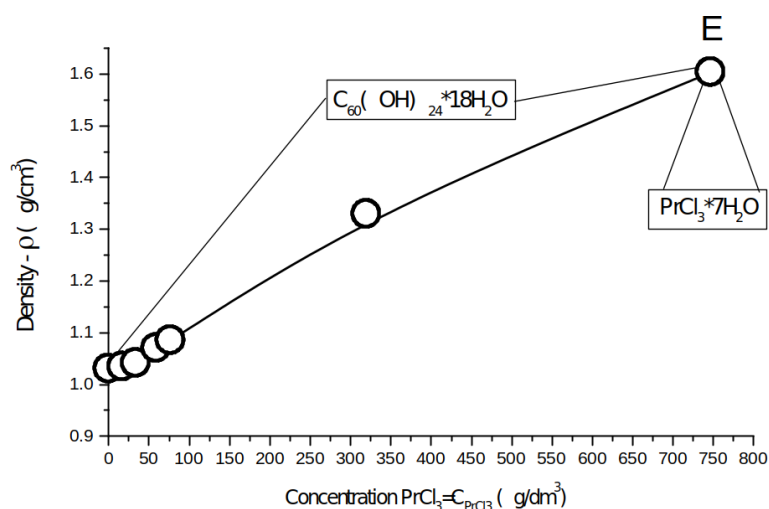


FIG. 3. Density of saturated solutions in the $PrCl_3$ - $C_{60}(OH)_{24}$ - H_2O ternary system at $25\text{ }^\circ\text{C}$

5. Interpretation of obtained solubility data according to empirical Sechenov equation and modified Debye equation

We also made an attempt to describe obtained solubility data according to the empirical Sechenov equation (eq. (2)) and modified Debye equation (eq. (3)):

$$\ln(C_{C_{60}(OH)_{24}}^0 / C_{C_{60}(OH)_{24}}) = K_s C_{PrCl_3}, \quad (2)$$

where: $C_{C_{60}(OH)_{24}}^0$ – solubility of non-electrolyte $C_{60}(OH)_{24}$ in H_2O , $C_{C_{60}(OH)_{24}}$ – solubility of $C_{60}(OH)_{24}$ in ternary system, C_{PrCl_3} – electrolyte $PrCl_3$ concentration, K_s – Sechenov empirical constant:

$$C_{C_{60}(OH)_{24}}^0 / C_{C_{60}(OH)_{24}} = K_D C_{PrCl_3} + A C_{PrCl_3}^{4/3}, \quad (3)$$

where: K_D and A – fitting parameters of Debye model.

The results of approximation by Sechenov equation is represented in Fig. 4.

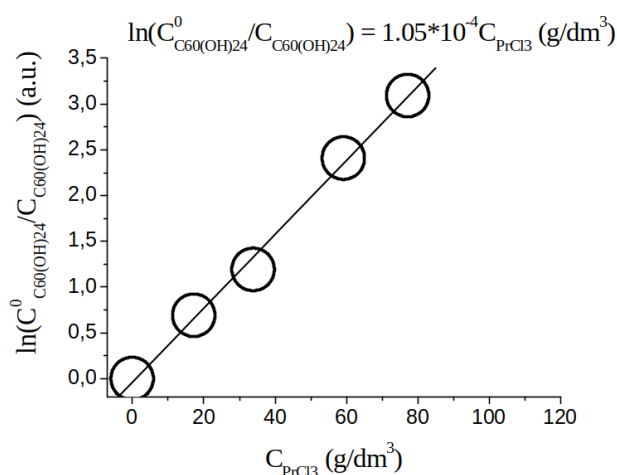


FIG. 4. Approximation of solubility diagram in ternary system $PrCl_3$ - $C_{60}(OH)_{24}$ - H_2O at $25\text{ }^\circ\text{C}$ by Sechenov equation in the $0 < C_{PrCl_3} < 77.2\text{ g/dm}^3$ concentration range

From Fig. 4, one can see, that eq. (2) very precisely describes the crystallization curve of $C_{60}(OH)_{24} \cdot 18H_2O$. In more concentrated solutions ($77.2 < C_{PrCl_3} < 747\text{ g/dm}^3$) the discrepancy between calculated and experimental data increases many times, to our opinion, for the following reasons:

- $PrCl_3$ even remotely ceases to be a strong electrolyte (ion pairs and ion associates formation);
- $C_{60}(OH)_{24}$ in all saturated solutions it detects huge positive deviations from ideality by implementing a multi-stage sequential hierarchical association [29].

Exactly the same occurs when applying the Debye equation (3) – see Fig. 5, but the concentration range maybe considerably expanded: $0 < C_{\text{PrCl}_3} < 320 \text{ g/dm}^3$ (calculation was provided with the help of software package Origin, subprogram Nonlinear curve fit).

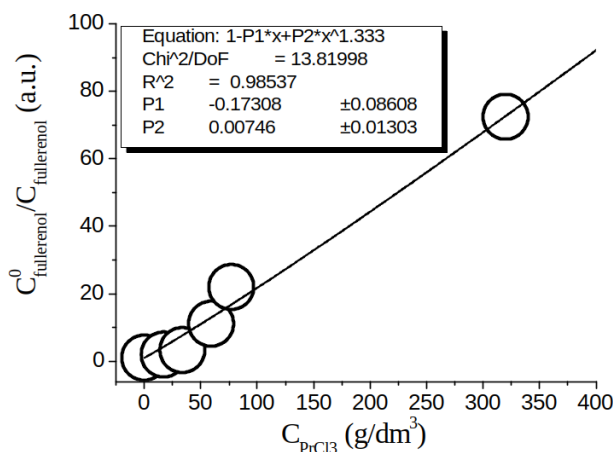


FIG. 5. Approximation of solubility diagram in ternary system $\text{PrCl}_3\text{-C}_{60}(\text{OH})_{24}\text{-H}_2\text{O}$ at 25°C by Debye equation in concentration range $0 < C_{\text{PrCl}_3} < 320 \text{ g/dm}^3$

6. Conclusions

The solubility diagram of the $\text{PrCl}_3\text{-C}_{60}(\text{OH})_{24}\text{-H}_2\text{O}$ ternary system at 25°C occurs as simple eutonics, consisting of two branches, corresponding to crystallization of crystal-hydrates: $\text{PrCl}_3 \cdot 7\text{H}_2\text{O}$ and $\text{C}_{60}(\text{OH})_{24} \cdot 18\text{H}_2\text{O}$. The diagram contains one non-variant point each – eutonics, which correspond to saturation with pair of crystal-hydrates simultaneously. The diagram also contains very short branch of $\text{PrCl}_3 \cdot 7\text{H}_2\text{O}$ crystallization, and long branch of $\text{C}_{60}(\text{OH})_{24} \cdot 18\text{H}_2\text{O}$, where the effect of fullereneol salt-out is distinctly observed. The diagram in the range of low rare earth salt concentrations may be more or less precisely described by Sechenov or Debye equations.

Acknowledgements

This work was supported by Russian Foundation for Basic Research (RFBR) (Projects Nos. 18-08-00143 A, 19-015-00469 A, and 19-016-00003 A).

References

- [1] Shestopalova A.A., Semenov K.N., et al. Physico-chemical properties of the C_{60} -arginine water solutions. *J. of Molecular Liquids*, 2015, **211**, P. 301–307.
- [2] Semenov K.N., Charykov N.A., Keskinov V.A. Cryometry and excess functions of the adduct of light fullerene C_{60} and arginine – $\text{C}_{60}(\text{C}_6\text{H}_{13}\text{N}_4\text{O}_2)_8\text{H}_8$ aqueous solutions. *Nanosystems: Physics, Chemistry, Mathematics*, 2015, **6** (5), P. 715–725.
- [3] Yur'ev G.O., Lelet M.I., et al. Thermodynamic and thermal properties of the C_{60} -L-Arg derivative. *J. Chem. Thermodynamics*, 2018, **127**, P. 39–44.
- [4] Panova G.G., Serebryakov E.B., et al. Bioactivity Study of the C_{60} -L-Threonine Derivative for Potential Application in Agriculture. *Journal of Nanomaterials*, 2019, 2306518.
- [5] Serebryakov E.B., Zakusilo D.N., et al. Physico-chemical properties of C_{70} -l-threonine bisadduct ($\text{C}_{70}(\text{C}_4\text{H}_9\text{NO}_2)_2$) aqueous solutions. *Journal of Molecular Liquids*, 2019, **279**, P. 687–699.
- [6] Sidorov L.N., Yurovskaya M.A., et al. *Fullerenes: textbook. allowance*. M.: Exam, 2005, 668 p. (In Russian)
- [7] Cataldo F., Ros T.Da. *Carbon Materials: Chemistry and Physics: Medicinal Chemistry and Pharmacological Potential of Fullerenes and Carbon Nanotubes*. Springer, 2008, 372 p.
- [8] Piotrovsky L.B., Kiselev O.I. *Fullerenes in biology*. Rostock, St. Petersburg, 2006, 336 p. (In Russian)
- [9] Djordjevic A., Bogdanovic G., Dobric S. Fullerenes in biomedicine. *J. B.U.ON*, 2006, **11**, P. 391–404.
- [10] Bianco C., Da Ros A., Prato T., Toniolo M. Fullerene-based amino acids and peptides. *J. Pept. Sci.*, 2001, **7**, P. 346–347.
- [11] Jiang G., Yin F., Duan J., Li G. Synthesis and properties of novel water-soluble fullerene-glycine derivatives as new materials for cancer therapy. *J. Mater. Sci. Mater. Med.*, 2015, **26** (1), 5348.
- [12] Grigoriev V.V., Petrova L.N., et al. Antioxidant properties of water soluble amino acid derivatives of fullerenes and their role in the inhibition of herpes virus infection. *Russ. Chem. Bull. Int.*, 2011, **60**, P. 1172–1176.
- [13] Liang Bing Gan, Chu Ping Luo. Water-soluble fullerene derivatives, synthesis and characterization of β -alanine C_{60} adducts. *Chinese Chemical letters*, 1994, **4** (5), P. 275–278.
- [14] Safyannikov N.M., Charykov N.A., et al. Cryometry data in the binary systems bis-adduct of C_{60} and indispensable aminoacids – lysine, threonine, oxyproline. *Nanosystems: Physics, Chemistry, Mathematics*, 2018, **9** (1), P. 46–49.

- [15] Serebryakov E.B., Semenov K.N., et al. Physico-chemical properties of the C_{70} -L-lysine aqueous solutions. *J. of Molecule Liquids*, 2018, **256**, P. 507–518.
- [16] Semenov K.N., Iurev G.O., et al. Physico-Chemical properties of the C_{60} -L-lysine water solutions. *Journal of Molecular Liquids*, 2017, **225**, P. 767–777.
- [17] Semenov K.N., Meshcheriakov A.A., et al. Physico-chemical and biological properties of C_{60} -L-hydroxyproline water solutions. *RSC Advances*, 2017, **7**, P. 15189–15200.
- [18] Lelet M.I., Semenov K.N., et al. Thermodynamic and thermal properties of the C_{60} -L-lysine derivative. *J. Chem. Thermodynamics*, 2017, **115**, P. 7–11.
- [19] Semenov K.N., Charykov N.A., et al. Physico-chemical properties of the C_{60} -L-threonine water solutions. *Journal of Molecular Liquids*, 2017, **242**, P. 940–950.
- [20] Keskinov V.A., Semenov K.N., et al. Phase Diagrams of Fullereneol-d-LaCl₃-H₂O and Fullereneol-d-GdCl₃-H₂O Systems at 25 °C. *Russian Journal of Physical Chemistry A*, 2019, **93** (12), P. 2555–2558.
- [21] Semenov K.N., Charykov N.A., et al. Phase equilibria in fullerene-containing systems as a basis for development of manufacture and application processes for nanocarbon materials. *Russ. Chem. Rev.*, 2016, **85** (1), P. 38–59.
- [22] Pestov I.A., Keskinov V.A., et al. Solubility of $[C_{60}(=C(COOH)_2)_3]$ in the $[C_{60}(=C(COOH)_2)_3]$ -SmCl₃-H₂O Ternary System at 25 °C. *Russian Journal of Physical Chemistry A*, 2015, **89** (6), P. 998–1000.
- [23] Semenov K.N., Charykov N.A. Solubility Diagram of a Fullereneol-d-NaCl-H₂O System at 25 °C. *Rus. J. Phys. Chem.*, 2012, **86** (10), P. 1636–1639.
- [24] Semenov K.N., Keskinov V.A., et al. The fullereneol-d solubility in the fullereneol-d-inorganic salt-water ternary systems at 25 °C. *Industrial and engineering chemical research*, 2013, **52**, P. 16095–16100.
- [25] Gschneidner K., Eyring L. *Handbook on physics and chemistry of rare earths*. Amsterdam, New York, Oxford: North-Holland Publishing Company, 1978.
- [26] Korovin S.S., Zimina G.V., et al. *Rare and scattered elements. Chemistry and technology*. In 3 books. Book 1: Textbook for universities. Ed. Korovin S.S., M.: MISIS, 1996, 376 p. (In Russian)
- [27] Charykov N.A., Charykova M.V., et al. Multiphase Open Phase Processes Differential Equations. *Processes*, 2019, **3** (7), P. 148–167.
- [28] Charykova M.V., Charykov N.A. *Thermodynamic modeling of evaporite sedimentation processes*. St. Petersburg: Nauka, 2003, 262 p.
- [29] Semenov K.N., Charykov N.A., et al. Fullerenols: Physicochemical properties and applications. *Progress in Solid State Chemistry*, 2016, **44** (2), P. 59–74.

Synthesis and magnetic properties of PrFeO₃ nanopowders by the co-precipitation method using ethanol

A. T. Nguyen¹, V. Y. Nguyen^{2,3}, I. Ya. Mittova⁴, V. O. Mittova⁵, E. L. Viryutina⁴,
C. Ch. T. Hoang¹, Tr. L. T. Nguyen¹, X. V. Bui⁶, T. H. Do⁷

¹Ho Chi Minh City University of Education, Ho Chi Minh City, 700000, Vietnam

²Institute of Theoretical and Applied Research, Duy Tan University, Ha Noi, 100000, Vietnam

³Faculty of Natural Sciences, Duy Tan University, Da Nang, 550000, Vietnam

⁴Voronezh State University, Universitetskaya pl.1, Voronezh, 394018, Russia

⁵Burdenko Voronezh State Medical University, Voronezh, 394036, Russia

⁶Faculty of Pedagogy in Natural Sciences, Sai Gon University, Ho Chi Minh City, 700000, Vietnam

⁷Thai Nguyen University of Education, Thai Nguyen University, Vietnam

tienna@hcmue.edu.vn, nguyenvanyen@duytan.edu.vn, imittova@mail.ru, vmittova@mail.ru,

viryutina.helena@yandex.ru,htcamchuong92@gmail.com, linhntt@hcmue.edu.vn,

buiquanvuongsgu@gmail.com, huongdt.chem@tinue.edu.vn

DOI 10.17586/2220-8054-2020-11-4-468-473

Praseodymium orthoferrite nanoparticles were synthesized by a simple co-precipitation method via the hydrolysis of Pr (III) and Fe (III) cations in boiling ethanol with 5% aqueous ammonia. The single-phase PrFeO₃ product formed after annealing the precipitates at 650, 750, and 850°C for 1 h had an average crystal size of 20–30 nm (XRD, SEM, TEM). The synthesized nanopowders were soft ferromagnetic materials with low coercive force and excessive magnetization values.

Keywords: o-PrFeO₃, nanoparticles, magnetic properties, co-precipitation, ethanol.

Received: 28 May 2020

Revised: 29 June 2020

1. Introduction

Among semiconductors, oxides with a perovskite-like structure of the ReMeO₃ type (Re – rare-earth elements; Me – transition metals) have both significance and importance for their application and fundamental research [1–8], since these oxides have a high sensitivity of properties to decrease in particle size to nanometer values. Among the rare-earth orthoferrites, PrFeO₃ was obtained and used in some fields, such as magneto-optical devices and electromagnetic equipment [9–13], photocatalysts [14–16], dyes, and inorganic pigments [17, 18].

A wide variety of techniques have been developed for the synthesis of praseodymium orthoferrite nanoparticles (o-PrFeO₃), for example, high-temperature ceramic fabrication [9, 11, 18], hydrothermal methods [13, 16], and sol-gel complex methods [14, 15, 17, 19]. Several studies [20–25] describe the formation of ReFe_{1-x}M_xO₃ orthoferrites nanoparticles (Re = Nd, Y, La; M = Mn, Co, Ni), by a simple co-precipitation method in boiling water followed by the addition of appropriate precipitants. According to published data, the replacement of water as a solvent with ethanol for the synthesis of o-PrFeO₃ nanoparticles was not studied.

The goal of this study the synthesis of praseodymium orthoferrite (o-PrFeO₃) nanoparticles with low coercive force and excessive magnetization by co-precipitation via hydrolysis of praseodymium (III) and iron (III) cations in boiling ethanol with the addition of an ammonia solution.

2. Experimental

In this study, we used Pr(NO₃)₃·6H₂O, Fe(NO₃)₃·9H₂O, absolute ethanol (d=0.79 g/ml), 25 % ammonia solution (d=0.901 g/ml) (all reagents were of CP grade), distilled water. The procedure for PrFeO₃ nanoparticles synthesis was similar to that of ReFeO₃ (Re = Nd, Y, La) nanomaterials [20, 21], with ethanol as the solvent instead of water.

Complex thermal analysis of the PrFeO₃ sample was carried out TG-DSC analyzer (Labsys Evo, TG-DSC 1600°C, SETARAM Instrumentation). The sample was placed in a platinum cylindrical crucible and heated from 30 to 1000°C at 10 K min⁻¹ in dried air. X-ray phase analysis was carried out on a D8-ADVANCE diffractometer (CuK α radiation, $\lambda = 0.15418$ Å). The qualitative and quantitative elemental composition was established using a local X-ray spectral microanalysis (EDX, Horiba H-7593). Particle size and morphology were determined using

scanning electron microscopy (FESEM S-4800) and high voltage transmission electron microscopy (HRTEM; JEOL-1400). The average crystal size was determined according to the Debye Scherrer equation; parameters *a*, *b*, *c* and the unit cell volume *V* were determined using the Rietveld method, implemented in the X'pert High Score Plus 2.2b software package.

The magnetic characteristics of PrFeO₃ nanopowders (coercive force *H_c*, remanent magnetization *M_r*, and magnetization *M_s*) were studied using vibrating sample magnetometer at room temperature (VSM, MICROSENE EV11).

3. Results and discussions

The complex thermal analysis of the dried precipitate showed (Fig. 1) that the mass loss during heating of the sample in the range of 60–1000°C was 27.01 %. The most significant mass loss (about 25.85 %) was observed in the range of 50–600°C. The processes occurring during heating of the precipitate were accompanied by three endothermic thermal effects at 93.38, 327.62, and 420.78°C (Fig. 1), characteristic for water evaporation, decomposition of iron (III) hydroxides and praseodymium (III) (20, 26 In the 600–700°C range, an exothermic thermal effect (636.10°C, Fig. 1) was observed corresponding to the formation of perovskite PrFeO₃.

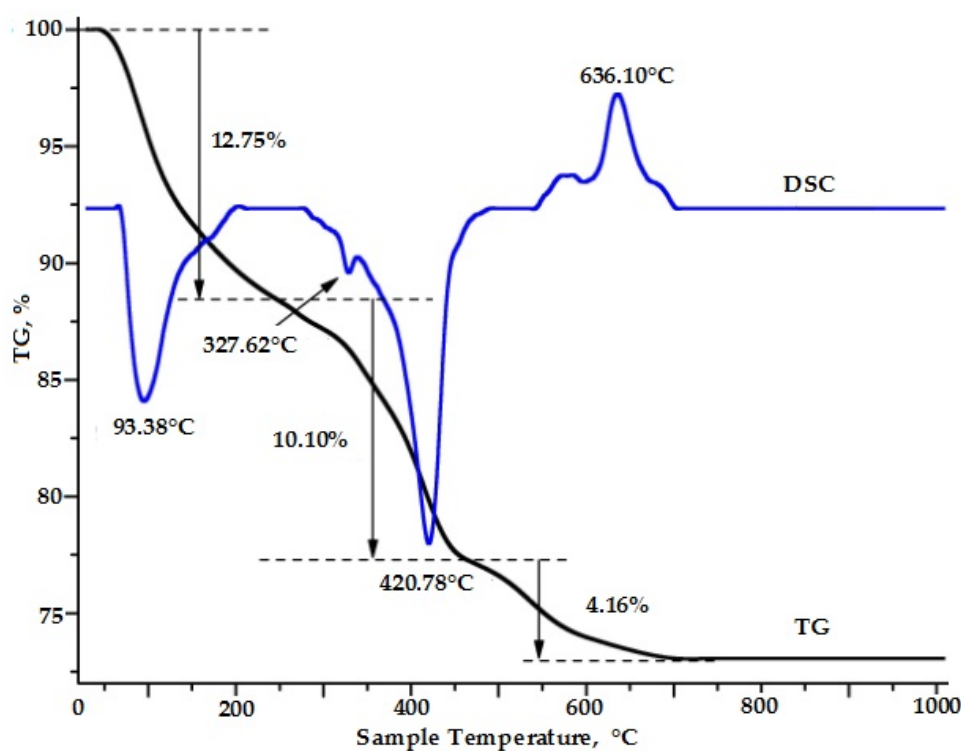


FIG. 1. TG-DSC curves of the powders prepared by a simple co-precipitation method using ethanol

In accordance with the data of complex thermal analysis for the synthesis of praseodymium orthoferrite, the temperatures of 650, 750 and 850°C were chosen to calcine the precipitate for 1 h. XRD patterns of the samples annealed at 650, 750, and 850°C for 1 h showed single-phase orthoferrite PrFeO₃ (JCPDC No 00-047-0065) (Fig. 2). The average crystal diameter and cell volume of PrFeO₃ samples increase with increasing annealing temperature, (Table 1).

According to the results of local X-ray spectral microanalysis, PrFeO₃ sample contained only three elements – Pr, Fe, and O (Fig. 4). Mass percentage and elemental percentage of obtained PrFeO₃ nanopowders are rather close to expected chemical composition (Fig. 4). It can be seen from SEM, TEM, and HRTEM images (Fig. 5) that, after annealing at 750°C for 1 h, PrFeO₃ nanoparticles were isometric, and the average size of individual particles was about 30 nm. Interestingly, the synthesized PrFeO₃ nanoparticles were characterized by a lower degree of agglomeration compared to the orthoferrites of other rare-earth elements, such as NdFeO₃ [20], YFeO₃ [21], and LaFeO₃ [25], obtained by the co-precipitation method via the hydrolysis of cations in boiling water. This was explained by the fact that a lower polarity of ethanol than water (the dipole moments of water and ethanol are 1.85 and 1.66 D, respectively [26, 27]) led to an insignificant interaction between the cations of iron (III) and praseodymium (III) with

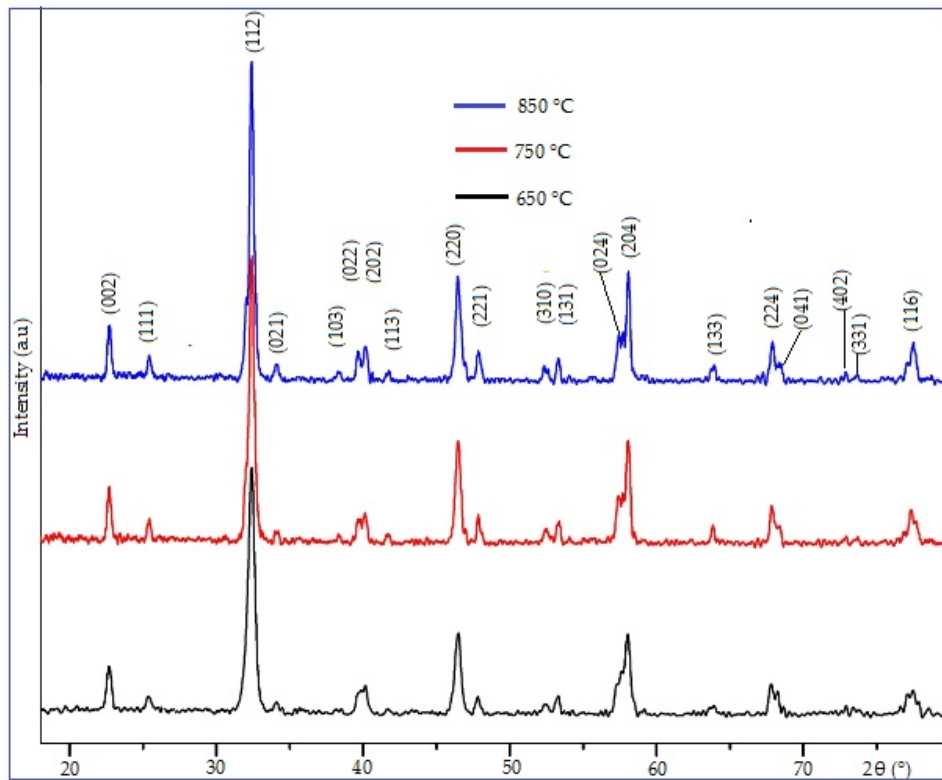


FIG. 2. XRD patterns of PrFeO_3 nanopowders annealed at 650, 750, and 850°C for 1 h

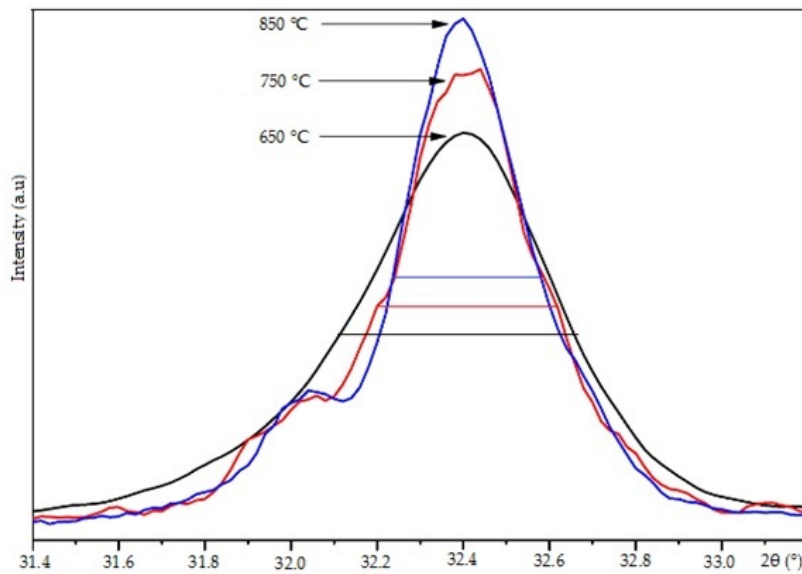


FIG. 3. Slow-scan XRD patterns of peak (121) of PrFeO_3 nanopowders annealed at 650, 750, and 850°C for 1 h

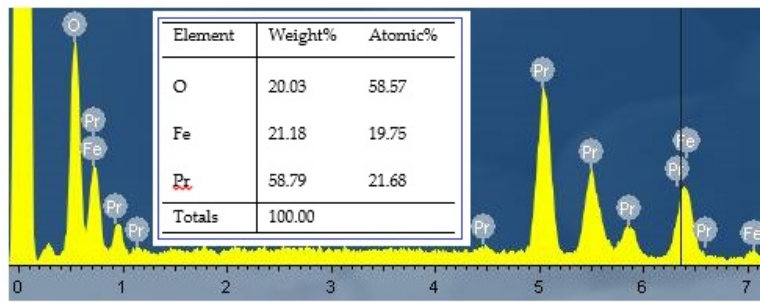


FIG. 4. EDX image of PrFeO₃ sample annealed at 750°C for 1 h

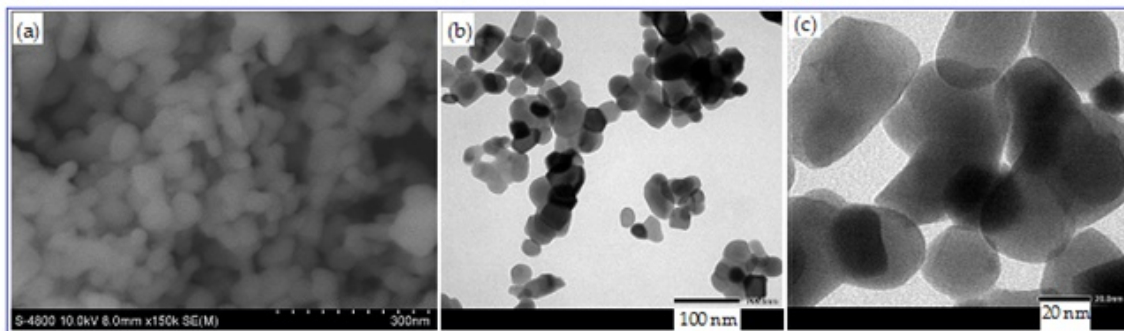


FIG. 5. SEM (a), TEM (b), and HRTEM (c) images of PrFeO₃ nanoparticles annealed at 750°C for 1 h

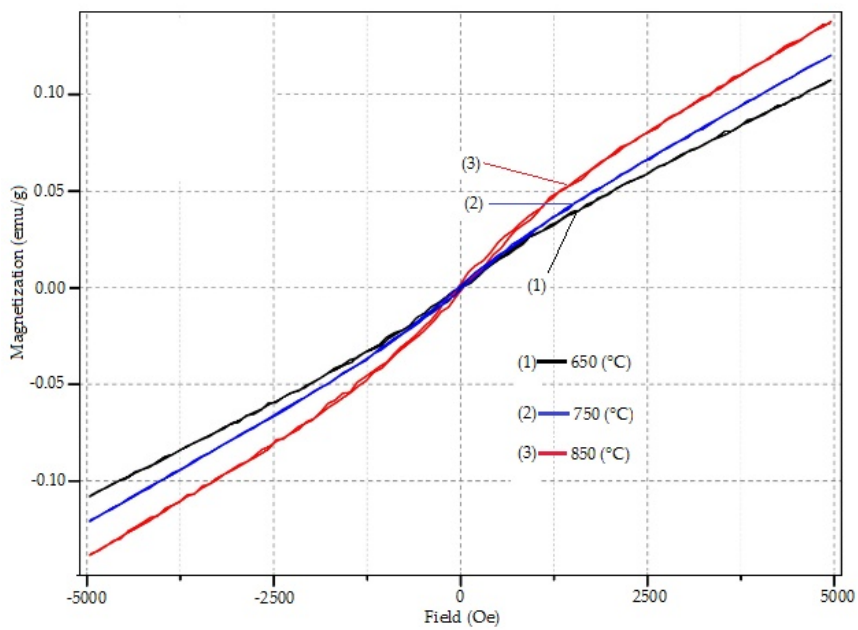


FIG. 6. Field dependence of the magnetization of PrFeO₃ nanopowders, annealed at 650, 750, and 850°C for 1 h

TABLE 1. XRD patterns of PrFeO₃ nanopowders annealed at 650, 750, and 850°C for 1 h

Indices	PrFeO ₃		
	650°C	750°C	850°C
a, Å	5.4576	5.4732	5.4513
b, Å	5.5742	5.5831	5.6207
c, Å	7.8110	7.7995	7.8178
Volume, Å ³	237.62	238.33	239.54
Average crystal diameter, nm	19.73	22.37	25.48
Coercive force H _c , Oe	17.45	29.45	33.38
Remanent magnetization M _r , emu/g	0.44·10 ⁻³	1.10·10 ⁻³	1.77·10 ⁻³
Magnetization M, emu/g	0.11	0.12	0.14

ethanol molecules. Accordingly, the formed sediment particles were more easily separated from each other and from the solvent.

The study of PrFeO₃ samples using the magnetometer MICROSENE EV11 at 300 K in a maximum field of 5000 Oe showed that all certain magnetic characteristics H_c, M_r and M_s (Fig. 6, Table 1). Probably, this was due to the fact that annealing at a higher temperature led to larger PrFeO₃ particles (Table 1). Nanoscale particles (*D* < 100 nm) can be considered as single-domain particles. Then, H_c depends on the particle size according to the following formula [28]:

$$H_c = g - \frac{h}{D^{3/2}} \quad (1)$$

where *g* and *h* are constants, and *D* is the particle diameter. Clearly, H_c will increase with the particle size. Indeed, when the crystallite size rises from 19.73 to 25.48 nm, H_c also increases from 17.45 to 33.38 Oe. A similar pattern was observed in [25]. It is more interesting that the synthesized PrFeO₃ nanocrystals were characterized by lower H_c and M_r values, but higher M_s at 300 K compared to the orthoferrite particles of other rare-earth elements, such as HoFeO₃ (H_c=2659 Oe, M_r=4.08, [29]), LaFeO₃ (H_c=1217.6 Oe, M_r=5.43·10⁻⁴ emu/g, M_s=6.49·10⁻³ emu/g, [30]), NdFeO₃ (H_c ~850 Oe, M_r=1.5 emu/g, [31]) and even o-PrFeO₃ (M_s=0.05 emu/g, [13]).

The studied o-PrFeO₃ samples with low values of coercive force, excess magnetization, and higher magnetization not reaching magnetic saturation at a maximum field of 5000 Oe were a soft magnetic ferromagnet and can be used for the manufacture of magnetic cores, transformers, electric motors, and generators.

4. Conclusion

In this study, o-PrFeO₃ nanoparticles with an average crystal size < 30 nm were formed by co-precipitation method by aqueous ammonia solution via simple process of the hydrolysis of Pr (III) and Fe (III) cations in boiling ethanol, followed by annealing at 650, 750, and 850°C for 1 h. The synthesized o-PrFeO₃ nanopowders were characterized by a narrow hysteresis loop, low values of excess magnetization and coercive force, but high magnetization, which makes them promising for use as soft ferromagnetic material in the manufacture of magnetic cores, transformers, electric motors, generators, and radio engineering.

Conflict of interests

The authors maintain that they have no conflict of interest with respect to this communication.

Acknowledgements

Nguyen Anh Tien thanks the financial support of Ho Chi Minh City University of Education, Ho Chi Minh City, Vietnam through Grant No. CS.2019.19.19.

References

- [1] Popkov V.I., Almjasheva O.V., Nevedomskii V.N., Panchuk V.V., Semenov V.G., Gusarov V.V. Effect of spatial constraints on the phase evolution of YFeO₃-based nanopowders under heat treatment of glycine-nitrate combustion products. *Ceramics International*, 2018, **44**(17), P. 20906–20912.
- [2] Bachina A., Ivanov V.A., Popkov V.I. Peculiarities of LaFeO₃ nanocrystals formation via glycine-nitrate combustion, *Nanosystems: Physics, Chemistry, Mathematics*, 2017, **8**(5), P. 647–653.
- [3] Shanker J., Rao G.N., Venkataramana K., Babu D.S., Investigation of structural and electrical properties of NdFeO₃ perovskite nanocrystalline. *Physics Letter A*, 2018, **382**(4), P. 2974–2977.
- [4] H. El Moussaoui, Mounkachi O., Masrou R., Hamedoun M., Hlil E.K., Benyoussef A. Synthesis and super-paramagnetic properties of neodymium ferrites nanorods. *Journal of Alloys and Compounds*, 2013, **581**, P. 776–781.
- [5] Zh.-Qi. Wang, Ya.-Sh. Lan, Zh.-Yi. Zeng, X-R. Chen, Q.-F. Chen. Magnetic structures and optical properties of rare-earth orthoferrites RFeO₃ (R = Ho, Er, Tm and Lu). *Solid State Communications*, 2018.
- [6] Jeffrey W. Fergus, Perovskite oxides for semiconductor-based gas sensors. *Sensors and Actuators B: Chemical*, 2007, **123**(2), P. 1169–1179.
- [7] Popkov V.I., Tugova E.A., Bachina A.K., Almjasheva O.V. The formation of nanocrystalline orthoferrites of rare-earth elements XFeO₃ (X = Y, La, Gd) via heat treatment of co-precipitated hydroxides. *Russian Journal of General Chemistry*, 2017, **87**(11), P. 1771–1780.
- [8] Kondrashkova I.S., Martinson K.D., Zakharova N.V., Popkov V.I. Synthesis of nanocrystalline HoFeO₃ photocatalyst via heat treatment of products of glycine-nitrate combustion. *Russian Journal of General Chemistry*, 2018, **88**(12), P. 2465–2471.
- [9] Abdellahi M., Abhari A.Sh., Bahmanpour M. Preparation and characterization of orthoferrite PrFeO₃ nanoceramic. *Ceramics International*, 2016, **42**(4), P. 4637–4641.
- [10] Sultan K., Ikram M., Asokan K. Structural, optical and dielectric study of Mn doped PrFeO₃ ceramics. *Vacuum*, 2014, **99**, P. 251–258.
- [11] Panchwane A., Reddy V.R., Gupta A. Electrical and Mossbauer study of polycrystalline PrFeO₃. *Journal of Physics: Conference Series*, 2016, **755**, P. 012033.
- [12] Mir F.A., Sharma S.K., Ravi Kumar. Magnetization and magneto-transport properties of Ni-doped PrFeO₃ thin film. *Chinese Physics B*, 2014, **23**(4), P. 048101.
- [13] Zhou Zh., Guo L., Yang H., Liu Q., Ye F. Hydrothermal synthesis and magnetic properties of multiferroic rare-earth orthoferrites. *Journal of Alloys and Compounds*, 2014, **583**, P. 21–31.
- [14] Tijare S.N., Bakardjieva S., Subrt J., Joshi M.V., Rayalu S.S., Hishita S., Labhsetwar N. Synthesis and visible light photocatalytic activity of nanocrystalline PrFeO₃ perovskite for hydrogen generation in ethanol-water system. *Journal of Chemical Sciences*, 2014, **126**(2), P. 517–525.
- [15] Peisong T., Xinyu X., Haifeng Ch., Chunyan L., Yangbin D., Synthesis of nanoparticulate PrFeO₃ by sol-gel method and its visible-light photocatalytic activity. *Ferroelectrics*, 2019, **546**, P. 181–187.
- [16] Megarajan S.K., Rayalu S., Nishibori M., Labhsetwar N. Improved catalytic activity of PrMO₃ (M = Co and Fe) perovskite: synthesis of thermally stable nanoparticles by a novel hydrothermal method, *New Journal Chemistry*, 2015, **39**, P. 2342–2348.
- [17] Opuhovici O., Kreiza G., Senvaitiene J., Kazlauskas K., Beganskiene A., Kareiva A. Sol-gel synthesis, characterization and application of selected sub-microsized lanthanide (Ce, Pr, Nd, Tb) ferrites. *Dyes and Pigments*, 2015, **118**, P. 176–182.
- [18] Luxova J., Sulcova P., Trojan M. Influence of firing temperature on the color properties orthoferrite PrFeO₃. *Thermochimica Acta*, 2014, **579**, P. 80–85.
- [19] Pekinchak O., Vasylechko L., Lutsyuk I., Vakhula Ya., Prots Yu., Carrillo-Cabrela W. Sol-gel-prepared nanoparticles of mixed praseodymium cobaltites-ferrites. *Nanoscale Research Letters*, 2016, **11**(75).
- [20] Nguyen T.A., Pham V., Pham T.L., Nguyen L.T.Tr., Mittova I.Ya., Mittova V.O., Vo L.N., Nguyen B.T.T., Bui V.X., Viryutina E.L. Simple synthesis of NdFeO₃ by the so-precipitation method based on a study of thermal behaviors of Fe (III) and Nd (III) hydroxides. *Crystals*, 2020, **10**, P. 219.
- [21] Nguyen A.T., Almjasheva O.V., Mittova I.Ya., Stognei O.V., Soldatenko S.A. Synthesis and magnetic properties of YFeO₃ nanocrystals. *Inorganic Materials*, 2009, **45**(11), P. 1304–1308.
- [22] Nguyen A.T., Mittova I.Ya., Almjasheva O.V., Kirillova S.A., Gusarov V.V. Influence of the precipitation conditions on the size and morphology of nanocrystalline lanthanum orthoferrite. *Glass Physics and Chemistry*, 2008, **34**(6), P. 756–761.
- [23] Nguyen A.T., Vinh N.T. Pham, Nguyen T.Tr.L., Mittova V.O., Vo Q.M., Berezhnaya M.V., Mittova I.Ya., Do Tr.H., Chau H.D. Crystal structure and magnetic properties of perovskite YFe_{1-x}Mn_xO₃ nanopowders synthesized by co-precipitation method. *Solid State Sciences*, 2019, **96**, P. 105922.
- [24] Nguyen A.T., Chau H.D., Tr.L. Nguyen Thi, Mittova V.O., Do Tr.H., Mittova I.Ya. Structural and magnetic properties of YFe_{1-x}Co_xO₃ (0.1 ≤ x ≤ 0.5) perovskite nanomaterials synthesized by co-precipitation method. *Nanosystems: Physics, Chemistry, Mathematics*, 2018, **9**(3), P. 424–429.
- [25] Tien A. Nguyen, Vinh N.T. Pham, Hanh T. Le, Diem H. Chau, Mittova V.O., Linh T.Tr. Nguyen, D.A. Dinh, T.V. Nhan Hao, I.Ya. Mittova. Crystal structure and magnetic properties of LaFe_{1-x}Ni_xO₃ nanomaterials prepared via a simple co-precipitation method. *Ceramics International*, 2019, **45**, P. 21768–21772.
- [26] Housecroft C.E., Sharpe A.G. *Inorganic Chemistry*, second ed., Pearson, Prentice Hall, 2005.
- [27] David Klein. *Organic Chemistry*, 2-nd edition, Wiley, 2016, chapt 13.
- [28] Cullity B.D., Graham C.D. *Introduction to Magnetic Materials*. John Wiley and Sons, Piscataway, NJ, 2011.
- [29] Habib Z., Majid K., Ikram M., Sultan Kh. Influence of Ni substitution at B-site for Fe³⁺ ions on morphological, optical, and magnetic properties of HoFeO₃ ceramics. *Applied Physics A. Materials Science & Processing*, 2016, **122**(550).
- [30] Sasikala C., Durairaj N., Baskaran I., Sathyaseelan B., Henini M. Transition metal titanium (Ti) doped LaFeO₃ nanoparticles for enhanced optical structure and magnetic properties. *Journal of Alloys and Compounds*, 2017, **712**, P. 870–877.
- [31] Babu P.R., Babu R. Starch assisted sol-gel synthesis and characterization of NdFeO₃. *International Journal of ChemTech Research*, 2016, **9**(4), P. 364–369.

The effect of MgO additive on the g-C₃N₄ performance in electrochemical reforming of water-ethanol solution

M. I. Chebanenko^{1,*}, K. D. Martinson¹, I. V. Matsukevich², V. I. Popkov¹

¹Ioffe Institute, St. Petersburg, 194021, Russia

²Institute of General and Inorganic Chemistry of the National Academy of Sciences of Belarus,
Minsk BY-220072, Republic of Belarus

*m_chebanenko@list.ru

PACS 82.45.Yz

DOI 10.17586/2220-8054-2020-11-4-474-479

In this work, a simple wet-chemical route was proposed to synthesize g-C₃N₄/MgO (5% wt.) with enhanced electrocatalytic activity toward hydrogen evolution from water-ethanol (10% vol.) solution. It was found that synthesized nanocomposite is a single phase and chemically pure, consisting of graphitic carbon nitride (g-C₃N₄) and cubic magnesium oxide (MgO, periclase) with an average crystallite size of 15.5 nm and 9.5 nm, respectively. It was shown that magnesia nanoparticles are evenly distributed on the surface of g-C₃N₄ nanosheets and uniform distribution of components is observed over the nanocomposite volume. It was found that this feature leads to an improvement in the electrocatalytic characteristics of the synthesized nanocomposite. So, the g-C₃N₄/MgO-coated electrode has an overpotential of –251 mV, which is better than for a g-C₃N₄-coated (–264 mV) or pure nickel (–293 mV) electrode. Moreover, the nanocomposite-based electrode possesses a low Tafel slope (–106.7 mV/dec) and high cyclic and chronopotentiometry stability.

Keywords: graphitic carbon nitride, magnesia, nanopowders, electrocatalytic reforming, hydrogen evolution reaction.

Received: 8 June 2020

Revised: 16 July 2020

1. Introduction

Currently, the production of hydrogen using photo- and electrocatalytic conversion of solar energy into chemical energy seems to be a rather promising solution for main problems associated with environmental and energy crises [1]. The key task, in this case, is the search for an inexpensive and effective photo- and electrocatalysts exhibiting activity under the influence of visible light and effective electron transfer. Among them, the graphite-like carbon nitride (g-C₃N₄) stands out, which is a semiconductor with high stability, and photo- and electrocatalytic activity [2–4]. At the same time, in its pure form, graphite-like carbon nitride is characterized by a low specific surface area, a lack of active centers on its surface, rapid recombination of photogenerated electron-hole pairs, and a wide bandgap (2.7 eV), which all together causes insufficiently high photo- and electrocatalytic activity [5, 6].

But the synthesis of heterogeneous structures based on graphite-like carbon nitride and some oxide can neutralize the disadvantages mentioned above. For example, it was shown that the preparation of the g-C₃N₄/MgO nanocomposite allows one to achieve a high rate of hydrogen evolution – up to 30.1 μmol/h in the photoinduced hydrogen evolution reaction (HER) process, which is almost 6 times higher than for pure graphite-like carbon nitride [7]. The authors explain this by the fact that in this case, the presence of a heterojunction possesses quick transfer of photoinduced electrons from the conduction band of g-C₃N₄ to the conduction band of MgO, which contributes to a significant separation of photoinduced electrons and holes and effectively suppresses the recombination of electron-hole pairs. Moreover, it can be assumed that the intercalation of magnesium oxide into the interlayer space of graphite-like carbon nitride may lead to the enhanced specific surface area providing higher catalytic activity of obtained nanocomposite.

However, another important direction of hydrogen production is through the electrocatalytic reforming of aqueous-ethanol solutions using catalysts based on graphite-like carbon nitride nanocomposites is still largely unexplored. In the case of g-C₃N₄/MgO nanocomposite, the mesoporous g-C₃N₄ can be tuned by different amounts of MgO to significantly enhance its electrocatalytic performance and reduce the absolute value of its overpotential. However, previously it was shown that an excessive amount of second component (MgO) may also decrease the activity and stability of g-C₃N₄ [8]. Based on this work 5 wt% can be considered as optimal MgO content for g-C₃N₄/MgO electrocatalyst production. Thus, this work aimed to synthesize and complex study the structural, morphological, and electrochemical features of the g-C₃N₄/MgO nanocomposite. A simple wet-chemistry technique is proposed to synthesize a nanocomposite of graphitic carbon nitride and magnesium oxide as a promising material for hydrogen production from water-ethanol solution. A comprehensive study of the structure and morphology of g-C₃N₄/MgO was

carried out using the complex physicochemical analysis to better understand the origin of its enhanced electrocatalytic activity.

2. Experimental section

2.1. Synthesis procedure

The nanopowder of the initial graphitic carbon nitride ($g\text{-C}_3\text{N}_4$) was synthesized by heat treatment of urea ($(\text{NH}_2)_2\text{CO}$) under aerobic conditions. A detailed description of its synthesis procedure and preparation of a $g\text{-C}_3\text{N}_4$ -based colloidal solution was previously given in [9, 10]. After homogenization, 1.5 mg of magnesium acetate tetrahydrate ($\text{Mg}(\text{CH}_3\text{COO})_2 \cdot 4\text{H}_2\text{O}$ or $\text{Mg}(\text{Ac})_2 \cdot 4\text{H}_2\text{O}$) was dissolved in 10 ml of distilled water using magnetic stirring. The mixture then was evaporated at 100°C and calcined at 350°C for 30 minutes followed by grinding. As a result, initial $g\text{-C}_3\text{N}_4$ powder and $g\text{-C}_3\text{N}_4/\text{MgO}$ nanocomposite (mass fraction of magnesia is 5%) were prepared. MgO to $g\text{-C}_3\text{N}_4$ proportion was selected based on [8] work. The generalized synthesis scheme of both $g\text{-C}_3\text{N}_4$ and $g\text{-C}_3\text{N}_4/\text{MgO}$ shown in Fig. 1. All the chemicals used were of analytical grade.

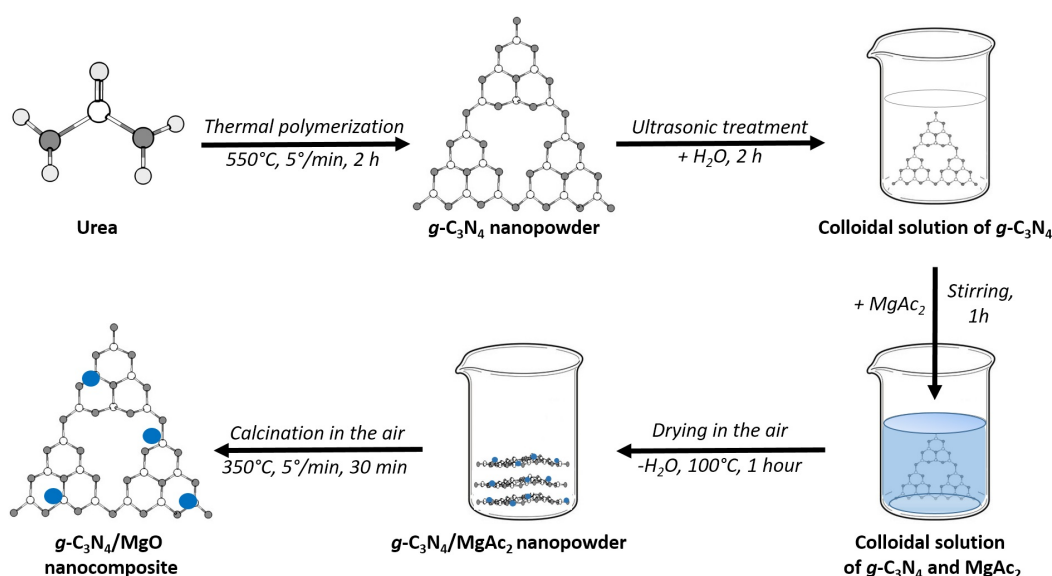


FIG. 1. Schematic representation of the synthesis procedure for $g\text{-C}_3\text{N}_4$ and $g\text{-C}_3\text{N}_4/\text{MgO}$ nanopowders

2.2. Physicochemical characterization

The elemental composition and morphology of the synthesized samples were studied by energy-dispersive X-ray spectroscopy (EDS) and scanning electron microscopy (SEM) using Tescan Vega 3 SBH scanning electron microscope equipped with an Oxford INCA x-act X-ray microanalysis device. An Oxford Instruments INCA system was used for chemical analysis, including both line scan EDS and elemental mapping utilizing a 10 nm probe size. All concentration profiles were plotted using elements percentage. SEM-images of the samples were acquired in both SE (morphological contrast) and BSE (phase contrast) modes. X-ray phase analysis was performed on a Rigaku SmartLab 3 X-ray powder diffractometer ($\text{CuK}\alpha$ radiation, $\lambda = 0.154051$ nm, Bragg angle range $10\text{--}80^\circ$), phase analysis of the compositions was performed using JCPDS PDF-2 database. The average crystallite size (coherent-scattering regions) was calculated from the broadening of X-ray diffraction lines using the fundamental parameter method implemented in the SmartLab Studio II software.

2.3. Electrocatalytic performance

The electrochemical measurements were carried out on Elins P20X potentiostat using a three-electrode cell. The working electrode was a nickel (Ni) substrate used as a reference or initial $g\text{-C}_3\text{N}_4$ and $g\text{-C}_3\text{N}_4/\text{MgO}$ nanocomposite deposited on a Ni substrate as a suspension from a 0.5% solution of Nafion in isopropyl alcohol. Ag/AgCl and platinum electrodes were used as reference and counter electrodes, respectively. The overpotentials values were calibrated with respect to the reversible hydrogen electrode (ERHE) according to the Nernst equation. All measurements were carried out at standard conditions ($T=25^\circ\text{C}$, $P=1$ atm.) in an aqueous solution consisting of ethanol $\text{C}_2\text{H}_5\text{OH}$ (10% vol.) and

1M KOH (pH = 14). Cyclic CV curves were taken in the potential range from open circuit potential to 1.5 V with a sweep rate of 5-10 mV/s. Qualitatively, the working overpotential of the sample was determined from the CV curves at a current density of 10 mA/cm². Electrocatalytic stability of the g-C₃N₄/MgO-based electrode was additionally characterized by cyclic voltammetry (100 cycles) and chronopotentiometry (10000 s). Electrochemical measurements were performed without IR-compensation.

3. Results and discussion

The EDS investigations were performed to obtain information about the gross chemical composition of the g-C₃N₄/MgO sample. Five different areas were selected in the sample for analysis to ensure the representativeness (Fig. 2(a)). It was shown that the typical EDS spectrum contains the lines that can be assigned to Mg, O, C and N elements (Fig. 2(b)). The quantitative elemental composition of the sample in the selected areas and on average indicates its compliance with the composition planned in the synthesis. Thus, the EDS results confirm that MgO weight fraction in g-C₃N₄/MgO nanocomposite is 5% within a method error. Further, this sample will be designated as g-C₃N₄/5%MgO.

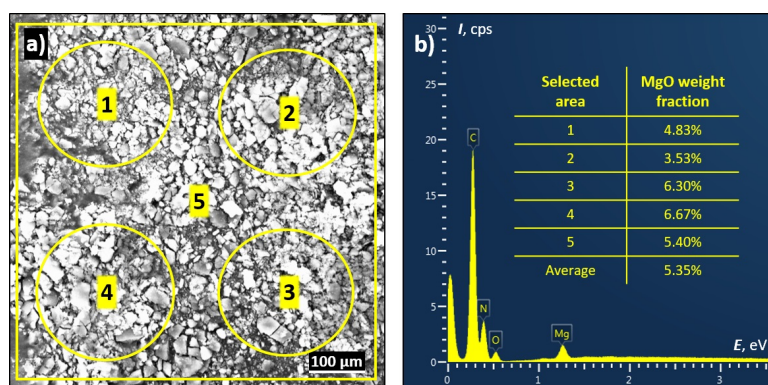


FIG. 2. Results of the selected area EDS analysis of g-C₃N₄/MgO nanocomposite: (a) SEM image of the sample and selected areas, (b) EDS spectrum of area #5. The table inset in (b) shows data on the MgO weight fraction in g-C₃N₄/MgO nanocomposite by selected areas and on average

The overview SEM image of the g-C₃N₄/MgO nanocomposite in BSE mode and the distribution of C, N, Mg and O elements on its surface are presented in Fig. 3. The BSE SEM image (Fig. 3(a)) does not show any phase contrast in the synthesized sample. The element mapping of both individual (Fig. 3(b-e)) and superposed (f) elements confirms the homogeneous distribution of all the elements in the g-C₃N₄/MgO nanocomposite without the formation of any clusters of individual MgO or g-C₃N₄ phases on a microscale.

Figure 4 shows the SEM images of g-C₃N₄/5%MgO nanocomposite at different magnification acquired in SE mode. As one can see the morphology of g-C₃N₄, which is the main component of g-C₃N₄/5%MgO nanocomposite (95% wt.), at low magnifications (Fig. 4(a,b)) is quite lumpy with a large number of micron-size aggregates. But at higher magnification (Fig. 4(c)), it becomes clear that each such aggregates consist of individual g-C₃N₄ nanosheets, some of which are gradually flaked off. Besides, in Fig. 4(b,c), it can be seen that MgO nanoparticles are also present and contrastingly differ from graphitic carbon nitride; it's clear that these nanoparticles are evenly distributed over the surface of g-C₃N₄ nanosheets. Thus, even at the nanoscale, the synthesized g-C₃N₄/5%MgO nanocomposite is characterized by a high homogeneity of the spatial distribution of the main components.

Figure 5 shows the PXRD patterns of initial g-C₃N₄ and g-C₃N₄/MgO (5%) nanocomposite. In the case of pure g-C₃N₄, there are two distinct well-defined diffraction peaks at 13.6 and 27.7 degrees, related to the (100) and (002) diffraction planes of graphitic carbon nitride (JCPDS 87-1526). The diffraction pattern of g-C₃N₄/5%MgO nanocomposite shows additional peaks located at 36.8°, 43.2°, 62.5° that can be attributed to (111), (200), (220) planes of magnesia (MgO) with periclase cubic structure (JCPDS 78-0430). As can be seen from the inset in Fig. 5, the average crystallite size of g-C₃N₄ in pure form and nanocomposite is 16.9 nm and 15.5 nm, correspondingly. This decrease in the crystallite size can be associated with the influence of magnesium oxide, which can be formed between individual g-C₃N₄ nanosheets during the synthesis and thereby lead to partial exfoliation of graphitic carbon nitride. These results also confirmed that MgO nanoparticles with an average crystallite size of 9.5 nm are preferably formed in close contact with g-C₃N₄.

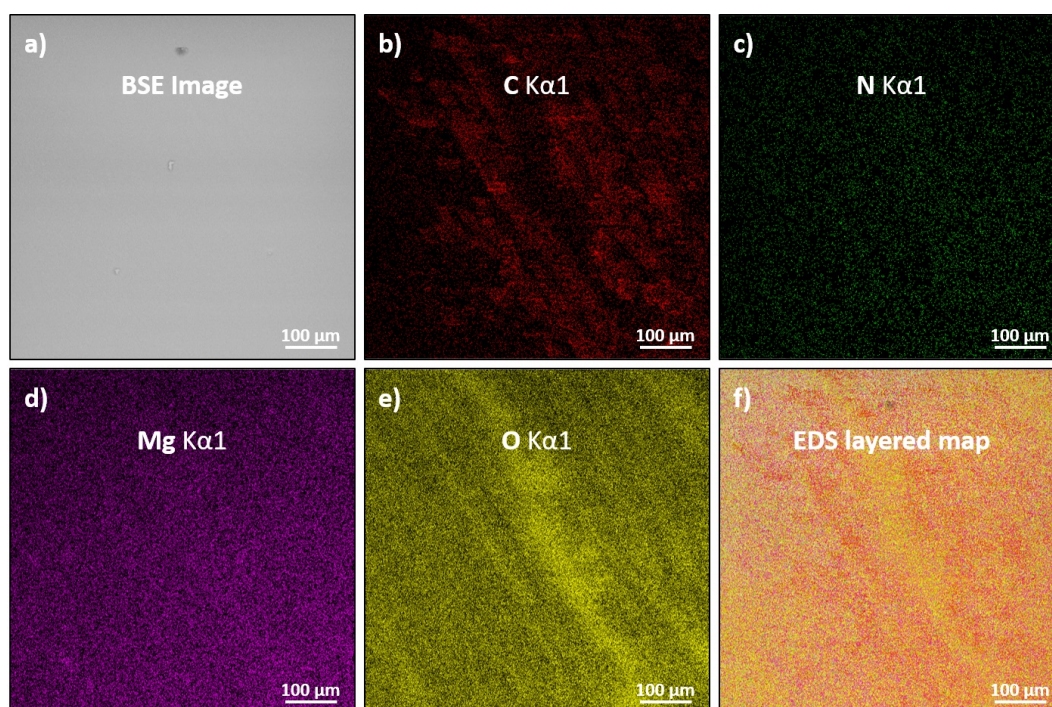


FIG. 3. EDS mapping of g-C₃N₄/5%MgO nanocomposite: (a) SEM image of the area under analysis in BSE mode, (b) carbon (C K α 1) mapping, (c) nitrogen (N K α 1) mapping, (d) magnesium (Mg K α 1) mapping, (e) oxygen (O K α 1) mapping, (f) EDS layered map as a result of (b–e) maps superposition

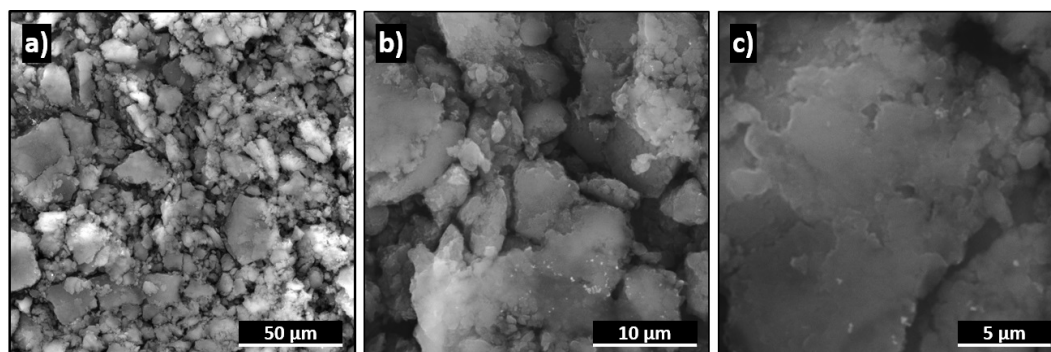


FIG. 4. SEM images of g-C₃N₄/5%MgO nanocomposite at different magnifications (a–c)

A linear potential sweep method with a constant sweep speed of 10 mV/s was used as the main measurement procedure to evaluate the electrocatalytic activity of the synthesized g-C₃N₄/5%MgO nanocomposite with respect to pure Ni substrate and initial g-C₃N₄ (Fig. 6). As shown in Fig. 6(a), the overpotential on a Ni substrate at a current density of 10 mA/cm² is 293 mV, which matches to the literature data [11]. In the case of g-C₃N₄ and g-C₃N₄/MgO nanocomposite, the overpotential value at the same current density is 264 and 251 mV, respectively. This overpotential value (–251 mV) for the nanocomposite is significantly lower than for known MgO-based electrocatalysts [12]. The observed reduction in overpotential of the g-C₃N₄-coated electrodes with the MgO addition can be explained by the higher surface area and morphological features of nanocomposite which promote free removal of evolved hydrogen bubbles (kinetic factor). From the other hand, direct and numerous contact of nanoparticles of the two components (g-C₃N₄ and MgO) leads to the formation of new interfaces, where a redistribution of electron densities occurs, which makes it easier to initiate the hydrogen evolution process (thermodynamic factor). Additional information was obtained using this data recalculation to the Tafel coordinates (so-called Tafel plot), where the Tafel slope indicates a change in overpotential value with a 10-fold increase in current density. Fig. 6(b) presents the results of the voltamogram analysis in the Tafel plot. Tafel slope for g-C₃N₄ and g-C₃N₄/5%MgO samples was found to be equal to

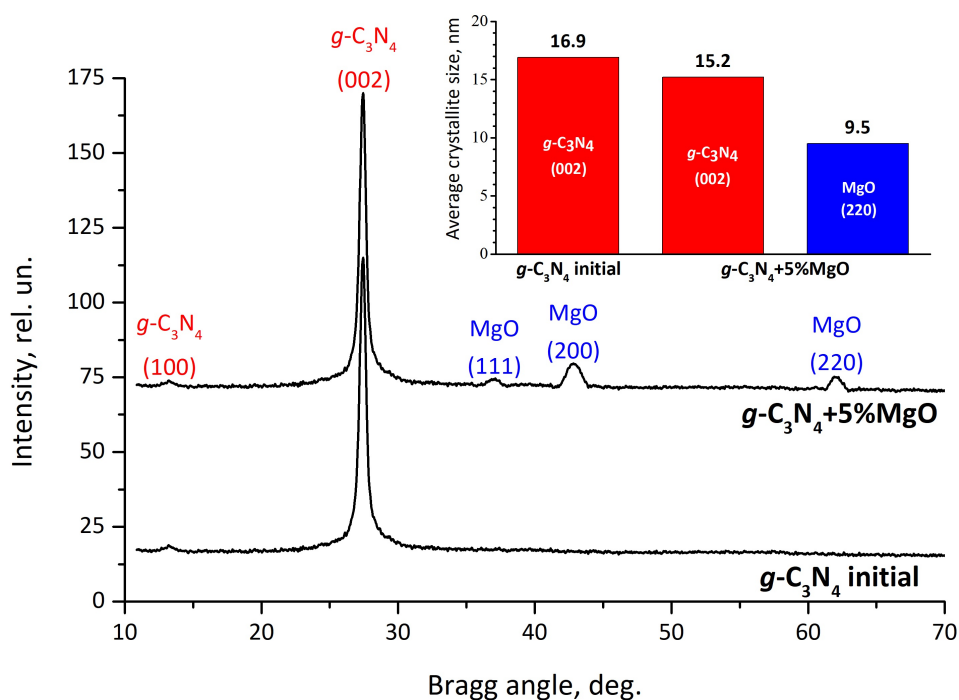


FIG. 5. PXR D patterns of initial $g\text{-C}_3\text{N}_4$ and $g\text{-C}_3\text{N}_4/5\%\text{MgO}$ nanocomposite and assignment of the main diffraction reflections of graphitic carbon nitride ($g\text{-C}_3\text{N}_4$) and magnesia (MgO). The inset shows the average crystallite sizes of $g\text{-C}_3\text{N}_4$ and MgO nanocrystals of initial $g\text{-C}_3\text{N}_4$ and $g\text{-C}_3\text{N}_4/5\%\text{MgO}$ nanocomposite

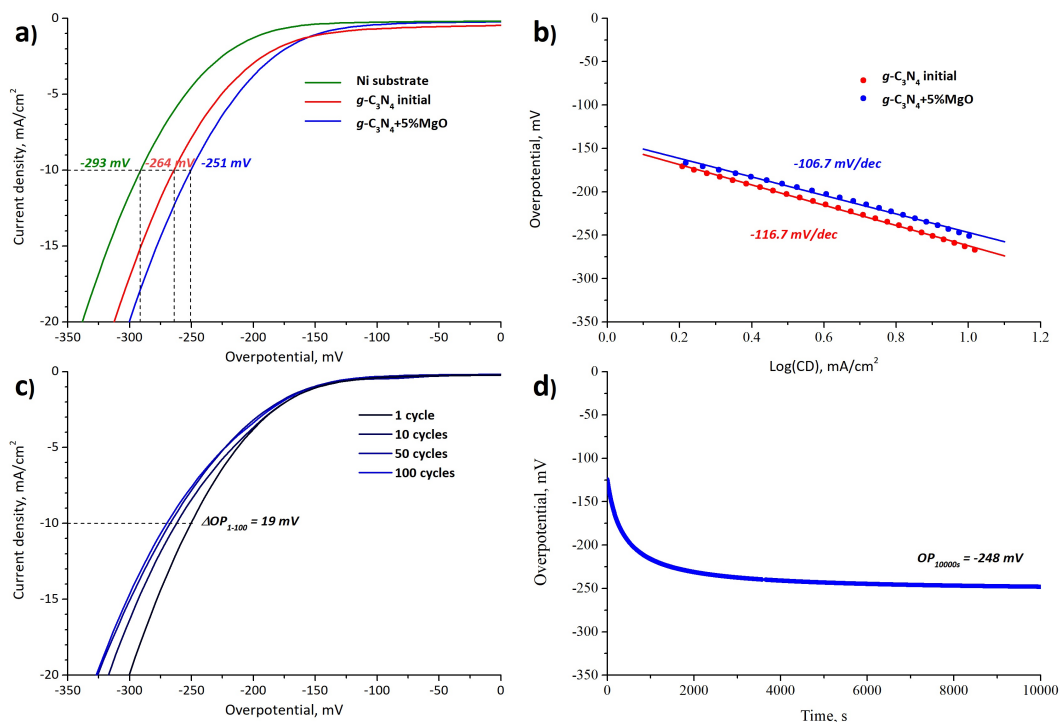


FIG. 6. Electrocatalytic performance of $g\text{-C}_3\text{N}_4/5\%\text{MgO}$ nanocomposite in hydrogen production via reforming of water-ethanol (10% vol.) solution: (a) HER polarization curves, (b) Tafel plot, (c) cycling stability, (d) chronopotentiometry stability

116 mV and 106 mV, respectively. Both values are lower than for the pure nickel electrode (120 mV) which provides an economic advantage in electrochemical reforming.

Then, the standard cyclic voltammetry and chronopotentiometry techniques [13, 14] were used to estimate the electrochemical stability of the g-C₃N₄/MgO-based electrode. Fig. 6(c) shows the polarization curves obtained at a sweep rate of 5 mV/s for the g-C₃N₄/5%MgO after 1, 10, 50 and 100 cycles of cyclic voltammetry (CVA). After 100 times cycling of the electrode, the value of overpotential slightly degrades, reaching values of about -270 mV. But, according to the results of chronopotentiometry (Fig. 6(d)), the value of overpotential for g-C₃N₄/MgO sample at a time, when the non-stationary mode ends, is 248 mV. The time-value for this sample is about 2000 s and doesn't change, even after a 10000 s testing. These results of both cyclic voltammetry and chronopotentiometry allow us to declare the high electrochemical stability of the synthesized g-C₃N₄/5%MgO nanocomposite in a water-ethanol reforming process.

4. Conclusion

In summary, a simple wet-chemical approach was proposed and used to synthesize g-C₃N₄/MgO nanocomposite with enhanced electrocatalytic activity compared with pure g-C₃N₄. This approach allowed synthesis of a high chemical and phase purity of g-C₃N₄-based nanocomposite with 5% wt. MgO content, as well as to ensure the uniform distribution of the individual components (g-C₃N₄ and MgO) over the volume of the synthesized electrocatalyst. It was found that the electrochemical characteristics (overpotential, Tafel slope, etc) of the g-C₃N₄/MgO nanocomposite electrode was significantly improved compared to both g-C₃N₄-coated and pure nickel electrode. At the same time, it was shown that the cyclic and chronopotentiometry stabilities of the nanocomposite-coated electrode are at a high and practically significant level. Thus, it was established and confirmed that synthesized g-C₃N₄/5%MgO nanocomposite is an effective and high stable electrode material that seems to be perspective as electrode base for electrocatalytic reforming of a water-alcohol solution toward hydrogen production.

References

- [1] Yuan Y., Ruan L., Barber J., Joachim Loo S.C., Xue C., Hetero-nanostructured suspended photocatalysts for solar-to-fuel conversion. *Energy Environ. Sci.*, 2014, **7**, P. 3934–3951.
- [2] Cao S., Low J., Yu J., Jaroniec M. Polymeric photocatalysts based on graphitic carbon nitride. *Adv. Mater.*, 2015, **27**, P. 2150–2176.
- [3] Wang X., Maeda K., Thomas A., Takahashi K., Xin G., Carlsson J.M., Domen K., Antonietti M. A metal-free polymeric photocatalyst for hydrogen production from water under visible light. *Nat. Mater.*, 2009, **8**, P. 76–80.
- [4] Mishra A., Mehta A., Basu S., Shetti N.P., Reddy K.R., Aminabhavi T.M. Graphitic carbon nitride (g-C₃N₄)-based metal-free photocatalysts for water splitting: A review. *Carbon*, 2009, **149**, P. 693–721.
- [5] Wen J., Xie J., Chen X., Li X., A review on g-C₃N₄-based photocatalysts. *Appl. Surf. Sci.*, 2017, **391**, P. 72–123.
- [6] Sudhaik A., Raizada P., Shandilya P., Jeong D.Y., Lim J.H., Singh P. Review on fabrication of graphitic carbon nitride based efficient nanocomposites for photodegradation of aqueous phase organic pollutants. *J. Ind. Eng. Chem.*, 2018, **67**, P. 28–51.
- [7] Mao N., Jiang J.-X., MgO/g-C₃N₄ nanocomposites as efficient water splitting photocatalysts under visible light irradiation. *Appl. Surf. Sci.*, 2019, **476**, P. 144–150.
- [8] Chaudhary P., Ingole P.P. In-Situ solid-state synthesis of 2D/2D interface between Ni/NiO hexagonal nanosheets supported on g-C₃N₄ for enhanced photo-electrochemical water splitting. *International Journal of Hydrogen Energy*, 2020, **45**(32), P. 16060–16070.
- [9] Chebanenko M.I., Zakharova N.V., Lobinsky A.A., Popkov V.I. Ultrasonic-Assisted Exfoliation of Graphitic Carbon Nitride and its Electrocatalytic Performance in Process of Ethanol Reforming. *Semiconductors*, 2019, **53**(16), P. 28–33.
- [10] Chebanenko M.I., Zakharova N.V., Popkov V.I., Synthesis and Visible-Light Photocatalytic Activity of Graphite-like Carbon Nitride Nanopowders. *Russ. J. Appl. Chem.*, 2020, **93**(4), P. 494–501.
- [11] Nikolic V.M., Maslovara S.L., Tasic G.S., et al. Kinetics of hydrogen evolution reaction in alkaline electrolysis on a Ni cathode in the presence of Ni-Co-Mo based ionic activators. *Appl. Catal. B Environ.*, 2015, **179**, P. 88–94.
- [12] Thomas S., Medhekar N.V., Frankel G.S., Birbilis N. Corrosion mechanism and hydrogen evolution on Mg. *Curr. Opin. Solid St. M.*, 2015, **19**(2), P. 85–94.
- [13] Kodintsev I.A., Martinson K.D., Lobinsky A.A., Popkov V.I. SILD synthesis of the efficient and stable electrocatalyst based on CoO–NiO solid solution toward hydrogen production. *Nanosystems: Phys. Chem. Math.*, 2019, **10**(6), P. 681–685.
- [14] Dmitriev D.S., Nashchekin A.V., Popkov V.I. The interfacial surface of an electrode for a supercapacitor as a factor affecting the capacitance and energy density. *Appl. Surf. Sci.*, 2020, **501**, P. 144216.

Visible light photoluminescence in TiO₂/CdS nanopowders synthesized by sol-gel route: effect of gel aging time

E. S. Ulyanova¹, D. A. Zamyatin^{2,3}, V. Yu. Kolosov³, E. V. Shalaeva¹

¹Institute of Solid State Chemistry of Ural Branch of the Russian Academy of Sciences, Pervomayskaya, 91, Ekaterinburg, 620990, Russia

²Institute of Geology and Geochemistry of Ural Branch of the Russian Academy of Sciences, Vonsovskogo, 15, Ekaterinburg, 620075, Russia

³Ural Federal University named B. N. Yeltsin, Mira, 9, Ekaterinburg, 620002, Russia

tsivileva.yekaterina@yandex.ru, dzamyatin85@gmail.ru, Kolosov@urfu.ru, shalaeva@ihim.uran.ru

PACS 81.07.-b, 32.50.+d, 73.20.Hb

DOI 10.17586/2220-8054-2020-11-4-480-487

A series of sol-gel TiO₂/CdS, TiO₂ powders and coagulated CdS nanoparticles were studied by XRD, HRTEM and Raman spectroscopy to elucidate the effect of low-temperature gel aging time on visible photoluminescence (PL) emission of the TiO₂/CdS composites. With an increase in aging time a content of amorphous titania and incorporated CdS nanoparticles decreases in composites. For all composites, visible PL emission includes bands attributed to surface oxygen vacancies and hydroxyl group of TiO₂ nanocrystals, as well as yellow-green and red bands related to lattice defect states of CdS nanoparticles. It was found that gel aging time is a crucial parameter to influence visible PL emission in composites. This emission is suppressed with increasing aging time, and its evolution shows that healing of oxygen vacancy defects and hydroxyl group affect visible emission more significantly than improving crystallinity degree. The correlation between visible PL emission in TiO₂/CdS and their visible-light photocatalytic activity was discussed.

Keywords: TiO₂/CdS composites, nanoparticles, photoluminescence, defect states, sol-gel route.

Received: 20 August 2020

Revised: 24 August 2020

1. Introduction

Semiconductor TiO₂/CdS composites represent an important group of visible-light photoactive materials and are attracting considerable attention due to the fact that cadmium sulfide has a relatively narrow band gap and is well combined with the band structure of titanium dioxide [1–3]. The development of physical and chemical methods for the synthesis of nanoscale semiconductor particles and quantum dots has provided new possibilities for the creation of photoactive heterogeneous structures based on these phases. In nanosized systems, a more efficient carrier transfer takes place owing to the improved interface contacts [4, 5]. The efficiency of the photon energy conversion into photocurrent and the photocatalytic activity depend not only on a charge carrier transfer rate across the interface of the TiO₂/CdS couple but also on a recombination rate of the photogenerated electron-hole pair within titanium dioxide and CdS layers [2].

For visible-light photoactive nano-sized TiO₂/CdS composites [6–8], as well as for the visible photoactive TiO₂-doped materials [9, 10], the direct correlation has been often found between the increased photoactivity and decreased radiative recombination in the visible range. Visible-light emission, related to the radiative recombination in nanosized TiO₂ is mainly attributed to (I) the self-trapped excitons, (II) oxygen vacancies and (III) surface states [11–14]. For CdS nanocrystals and nanoparticles, visible PL includes a number of emission bands associated with both surface electron states and states of complex defect centers [15–18]. Visible PL emission is affected not only by surface and lattice defects of TiO₂ nanocrystals but their morphology [13], and as well as by the crystallinity degree of titania [19]. For TiO₂/CdS composites, recombination rate has been found to increase with increasing degree of defects in TiO₂ layers [20] and imperfection of TiO₂||CdS interface [5]. Concentration ratio of TiO₂:CdS is also an essential parameter which affects the visible PL emission, with the concentration dependence of PL emission being non-monotonic [6].

Currently, several synthesis strategies are being actively developed to obtain visible photoactive TiO₂/CdS nanocomposites, and by varying the synthesis conditions it is possible to change their structural properties, defect states and electron structure for tuning PL emission. In one of them, pre-synthesized CdS nanoparticles are directly incorporated into TiO₂ matrix during titania formation process via sol-gel route [21–24]. As a rule, the influence of the initial concentrations of the sensitizing additive on the emission and photocatalytic properties of sol-gel TiO₂/CdS composites is studied [21]. At the same time, when preparing TiO₂/CdS composites, the sol-gel route is sometimes used with low-temperature heating of the sol-gel [23, 24], the effect of which on PL emission was not monitored. Recently, a new

technique for producing photoactive composites TiO₂/CdS was proposed, based on a modified sol-gel method using pre-synthesized CdS colloidal nanoparticles and low-temperature gel aging stage at boiling point [24]. Gel aging time, as has been shown, can affect the crystallinity degree of titania (amorphous/nanocrystalline ratio), and content of the incorporated CdS nanoparticles [25]. In addition, it must be taken into account that the stage of low-temperature gel aging promotes polycondensation of hydrolysis products to form titania and decrease of the oxygen vacancy and the hydroxyl group in synthesized titania [26].

The aim of work is to elucidate the effect of gel aging time on visible PL emission in TiO₂/CdS composites prepared by sol-gel route using pre-synthesized CdS nanoparticles and gel aging stage at boiling point. To gain more insight into the defect-related PL emission, a series of TiO₂/CdS and bare TiO₂ powders as well as CdS coagulated nanoparticles were studied. XRD, HRTEM and Raman spectroscopy were employed to characterize the structure of the samples and revealed decrease in content of amorphous TiO₂ and incorporated CdS nanoparticles with aging time. For all TiO₂/CdS composites, PL emission was found to include bands related to the surface defect states of TiO₂ nanocrystallites and two emission bands (as yellow-green and red), related to lattice defect states of CdS nanoparticles. Significant and non-additive growth of visible emission bands contributed by both phases was detected at the early aging stage and discussed in terms of TiO₂||CdS interface defects. The increase in gel aging time was demonstrated to be a crucial factor to suppress visible PL emission in TiO₂/CdS composites. It was concluded that the surface defects of TiO₂ and content of the incorporated CdS nanoparticles predominantly affect the visible emission, unlike the crystallinity degree of titania. A TiO₂/CdS composite with suppressed visible PL emission was found to exhibit the enhanced visible light photoactivity.

2. Experimental part

TiO₂/CdS composites were prepared by direct hydrolysis technique using pre-synthesized aqueous colloidal solution of CdS nanoparticles. The details of TiO₂/CdS preparation can be found in [24]. In brief, a certain amount of titanium (IV) n-butoxide was dissolved in the aqueous colloidal CdS solution. Sol-gel samples were heated up to the boiling point under continuous stirring and aged at this temperature for 1, 3 and 4 h. To remove the remaining organic species, the powders were centrifuged and dried in air at 120°C for 3 h. Bare TiO₂ powders were also prepared by the same hydrolysis route in the pure deionized water. The aging time at boiling point was 1 and 4 h.

X-ray diffraction (XRD), high resolution transmission electron microscopy (HRTEM) and Raman micro-spectroscopy in resonance and off-resonance modes were employed to study structural state of TiO₂/CdS composites. The XRD patterns of samples were recorded by a Shimadzu MAXima-X XRD-7000 (Shimadzu, Japan) automatic diffractometer with CuK α radiation ($\lambda = 1.5406 \text{ \AA}$) in 2θ angle range 10–80° with a step 0.03° and an exposure time of 10 sec at each step. The volume fractions and structural characteristics of constituent phases were calculated employing PCW 2.4 software [27]. High resolution TEM images and electron diffraction patterns were obtained with the help of a JEM-2100 microscope (JEOL, Japan) equipped with an Energy Dispersive X-ray Analyzer (EDX). HRTEM images were processed with the Digital Micrograph software package. Raman and photoluminescence spectra were excited by a low-power (up to 10 mW) laser irradiation at wave length of 480, 514 and 633 nm at room temperature, and they were recorded by a LabRAM HR800 (Horiba, Japan) spectrometer, providing a focal spot on the samples of 1 – 2 μm diameter. The spectral resolution was about 1 cm^{-1} . Raman and photoluminescence spectra were analyzed with multi-peak Gaussian fitting method using the “Peakfit v 4.11” software package.

3. Results and discussion

3.1. Structure characterization of TiO₂/CdS composites

Figure 1(a) shows XRD patterns for TiO₂/CdS powder composites synthesized by sol-gel technique with varying gel aging time at boiling point. Curve fitting of XRD spectra indicates that all the samples contain anatase and brookite titanium dioxide phases with the approximate ratio 2:1. The average crystal sizes in powders, as estimated by Debye–Scherrer equation, change slightly with aging time and are equal to 6 – 7 nm for the sample TiO₂/CdS at the early aging time and about 7 – 8 nm for the sample with a deeper aging (3 or 4 h). According to HRTEM, the samples contain amorphous titanium dioxide, the concentration of which decreases from 15% to less than 5% with an increase in gel aging time. In the XRD spectra, in addition to dioxide titanium diffraction peaks there are the blurred diffraction peaks at 26.1, 43.5 and 51.0 degrees that can be attributed to CdS nanoparticles with randomly lattice-packed hexagonal structure [28]. The bare CdS nanoparticles coagulated from the initial colloidal solution exhibit similar crystalline structure. The sizes of incorporated CdS nanoparticles are 5-7 nm, which are close to those in the initial colloid solution characterized by the log-normal size distribution of particles with the average value of 4.5 nm [29]. Estimations made by Peakfit decomposition of XRD spectra showed that CdS nanoparticles concentration decreases with increasing gel aging time and is 9, 2 – 3 and about 1% CdS for TiO₂/CdS samples with 1, 3 and 4 h

aging, respectively. This effect was discussed in detail using the Molecular Dynamic simulations in our previous work [26]. The drop in the concentration of CdS nanoparticles is associated with the decreases in the content of the amorphous phase in the TiO₂ matrix and the calculated thermodynamic stability of the composite CdS @ TiO₂ nanoparticles depending on the structure of the titanium shell: amorphous titania > polycrystalline titania (anatase or brookite). HRTEM images confirmed that colloidal CdS nanoparticles are incorporated into all anatase/brookite matrices [26]. A typical HRTEM image of the incorporated CdS nanoparticle with zone axis [001] is given in the Fig. 1(b).

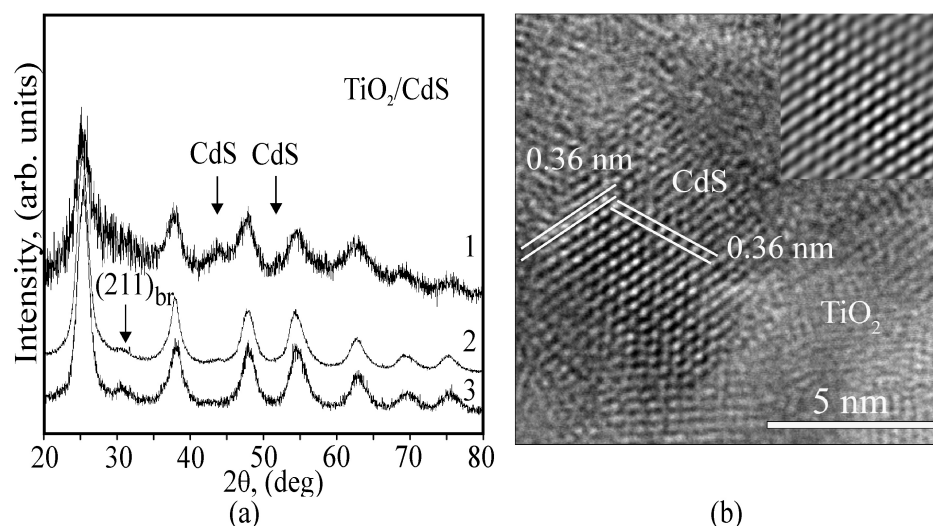


FIG. 1. X-ray diffraction patterns for the sol-gel TiO₂/CdS composites synthesized with varying gel aging time. The lines (1), (2) and (3) correspond to 1, 3 and 4 hours of aging (a). HRTEM image of a CdS nanoparticle incorporated into the TiO₂ matrix, [001] zone axis. The filtered image is presented in the inset (b)

A series of the micro-Raman spectra recorded from the different regions of powders demonstrates the good uniformity of structural properties of all synthesized samples TiO₂/CdS. Fig. 2 presents the typical untreated and treated Raman spectra for the TiO₂/CdS powders recorded with wavelength excitation equal to 633 nm. The most intense peaks in the treated spectra belong to titania phases (anatase and brookite). All 6 active modes of anatase phase (149 (E_{1g}), 200 (E_{2g}), 640 (E_{3g}), 401 (B_{1g(1)}), 517 cm⁻¹ (A_{1g} and B_{1g(2)})) can be detected for powders. There are weaker peaks which can be attributed to the modes of brookite phase [30]. These peaks are 128 (A_{1g}), 166 (A_{1g}), 218 (B_{1u}), 245 (A_{1g}), 323 (B_{1g}), 366 (B_{2g}) and 622 (B_{1u}) cm⁻¹. It can be seen that the corresponding peaks are shifted to the higher frequencies and smeared as compared to that of standard microcrystalline TiO₂-anatase, indicating that the size effect for nanocrystals takes place. For all TiO₂/CdS powders, including powder with CdS concentration about 1%, in Raman spectra excited at 633 nm (1.95 eV), there is a smeared band with maximum around 300–302 cm⁻¹ which becomes stronger for laser wavelength of 514 nm at resonance condition and can be uniquely assigned to the first longitudinal optical (LO) mode of CdS [31].

XRD, HRTEM and Raman spectroscopy revealed that all TiO₂/CdS composite powders have an anatase / brookite matrix with a phase ratio close to 2:1 and a small content of amorphous titanium dioxide. With an increase in the gel aging time at boiling point, the content of the amorphous component decreases from 15 to 5%, and the average crystallite size of the anatase and brookite phases increases slightly from 6.5 to 8 nm. The CdS particles incorporated into the TiO₂ matrix have an average size of approximately 5–7 nm, which is close to the average particle size in the initial CdS colloidal solution. The structure of the incorporated particles, as in the initial solution, is characterized by a random hexagonal close-packed lattice.

3.2. Photoluminescence properties of TiO₂/CdS composites

The inset in Fig. 2(a) presents the untreated Raman spectra recorded with a 633 nm excitation wavelength. As can be seen, with a decrease of gel aging time the untreated spectra demonstrate consistently increasing background due to visible light luminescence. In order to investigate the effects of luminescence and their aging time dependence in more detail, Raman spectra were recorded with a 480 nm excitation wavelength for TiO₂/CdS composites, CdS nanoparticles coagulated from the colloidal initial solution and bare TiO₂ powder synthesized by the same sol-gel

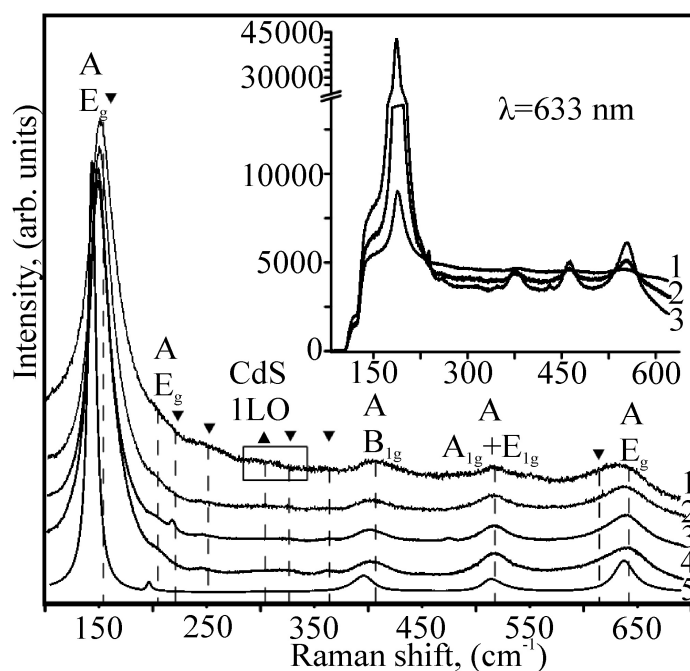


FIG. 2. Raman spectra for the sol-gel TiO₂/CdS (1, 2, 3), bare TiO₂ (4) nanopowders and microcrystalline anatase (5), excitation is 633 nm. The peaks of anatase (A) are signed. The peaks of CdS and brookite are marked with triangles and upside-down triangles, respectively. Notations (1, 2, 3) are the same as on Fig. 1(a). The untreated spectra are shown in insert

route with varying gel aging time. Deconvolution of the peaks was performed to gain more insight into the nature of defect states which determine the observed luminescence in different samples.

At first, consider the PL spectra of the bare TiO₂ nanopowder and CdS nanoparticles. Fig. 3(a,b) demonstrate visible light and NIR (near infrared) PL emission for the bare TiO₂ nanopowder synthesized with gel aging time of 1 and 4 h. For both sample, broad visible PL emission can be fitted with four Gaussian sub-bands centered at 533 nm (2.3 eV), 580 nm (2.1 eV), 633 nm (1.95 eV) and 670 nm (1.85 eV). One band at 850 nm (1.46 eV) is observed in NIR region. The all visible emission bands can be associated to the radiative recombination at the surface defects sites such as oxygen vacancy and hydroxyl groups which are the dominant trapped sites for nano-powders fabricated by low-temperature sol-gel. One set visible emissions at 2.3 and 1.95 eV are attributed to the deexcitation from the lower levels of oxygen vacancies associated with Ti³⁺ in anatase lattice to the ground state [12, 14]. The sub-band at 2.1 eV is due to the deexcitation from lower levels in Ti³⁺ 3d states of TiO₂ lattice to the deep levels created by OH⁻ group [12]. The observed NIR PL emission at 1.46 eV is a signature of the brookite phase and appears due to the radiative recombination at the intrinsic lattice defects acting as trapped sites [32]. As a consequence of the fabrication process (sol-gel route), we can suppose that visible emission appears owing to the surface oxygen vacancies in brookite nanoparticles, and one additional sub-band centered at 1.85 eV is attributed to these defects.

For bare TiO₂ nanopowders, the intensity of all sub-bands of the visible light PL emission noticeably decreases with the increasing gel aging time at boiling point. Therefore, the changes in the surface defect concentrations in TiO₂ nano-powder with gel aging time significantly affect the visible PL emission, unlike the phase transformation of amorphous TiO₂ into a crystalline state which proceeds during the aging stage. In the latter case, the intensity of PL emission should have increased with the increases in the content of the crystalline phase [19].

A PL emission spectrum for CdS nanoparticles coagulated from the colloidal solution is presented in Fig. 3(c). A broad sub-band centered at 540 nm (2.3 eV) and a shoulder at 710 nm (1.75 eV) extended up to 940 nm (1.3 eV) are revealed. A similar PL band structure was observed earlier for CdS nanopowder which exhibits a structure related to that of CdS coagulated nanoparticles and is characterized by a high concentration of lattice stacking faults [17]. The yellow-green emission at 540 nm can be endorsed to the deexcitation from the Cd interstitial states to the valence band [15, 17, 18], and the red emission shoulder is believed to be caused by transitions of electrons trapped in the surface states to the valence band and to be increased with the accumulation of crystallographic defects in CdS structure [18].

Figure 3(d-f) demonstrates PL emission spectra for TiO₂/CdS composites fabricated by sol-gel using pre-synthesized CdS colloidal nanoparticles and with varying gel aging. The PL spectra of TiO₂/CdS composites managed to

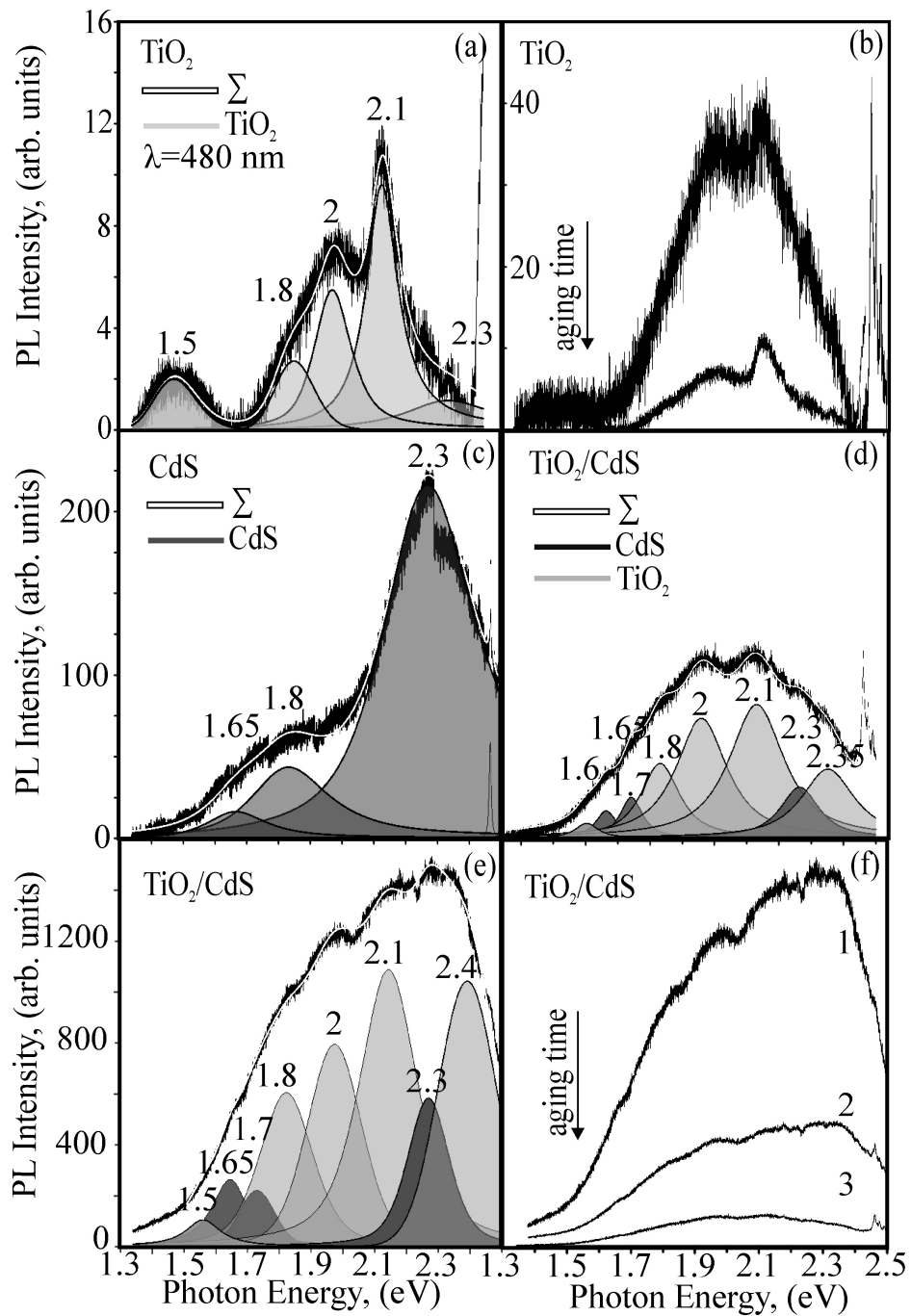


FIG. 3. PL emission for sol-gel TiO_2 (a,b), coagulated CdS nanoparticles (c) and sol-gel TiO_2/CdS nanopowders (d-f), excitation is 480 nm. For TiO_2 , gel aging time is 1 and 4 hours. For TiO_2/CdS , notations (1, 2, 3) are the same as on Fig. 1(a)

be decomposed by the same sub-bands as in bare TiO₂ nanopowder and CdS particles, with sub-band positions being changed slightly. The main difference in the spectra recorded for TiO₂/CdS powders with 1, 3 and 4 hours of gel aging stage is the decrease in the intensity of all emission sub-bands related to both the TiO₂ matrix and the incorporated CdS nanoparticles, with increasing gel aging time. As in the case of pure TiO₂, the effect of the phase transformation from amorphous TiO₂ to crystalline phases, which occurs during gel aging, on the emission of TiO₂/CdS composite powders is insignificant. In samples with short aging time (1 h) and containing the maximum amount of CdS nanoparticles up to 9%, visible emission is maximum, and is significantly higher than in the original pure components. As shown above and discussed in detail in our previous work [26], there are no significant differences between the structural properties of the components of the TiO₂/CdS composite and the original bare sol-gel TiO₂ nano-powder and CdS nanoparticles. However, the increased defect concentrations in the TiO₂/CdS interface region, detected by MD simulations of CdS @ TiO₂ composite particles, will affect surface defect states and lead to an increased visible PL emission, especially in the early stages of aging. With an increase in the aging time to 4 hours, PL emission drops significantly due to the decrease in the content of incorporated CdS nanoparticles to 1% and due to the healing of TiO₂/CdS interface defects and surface defects of TiO₂ nanocrystallites as in the case of the bare TiO₂ nanopowder.

Consider the relation between the observed visible PL emission for TiO₂/CdS powders synthesized with varying gel aging time and their visible light photocatalytic activity, previously tested in the oxidative degradation of benzene-1,4-diol (hydroquinone) [24]. Fig. 4 shows the rates of the oxidation reaction of benzene-1, 4-diol, the intensity of PL sub-band at 580 nm (2.1 eV) attributed to the surface hydroxyl group and content of CdS nanoparticles incorporated into TiO₂ matrix. It can be seen that the highest photoactivity is exhibited by composites with the lowest visible PL emission and the lowest CdS nanoparticle content. For a composite with short aging time and increased CdS content, a delayed decrease in photoactivity is observed, seemingly due to the competition of several alternative effects – (I) an increase in visible PL emission associated with harmful radiative recombination at the surface defect states, (II) an increase in the number of TiO₂||CdS heterojunctions which can improve the transfer and separation of charge carriers and (III) an increase in the number of titania surface defects serving as centers of photo-induced redox reactions.

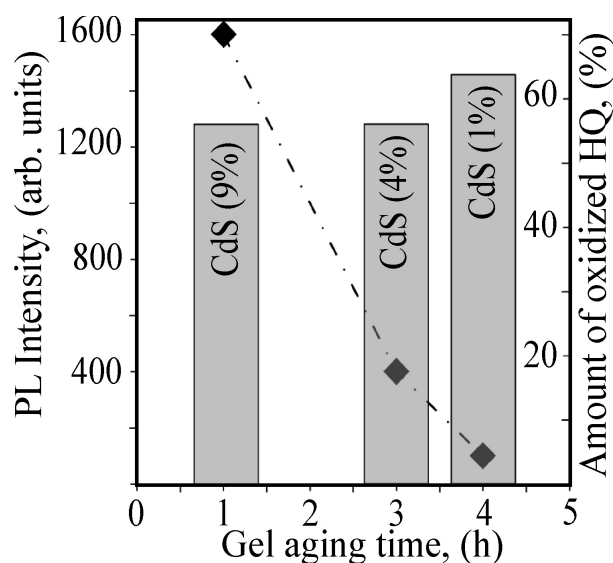


FIG. 4. Correlation dependences between the rate of hydroquinone (HQ) oxidation [24], PL emission related to the surface hydroxyl group and content of the incorporated CdS nanoparticles in the TiO₂/CdS nanopowders synthesized with varying gel aging time (1, 3 and 4 hours)

4. Conclusions

The paper explores the effect of gel aging time on visible light photoluminescence of TiO₂/CdS composites fabricated by modified sol-gel route using pre-synthesized CdS colloidal nanoparticles. For this, a series of TiO₂/CdS and bare TiO₂ powders prepared with varying gel aging time as well as bare CdS coagulated nanoparticles were studied. TiO₂/CdS and TiO₂ exhibit an amorphous-nanocrystalline structure, and with an increase in gel aging time, the content of amorphous titania decreases as phase transformation from amorphous into crystalline titania proceeds and the content of incorporated CdS nanoparticles decreases.

It was found that for sol-gel TiO₂/CdS powders, gel aging time at boiling point is a crucial parameter to affect visible light PL emission. With increasing aging time, visible PL emission associated with TiO₂ surface defects such as oxygen vacancy and hydroxyl group as well as yellow-green and red emission is suppressed, related to the defect states of CdS nanoparticles. At short aging times, a significant non-additive increase in the intensity of visible luminescence bands of both phases is observed, which is considered as a result of the increased structural imperfection in the TiO₂||CdS interface, especially at the early stages of aging. Surface defect states and concentration of CdS nanoparticles are concluded to significantly affect visible PL emission, unlike the crystallinity degree of titania.

There is a correlation between visible PL emission and visible-light photoactivity of TiO₂/CdS composites. Composites with suppressed visible PL emission exhibit the enhanced visible-light photoactivity.

Acknowledgements

The research was carried out in accordance with the state assignment for ISSC UB RAS and financial support from ISSC UB RAS (theme AAAA-A19-119031890025-9). TEM study was supported by RFBR (grant No. 20-02-00906). The authors are grateful to Dr. Kozhevnikova N. S. and Dr. Gorbunova T. I. for the provided samples TiO₂/CdS and CdS.

References

- [1] Vogel R., Honyer P., Weller H. Quantum-sized PbS, CdS, Ag₂S, Sb₂S₃, and Bi₂S₃ particles as sensitizers for various nanoporous wide-bandgap semiconductors. *J. Phys. Chem.*, 1994, **98**, P. 3183–3188.
- [2] Zhao D., Yang C.-F. Recent advances in the TiO₂/CdS nanocomposite used for photocatalytic hydrogen production and quantum-dot-sensitized solar cells. *Renewable and sustainable energy reviews*, 2016, **54**, P. 1048–1059.
- [3] Wang Y., Wang Q., Zhan X., Wang F., Safdar M., He J. Visible light driven type II heterostructures and their enhanced photocatalysis properties: a review. *Nanoscale*, 2013, **5**(18), P. 8326–8339.
- [4] He D., Chen M., Teng F., Li G., Shi H., Wang J., Xu M., Lu T., Ji X., Lv Y., Zhu Y. Enhanced cyclability of CdS/TiO₂ photocatalyst by stable interface structure. *Superlattices and Microstructures*, 2012, **51**, P. 799–808.
- [5] Zhang B., Zheng J., Li X., Fang Y., Wang L.-W., Lin Y. Pan F. Tuning band alignment by CdS layers using a SILAR method to enhance TiO₂/CdS/CdSe quantum-dot solar-cell performance. *Chem. Comm.*, 2016, **52**, P. 5706–5709.
- [6] Xie Z., Liu Z., Wang W., Liu C., Li Z. Zhang Z. Enhanced photoelectrochemical properties of TiO₂ nanorod arrays decorated with CdS nanoparticles. *Sci. Technol. Adv. Mater.*, 2014, **15**(5), P. 055006.
- [7] Huo Y., Yang X., Zhu J., Li H. Highly active and stable CdS-TiO₂ visible photocatalyst prepared by in situ sulfurization under supercritical conditions. *Appl. Catalysis B: Environmental*, 2011, **106**, P. 69–75.
- [8] Zhao H., Cui S., Yang L., Li G., Li N., Li X. Synthesis of hierarchically meso-macroporous TiO₂/CdS heterojunction photocatalysts with excellent visible-light photocatalytic activity. *Journal of Colloid and Interface Science*, 2018, **512**, P. 47–54.
- [9] Devi L.G., Kavitha R. Enhanced photocatalytic activity of sulfur doped TiO₂ for the decomposition of phenol: A new insight into the bulk and surface modification. *Materials Chemistry and Physics*, 2013, **143**(3), P. 1300–1308.
- [10] Zhang J., Chen X., Shen Y., Li Y., Hu Z., Chu J. Synthesis, surface morphology, and photoluminescence properties of anatase iron-doped titanium dioxide nano-crystalline films. *Phys. Chem. Chem. Phys.*, 2011, **13**, P. 13096–13105.
- [11] Abazovic N.D., Comor M.I., Dramicanim M.D., Jovanovic D.J., Ahrenkiel S.P., Nadeljkovic J.M. Photoluminescence of anatase and rutile TiO₂ particles. *J. Phys. Chem. B*, 2006, **110**, P. 25366–25370.
- [12] Mathew S., Prasad A.K., Benoy T., Rakesh P.P., Hari M., Lishish T.M. UV-Visible photoluminescence of TiO₂ nanoparticles prepared by hydrothermal method. *J. Fluoresc.*, 2012, **22**, P. 1593–1599.
- [13] Zhang H., Zhou M., Fu Q., Lei B., Lin W., Guo H., Wu M., Lei Y. Observation of defect state in highly ordered titanium dioxide nanotube arrays. *Nanotechnology*, 2014, **25**(27), P. 275603.
- [14] Chetibi L., Busko T., Kulish N.P., Hamana D., Chaieb S., Achour S. Photoluminescence properties of TiO₂ nanofibers. *J. Nanopart. Res.*, 2017, **19**, P. 129.
- [15] Tsai C.T., Chuu D.S., Chen G.L., Yang S.L. Studies of grain size effects in rf sputtered CdS thin films. *J. Appl. Phys.*, 1996, **79**(12), P. 9105–9109.
- [16] Yang Y., Chen H., Mei Y., Chen J., Wu X., Bao X. CdS nanocrystallinities prepared by chemical and physical templates. *Acta Materialia*, 2002, **50**, P. 5085–5090.
- [17] Kumar P., Saxena N., Singh F., Agarwal A. Nanotwinning in CdS quantum dots. *Physica C*, 2012, **407**, P. 3347–3351.
- [18] Abken A.E., Halliday D.P., Durose K. Photoluminescence study of polycrystalline photovoltaic CdS thin film layers grown by close-spaced sublimation and chemical bath deposition. *J. Appl. Phys.*, 2009, **105**, P. 064515.
- [19] Jin C., Liu B., Lei Z., Sun J. Structure and photoluminescence of the TiO₂ films grown by atomic deposition using tetrakis-dimethylamino titanium and ozone. *Nanoscale Research Letters*, 2015, **10**(1), P. 95.
- [20] Han S., Pu Y.-C., Zheng L., Zhang J., Fang X. Shell-thickness dependent electron transfer and relaxation in type-II core-shell CdS/TiO₂ structures with optimized photoelectrochemical performance. *J. Materials Chem. A*, 2015, **3**, P. 22627–22635.
- [21] Li X., Xia T., Xu C., Murowchick J., Chen X. Synthesis and photoactivity of nanostructured CdS-TiO₂ composite catalysts. *Catalysis Today*, 2014, **225**, P. 64–73.
- [22] Thakur P., Chadha R., Biswas N., Sarkar S.K., Mukherjee T., Joshi S.S., Kapoor S. Synthesis and characterization of CdS doped TiO₂ nanocrystalline powder: A spectroscopic study. *Materials Research Bulletin*, 2012, **47**, P. 1719–1724.
- [23] Guo X., Chen C., Song W., Wang X., Di W., Qin W. CdS embedded TiO₂ hybrid nanospheres for visible light photocatalysis. *J. Molecular Catalysis A: Chemical*, 2014, **387**, P. 1–6.

- [24] Vorokh A.S., Kozhevnikova N.S., Gorbunova T.I., Gyrdasova O.I., Baklanova I.V., Yanchenko M.Yu., Myrzakaev A.M., Shalaeva E.V., Enyashin A.N. Facile, rapid and efficient doping of amorphous TiO₂ by pre-synthesized colloidal CdS quantum dots. *J. Alloys and Comp.*, 2017, **706**, P. 205–214.
- [25] Ulyanova E.S., Zamyatin D.A., Murzakaev A.M., Yushkov A.A., Kozhevnikova N.S., Gorbunova T.I., Vorokh A.S., Enyashin A.N., Shalaeva E.V. Local environment of CdS nanoparticles incorporated into anatase/brookite matrix via sol-gel route: HRTEM, Raman spectroscopy and MD simulation. *Materials Today Communications*, 2020, **25**, P. 101465.
- [26] Kozhevnikova N.S., Ulyanova E.S., Shalaeva E.V., Zamyatin D.A., Bokunyaeva A.O., Yushkov A.A., Kolosov V.Yu., Buldakova L.Yu., Yanchenko M.Yu., Gorbunova T.I., Pervova M.G., Enyashin A.N., Vorokh A.S. Low-temperature sol-gel synthesis and photoactivity of nanocrystalline TiO₂ with the anatase/brookite structure and an amorphous component. *Kinetics and Catalysis*, 2019, **60**, P. 325–336.
- [27] <http://powdercell-forwindows.software.informer.com/2.4>
- [28] Vorokh A.S., Rempel A.A. Direct-space visualization of the short and “average” long-range orders in the nanocrystalline structure of a single cadmium sulfide nanoparticle. *JETP Letters*, 2010, **91**(2), P. 100–104.
- [29] Kuznetsova Yu.V., Letofsky-Papst I., Sochor B., Schummer B., Sergeev A.A., Hofer F., Rempel A.A. Greatly enhanced luminescence efficiency of CdS nanoparticles in aqueous solution. *Colloids and Surfaces A*, 2019, **581**, P. 123814.
- [30] Iliev M.N., Hadjiev V.G., Litvinchuk A.P. Raman and infrared spectra of brookite (TiO₂): Experiment and theory. *Vibrational spectroscopy*, 2013, **64**, P. 148–152.
- [31] Prabhy R., Khadar M.A. Study of optical phonon modes of CdS nanoparticles using Raman spectroscopy. *Bull. Mater. Sci.*, 2008, **31**, P. 511–515.
- [32] Vequizo J.M., Kamimura S., Ohno T., Yamakata A. Oxygen induced enhancement of NIR emission in brookite TiO₂ powders: comparison with rutile and anatase powders. *Phys. Chem. Chem. Phys.*, 2018, **20**, P. 3241–3248.

Fabrication and characterization of spectrally selective glazing dielectric multilayer structures

Venkatesh Yepuri^{1,2}, R. S. Dubey^{1,*}, Brijesh Kumar²

¹Department of Nanotechnology, Swarnandhra College of Engineering and Technology, Seetharampuram, Narsapur (A.P.), India

²Amity Institute of Nanotechnology, Amity University, Gurgaon, (Haryana), India

*rag_pcw@yahoo.co.in

DOI 10.17586/2220-8054-2020-11-4-488-492

We report the fabrication of three- and five-layered based TiO₂/SiO₂ dielectric structures as the back-end reflector application in thin film silicon solar cells. These dielectric structures are prepared by the combined sol-gel and spin-coating techniques. X-ray diffraction (XRD) analysis of both the three- and five-layered based structures confirmed the anatase phase of TiO₂ with its dominant peak at $2\theta = 25^\circ$. Field-emission scanning electron microscopy (FESEM) study demonstrated the formation of three and five alternate layers of TiO₂ and SiO₂ films. Comparatively, five-layered based reflector yielded the maximum (100 %) reflectance in the near-infrared (NIR) wavelength region as evidenced by the UV-Vis spectroscopy investigation.

Keywords: sol-gel method, thin films, bragg reflectors, dielectric materials.

Received: 13 May 2020

Revised: 8 June 2020, 12 July 2020

1. Introduction

A Bragg reflector is an optical component which is nothing but the multilayer structure of two alternating materials of distinct refractive index. This optical device has got various applications as in listed in Fig. 1. These includes as the back-end reflector in solar cells, clads in optical waveguiding, as reflector in light-emitting devices, light splitter in photonic devices and their smart applications in new-generation fabrics, heat-resistance smart windows, and windshielding in automobiles [1–3].

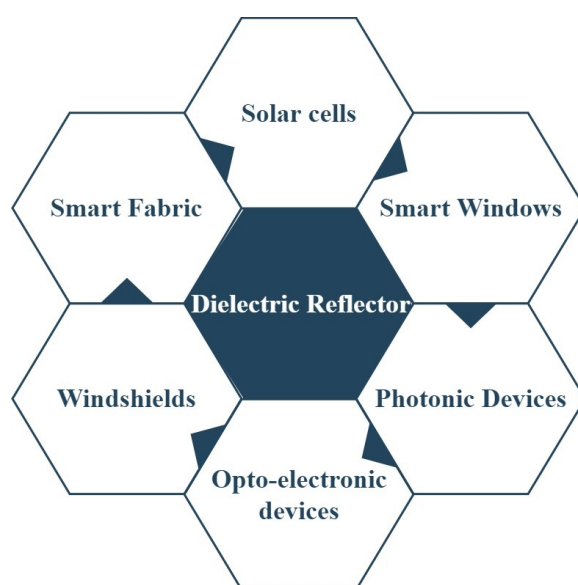


FIG. 1. Applications of dielectric reflectors

In thin film solar cells, the longer wavelength light is unabsorbed through the thin absorbing region and transmitted to the bottom-end [4]. Therefore, harvesting of light is very important in such thin film solar cells so that unabsorbed light can be reutilized. In this view, such reflectors are promising for the enhancement of light absorption in the

thin absorbing layer and hence, conversion efficiency. Other than dielectric materials such as zinc oxide, zirconium oxide, etc., the TiO_2 and SiO_2 are the best opted dielectric materials due to their high refractive index contrast and non-hazardous during the processing by the sol-gel method. These materials have also been demanded for their potential applications such as anti-reflection coating, optical waveguides, photonic crystals etc. [5]. Sol-gel spin coating approach needs optimization of the process to attain the good step coverage, uniformity and crack free films [6]. The properties of $\text{TiO}_2/\text{SiO}_2$ layered based multilayer structure can be tuned for the specific applications, i.e., as the UV, visible and IR filters including lasers. Several investigations have been reported on the fabrication of reflective and anti-reflective coatings [7–14]. Calvo et al. introduced a synthetic route in fabricating Bragg mirrors with TiO_2 thin-films by adopting the sol-gel spin coating [15]. He prepared the visible reflector with six layers of TiO_2 - TiO_2 with periodic variation of refractive index and controlled porosity. The reflector showed reflectance below 100% in the visible spectrum and further, suggested the preparation of Bragg reflectors by tuning the precursor solution. Hinczewski et al. presented the preparation of optical filters based on SiO_2 and TiO_2 multi-layers by adopting the sol-gel spin coating technique [16]. The prepared structure was composed of nine alternate layers of $\text{TiO}_2/\text{SiO}_2$ which endorsed 90 % reflectivity in near-UV region with 90%. The experimental results were also in good agreement with the theoretical investigations. Nagayoshi et al. prepared and studied the dielectric structure fabricated by using TiO_2 nanoparticles mixed in SiO_2 solution [17]. The spin coated films evidenced good reflectance (90 %) in the near-infrared region. These studies were explored by varying the number of dielectric layers, optical thickness, and the choice of coating techniques i.e. spin or dip coating. Sol-gel spin coating is an inexpensive and simple process based technique. Under the atmospheric conditions one can maintain the good homogeneity of the coating. To attain this, annealing temperature and the molar ratio of the precursors are the essential factors.

This paper mainly deals with the fabrication of three and five layered based dielectric structures of TiO_2 and SiO_2 film which serves as distributed Bragg reflector (DBR). The periodic arrangement of three- and five-consecutive layers of TiO_2 and SiO_2 films showed as much as 74 % and 100 % reflectance in the NIR region respectively. Section 2 presents the experimental process for fabricating the dielectric reflectors. The investigations are discussed in the Section 3 and Section 4 concludes the work.

2. Experimental process

Titanium Isopropoxide (TTIP) and Tetra Ethyl Ortho Silicate (TEOS) precursors procured by Sigma-Aldrich were used as the Ti and Si sources. De-ionized and ethanol procured by Changshu Hongsheng Fine Chemicals were used as the solvent while hydrochloric acid supplied by Fischer Scientific as the chelating agent. All the reagents were of analytical grade and used without any further purification. The preparation of dielectric reflectors is presented in the typical flow chart as shown in Fig. 2.

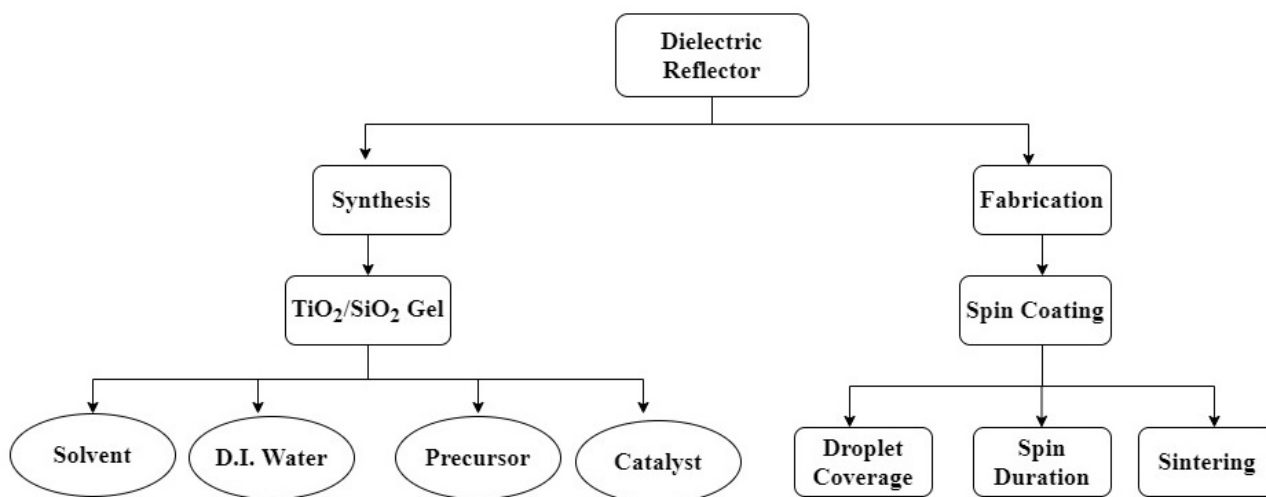


FIG. 2. Flow chart of synthesis and fabrication of dielectric reflector

To prepare the gels of TiO_2 and SiO_2 , at first 20 ml ethanol was added in 1 ml DI water and kept for 5 min stirring. Afterwards, 1 ml precursor TTIP/TEOS drop-wise was added under vigorous stirring while maintaining 2 min interval in order to prepare the $\text{TiO}_2/\text{SiO}_2$ solution. Finally 0.2 ml HCl was added to the above solutions in order to promote the rate of reaction and kept for continuous stirring for two hr. Later, both the solutions were aged for 24 hours to

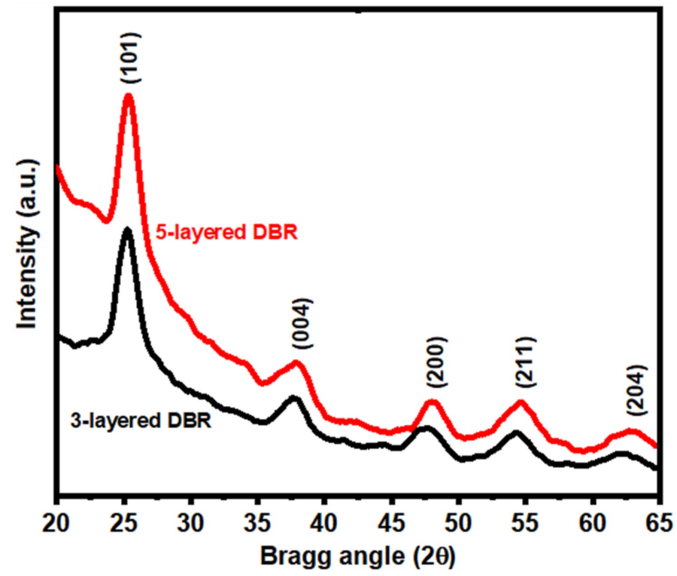


FIG. 3. XRD pattern of three and five-layered based DBR

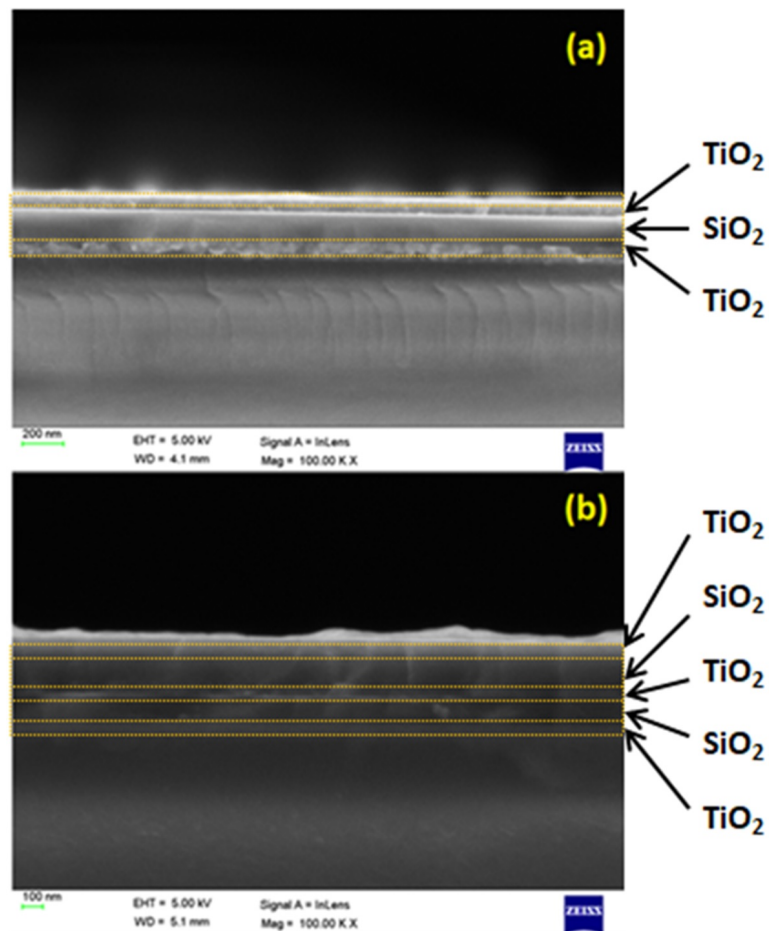


FIG. 4. (a) Cross-section FESEM images of three-layered based DBRs. (b) Cross-section FESEM images of five-layered based DBRs

get the enough viscous and transparent gels. For the preparing the multilayer structures of TiO_2 and SiO_2 films, the glass substrates were thoroughly cleaned with the soap solution and sonicated in ethanol for 30 min. Further, after rinsing in water and drying, alternate layers were deposited by the spin coating process at 3000 RPM speed for 30 sec. After deposition of each film, these were dried in the hot air oven at temperature 100°C for 30 min, in order to remove the volatile solvents. The as-prepared TiO_2 and SiO_2 films were sintered at temperature 500°C and 300°C for 1 hr to eliminate the organic compounds and to form the crystalline structure. Further, the fabricated multilayer structures were examined by using XRD, FESEM and UV-Vis spectroscopy.

3. Results and discussion

XRD study was carried out to investigate the crystallization phase presence in the spin coated three and five-layered based structures. Fig. 3 depicts the XRD pattern which endorses the anatase phase of TiO_2 .

The diffraction peaks located at $2\theta = 25^\circ, 37^\circ, 48^\circ, 55^\circ$ and 62° are indexed corresponding to the planes (101), (004), (200), (211), and (204) respectively of anatase- TiO_2 [17]. Our XRD results coincide with the JCPDS File No. 21-1272. One can notice the broadening of a Bragg peak located at $2\theta = 25^\circ$ ascribed to the plane (101) of TiO_2 , which usually indicates the existence of amorphous phase of SiO_2 . In addition, it is observed that the sequential annealing of each film did not affect the crystallinity of the multilayer structures.

Figure 4(a,b) shows the cross-section FESEM images of three and five-layered based $\text{TiO}_2/\text{SiO}_2$ reflectors. The brighter and lighter layers shown in cross-section FESEM images indicate the deposition of TiO_2 and SiO_2 film respectively. The estimated thicknesses of each layer from bottom to top were 71 nm, 127 nm and 53 nm, and 56 nm, 97 nm, 59 nm, 135 nm and 56 nm corresponding to three- and five-layered based $\text{TiO}_2/\text{SiO}_2$ reflectors. Here, we can observe the periodic structure of titania and silica films with their high and low refractive indices.

Figure 5 depicts the reflectance spectra of three- and five-layered based reflectors. The three-layered reflector showed as much as 70 % reflectance in the wavelength range from 500–1100 nm with its center wavelength 745 nm.

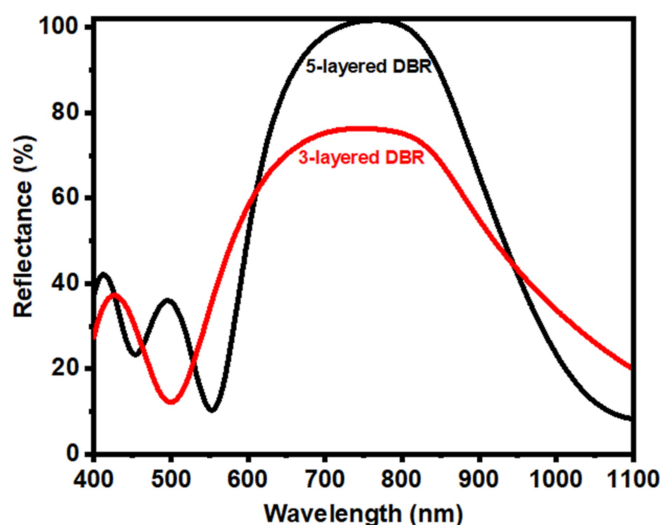


FIG. 5. Reflectance spectra of three- and five-layered based DBRs

Further, the increased layers of TiO_2 and SiO_2 films i.e. five-layered structure demonstrated the 100 % reflectance with its center wavelength 764 nm. Remarkably, both the reflectors dominated their reflectance bands in the near-infrared region. Finally, we could attain maximum 100 % reflectance with the use of only five layers of TiO_2 and SiO_2 films by depositing the films using spin coating process.

4. Conclusion

We have prepared the dielectric reflectors of $\text{TiO}_2/\text{SiO}_2$ films on glass substrates and studied the structural and optical properties. XRD results endorsed the presence of anatase- TiO_2 phase in both the samples of three- and five-layered structures of TiO_2 and SiO_2 films. Cross-section FESEM studies revealed the formation of alternate layers of TiO_2 and SiO_2 . Finally, both the reflectors characterized to study the light behavior. As compared to three-layered reflector, the five-layered one showed the maximum reflectance i.e., 100 % in the broad wavelength range with its

center wavelength 764 nm. This investigation is useful to tune the reflectivity in the desired wavelength range by adopting a simple and cost-effective fabrication technique.

Acknowledgement

We acknowledge the support provided by the UGC-DAE CSR, Indore (India) for the XRD measurements.

References

- [1] Isabella O., Dobrovolskiy S., Kroon G., Zeman M. Design and application of dielectric distributed Bragg back reflector in thin-film silicon solar cells. *J. Non-Cryst. Solids*, 2012, **358**(17), P. 2295–2298.
- [2] Fu A., Gao H., Petrov P., Yang P. Widely tunable distributed Bragg reflectors integrated into nanowire waveguides. *Nano Lett.*, 2015, **15**(10), P. 6909–13.
- [3] Lee S.M., Gong S.H., Kang J.H., Ebaid M., Ryu S.W., Cho Y.H. Optically pumped GaN vertical cavity surface emitting laser with high index-contrast nanoporous distributed Bragg reflector. *Opt. Express*, 2015, **23**(9), P. 1687–1689.
- [4] Dubey R.S., Ganesan V. Fabrication and characterization of TiO₂/SiO₂ based Bragg reflectors for light trapping applications. *Results Phys.*, 2017, **7**, P. 2271–2276.
- [5] Jeong S.H., Jae K.K., Bong S.K., Seok H.S., Byung T.L. Optical application and characterization of SiO₂ and TiO₂ films prepared using a reactive RF Magnetron sputtering. *Vacuum*, 2004, **76**(4), P. 507–515.
- [6] Rabaste S. Sol gel fabrication of thick multilayers applied to Bragg reflectors and microcavities. *Thin Solid Films*, 2002, **416**(1-2), P. 242–247.
- [7] Zhang Q., Wang J., Wu G., Shen J., Buddhudu S. Interference coating by hydrophobic aerogel-like SiO₂ thin films. *Mater. Chem. Phys.*, 2001, **72**(1), P. 56–59.
- [8] Mennig M., Oliveira P.W., Schmidt H. Interference coatings on glass based on photopolymerizable nanomer material. *Thin Solid Films*, 1999, **351**(1-2), P. 99–102.
- [9] San Vicente G., Morales A., Gutierrez M.T. Preparation and Characterization of Sol–Gel TiO₂ Antireflective Coatings for Silicon. *Thin Solid Film*, 2001, **391**(1), P. 133–137.
- [10] Hammarberg E., Roos A. Antireflection treatment of low-emitting glazings for energy efficient windows with high visible transmittance. *Thin Solid Films*, 2003, **442**(1-2), P. 222–226.
- [11] Bautista M.C., Morales A. Silica antireflective films on glass produced by the sol–gel method. *Sol. Energy Mater. Sol. Cells*, 2003, **80**(2), P. 217–225.
- [12] Vong M.S.W., Sermon P.A. Observing the breathing of silica sol-gel-derived anti-reflection optical coatings. *Thin Solid Films*, 1997, **293**(1-2), P. 185–195.
- [13] Nostell P., Roos A., Karlsson B. Optical and mechanical properties of sol-gel antireflective films for solar energy applications. *Thin Solid Films*, 1999, **351**(1-2), P. 170–175.
- [14] San Vicente G., Morales A., Gutierrez M.T. Sol–gel TiO₂ antireflective films for textured monocrystalline silicon solar cells. *Thin Solid Films*, 2002, **403–404**, P. 335–338.
- [15] Calvo M.E. Photoconducting Bragg Mirrors based on TiO₂ Nanoparticle. *Adv. Funct. Mat.*, 2008, **18**(18), P. 2708–2715.
- [16] Saygin Hinczewski D., Hinczewski M., Tepehan F.Z., Tepehan G.G. Optical filters from SiO₂ and TiO₂ multi-layers using sol–gel spin coating method. *Sol. Energy Mater. Sol. C*, 2005, **87**(1-4), P. 181–196.
- [17] Nagayoshi H., Takuya Murooka. TiO₂ nanoparticle/SiO₂ composite back reflector for solar cells. *Energy Procedia*, 2015, **77**, P. 242–247.
- [18] Nandanwar R., Singh P., Syed F.F., Haque Z.F. Preparation of TiO₂/SiO₂ Nanocomposite with Non-ionic Surfactants via Sol-gel Process and their Photocatalytic Study. *Orient. J. Chem.*, 2014, **30**(4), P. 1577–1584.



NANOSYSTEMS:

PHYSICS, CHEMISTRY, MATHEMATICS

INFORMATION FOR AUTHORS

The journal publishes research articles and reviews, and also short scientific papers (letters) which are unpublished and have not been accepted for publication in other magazines. Articles should be submitted in English. All articles are reviewed, then if necessary come back to the author to completion.

The journal is indexed in Web of Science Core Collection (Emerging Sources Citation Index), Chemical Abstract Service of the American Chemical Society, Zentralblatt MATH and in Russian Scientific Citation Index.

Author should submit the following materials:

1. Article file in English, containing article title, the initials and the surname of the authors, Institute (University), postal address, the electronic address, the summary, keywords, MSC or PACS index, article text, the list of references.
2. Files with illustrations, files with tables.
3. The covering letter in English containing the article information (article name, MSC or PACS index, keywords, the summary, the literature) and about all authors (the surname, names, the full name of places of work, the mailing address with the postal code, contact phone number with a city code, the electronic address).
4. The expert judgement on possibility of publication of the article in open press (for authors from Russia).

Authors can submit a paper and the corresponding files to the following addresses: nanojournal.ifmo@gmail.com, popov1955@gmail.com.

Text requirements

Articles should be prepared with using of text editors MS Word or LaTeX (preferable). It is necessary to submit source file (LaTeX) and a pdf copy. In the name of files the English alphabet is used. The recommended size of short communications (letters) is 4-6 pages, research articles– 6-15 pages, reviews – 30 pages.

Recommendations for text in MS Word:

Formulas should be written using Math Type. Figures and tables with captions should be inserted in the text. Additionally, authors present separate files for all figures and Word files of tables.

Recommendations for text in LaTeX:

Please, use standard LaTeX without macros and additional style files. The list of references should be included in the main LaTeX file. Source LaTeX file of the paper with the corresponding pdf file and files of figures should be submitted.

References in the article text are given in square brackets. The list of references should be prepared in accordance with the following samples:

- [1] Surname N. *Book Title*. Nauka Publishing House, Saint Petersburg, 2000, 281 pp.
- [2] Surname N., Surname N. Paper title. *Journal Name*, 2010, **1** (5), P. 17-23.
- [3] Surname N., Surname N. Lecture title. In: Abstracts/Proceedings of the Conference, Place and Date, 2000, P. 17-23.
- [4] Surname N., Surname N. Paper title, 2000, URL: <http://books.ifmo.ru/ntv>.
- [5] Surname N., Surname N. Patent Name. Patent No. 11111, 2010, Bul. No. 33, 5 pp.
- [6] Surname N., Surname N. Thesis Title. Thesis for full doctor degree in math. and physics, Saint Petersburg, 2000, 105 pp.

Requirements to illustrations

Illustrations should be submitted as separate black-and-white files. Formats of files – jpeg, eps, tiff.



NANOSYSTEMS:

PHYSICS, CHEMISTRY, MATHEMATICS

Журнал зарегистрирован

Федеральной службой по надзору в сфере связи, информационных технологий и массовых коммуникаций

(свидетельство ПИ № ФС 77 - 49048 от 22.03.2012 г.)

ISSN 2220-8054

Учредитель: федеральное государственное автономное образовательное учреждение высшего образования

«Санкт-Петербургский национальный исследовательский университет информационных технологий, механики и оптики»

Издатель: федеральное государственное автономное образовательное учреждение высшего образования

«Санкт-Петербургский национальный исследовательский университет информационных технологий, механики и оптики»

Отпечатано в Учреждении «Университетские телекоммуникации»

Адрес: 197101, Санкт-Петербург, Кронверкский пр., 49

Подписка на журнал НФХМ

На первое полугодие 2021 года подписка осуществляется через

ОАО Агентство «Роспечать»

Подписной индекс 57385 в каталоге «Издания органов научно-технической информации»